

H 24/3414

MONASH UNIVERSITY
THESIS ACCEPTED IN SATISFACTION OF THE
REQUIREMENTS FOR THE DEGREE OF
DOCTOR OF PHILOSOPHY

ON..... 7 March 2003


.....
For Sec. Research Graduate School Committee

Under the copyright Act 1968, this thesis must be used only under the normal conditions of scholarly fair dealing for the purposes of research, criticism or review. In particular no results or conclusions should be extracted from it, nor should it be copied or closely paraphrased in whole or in part without the written consent of the author. Proper written acknowledgement should be made for any assistance obtained from this thesis.

Addendum and Errata

Alterations and additions to the original text are highlighted in bold; negative line numbers indicate the number of lines from the bottom of the page.

Page number	Line number	Original text	Corrected text
i	6	its complexity	their complexity
	11	spectroscopist	spectroscopists
	-11	and, record	and record
ii	-13	underlying the theory	of the theory
2	-12	reduced mass the two	reduced mass of the two
4	Table I-1	Matrix	Matrix elements
	-10	net-effect	net effect
9	10	in-plane and out-of-plane bend	doubly degenerate bend
10	-10	Figure I-2	Figure I-3
14		I ^r	III^r
	-5	and, thus, is cannot	and, thus, it cannot
16	Definition		where in equation I.30
	of \bar{B}_v		$\bar{B}_v = (\bar{B} + \bar{C})/2$
32	9	Jovin-Yvon	Jobin-Yvon
33	Figure II-6	defracted	diffracted
	caption	defracted	diffracted
35	7	using a software	using software
38	-1	PC's	PC
		It's	Its
42	4	pen	pens
	11	Charge-Couple	Charge-Coupled
43	Figure III-1	CCD fornt	CCD front
44	1	<i>et.al.</i>	<i>et al.</i>
47	1	source of noises	source of noise
57	9	in Figure III.11	in Figure III.12
63	9	InfraRed Laser	Infrared Laser
	17	is an alternate	is an alternative
67	Eqn IV.1	$\bar{\epsilon}_0$	λ_0
73	1	called plasma	called a plasma
74	-1	few milli	few milliTorr by a
85	9	electron spin resonannce	electron spin resonance
90	2	the UV/vies emission	the UV/vis emission
95	16	to indicate that is generated	to indicate that it is generated
	-2	be generated in it's A-state	be generated in its A-state
	1	in Figure V-5	in Figure V-4
98	caption	seeded in New	seeded in Ne
103	1	SF ₆	SF₆ through loosely packed NaN₃ powder

Page number	Line number	Original text	Corrected text
111	7	The	They
116	Figure VI-2	cm^{-1}	nm
121	-2	in Fig. x	in Figure IV-5
122	4	shown in fig.	shown in Figure IV-5
125	3	provided a 3.5" Disk	provided on a 3.5" disk
128	5	Comparison the standard	Comparison of the standard
130	Table VI-6	D_v	$D_v \times 10^6$
132	7	Transition belonging	Transitions belonging
	26	deviation was of 1.02	deviation of 1.02
134	Ref	Phillips	Phillips
144	1	Five sets of thermocouples wires	Five sets of thermocouple wires
146	-1	collides with the	collides with the gas
149	-6	proportional to the volume.	proportional to the volume for the same number of gas molecules.
154	Heading	HFC 152a	HFC R152a
	Header	HFC 152a	HFC R152a
168	4	$v_4 + 4 v_{16}$	$v_4 + 4 v_{18}$
169	9	$v_4 + 4 v_{16}$	$v_4 + 4 v_{18}$
173	2	absorbing at 10.6 mm	absorbing at 10.6 μm
	22	As $\lambda > 1.4\text{mm}$	As wavelength with $\lambda/2 > 1.4\mu\text{m}$

Title - Explanatory Statement

Because the major part of this project involved instrumental design and development it was decided that the present structure, where the theory and description of the instruments are followed by their spectroscopic application best emphasizes the instrumental design and construction aspect of this work. Hence the application of the instrumental techniques to the spectroscopic studies of gases is treated as applying the developments to real problems. The technique used in chapter five is dispersive (not FT) and the infrared laser powered pyrolysis technique described in chapter four does not lead to spectral simplification and, thus, these techniques are not described by the title. Nevertheless, they have been included in the body of work of the thesis as they were pertinent to the development and testing of the CCD detection system constructed for monitoring emitting species generated by corona excited supersonic expansion, and, in addition, they helped to gain experience in generating NCN and CN in an alternate fashion.

*SPECTRAL SIMPLIFICATION TECHNIQUES FOR
HIGH RESOLUTION FOURIER TRANSFORM
SPECTROSCOPIC STUDIES*

*A dissertation submitted for the degree of
Doctor of Philosophy
In the School of Chemistry,
Monash University*

*Dominique R. T. Appadoo,
Bachelor of Science (Hons),
Master of Science,*

April 2002

Except where otherwise stated, the work described in this dissertation is original, and to the author's knowledge, has not yet been published or presented at any other university, either by the author himself or by any other person.

A handwritten signature in black ink, appearing to read 'Appadoo', with a stylized, cursive script.

Dominique R.T. Appadoo

*This thesis is dedicated to my Wife, Pascale,
my Daughter, Anaïs, and my Son, Joshua.*

Acknowledgements

First and foremost, I thank you, Pascale, for your support throughout the duration of the Ph.D. and much more. Your love, patience and understanding is unequalled. Anaïs and Joshua, you are the true meaning of Unconditional Love. The road has been a little bumpy for you guys, but I promise to make up for lost time.

Mum, thank you for all your Love, Encouragement and words of wisdom, and unconditional support. Thank you also for staying back, it meant an awful lot to me.

Dr. Don McNaughton and Dr. Richard Morrisson, my co-supervisors, thank you for giving me a chance. Your patience and tolerance has not gone unnoticed or unappreciated. Don, thanks for kicking my behind (every now and then) to put me back on track; I do also appreciate your encouragements and guidance throughout the long and winding road! I have learned a lot over the years and have really enjoyed working for you.

Dr. Evan Robertson, thank you for your Friendship. I also would like to thank you for all the repeated discussions about Mr. Coriolis and Mr. Fermi, and much more ... Your timely arrival in the laboratory has had a significant impact, and I am indebted to you. It was great fun being your lab partner for a short while though. All the best to you!

A huge thanks to Finlay Shanks (the FT 'Guru') and Dr Don McGilvery for solving the many frustrating printing problems by waving his magical hands. I would like also to thank Dr. Peter Thomas for showing the ropes when I was a rookie.

Thank you to John Taylor, Alan Holland, Merv and the rest of the Physics workshop for their help 'above and beyond' the call of duty. Thank you to Steve Morton for the wonderful digital pictures of the instruments I designed. Thank you to Nino Benci for your advice on various electrical jam I put myself into and for the 'free' electrical bits and pieces.

Dr. Melissa Romeo, thank you for your friendship and assisting me at polluting Bernd's air with our cigs. Dr. Bayden Wood, thank you for your friendship as well as your various invites to your parties (although I only showed up once!). Bernd, what can I say, hmm ... that's a hard one... You know I am just kidding, I am indebted to you as you have helped me tremendously with that thing called "Thesis". Our friendship has grown over the years, and I value it a lot. The 'completion' of the thesis 'on time' is partly due to you although the Table of Contents could have waited a bit longer. I still think it was 5-0, sure felt like it!

Mr. T, I am passing you the High-Res 'Baton', you're IT!! I have really enjoyed your friendship, wit and country sayings such as in "cri-bi-ji-bees!". Fei, what a.. I going to do without them muffins, cakes and cookies!!! Thank you for your friendship, and every muffin and cake you have cooked for us. It's been nice meeting you, Larissa and Mel C., all the best to you guys!!

Table of Contents

INTRODUCTION.....	i
OUTLINE OF CHAPTERS.....	ii
I SPECTROSCOPIC THEORY.....	I-1
I.1 DIATOMIC RO-VIBRATIONAL HAMILTONIAN FOR $^2\Sigma$ AND $^3\Pi$ ELECTRONIC STATES.....	I-1
I.2 LINEAR TRIATOMIC ENERGY LEVELS AND RENNER-TELLER EFFECT	I-8
I.3 ASYMMETRIC ROTOR HAMILTONIAN & SELECTION RULES	I-13
I.3.1 <i>Fermi and Coriolis resonances</i>	I-19
I.4 BIBLIOGRAPHY.....	I-21
II TOOLS FOR SPECTRAL MEASUREMENT & ANALYSIS.....	II-22
II.1 SPECTRAL MEASUREMENT	II-22
II.1.1 <i>Fourier transform spectrometry</i>	II-22
II.1.2 <i>Dispersive spectrometry</i>	II-32
II.2 SPECTRAL ANALYSIS	II-35
II.2.1 <i>Assignment</i>	II-35
II.2.2 <i>Data Reduction</i>	II-38
II.3 BIBLIOGRAPHY	II-39
III A CHARGE-COUPLED DEVICE CAMERA FOR QUICK SPECTRAL PROFILING	III-41
III.1 INTRODUCTION	III-41
III.2 THE CCD DETECTOR	III-43
III.2.1 <i>CCD features</i>	III-46
III.2.2 <i>Noise considerations</i>	III-47
III.2.3 <i>Design and Construction of CCD imager</i>	III-49
III.2.4 <i>CCD Electronics and Logic Design</i>	III-50
III.2.5 <i>Performance Testing of ST-001A imager</i>	III-55
III.3 BIBLIOGRAPHY.....	III-60

IV TOWARDS HIGH RESOLUTION SPECTROSCOPY OF TRANSIENTS WITH LOW INTERNAL ENERGIES.....	IV-61
IV.1 INTRODUCTION.....	IV-61
IV.2 INFRARED LASER POWERED PYROLYSIS.....	IV-63
IV.2.1 IRLPP cell and optical setup.....	IV-64
IV.3 CORONA EXCITED SUPERSONIC EXPANSION.....	IV-66
IV.3.1 Supersonic Free Jet Expansions.....	IV-66
IV.3.2 Corona Discharge.....	IV-71
IV.3.3 Corona Excited Supersonic Expansion.....	IV-73
IV.3.4 CESE Chamber and performance testing.....	IV-74
IV.4 BIBLIOGRAPHY.....	IV-83
V UV/VIS EMISSION SPECTRUM OF THE CYANONITRENE RADICAL.....	V-84
V.1 INTRODUCTION.....	V-84
V.2 EXPERIMENTAL.....	V-87
V.3 RESULTS & DISCUSSIONS.....	V-90
V.3.1 Production of NCN_3	V-90
V.3.2 Characterisation of IRLPP & CESE emission spectra.....	V-91
V.3.3 UV/vis emission spectrum of NCN	V-97
V.4 CONCLUSIONS.....	V-103
V.5 BIBLIOGRAPHY.....	V-105
VI HIGH RESOLUTION FT JET-EMISSION SPECTRUM OF THE CYANO RADICAL FROM THE MID TO NEAR-IR.....	VI-107
VI.1 INTRODUCTION.....	VI-107
VI.2 EXPERIMENTAL.....	VI-112
VI.3 RESULTS & DISCUSSIONS.....	VI-113
VI.3.1 Characterisation of CESE emission spectra.....	VI-116
VI.3.2 High Resolution FT emission spectrum of the A-X system of jet-cooled CN	VI-117
VI.4 CONCLUSIONS.....	VI-132
VI.5 BIBLIOGRAPHY.....	VI-134

VII AN ENCLOSIVE FLOW COOLING CELL FOR SIMPLIFICATION OF GAS-PHASE SPECTRA.....	VII-136
VII.1 INTRODUCTION.....	VII-136
<i>VII.1.1 Spectral simplification by cooling</i>	<i>VII-136</i>
<i>VII.1.2 Available non-equilibrium cooling techniques</i>	<i>VII-137</i>
VII.2 METHODOLOGY	VII-141
<i>VII.2.1 Design of Enclosive Flow-Cooling cell</i>	<i>VII-141</i>
<i>VII.2.2 Design of Transfer Optics</i>	<i>VII-145</i>
<i>VII.2.3 Mode of operation</i>	<i>VII-146</i>
<i>VII.2.4 Experimental Setup and Conditions</i>	<i>VII-147</i>
VII.3 RESULTS & DISCUSSIONS.....	VII-149
<i>VII.3.1 Test for efficiency of EFC cell: N₂O spectra</i>	<i>VII-149</i>
VII.4 CONCLUSIONS.....	VII-152
VII.5 BIBLIOGRAPHY	VII-153
VIII HIGH RESOLUTION FTIR SPECTRUM OF THE ν_4 MODE OF HFC 152A.....	VIII-154
VIII.1 INTRODUCTION	VIII-154
<i>VIII.1.1 Previous Spectroscopic and Theoretical studies of R152a</i>	<i>VIII-156</i>
VIII.2 EXPERIMENT	VIII-157
VIII.3 RESULTS, ANALYSIS & DISCUSSIONS	VIII-158
<i>VIII.3.1 Data Analysis & Discussions</i>	<i>VIII-163</i>
VIII.4 CONCLUSIONS	VIII-169
VIII.5 BIBLIOGRAPHY	VIII-170
IX APPENDIX.....	IX -171
IX.A SAFETY ISSUES	IX -171
IX.B TECHNICAL DRAWINGS.....	IX -177
IX.C R^2 TO N^2 HAMILTONIAN TRANSFORMATION.....	IX -187
IX.D CS CHARACTER TABLE & SAMPLE GSCD CALCULATION	IX -188

Introduction

Molecules have long been known to exhibit unique spectral signatures characteristic of their geometry and symmetry. From the analysis of such spectra, fundamental molecular parameters have been extracted, which have in turn been used to obtain experimental estimates of factors such as force constants, bond strengths, lengths and angles, potential surfaces and thermodynamic properties. The ease of extraction of molecular parameters from the observed spectra is dictated by its complexity. Theory has shown that the degree of complexity depends on factors such as the molecular mass, symmetry, the number of atoms in the molecule and most importantly, the temperature, as these factors dictate spectral linewidths and line spacings, as well as bandwidths and band structures. However, of all these factors, only the temperature is experimentally controllable and, as a result, spectroscopists have resorted to cooling techniques to simplify spectra congested with closely spaced transitions and overlapping band structures. However, traditional cooling techniques are hampered by accompanying reductions in the vapour pressure of spectroscopic gases, thereby limiting this type of study to gases with appreciable vapour pressures at these cryogenic temperatures. Over the years, cooling techniques such as supersonic expansion, diffusive trapping and enclosure-flow cooling have been developed by spectroscopists to study gases at temperatures well below their freezing point when they have vanishing vapour pressures.

The focus of this study is to generate rotationally cold stable and labile gas-phase molecules and, record and analyse the simplified spectra. A Corona-Excited Supersonic Expansion (CESE) system has been designed and built to produce rotationally cold transient molecules. In order to characterise and monitor molecular species generated in the discharge, and optimise experimental conditions for high-resolution spectroscopic studies in emission, a Charge-Coupled Device (CCD) detector has also been designed and built. The CCD detector coupled to a grating spectrometer was first tested by recording the low-resolution UV emission spectrum of NCN generated by infrared laser powered pyrolysis and CESE. Transitions previously observed were confirmed and, in addition, new transitions were observed. The spectrum of the CN radical generated by CESE was then recorded at low resolution with the CCD-based detection system in the UV/vis regions before a Fourier transform spectrometer was used to record the CN

spectrum at high resolution in the visible, near and mid-IR regions. Improved molecular parameters were obtained from the ensuing analysis of the CN spectrum.

In addition, an Enclosive-Flow Cooling (EFC) cell was designed and built to generate rotationally cold stable molecules for absorption studies. The cell's efficiency was tested by recording the high resolution Fourier transform infrared absorption spectrum of N_2O . This study enabled the determination of the optimum rotational temperature realisable with the present EFC cell. The high resolution Fourier transform infrared spectrum of CH_3CHF_2 was then recorded and studied. The weak ν_4 band has been measured and analysed, and its spectroscopic constants extracted.

Outline of Chapters

In Chapter I, a description of the spectroscopic theory pertaining to the molecular systems being studied is offered. In particular, Hamiltonians describing rotational, vibrational and electronic (ro-vibronic) energy levels of $^2\Sigma$ and $^2\Pi$ electronic states of diatomic molecules, vibrational and electronic (vibronic) energy levels of $^3\Sigma$ and $^3\Pi$ electronic states of linear triatomic molecules, and rotational and vibrational (rovibrational) energy levels of ground electronic states of oblate asymmetric top molecules are presented. In addition, selection rules and expected spectrum are described.

In Chapter II, a brief account underlying the theory behind Fourier transform and dispersive spectrometry is presented. The Brüker IFS120HR spectrometer, and the Jobin-Yvon HR1000 monochromator coupled to a Charge Couple Device (CCD) used to measure and record spectra in this study are also described and illustrated. Software used for assigning and fitting spectra are briefly described.

In Chapter III, a brief background and description of charge-coupled devices along with a detailed description of the custom-built CCD detector designed to characterise and monitor the emission of transients are presented. Tests performed to assess the efficiency of the CCD detector are also presented and discussed.

In Chapter IV, the backgrounds and theories of the two emission techniques used in this study to generate transients are presented. The first method, the relatively new technique of InfraRed Laser Powered Pyrolysis (IRLPP), was used as an emission source of molecular origin to test the CCD-detection system. The second method, the

Corona-Excited Supersonic Expansion (CESE) technique, was used to generate rotationally cold radicals. A detailed description of the CESE system is also offered as well as tests performed on it.

In Chapter V, low-resolution UV/vis emission CCD spectra of transients generated by IRLPP and CESE of NCN_3 are presented. These spectra have been used to characterise the products of both experiments. Vibronic transitions of the NCN emission spectrum are assigned, and both qualitative and quantitative analyses are presented.

In Chapter VI, high-resolution visible, near and mid-IR FT emission spectra of CN generated by CESE of CH_3CN are presented. The spectra are then analysed, and the results from the ensuing data reduction are presented and discussed.

In Chapter VII, the background and theory of the Enclosive-Flow Cooling (EFC) technique used to cool the internal degrees of freedom of molecules are presented. A detailed description of the design and construction of the EFC cell and the optical set-up used to couple the EFC cell to the FT spectrometer are presented. Tests performed on the EFC system are presented and its efficiency discussed.

In Chapter VIII, the background to ozone depleting gases and their proposed replacements gases is offered with a focus on CH_3CHF_2 (R152a). The high resolution Fourier transform infrared spectrum of CH_3CHF_2 is presented followed by the analysis of the ν_4 band and a discussion of the results.

The Appendix contains four major sections. The first section, Section A, deals with safety issues. In particular, potential hazards are identified and precautionary steps taken to minimise the health risk are presented. Section B is divided in 2 sub-sections which contain technical drawings used to build both the CCD detector described in Chapter III and the Enclosive Flow Cooling system described in Chapter VII. In Section C, the equations enabling transformation from the R^2 -Hamiltonian to N^2 -Hamiltonian are presented. In Section D, the C_s Character table along with sample calculations of ground state combination differences which were used to confirm the J-assignment of the ν_4 band of R152a are presented.

I Spectroscopic Theory

I.1 Diatomic Ro-Vibrational Hamiltonian for $^2\Sigma$ and $^2\Pi$ electronic states

The rotational-vibrational-electronic (rovibronic) energy levels of a diatomic molecule can be obtained by solving the well-known Schrödinger equation

$$\hat{H}\Psi = E\Psi \quad (1.1)$$

where \hat{H} , Ψ and E are the overall Hamiltonian operator, wavefunction and eigenvalues of the system respectively. According to the Born-Oppenheimer approximation internal molecular energies can be treated separately, leading to $\hat{H} = \hat{H}_{elec} + \hat{H}_{vib} + \hat{H}_{rot}$ and $\Psi = \Psi_{elec} \Psi_{vib} \Psi_{rot}$. Thus, the eigenvalues of closed-shell molecules (molecules with no unpaired electrons *i.e.* $^1\Sigma$) representing the rovibronic energy levels of such systems can be expressed as

$$E(\nu, J) = T_e + G(\nu) + F_v(J) \quad (1.2)$$

where ν and J are the vibrational and rotational quantum numbers respectively, T_e , the electronic energy, and, $G(\nu)$ and $F_v(J)$ the vibrational and rotational energy expressions respectively.

The vibrational energy expression for a diatomic molecule has the form

$$G(\nu) = \omega_e \left(\nu + \frac{1}{2}\right) - \omega_e x_e \left(\nu + \frac{1}{2}\right)^2 + \omega_e y_e \left(\nu + \frac{1}{2}\right)^3 + \omega_e z_e \left(\nu + \frac{1}{2}\right)^4 + \dots \quad (1.3)$$

where ω_e represents the equilibrium vibrational frequency, and $\omega_e x_e$, $\omega_e y_e$ and $\omega_e z_e$ are constants accounting for anharmonicities in the potential energy function.

Whereas the rotational energy expression has the form

$$F_v(J) = B_v [J(J+1) - \Omega^2] - D_v [J(J+1) - \Omega^2]^2 + \dots \quad (1.4)$$

where Ω represents the total electronic angular momentum (orbital + spin: $|\Lambda + \Sigma|$) about the internuclear axis and, B_v and D_v , the vibrationally dependent inertial rotational constant and first-order centrifugal distortion constant (CDC) respectively.

The rotational constant is expressed as a polynomial in $(\nu + \frac{1}{2})$

$$B_v = B_e - \alpha_e \left(\nu + \frac{1}{2}\right) + \gamma_e \left(\nu + \frac{1}{2}\right)^2 + \dots \quad (1.5)$$

where B_e , the inertial rotational constant with fixed nuclei, is defined by

$$B_e = \frac{\hbar}{4\pi c I_{B_e}} \quad (1.6)$$

where $I_{B_e} = \mu r_e^2$ with r_e being the equilibrium distance and μ the reduced mass of the two atoms; α_e is a small correction constant accounting for the change in the bond length during rotation due to anharmonic vibrations. An analogous expression is used to describe the vibrational dependence of CDC's that account for the non-rigidity of the molecule

$$D_v = D_e + \beta_e \left(\nu + \frac{1}{2}\right) + \dots \quad (1.7)$$

where D_e represents the CDC for a vibrationless state and β_e is similar to α_e . Higher order CDC's, H_v, L_v, \dots , are expressed in similar fashion.

Rovibronic energies can also be represented in a more compact form by using the Dunham expansion¹

$$E(\nu, J) = \sum_{l,m} Y_{l,m} \left(\nu + \frac{1}{2}\right)^l [J(J+1) - \Omega^2]^m \quad (1.8)$$

where the $Y_{l,m}$'s are explicitly tied to the coefficients of a power series defining the diatomic potential, and, for heavy molecules, are closely related to the equilibrium constants of Equations (I.3), (I.5) and (I.7)

$$Y_{1,0} \approx \omega_e, \quad Y_{0,1} \approx B_e \quad (I.9)$$

When the electron spin, S , and orbital, L , angular momenta contribute to the overall angular momentum of the molecule, coupling of the various types of angular momenta (including rotation) can occur giving rise to two additional terms, \hat{H}_β and \hat{H}_{hfs} , to the overall Hamiltonian operator described in Equation (I.1).² The contribution to the rotational energy of the latter term is negligible and, thus, is assumed to be zero. The rotational Hamiltonian operator is defined as

$$\hat{H}_{rot} = B\hat{R}^2 = B(\hat{J} - \hat{L} - \hat{S})^2 \quad (I.10)$$

where $\hat{J} = \hat{L} + \hat{S} + \hat{R}$ is the total angular momentum operator. The fine structure Hamiltonian operator, \hat{H}_β , consists of three terms

$$\hat{H}_\beta = \hat{H}_{so} + \hat{H}_r + \hat{H}_{ss} \quad (I.11)$$

where \hat{H}_{so} represents the spin-orbit interaction, \hat{H}_r the spin-rotation and \hat{H}_{ss} the spin-spin interaction operators. The matrix elements of \hat{H}_{ss} contribute negligibly to the rotational energy and cannot be detected at the resolution used in this study and, consequently, \hat{H}_{ss} is assumed to be zero. However, both \hat{H}_{so} and \hat{H}_r contribute significantly to the rotational energy of the molecule. The spin-orbit Hamiltonian has the form

$$\hat{H}_{so} = A(r)\hat{L} \cdot \hat{S} \quad (I.12)$$

where $A(r)$ is the spin-orbit coupling constant (is zero for electronic states with $\Lambda = 0$), \hat{L} and \hat{S} are the electronic orbital and spin angular momentum operators respectively. The spin-rotation Hamiltonian is defined by

$$\hat{H}_r = \gamma(r)\hat{R} \cdot \hat{S} = \gamma(r)(\hat{J} - \hat{L} - \hat{S}) \cdot \hat{S} \quad (I.13)$$

where $\gamma(r)$ is the spin-rotation coupling constant and \hat{R} the rotational angular momentum operator.

In this study, an effective Hamiltonian as described by Brown *et al.*³ is used where \hat{N} , the total angular momentum excluding spin, is used in place of \hat{R} and is defined as $\hat{N} = \hat{J} - \hat{S}$. Thus, $(\hat{J} - \hat{L} - \hat{S})$ in Equations (I.10) and (I.13) needs to be replaced with $(\hat{N} - \hat{L})$. Explicit forms of these Hamiltonians can be found in the paper by Brown *et al.*³ The matrix elements of the ${}^2\Sigma$ and ${}^2\Pi$ \hat{N}^2 - Hamiltonians have been described by Amiot *et al.*⁴ and Douay *et al.*⁵ and are displayed in Table I-1 and Table I-2 respectively.

Table I-1 Matrix elements for the ground ${}^2\Sigma^+$ of CN $X_- = J - 0.5$, $X_+ = J + 0.5$, $Y = J + 1.5$ adapted from Douay *et al.*⁵

Constant	Parity	Matrix	Constant	Matrix
T	e	1	L	$-X_-^4 X_+^4$
	f	1		$-X_+^4 Y^4$
B	e	$X_- X_+$	γ	$0.5 X_-$
	f	$X_+ Y$		$-0.5 Y$
D	e	$-X_-^2 X_+^2$	γ_D	$0.5 X_-^2 X_+$
	f	$-X_+^2 Y^2$		$-0.5 Y^2 X_+$
H	e	$X_-^3 X_+^3$	γ_H	$0.5 X_-^3 X_+^2$
	f	$X_+^3 Y^3$		$-0.5 Y^3 X_+^2$

The above-mentioned interactions have the net-effect of splitting the rotational energy levels into a number of components. For the non-degenerate ${}^2\Sigma^+$ electronic state each rotational level, N , is split into two sub-levels, F_1 and F_2 , of parity e and f respectively due to spin-rotation interaction. Whereas the doubly-degenerate ${}^2\Pi_i$ has two components, ${}^2\Pi_{\frac{1}{2},i}(F_1)$ and ${}^2\Pi_{\frac{3}{2},i}(F_2)$, originating from the coupling of the spin and orbital angular momenta where the subscript 'i' indicates that the ${}^2\Pi_{\frac{1}{2},i}$ which normally lies at higher energy than the ${}^2\Pi_{\frac{3}{2},i}$ now lies below it. The degeneracy in each component is lifted through perturbation of neighbouring ${}^2\Sigma^\pm$ electronic states generating sub-levels with e and f parities. Electronic states of the same multiplicity with orbital angular momentum differing by one may perturb each other giving rise to

doubling which further 'splits' each rotational level into two components. In this case, the doubly-degenerate ${}^2\Pi (\pm\Lambda)$ state is perturbed by neighbouring ${}^2\Sigma^\pm$ states leading to Λ -doubling parameters p and q . The matrix elements of p and q have been determined by Amiot *et al.*⁴ and are listed in Table I-2.

The selection rules dictating the transitions between rovibrational levels of the ${}^2\Pi$ and ${}^2\Sigma^+$ electronic states are

$$\begin{aligned} \Delta J = 0, e \leftrightarrow f \\ \Delta J = \pm 1, e \leftrightarrow e \text{ and } f \leftrightarrow f \end{aligned} \quad (\text{I.14})$$

with each e sub-rotational level having parity $+(-1)^{J-\frac{1}{2}}$ while f sub-rotational levels have parities $-(-1)^{J-\frac{1}{2}}$ as defined by Kopp & Hougen.⁶ As a result, the $A^2\Pi_i - X^2\Sigma^+$ system of CN is composed of four sets of P , Q and R branches:

$$\begin{aligned} {}^2\Pi_{\frac{1}{2}} - {}^2\Sigma_{\frac{1}{2}} &\rightarrow F'_1 \rightarrow F''_1 \\ {}^2\Pi_{\frac{1}{2}} - {}^2\Sigma_{-\frac{1}{2}} &\rightarrow F'_1 \rightarrow F''_2 \\ {}^2\Pi_{\frac{3}{2}} - {}^2\Sigma_{\frac{1}{2}} &\rightarrow F'_2 \rightarrow F''_1 \\ {}^2\Pi_{\frac{3}{2}} - {}^2\Sigma_{-\frac{1}{2}} &\rightarrow F'_2 \rightarrow F''_2 \end{aligned} \quad (\text{I.15})$$

The parity of rotational levels along with the transitions dictated by the selection rules of Equation (I.14) are illustrated in Figure I-1.

Table I-2 Matrix elements for the first excited electronic state, ${}^2\Pi_1$, of CN:
 $X_+ = J + 0.5$, $z = (J - 0.5)(J + 1.5)$ from Amiot *et al.*⁴

	State Index	Matrix Element		State Index	Matrix Element
T	1,1	1	P _D	2,2	$\mp 0.5X_+(z+2)$
	2,2	1		1,2 & 2,1	$\pm 0.25X_+\sqrt{z}$
A	1,1	0.5	P _H	2,2	$\mp 0.5X_+^3(z+4)$
	2,2	-0.5		1,2 & 2,1	$\pm 0.5X_+^3\sqrt{z}$
A _D	1,1	0.5z	q	2,2	$\mp X_+$
	2,2	0.5(z+2)		1,2 & 2,1	$\pm 0.5X_+\sqrt{z}$
B	1,1	z	q _D	1,1	$\mp 0.5X_+z$
	2,2	z+2		2,2	$\mp 0.5X_+(3z+4)$
	1,2 & 2,1	$-\sqrt{z}$		1,2 & 2,1	$\pm 0.5X_+\sqrt{z}(z+2)$
D	1,1	$-z(z+1)$	q _H	1,1	$\mp 0.5X_+^3z$
	2,2	$-(z+1)(z+4)$		2,2	$\mp 2X_+^3(z+2)$
	1,2 & 2,1	$2\sqrt{z}(z+1)$		1,2 & 2,1	$\pm 0.5X_+^3\sqrt{z}(z+4)$
H	1,1	$z(z+1)(z+2)$	γ	2,2	-1
	2,2	$(z+1)(z^2+8z+8)$		1,2 & 2,1	$0.5\sqrt{z}$
	1,2 & 2,1	$-\sqrt{z}(z+1)(3z+4)$		1,1	-0.5z
L	1,1	$-z(z+1)^2(z+4)$	γ _D	2,2	$-0.5(3z+4)$
	2,2	$-(z+1)^2(z^2+12z+16)$		1,2	$0.5\sqrt{z}(z+2)$
	1,2 & 2,1	$4\sqrt{z}(z+1)^2(z+2)$		1,1	$-z(z+1)$
p	2,2	$\mp 0.5X_+$	γ _H	2,2	$-2(z+1)(z+2)$
				1,2	$0.5\sqrt{z}(z^2+5z+4)$

I.2 Linear triatomic energy levels and Renner-Teller effect

Since the NCN emission was recorded with a monochromator coupled to an array detector using first order dispersion only low resolution spectra were collected leading to the observation of vibrational band structures of electronic systems. As a result, only theoretical treatment concerning vibrational and electronic (vibronic) motions will be considered.

Vibronic energies of linear molecules are obtained by solving the Schrödinger equation

$$\hat{H}_e \Psi = E_e \Psi \quad (I.16)$$

where \hat{H}_e is the phenomenological Hamiltonian operator describing the electronic and vibrational motions. The Born-Oppenheimer approximation enables the separation of both types of motion ('calculation' of both types of motion separately) and thus, \hat{H}_e can be replaced by $\hat{H}_e + \hat{H}_{vib}$ leading to a vibronic energy expression for closed-shell molecules (in a non-degenerate electronic state) similar to that of diatomic molecules (see Equation (I.2))

$$E_{ev} = T_e + G(v_1, v_2, v_3) \quad (I.17)$$

where T_e is the electronic energy and $G(v_1, v_2, v_3)$ the vibrational energy of vibrational modes v_1 , v_2 and v_3 associated with vibrational quanta v_1 , v_2 and v_3 respectively. The vibrational energy including anharmonicities has the general form

$$\begin{aligned} G(v_1, v_2, v_3) = & \sum_i \omega_i (v_i + d_i/2) \\ & + \sum_i \sum_{k \neq i} x_{ik} (v_i + d_i/2)(v_k + d_k/2) \\ & + \sum_i \sum_{k \neq i} g_{ik} l_i l_k + \dots \end{aligned} \quad (I.18)$$

The parameters of Equation (I.18) are described in Table I-3.

Table I-3 Definition of parameters used in Equation (I.18). For non-degenerate vibrations, $g_{ik} = l_i = 0$, and $d_i = 1$.

Parameters	Definition
ν_i, ν_k	vibrational quantum numbers
ω_i	vibrational wavenumber
x_{ik}, g_{ik}	anharmonicity constants
d_i, d_k	degeneracies of ν_i, ν_k

NCN is a linear symmetrical triatomic molecule with $D_{\infty h}$ symmetry. It has four $(3N-5)$ normal modes of vibrations, two of which are degenerate: the symmetric stretch, ν_1 , the in-plane and out-of-plane bend, ν_2 , and the asymmetric stretch, ν_3 . The ν_1 mode is infrared inactive but Raman active, and ν_2 is doubly degenerate, and ν_3 is infrared active. The vibrational expression of triatomic linear molecules with doubly-degenerate ν_2 mode has the form

$$\begin{aligned}
 G(\nu_1, \nu_2, \nu_3) = & \omega_1 (\nu_1 + \frac{1}{2}) + \omega_2 (\nu_2 + 1) + \omega_3 (\nu_3 + \frac{1}{2}) + g_{22} l_2^2 \\
 & x_{11} (\nu_1 + \frac{1}{2})^2 + x_{12} (\nu_1 + \frac{1}{2})(\nu_2 + 1) + x_{13} (\nu_1 + \frac{1}{2})(\nu_3 + \frac{1}{2}) \\
 & x_{22} (\nu_2 + 1)^2 + x_{23} (\nu_2 + 1)(\nu_3 + \frac{1}{2}) \\
 & x_{33} (\nu_3 + \frac{1}{2})^2 + \dots
 \end{aligned} \tag{I.19}$$

When the bending vibrational mode is singly excited, the two degenerate modes cannot be uncoupled and hence, the molecule, in a bent position, precesses about the internuclear axis generating vibrational angular momenta. Not unlike other angular momenta, it is quantised; its component, l_2 , about the internuclear axis has magnitude

$$l_2 = \nu_2, \nu_2 - 2, \nu_2 - 4, \dots, 1 \text{ or } 0 \tag{I.20}$$

corresponding to vibrational species $\Sigma, \Pi, \Delta, \dots$ as indicated in Figure I-2

Λ	l	ν
\downarrow	\downarrow	\downarrow
Γ	4	
Δ	2	4
Π	0	
Φ	3	
Σ	1	3
Δ	2	
Σ	0	2
Π	1	1
Σ	0	0

Figure I-2 Symmetry species, Λ , of levels of a degenerate vibrational mode, ν , according to the vibrational angular momentum, l .

Coupling of vibrational and electronic orbital angular momenta lead to vibronic angular momenta with component, K , about the internuclear axis defined by

$$K = |\pm\Lambda \pm l| \quad (\text{I.21})$$

where $K = 0, 1, 2, \dots$ correspond to vibronic states $\Sigma, \Pi, \Delta, \dots$. Symmetry species of vibrational levels of a particular electronic state can be determined by taking the cross product the species of the vibrational levels by that of the electronic state involved. Thus, a singly excited degenerate vibration (a Π vibrational state) in a Π electronic state will yield

$$\Pi \otimes \Pi = \Sigma^+ + \Sigma^- + \Pi \quad (\text{I.22})$$

as shown in Figure I-2.

The interaction of vibrational and electronic orbital angular momenta of degenerate vibrational and electronic states 'causes' the vibrational levels to split into vibronic levels as first recognised by Herzberg and Teller⁷ in 1933, and Renner⁸ the following year. This splitting is commonly referred to the Renner-Teller effect by spectroscopists nowadays. Interaction with the electron spin angular momentum lead to further splitting similar to that of the spin-orbit splitting of diatomic molecules described by Equation (I.12). The splitting that occurs when these three angular momentum interact is illustrated in Figure I-3. It shows the case of the degenerate vibration, ν_2 , of a linear triatomic molecule in a ${}^3\Pi$ excited electronic state.

On the left of the diagram, the spin-orbit components are shown in the absence of Renner-Teller effects, while on the right the Renner-Teller components are depicted in the absence of spin-orbit interactions. The energy separation, E_{RT} , for a degenerate vibration in a ${}^3\Pi$ were determined by Hougen⁹ and are defined by

$$\begin{aligned}
 E({}^3\Sigma_1^-) &= +\sqrt{A^2 + (\epsilon\omega_2)^2} - \frac{\epsilon^2\omega_2}{4} \\
 E({}^3\Sigma_0^+) &= +|\epsilon\omega_2| - \frac{\epsilon^2\omega_2}{4} \\
 E({}^3\Delta_3) &= +A - \frac{3}{4}\epsilon^2\omega_2 \\
 E({}^3\Delta_2) &= -\frac{3}{4}\epsilon^2\omega_2 \\
 E({}^3\Delta_1) &= -A - \frac{3}{4}\epsilon^2\omega_2 \\
 E({}^3\Sigma_0^-) &= -|\epsilon\omega_2| - \frac{\epsilon^2\omega_2}{4} \\
 E({}^3\Sigma_1^+) &= -\sqrt{A^2 + (\epsilon\omega_2)^2} - \frac{\epsilon^2\omega_2}{4}
 \end{aligned} \tag{I.23}$$

where A is the spin-orbit coupling constant, ϵ is the Renner-Teller parameter and ω_2 the wavenumber value of the degenerate bending mode. The vibronic species on the left-hand side of the above-mentioned equations are depicted in Figure I-3.

The energy of such a system can now be described by

$$E_{ev} = T_e + G(v_1, v_2, v_3) + E_{RT} \tag{I.24}$$

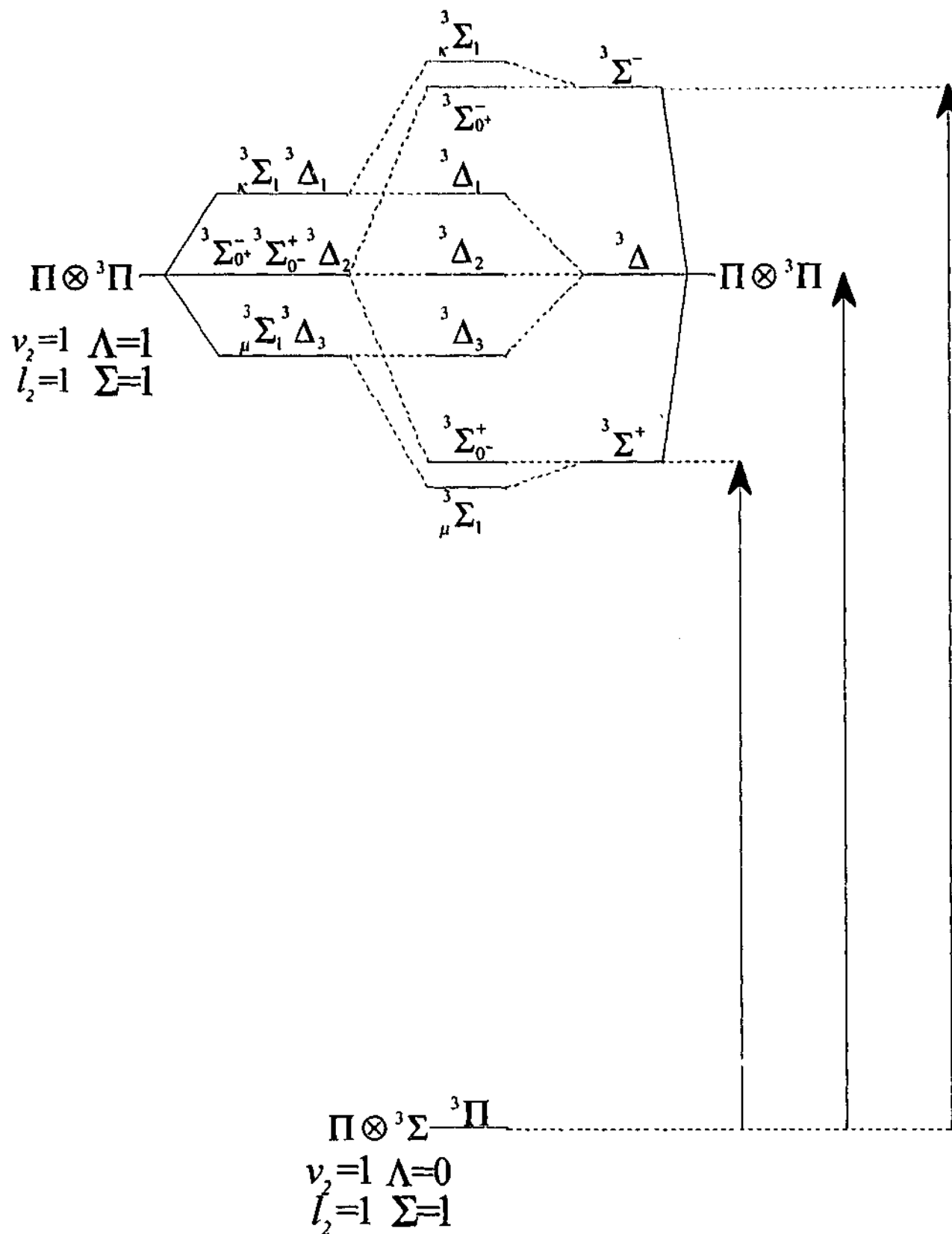


Figure I-3 Schematic of energy level diagram showing the splitting that occurs when vibrational and electronic orbital angular momenta of degenerate vibrational and electronic states couple.

I.3 Asymmetric Rotor Hamiltonian & Selection Rules

A detailed (but not thorough) description of the asymmetric rigid-rotor Hamiltonian and the selection rules governing the transition will be offered in this section while the non-rigid case will only be stated along with its matrix elements. The reader is referred to the excellent books written by Herzberg¹⁰, Bunker¹¹, Bernath¹², and Duxbury¹³ for a more thorough explanation.

A molecule is defined as asymmetric if none of its principal moments of inertia are zero and no two are equal

$$I_A \neq I_B \neq I_C \neq 0.$$

The Ray¹⁴ parameter, κ , defined by

$$\kappa = \frac{2B - A - C}{A - C} \quad (I.25)$$

determines the degree of asymmetry with respect to the limiting oblate and prolate cases where $\kappa = +1$ and -1 respectively; A , B and C are the usual inertial rotational constants of the asymmetric top molecule. The degree of asymmetry is also reflected in the complexity of the spectrum of such a molecule which is due in part to the lifting of the $(2J+1)$ degeneracy associated with each rotational level J . The Hamiltonian describing these energy levels is accordingly quite complex and, unlike the case for symmetric rotors and linear molecules, derivation of energy expressions describing the energy levels is not possible. The eigenvalues and eigenfunctions of asymmetric top molecule can be obtained however by setting up the Hamiltonian matrix in basis set consisting of linear combinations of symmetric top wavefunctions.

The general form of the rotational Hamiltonian operator, \hat{H}_{rot} , for an asymmetric top molecule is

$$\hat{H}_{rot} = (A\hat{J}_a^2 + B\hat{J}_b^2 + C\hat{J}_c^2) / \hbar^2 \quad (I.26)$$

where a , b and c are the principal axes corresponding to the conventional x , y , and z axes according to the representations listed in Table I-4.

The r and l notation correspond to the right-handed and left-handed cyclic association of the x , y , and z axes to the a , b and c .

Table I-4 Possible cyclic permutations of a , b and c principal axes used to represent the conventional x , y and z axes.

	I'	II'	III'	I'	II'	III'
x	b	c	a	c	a	b
y	c	a	b	b	c	a
z	a	b	c	a	b	c

Using the prolate basis set $|J,K\rangle$ with the I' representation the rotational Hamiltonian for asymmetric top molecules can be expressed as

$$\hat{H}_{rot} = \left\{ \left[\frac{(A+B)}{2} \right] \hat{J}^2 + \left[C - \frac{(A+B)}{2} \right] \hat{J}_c^2 + \left[\frac{(A-B)}{4} \right] \left[(\hat{J}_m^+)^2 + (\hat{J}_m^-)^2 \right] \right\} \quad (1.27)$$

with non-vanishing matrix elements

$$\begin{aligned} \langle J,K | \hat{J}^2 | J,K \rangle &= J(J+1) \\ \langle J,K | \hat{J}_z^2 | J,K \rangle &= K^2 \\ \langle J,K \pm 2 | (\hat{J}_m^+)^2 | J,K \rangle &= \left\{ \left[J(J+1) - (K \pm 1)(K \pm 2) \right] \left[J(J+1) - K(K \pm 1) \right] \right\}^{1/2} \end{aligned} \quad (1.28)$$

For asymmetric top molecules the component, K , of the total angular momentum, J , along the symmetry axis is no longer constant and, thus, is cannot be considered as a 'good' quantum number. The limiting cases of symmetric tops are used to define rotational states of asymmetric top molecules. The rotational energy levels are now labelled $J_{K_a K_c}$, and K_a or K_c is used in place of K depending on whether the molecule is near-prolate or near-oblate top respectively.

Dennison¹⁵ has shown that the symmetry species of a rotational level, $J_{K_a K_c}$, is '+' for $J_{0,0}$ and $J_{J,0}$ with subsequent pairs of levels having alternating parities as shown in Table I-5. The parity selection rule is such that only levels of the same K_a or K_c species can interact. As shown in Table I-5 the K -even levels have '+' parity and K -odd levels '-' where K represents K_a or K_c . As a result, the off-diagonal matrix elements, $\langle J, K \pm 2 | (\hat{J}_m^\pm)^2 | J, K \rangle$ are found to be non-vanishing and, thus, contribute to the rotational energy as indicated in Equation (I.28).

Table I-5 Assignment of symmetry species and parities to K rotational levels associated with $J=3$.

$J_{K_a K_c}$	$K_a K_c$ parity	Overall parity	King <i>et al.</i> notation ¹⁶	Wang ¹⁷
$3_{3,0}$	--	-	oe	O^+
$3_{3,1}$	--	+	oo	O^-
$3_{2,1}$	+-	-	eo	E^+
$3_{2,2}$	++	+	ee	E^-
$3_{1,2}$	--	-	oe	O^+
$3_{1,3}$	--	+	oo	O^-
$3_{0,3}$	+-	-	eo	E^+

With the inclusion of centrifugal forces distorting the molecule during rotation, the rotational Hamiltonian operator has the form

$$\begin{aligned} \hat{H}_{rot} = & \sum_{\alpha} B_{\alpha} \hat{J}_{\alpha}^2 + \sum_{\alpha\beta} T_{\alpha\beta} \hat{J}_{\alpha}^2 \hat{J}_{\beta}^2 + \sum_{\alpha} \Phi_{\alpha\alpha\alpha} \hat{J}_{\alpha}^6 + \\ & \sum_{\alpha\neq\beta} \Phi_{\alpha\alpha\beta} (\hat{J}_{\alpha}^4 \hat{J}_{\beta}^2 + \hat{J}_{\beta}^2 \hat{J}_{\alpha}^4) + \Phi_{xyz} (\hat{J}_x^2 \hat{J}_y^2 \hat{J}_z^2 + \hat{J}_z^2 \hat{J}_y^2 \hat{J}_x^2) \end{aligned} \quad (1.29)$$

Watson¹⁸ has shown that using symmetry arguments and some intricate manipulations this rather complex Hamiltonian can be reduced in two ways commonly referred to as the *A*-reduced and *S*-reduced Hamiltonians. Since only the *A*-reduced Hamiltonian in the *I'* representation is used in this study, accordingly only the matrix elements for the *A*-reduced case are reported

$$\begin{aligned} \langle \nu, J, K | \hat{H}_{rot} | \nu, J, K \rangle = & \nu + \bar{B}_v J(J+1) + (A_v - \bar{B}_v) K^2 - \Delta_v J^2 (J+1)^2 \\ & - \Delta_{JK} J(J+1) K^2 - \Delta_K K^4 + \Phi_{JJJ} J^3 (J+1)^3 + \\ & \Phi_{JJK} J^2 (J+1)^2 K^2 + \Phi_{JKK} J(J+1) K^4 + \Phi_{KKK} K^6 \\ & - \Lambda_{JJJ} J^4 (J+1)^4 - \Lambda_{JJK} J^3 (J+1)^3 K^2 \\ & - \Lambda_{JJK} J^2 (J+1)^2 K^4 - \Lambda_{JKK} J(J+1) K^6 - \Lambda_{KKK} K^8 + \dots \end{aligned} \quad (1.30)$$

$$\begin{aligned} \langle \nu, J, K | \hat{H}_{rot} | \nu, J, K \pm 2 \rangle = & (1/4)(B_v - C_v) - \delta_v J(J+1) - 1/2 \delta_K ((K \pm 2)^2 + K^2) \\ & + \phi_v J^2 (J+1)^2 + 1/2 \phi_{JK} J(J+1) ((K \pm 2)^2 + K^2) \\ & + 1/2 \phi_K ((K \pm 2)^4 + K^4) - \lambda_{JJJ} J^3 (J+1)^3 \\ & - 1/2 \lambda_{JJK} J^2 (J+1)^2 ((K \pm 2)^2 + K^2) \\ & - 1/2 \lambda_{JKK} J(J+1) ((K \pm 2)^4 + K^4) \\ & - 1/2 \lambda_{KKK} ((K \pm 2)^6 + K^6) + \dots F_{\pm}(J, K) F_{\pm}(J, K \pm 1) \end{aligned} \quad (1.31)$$

where $F_{\pm}(J, K) = \{J(J+1) - K(K \pm 1)\}^{1/2}$.

The selection rules dictating the transitions between ro-vibrational levels of an asymmetric top molecule are more complicated than that of a diatomic or linear molecule. In general, the dipole moment of any molecule has three components μ_a , μ_b , and μ_c along their principal axes a , b , and c respectively. Changes in the non-zero components of these dipole moments dictate which transitions can occur, leading to a set of selection rules. In the case of an asymmetric molecule, they are all non-zero and have different magnitudes. If the change in dipole moment occurs predominantly about the a -axis, the transition associated with this change is said to be of A -type; in a similar fashion, one obtains B -type and C -type transitions. The selection rules associated with these types of transitions are summarised in Table I-6. Thus, for a C -type transition like the ν_4 band of 1,1 difluoroethane three main structures will be observed when considering the ΔJ selection rule: the R, Q, and P branches. Each of these main branches consist of sub-structures due to the ΔK_a and ΔK_c selection rules, leading to a congested spectrum. Using the notation, $\Delta J_{\Delta K_a \Delta K_c}$, the sub-structures of such a spectrum can be labelled R_{PQ} , R_{RQ} , Q_{PQ} , Q_{RQ} , P_{PQ} , and P_{RQ} .

Table I-6 Band types and selection rules of asymmetric top molecules.

Axis of change in Dipole Moment	Band type	Selection Rule $K_a K_c$	ΔK_a	ΔK_c	ΔJ
a-axis	A-type	$ee \leftrightarrow eo$	0	± 1	0, ± 1
		$oe \leftrightarrow oo$			
b-axis	B-type	$ee \leftrightarrow oo$	± 1	± 1	0, ± 1
		$oe \leftrightarrow eo$			
c-axis	C-type	$ee \leftrightarrow oe$	± 1	0	0, ± 1
		$eo \leftrightarrow oo$			

Figure I-4 illustrates the sub structures that may be observed in the spectrum of a C -type band of an asymmetric top molecule according to the selection rules listed in Table I-6

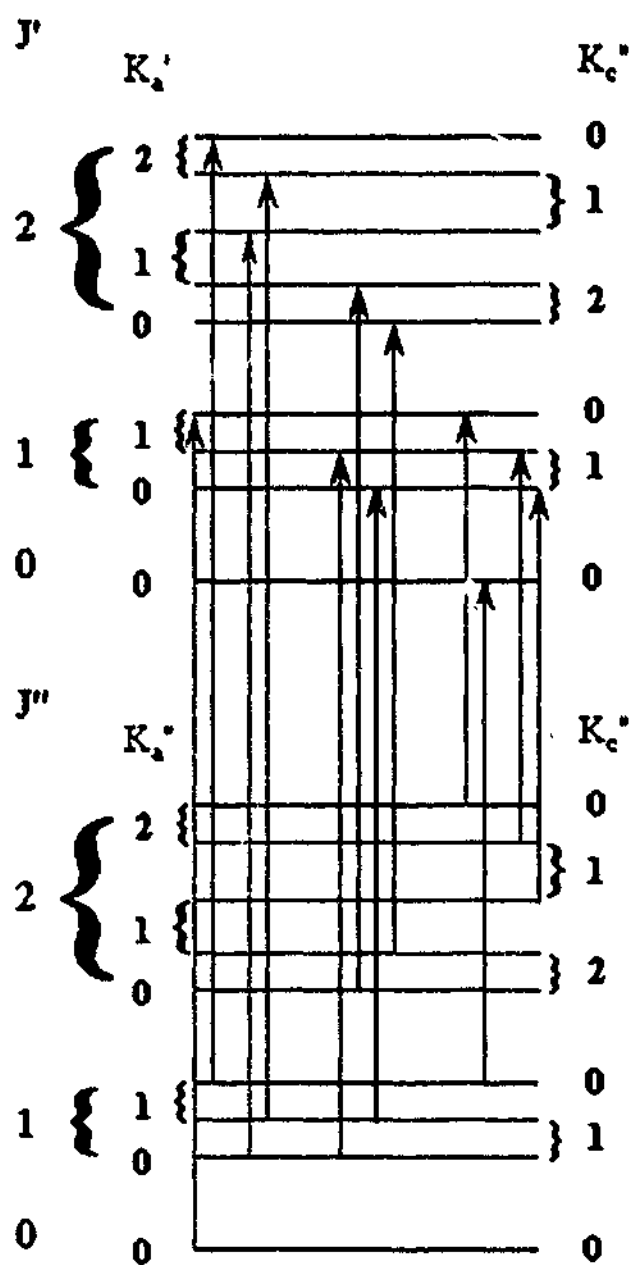


Figure I-4 Schematic Energy level diagram of a C-type band of an asymmetric top molecule depicting some of the first few allowed rovibrational transitions.

1.3.1 Fermi and Coriolis resonances

The already complex spectra of polyatomic molecules can be further complicated by perturbations mainly caused by Fermi and/or Coriolis resonances. Fermi resonances can only occur between states of the same symmetry, and can result in both vibrational and rotational perturbations. Such interaction can be expressed as

$$\begin{aligned}
 1^{st} \text{ order} \quad \langle v; J, K | \mathbf{H} | v'; J, K \rangle &= F_{v,v'} + F_{v,v'}^J J(J+1) + F_{v,v'}^K K^2 \\
 2^{nd} \text{ order} \quad \langle v; J, K | \mathbf{H} | v'; J, K \pm 2 \rangle &= \pm F_{v,v'}^a + F_{\pm}(J, K) F_{\pm}(J, K \pm 1)
 \end{aligned} \tag{I.32}$$

where $F_{\pm}(J, K) = \{J(J+1) - K(K \pm 1)\}^{1/2}$.

Coriolis interactions can only cause rotational perturbations. According to Jahn's rule¹⁹, Coriolis interaction can take place between two closely-lying vibrational states if the cross product of the symmetry species of the states involved contains a rotational species

$$\Gamma(v) \otimes \Gamma(v') \in \Gamma(R_{\alpha}) \tag{I.33}$$

In such cases, the first order Coriolis interaction can be expressed as

$$\langle v, v' | \hat{H}'_{21} | v+1, v'-1 \rangle = i \xi_{v,v'}^{\alpha} \hat{J}_{\alpha} \tag{I.34}$$

where $\xi_{v,v'}^{\alpha} = 2B^{\alpha} \zeta_{v,v'}^{\alpha} \Omega_{v,v'}$ with $\Omega_{v,v'} = \frac{1}{2} \left[\sqrt{(\omega_v/\omega_{v'})} + \sqrt{(\omega_{v'}/\omega_v)} \right]$.

The second order Coriolis interaction which usually occurs between more distant-lying states can be accounted for by

$$\langle v, v' | \hat{H}'_{31} | v+1, v'-1 \rangle = \eta_{v,v'}^{\beta\gamma} \{ \hat{J}_{\beta} \hat{J}_{\gamma} \} \tag{I.35}$$

where \hat{J}_{α} , \hat{J}_{β} , and \hat{J}_{γ} are the total angular momentum vectors about the molecular axes α , β and γ , respectively.

Vibrational states leading to A-type, B-type and C-type bands will undergo Coriolis interaction if Jahn's rule is observed, and, thus, the terms coupling these states can be evaluated in the I' representation using the following expressions

$$\begin{aligned}
 \langle v(c); J, K | H | v'(b); J, K \rangle &= \{ \xi_{v,v'}^a + \eta_{v,v'}^a J(J+1) + \eta_{v,v'}^{aK} K^2 \} K \\
 \langle v(c); J, K | H | v'(b); J, K \pm 2 \rangle &= \{ \pm \eta_{v,v'}^{Kc} + \eta_{v,v'}^a (K \pm 1) \} F_{\pm}(J, K) F_{\pm}(J, K \pm 1) \\
 \langle v(a); J, K | H | v'(c); J, K \pm 1 \rangle &= -\frac{1}{2} \{ \xi_{v,v'}^b + \eta_{v,v'}^b J(J+1) + \eta_{v,v'}^{bK} K^2 - (\pm K + 1) \eta_{v,v'}^{ac} \} F_{\pm}(J, K) \\
 \langle v(a); J, K | H | v'(b); J, K \pm 1 \rangle &= -\frac{1}{2} \{ \xi_{v,v'}^c + \eta_{v,v'}^c J(J+1) + \eta_{v,v'}^{cK} K^2 - (\pm K + 1) \eta_{v,v'}^{ab} \} F_{\pm}(J, K)
 \end{aligned}
 \tag{I.36}$$

II Tools for Spectral Measurement & Analysis

II.1 Spectral Measurement

In this study, the spectra were recorded using both a Fourier transform and a grating spectrometer. In the following sections, the techniques of interferential and dispersive spectroscopy will be briefly described with particular emphasis on some of their most important features. Details of the historical background of interferential and dispersive spectroscopy can be found in a book written by Johnston¹ and references therein.

II.1.1 *Fourier transform spectrometry*

II.1.1.1 *The Michelson Interferometer*

Unlike most dispersive spectrometers which use gratings or prisms, Fourier transform (FT) spectrometers are based on interferometry. In 1881, Michelson built the first interferometric instrument in an attempt detect *aether*[†] and to measure the speed of

[†] aether was thought to be a special medium enabling electromagnetic radiation to propagate

light. A schematic of such an instrument is illustrated in Figure II-1. It consists mainly of a source, *S*, a collimating lens, *L1*, a beamsplitter, *BS*, a stationary mirror, *SM*, a movable mirror, *MM*, a focusing lens, *L2*, and a detector, *DTC*. A wave form emanating from the source is directed at the beamsplitter where half of the wave is transmitted to a moving mirror, *MM*, a distance, d_1 , away while the other half is reflected onto the stationary mirror, *SM*, located a distance, d_2 , away. The waves from these mirrors are then reflected back onto the beamsplitter where each wave is further divided. The partial waves are spatially coherent and, thus, will interfere upon recombination on both sides of the beamsplitter. As mirror *MM* moves, in the case of a monochromatic source of wavelength, λ , the recombined waves form an interference pattern as the optical distance $\delta = 2(d_1 - d_2)$ changes from one multiple of λ to the following. One set of recombined waves reaches the source *S* while the other is focused onto the detector, *DTC*. There, the intensity, *I*, of the radiation is recorded as a function of the optical retardation, δ . The waveform collected over the total distance covered by the mirror is called an interferogram which is in fact the Fourier transform of the wavenumber-spectrum. Thus, mathematical manipulation of the interferogram yields the wavenumber-spectrum.

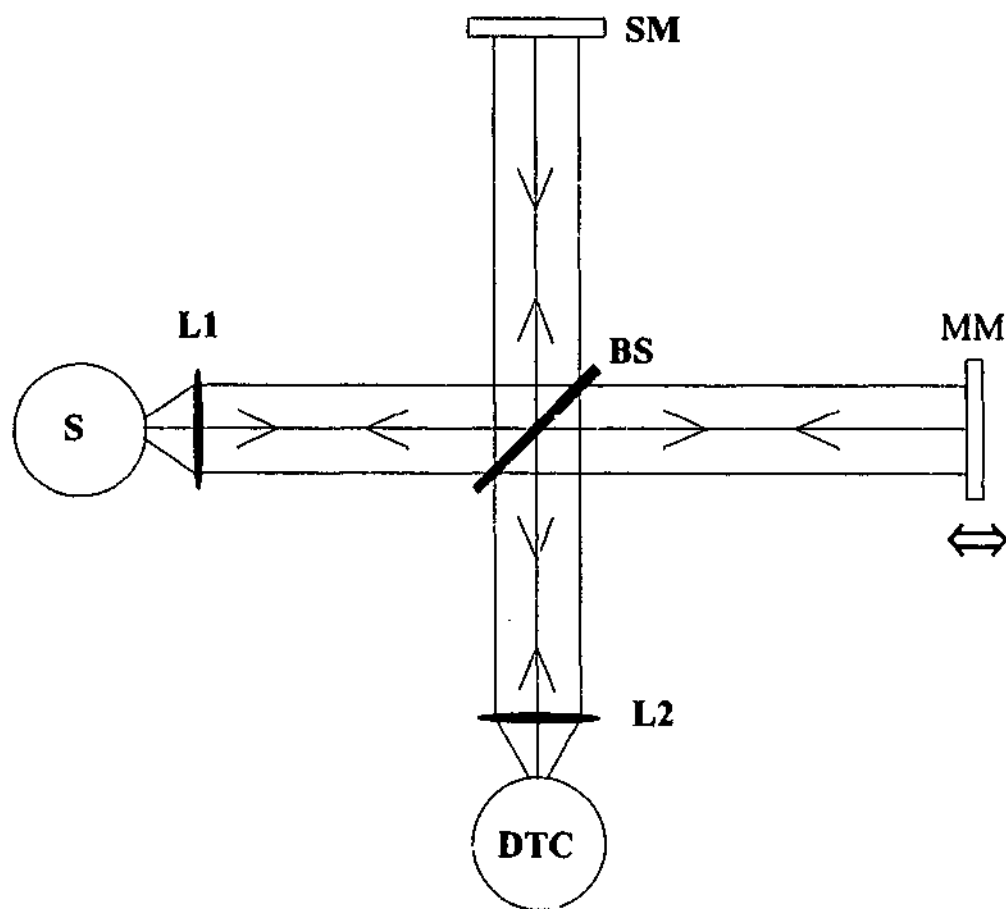


Figure II-1 Schematic illustration depicting the optical components and layout of an ideal Michelson interferometer (see text for a description of labelled components).

II.1.1.2 Brüker IFS 120 HR

The Brüker IFS 120 HR is one of the most powerful and versatile Fourier transform spectrometers used in spectroscopy. These attributes are characterised mainly by the ability to detect electromagnetic radiation from the far-infrared to the near-ultraviolet ($10 - 40,000 \text{ cm}^{-1}$) at high resolution. The resolution attainable by the interferometer is defined by $0.9/\delta$. Thus, with a maximum achievable optical retardation of 529 cm , the (unapodised) resolution is limited to 0.0017 cm^{-1} . The large spectral coverage is obtained by switching the sources, detectors and beamsplitters appropriately for the spectral region under study. A schematic diagram of the Brüker IFS 120 HR Fourier transform spectrometer used in this study can be seen in Figure II-2. Its principal components are the sources, Michelson interferometer, and sample and detector compartment. The IFS 120 HR spectrometer is equipped with an array of electronically exchangeable apertures, AC, (0.5 to 15 mm), optical filters, FC, and internal light sources (a mercury lamp, S1, a globar, S2, and a tungsten lamp, S3). It also has an external port, S4, enabling emission studies to be performed. The detectors are also electronically exchangeable.

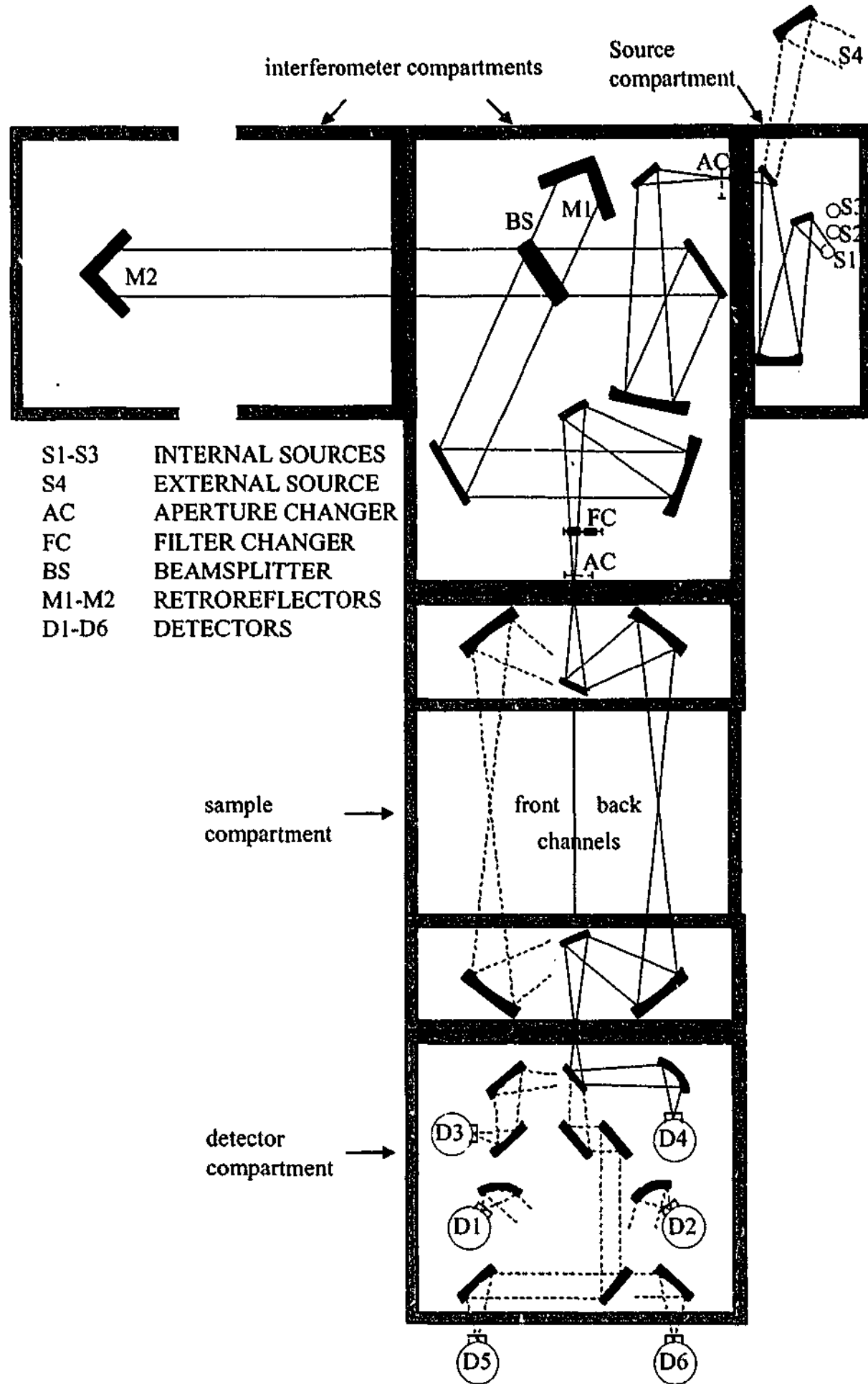


Figure II-2 Schematic diagram of the Bruker IFS 120 HR Fourier transform spectrometer showing the interferometer, and source, sample and detector compartments.

II.1.1.3 Main Advantages of FT spectrometry

The traditional way of producing spectra was to disperse a source of radiation with either a prism or a grating spectrometer. Narrow slits located at both the entrance and exit of a monochromator enable spectra to be recorded at high resolution. However, these devices are highly inefficient since the energy loss at the detector is approximately 99.97% when the slits are set for a resolution of 1 wavenumber.² In addition to signal loss, a monochromator has to be scanned one frequency at a time, thus rendering this method of collecting data rather slow.

Dispersive spectrometers have been superseded by the much more powerful and versatile Fourier transform spectrometers. Equipped with circular apertures instead of slits, the Michelson interferometer theoretically captures all the energy of the source radiation. Griffiths and de Haseth² have shown that when recording spectra at the same resolution, the Michelson interferometer offers a much larger throughput; this attribute is termed *Jacquinot or throughput advantage*. An additional advantage over conventional spectrometers where the frequencies need to be scanned one at a time is the fact that all frequencies are recorded simultaneously. This feature is called the *multiplex or Fellgett advantage*.

The IFS 120 HR uses the interference pattern of the monochromatic radiation of a HeNe laser to control the mirror displacement. The interferogram is sampled at the zero-crossings of the HeNe interference pattern. Since the accuracy of the sampling interval, Δx , between zero-crossings depends on the precision of the laser frequency, and the error in the sample spacing, $\Delta \nu$, is the same as in Δx , the spectrometer has a high precision built-in wavenumber calibration system. This attribute is termed *Connes' advantage*. The *Jacquinot* and *Fellgett* advantages have the combined effect of directly enhancing the S/N ratio while *Connes'* advantage enables multiple spectra to be co-added thereby reducing the noise level and thus, indirectly influences the S/N ratio.

A detailed account of FT advantages can be found in articles by Herres and Gronholz³, Glasser⁴⁻⁶, Perkins⁷ and Bell⁸.

II.1.1.4 Interferograms and their Fourier transforms

In spectroscopy, a waveform recorded by a detector usually originates from a polychromatic source and is therefore made up of waves of different frequencies and amplitudes. Figure II-3 shows how the combination of waves of different frequencies and amplitudes can produce a complex waveform or interferogram.

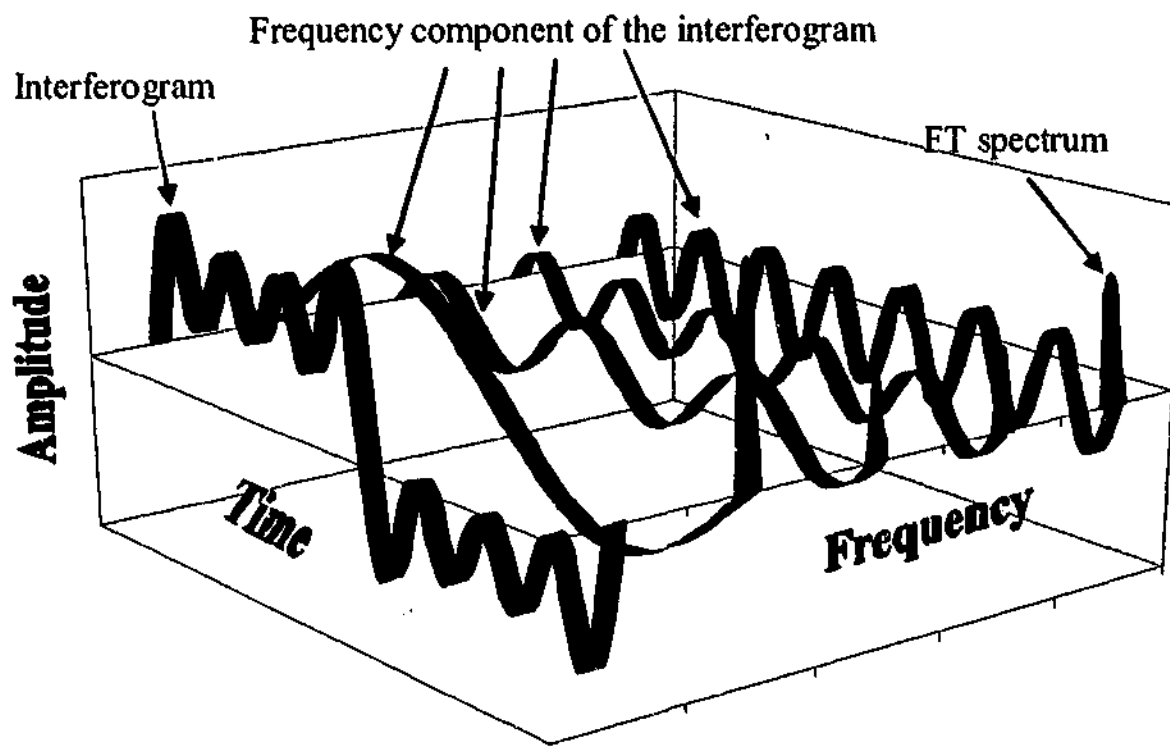


Figure II-3 Interferogram resulting from the sum of four frequencies.

If an algebraic approach is used to solve for the frequency and amplitude of each component, the number of readings required is at least equal to twice the number of components forming the interferogram. Thus, a very intricate waveform will require a large amount of data to be collected, and the solving task will become very tedious. However, with the use of Fourier transform any complex waveforms can be readily resolved into its frequency components. Michelson and Rayleigh were the first to realise that it was possible to obtain a frequency-domain spectrum from a time-domain interferogram generated by the Michelson interferometer through the computation of its Fourier transform. However, since the interferogram is sampled at the zero crossings of the interference pattern of a HeNe laser it will consist of discrete equidistant points. As a result, a discrete Fourier transform (DFT) needs to be performed on the waveform of

interest in order to generate a frequency spectrum. Consequences of the use of DFT's are briefly described in the following sections, however, for a detailed rendition of the ramifications of using DFT's the reader is referred to articles by Gronholz and Herres³, Glasser⁴⁻⁶ and Chesick.⁹

II.1.1.5 Consequences of Discrete Fourier Transformation

Zero-filling

DFT's have to be used with care as they can lead to spectral artifacts such as the picket-fence effect, aliasing and leakage. The picket-fence effect occurs if the total number of points, N , describing the interferogram is too small. Therefore, some contributing frequencies lying between sampled points would not be represented after the Fourier transformation. This effect can be overcome however, by simply adding at least N number of zeroes at the end of an interferogram thus, yielding an interferogram of size $2N$. This process is called zero-filling and has the effect of increasing the number of points per wavenumber in the spectrum. A parameter called zero-fill factor, ZFF, is used to control the amount of zero-filling required in an interferogram before it is Fourier transformed.

Aliasing & Undersampling

DFT equations such as

$$S(k, \Delta\bar{\nu}) = \sum_{n=0}^{N-1} I(n, \Delta x) \exp(i2\pi nk / N) \quad (I.1)$$

are commonly used to generate spectra from interferograms where $S(k, \Delta\bar{\nu})$ are the spectral elements of width $\Delta\nu \text{ cm}^{-1}$ constituting the spectrum, $I(n, \Delta x)$ the components of the interferogram sampled every $\Delta x \text{ cm}$, and $\exp(i2\pi nk / N)$ represents the sum of sine and cosine functions. Although fast Fourier transforms such as the Cooley-Tukey¹⁰ algorithm have been developed to considerably reduce the number of complex mathematical manipulations, the DFT expression of Equation (I.1) is used for explanatory purposes in the following. Equation (I.1) is reflective about $n = N/2$ since $S(k) = S(N - k)$. The point of reflection occurs at the 'folding' or 'Nyquist' wavenumber, $\bar{\nu}_f$, which is related to the sample spacing, Δx , by $\bar{\nu}_f = 1/2\Delta x$. The

original spectrum and its mirror image are also periodic at multiples of N since $S(k) = S(k + mN)$. In the case where a spectrum has non-zero intensity contributions lying at wavenumber values larger than $\bar{\nu}_f$, there will be a 'folding' of these non-zero spectral features back to lower wavenumbers. This artifact, called 'aliasing', causes spectral features to appear at the wrong frequencies. Aliases can be prevented by a few methods. First, optical and electronic filters can be used to ensure that no frequencies larger than the folding frequency reach the detector ($\bar{\nu}_{\max} \leq \bar{\nu}_f$). Secondly, reduction of the sampling spacing, Δx , will ensure that the spectrum and its mirrored alias are well separated in the frequency domain. However, this process will also increase the number of points describing the interferogram, resulting both in higher storage needs and longer computing times.

Now, if the sampling spacing is increased instead, a spectrum having intensities within a range defined by $\bar{\nu}_{\min}$ and $\bar{\nu}_{\max}$ (and zero outside that range) will be aliased to lower wavenumber values. This aliasing will occur only if the spectrum also lies within the folding limits $\bar{\nu}_{fl}$ and $\bar{\nu}_{fv}$ defined by

$$\bar{\nu}_{fl} = \frac{n-1}{n} \bar{\nu}_{fv} \quad (1.2)$$

where $n = 2, 3, \dots$ and $\bar{\nu}_{fv} = a \times 15800$ with $a = \dots, \frac{1}{3}, \frac{1}{2}, 1, 2, 3, \dots$

This process is called undersampling and, thus, the Michelson interferometer can act as a frequency modulator shifting high frequency radiation to much lower frequencies which also allows detectors to properly record the output data.

Apodisation

One of the inherent problems of Fourier transforms is the fact that the 'limits' of integration are $\pm\infty$ although, in practice, the movable mirror in the Michelson interferometer only offers an optical retardation of $\pm L$, where L is the maximum path length covered by the mirror. Hence, the interferogram needs to be truncated at the latter limits before Fourier transformation. However, this results in the formation of side-lobes or 'feet' as the intensity of a peak centered at ν_0 leaks and contributes to the intensities of the side-lobes. As can be observed in Figure II-4, the side-lobes can have

rather large amplitudes and thus, may mask real peaks of smaller amplitudes. It has been found that some mathematical expressions, called *apodisation* (removal of feet) functions, can be used to suppress the amplitude of these unwanted side-lobes. However, this procedure is performed at the expense of resolution. Table II-1 shows some of the most common apodisation functions used as well as the expected width of a peak halfway to its maximum (FWHM).

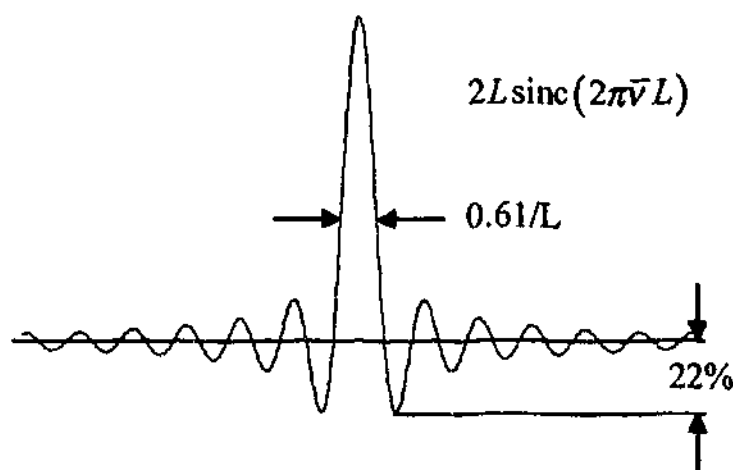


Figure II-4 Convolution of instrument lineshape with boxcar apodisation function showing the formation of side-lobes of considerable intensity (22%).

Table II-1 Apodisation functions available with the present FT spectrometer. RES represents the unapodised resolution.

Apodisation function	FWHM	Resolution /cm ⁻¹
Boxcar	0.61 / L	0.68×RES
Norton-Beer, Weak	0.73 / L	0.81×RES
Norton-Beer, medium	0.85 / L	0.95×RES
Trapezoidal	0.75 / L	0.84×RES
Blackman-Harris, 3-term	0.92 / L	1.02×RES
Norton-Beer, strong	0.98 / L	1.08×RES
Happ-Genzel	1.10 / L	1.23×RES
Blackman-Harris, 4-term	1.40 / L	1.52×RES

Linewidths and Resolution considerations

Careful attention has to be paid to linewidths as they dictate the resolution at which a spectrum needs to be recorded. The main contributions to the overall linewidth come from the instrument linewidth and the Doppler and collisional broadening. The instrument linewidth, $\Delta\bar{\nu}_{ILW}$, is dictated by the apodisation function and the optical path difference. Collisional (or pressure) broadening is a homogeneous mechanism whereby the dipole moments of the molecules are affected upon collision and result in an interruption of the interaction between molecules and electromagnetic radiation. The corresponding linewidth is defined by

$$\Delta\bar{\nu}_{col} = \frac{1}{\pi\tau_{col}} \quad (I.3)$$

with

$$\tau_{col} \approx \frac{\sqrt{MkT}}{16pr^2\sqrt{\pi}} \quad (I.4)$$

where M is the molecular mass, k the Boltzmann constant, T the temperature, p the pressure and r the molecular radius. As a 'rule of thumb', however, it can be approximated to a few MHz/Torr.

Doppler broadening is an inhomogeneous mechanism due to the random motion typical of gas molecules. It arises since molecules have different velocity components in the direction that radiation is collected, resulting in the Doppler-effect. The resultant linewidth is defined by

$$\Delta_{Dop} = 2\bar{\nu} \sqrt{\frac{2 \ln 2 kT}{Mc^2}} = 7.15 \times 10^{-7} \bar{\nu} \sqrt{\frac{T}{M}} \quad (I.5)$$

where $\bar{\nu}$ is the central wavenumber value of the peak, c the velocity of light and the remaining constants are as defined above. The different contributions can be added in a root-mean-square fashion to yield the expected overall linewidth

$$\Delta\bar{\nu} = \sqrt{(\Delta\bar{\nu}_{ILW})^2 + (\Delta\bar{\nu}_{col})^2 + (\Delta\bar{\nu}_{Dop})^2} \quad (I.6)$$

II.1.2 Dispersive spectrometry

The first spectra ever observed were 'recorded' with a prism spectroscope in the mid-eighteenth century. Prisms disperse polychromatic radiation into its wavelength components by refraction. Most of today's dispersive spectrometers are equipped with diffraction gratings although prisms are still used. Diffraction gratings consist of very narrow reflecting or transmitting parallel elements which act like slits and diffract the incoming radiation. The number of elements per mm usually ranges from a few tens to a few thousands. Over the years, monochromators have been constructed in numerous different ways using different optical components. One of the most popular optical layouts is a Czerny-Turner mount which is the main component of the Jovin-Yvon HR1000 monochromator used in this study as illustrated in Figure II-5.

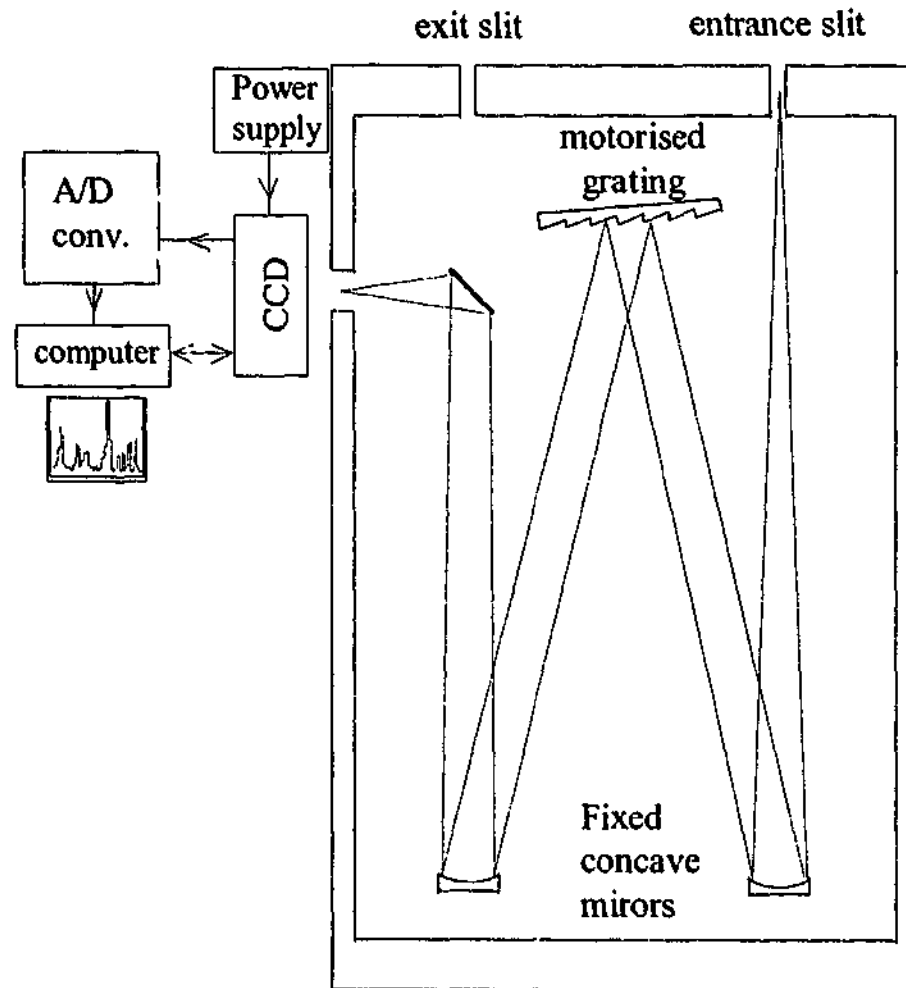


Figure II-5 Schematic of Jobin-Yvon HR 1000 monochromator coupled to a CCD detector. The optical layout is typical of a Czerny-Turner mount.

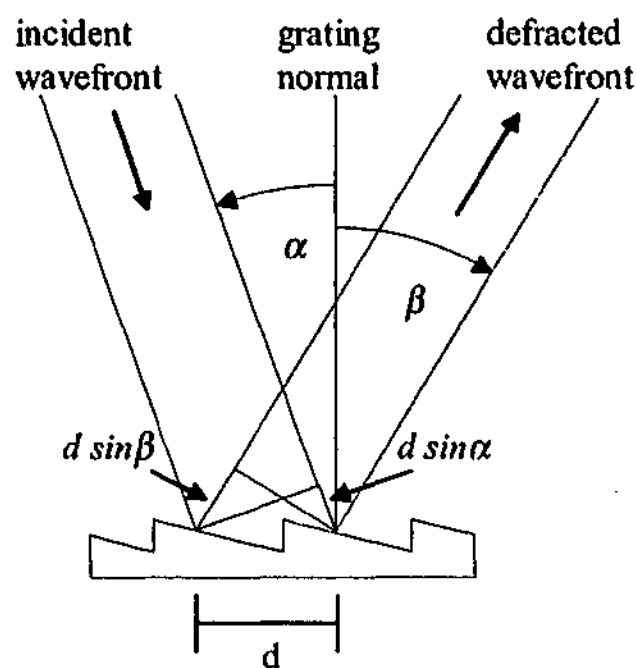


Figure II-6 Optical geometry of a planar wavefront incident on a diffraction grating. The optical paths covered by rays a and b differ by $d \sin \alpha$ and $d \sin \beta$ highlighted in blue where d is the groove spacing, and α and β are the angles of the incident and diffracted wavefronts relative to the grating normal respectively.

Light entering the monochromator expands through the entrance slits onto a concave mirror which produces a parallel beam. If the incident wavefront approaches a grating of groove size, d , at an angle, α , to the normal as illustrated by Figure II-6, it will be diffracted at an angle, β , such that rays (of same wavelength) separated by a distance d at the grating surface will experience optical paths differing in length by $d(\sin \alpha + \sin \beta)$. The diffracted wavefront is then brought into focus at the exit slits by the second concave mirror. Constructive interference will occur in the form of a bright slit-shaped image if

$$d(\sin \alpha + \sin \beta) = m\lambda \quad (I.7)$$

where m , the diffraction order, is an integer. Equation (I.7) is known as the grating equation. If the incident wavefront consists also of rays of wavelength, $\lambda + d\lambda$, they will be diffracted an angle, $\beta + d\beta$. Thus, the angular dispersion, D_{ang} , corresponds to the change in diffraction angle with respect to wavelength and can be obtained by differentiating Equation (I.7)

$$D_{ang} = \frac{d\beta}{d\lambda} = \frac{m}{d \cos \beta} \quad (I.8)$$

while the linear dispersion, D_{lin} , determining the change in wavelength with respect to its position at the exit port has the form

$$D_{lin} = f' \frac{d\beta}{d\lambda} \quad (1.9)$$

where f' is the effective focal length which depends on the wavelength.

Thus, by rotating the grating all dispersed wavelengths can be scanned and observed on at a time with a detector located at the exit port. It follows that monochromators with small f' will offer larger spectral coverage.

II.1.2.1 The Jobin-Yvon HR1000 monochromator

The Jobin-Yvon HR1000 depicted in Figure II-5 is a Czerny-Turner type monochromator. It consists of an entrance and an exit port both equipped with adjustable slit mechanisms having a maximum range of 3000 μm at 10 μm intervals; another exit port located laterally is not equipped with slits thus, providing a wide bandpass. The HR1000 also has a pair of concave mirrors of focal length 1000 mm are located a focal length away from the slits, and a motorised 1200 grooves/mm plane reflection grating. The latter has a spectral range between 175 and 1500 nm and offers a reciprocal linear reciprocal dispersion of 0.8 nm/mm at 200 nm. When the slit-width is reduced to 10 μm , a resolution of 0.008 nm is achievable. The exit slit is ideal for coupling a Photo-Multiplier Tube (PMT) to the monochromator as it allows only 'one' spectral element at a time to reach the sensitive PMT. The lateral exit port however, is not equipped with slits and, as a result, has a rather large opening which is ideal for multi-channel photographic plates or CCD detectors.

II.1.2.2 The CCD detector

Only a brief description of the CCD detector will be offered at this stage as it will be discussed in greater detail later. The custom-built CCD camera coupled to the dispersive spectrometer is based on the SITE ST001A chip. The latter is a two-dimensional CCD consisting of 330 rows and 1132 columns of square pixels each 24 μm in dimension. The pixel-size, slit-width and wavelength dictate the resolution. The highest resolution achieved with the present system was 6 pixels in width or 144 μm which translates to approximately 0.08 nm at a wavelength of 1100 nm with a slit-width of 150 μm ; this also leads to a bandpass estimated at 14.5 nm.

Although dispersive spectrometers cannot compete with Fourier transform spectrometers (see section II.1.1.3), the present CCD-based detection system is much faster in collecting data as no Fourier transformation is required and, moreover, it is more sensitive. These attributes make CCD-based detection systems quite useful for either monitoring emitting species during an experiment or characterizing reaction-products emitting electromagnetic radiation.

II.2 Spectral Analysis

II.2.1 Assignment

All spectral assignments of rotational transitions were performed using a software developed by McNaughton *et al.* called MacLoomis.¹¹ This interactive program is based on the Loomis-Wood diagrams whereby a spectrum is rearranged such that consecutive segments $2B \text{ cm}^{-1}$ wide are displayed vertically one on top of the other as illustrated in Figure II-7. If the energy of the molecular system under study can be reasonably predicted (for the first few rotational levels at least) using the energy expression for linear molecules and the line-spacing of the spectrum roughly matches the $2B$ -value, the Loomis-Wood plot will reveal the presence of the various branches as patterns of transitions as illustrated in Figure II-8. Once selected, the transitions are fitted to the polynomial expression describing ro-vibrational or ro-vibronic bands

$$\begin{aligned} \nu = \nu_0 + (B'' + B')m - (B'' - D'' - B' + D')m^2 - (2D'' - H'' + 2D' - H')m^3 \\ + (D'' - 3H'' + D' - 3H')m^4 + 3(H'' + H')m^5 - (H'' - H')m^6 \end{aligned}$$

where $m = J''$ and $J'' + 1$ for $P(J)$ and $R(J)$ branches, respectively, ν_0 is the band-origin. Although primarily developed to assist in the analysis of diatomics, linear polyatomic and spherical molecules, it has also been successfully used in the case of moderately asymmetric molecules ($\kappa = -0.57$) by McNaughton *et al.*¹²

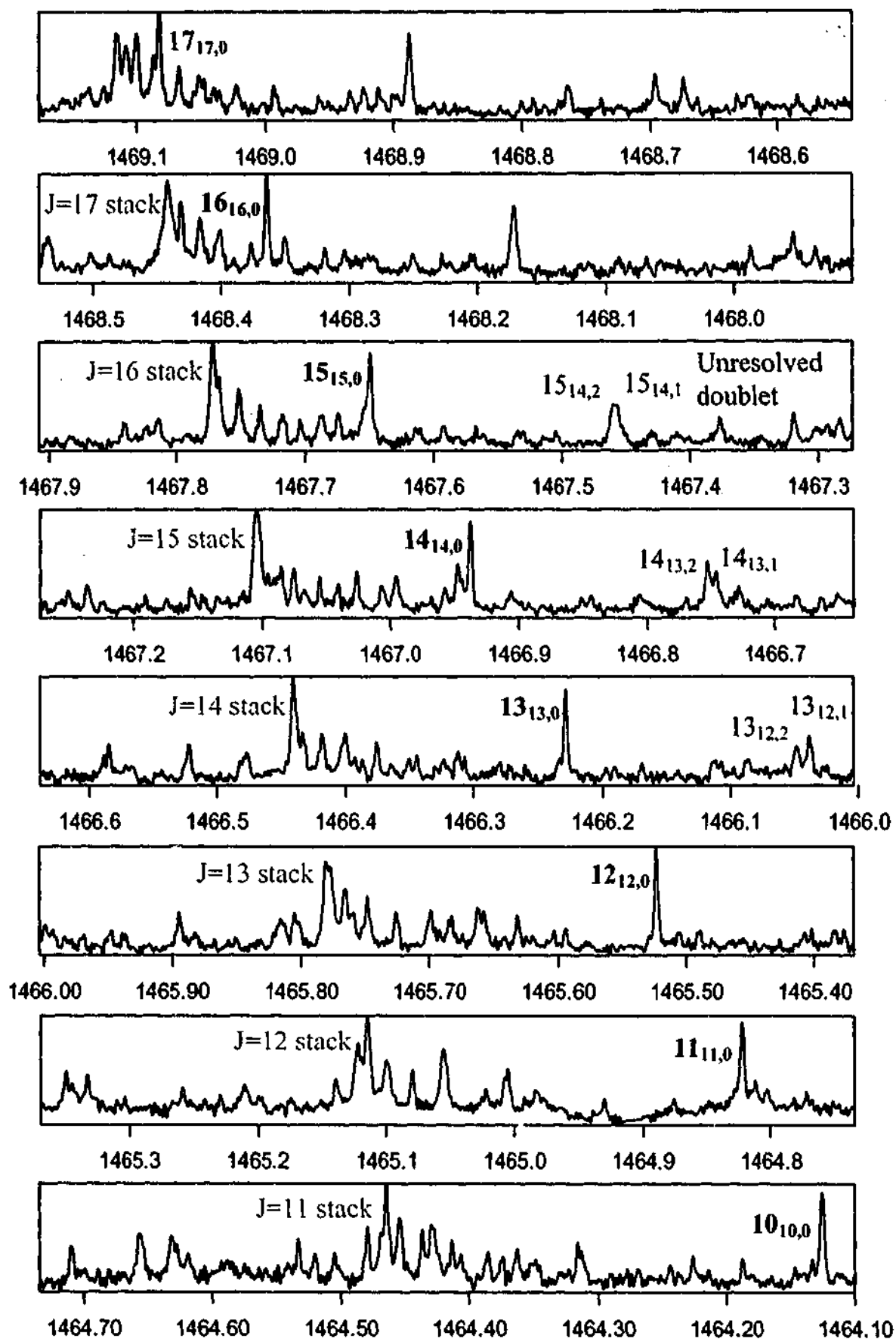


Figure II-7 Portion of IR spectrum of ν_4 of 1,1 difluoroethane truncated in $2B$ -segments (roughly 0.62 cm^{-1}). Transitions belonging to the same series form a pattern as shown in red. Other series with similar $2B$ -value will also form patterns like the ones shown in blue and green.

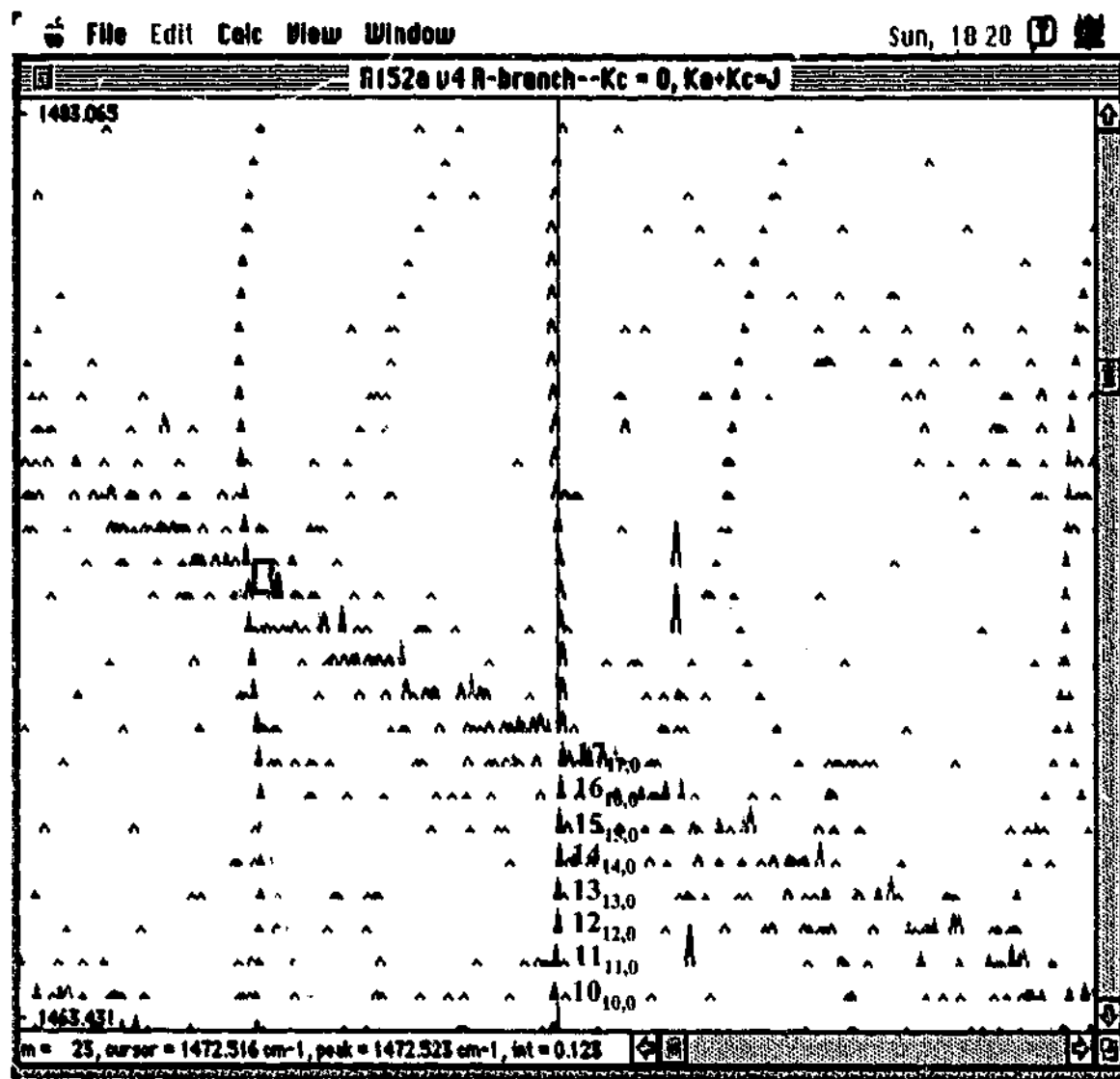


Figure II-8 Loomis-Wood plot of the transitions displayed in Figure II-7. Highlighted in blue in the center of the plot are the ν_4 transitions of 1,1 difluoroethane belonging to the $K_c = 0$ series. The green and yellow series lying to the left of the $K_c = 0$ series are the transitions labelled in green in Figure II-7 which eventually 'become' degenerate.

II.2.2 Data Reduction

II.2.2.1 LSQFIT for Diatomic Molecules

LSQFIT is a non-linear least-squares fitting program written in FORTRAN by Clive Jarman, which can fit assigned rovibronic transitions for diatomic molecules to a series of effective Hamiltonians as well as Dunham polynomials and term values. It can also perform fits simultaneously to pure rotational, ro-vibrational and ro-vibronic transitions as well as band origins. The possible types of Hamiltonians describe the energy levels of states with spin angular momentum, S , ranging from 0 to 2.5, orbital angular momentum, L , from 0 to 4 as well as a Hamiltonian matrix in the A-reduced form for a doublet asymmetric top using Hunds case (b). This program has been used on numerous occasions the Bernath group at the University of Waterloo (Canada) and the results reported in scientific journals.¹³

II.2.2.2 DSPFIT for Polyatomic Molecules

DSPFIT is a non-linear least-squares fitting program for asymmetric rotors written both in C and FORTRAN by Herbert Pickett.¹⁴ It has the flexibility of fitting and predicting ro-vibrational spectra with multiple spin states. Using a modified Wang basis set and Watson's A and S reduced Hamiltonians, it can fit to high-order centrifugal distortion constants as well as Coriolis and Fermi interactions of first and second order of 99 multi-spin vibrational states. Some details of the program are described in Ref1. and the program can be downloaded from a few websites. The program has been tested on a variety of platforms such as VAX-VMS, SUN-UNIX, HP1000A, PRIME, ALLIANT-UNIX, CDC, and CRAY-UNICOS as well as on a PC's. It's use however, requires a substantial knowledge of spectroscopy.

III A Charge-Coupled Device camera for quick spectral profiling

III.1 Introduction

By the turn of last century, spectroscopists were routinely recording spectra predominantly by photographic means. This technology was a great improvement over the eye (the detector of the early days!) as it enabled spectroscopists (and astronomers) to accurately measure spectral features, store spectral information and compare spectral images. Photographic technology is particularly well-suited for dispersive spectroscopic techniques as it offers multi-channel detection with large surface areas, however, it has some severe shortcomings. Photographic emulsions have low quantum efficiencies (QE) as less than two percent of the total photons emitted are detected (see Figure III-1). They also have limited dynamic range as intensities differing by approximately a factor of a hundred or more cannot be reliably distinguished. The detector's response to the level of brightness from different exposure-times is non-linear (twice the exposure-time does not yield twice the intensity), thus, each plate has to be calibrated individually which often leads to inaccurate spectral measurements. In addition, photographic plates can only be used once. Nevertheless, there has been a resurgence of this technology lately, in the field of astronomy with the advent of fast computer-controlled micro-

densitometers and automatic image processing leading to high-speed digitisation of photographic data.

By the 1930's, photoelectric-cells (*i.e.* photocathode, photomultiplier-tube,...) had been developed and spectroscopists used them to directly drive recording pen, thereby enabling spectral features to be traced out. These cells provide higher QE and sensitivity, and larger dynamic range than photographic plates, and, in addition, their spectral response is linear. The main disadvantage of this technology is that it has only one detecting element (the anode) and, thus, can only be exposed to one spectral element at a time.

The 'discovery' of the unique properties of semiconducting materials eventually led to the invention of Charge-Couple Devices (CCD) in 1970. Advances in CCD and computer technologies since then have enabled CCD's to compete with photographic films and even the highly sensitive photomultiplier tubes (PMT). This is mainly due to the CCD's high sensitivity and quantum efficiency, its large dynamic range and linear response. In addition, the CCD is sensitive to longer wavelengths than the previously mentioned detectors as illustrated in Figure III-1. Details about photographic and photoelectronic photometry can be obtained from articles written by Sterken and Manfroid,¹ and McLean.²

Ever since their invention, charge-coupled device (CCD) arrays have been the subject of a tremendous amount of attention and success in a variety of fields. CCD's are routinely used as imaging devices in astronomy, medicine and in the military. They have however, also been used as spectral measuring devices. CCD's have been coupled to echeile³ and holographic⁴ gratings to record high-resolution spectra. CCD's have been used as multichannel detectors to monitor emission from microwave-induced plasmas⁵, radio-frequency glow discharges⁶, laser-induced plasmas^{7,8}, furnace plasma emission^{9,10} and fluorescence of biological molecules.¹¹⁻¹³

CCD's also have wide commercial applications such as facsimile and copying machines, barcode readers, image scanners, video cameras, CCD cameras are readily available to suit a variety of needs but are quite expensive depending on the type and grade of arrays required. However, through careful design of the electronics and housing the cost of a CCD camera can be considerably reduced (at least by a factor of 5).

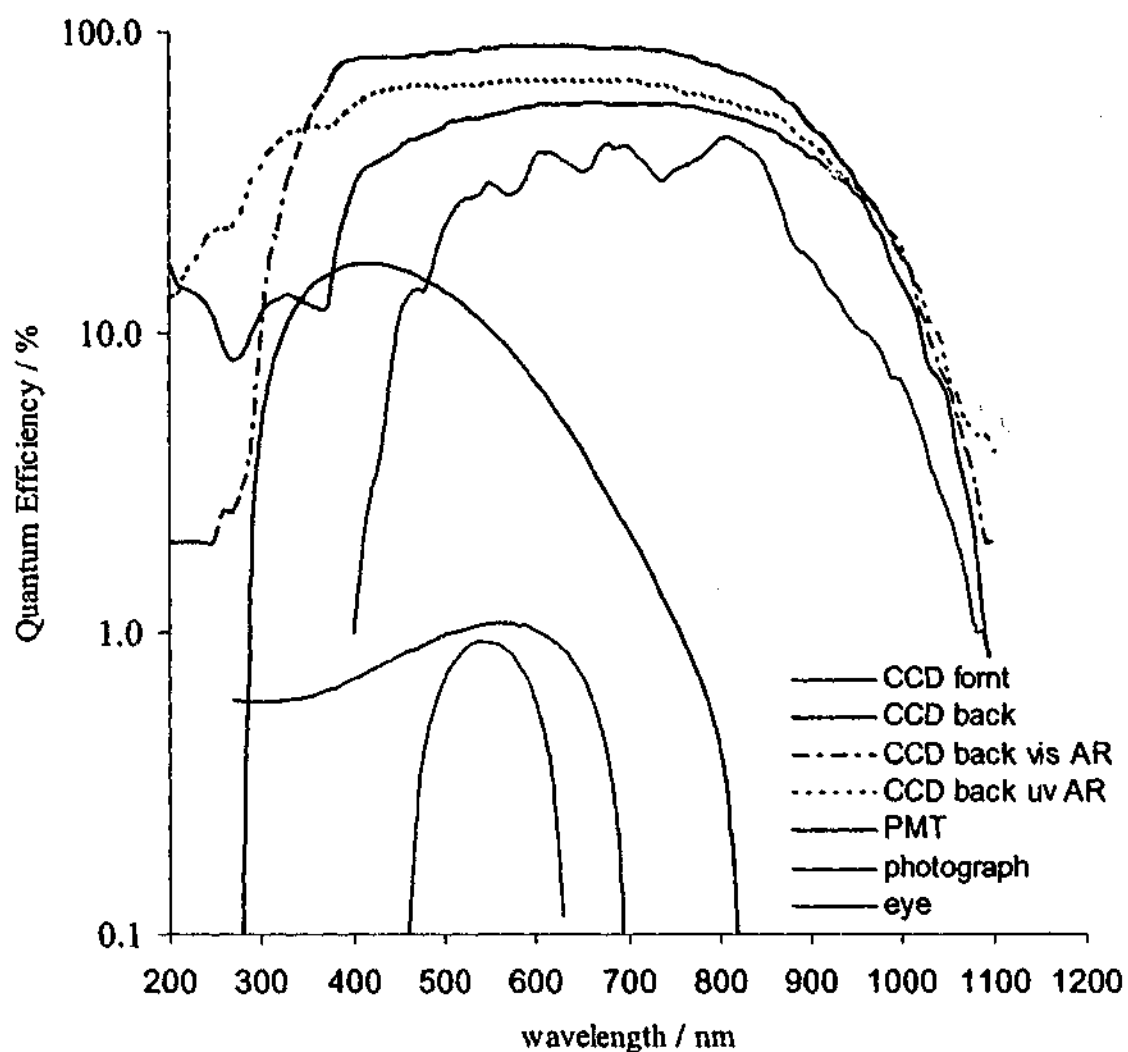


Figure III-1. Plots of Quantum Efficiency profiles as a function of wavelength of some of the most routinely used detectors in spectroscopy and CCD's equipped with different features. This figure was adapted from McLean², and Kristian and Blouke¹⁴.

III.2 The CCD detector

Charge transfer and amplification devices have come a long way since the vacuum tube "audion" at the turn of last century. Today's devices are called transistors; they are smaller, more effective and sophisticated but they perform essentially the same task of storing, transferring and amplifying charges. These transistors are made of semiconductor material such as germanium, silicon, gallium arsenide, indium antimony ... Under standard conditions, a semiconductor is both a poor insulator and a poor conductor. Its electrical properties can be tailored by doping the substrate with impurities with higher or lower valencies leading to *n-type* and *p-type* semiconductors respectively. When these two types of material are coupled, they form a *p-n junction*, which is the heart of most of today's semiconducting devices.

In 1970 at Bell Laboratories, Boyle and Smith¹⁴, and Amelio *et.al.*¹⁵ devised a new semiconductor device concept called a Charge-Couple Device (CCD). A CCD is a photoconductive detector consisting of light-sensitive elements (picture elements or pixels) in the form of Metal-Oxide-Silicon (MOS) capacitors. In its original design, the CCD consisted of an array of eight pixels with each MOS capacitor comprising of a thin gate electrode strategically placed over a thin layer ($\sim 0.1 \mu\text{m}$) of insulating material (SiO_2). The latter was deposited on a p-type silicon substrate.

Today's CCD's are more sophisticated and complex, and come in different sizes and architectures with a wide variety of features but the charge transfer process is the same. In a 3-phase architecture, as illustrated in Figure III-2, the three metal electrodes, P1, P2 and P3, make up a pixel with every third electrode being interconnected. The application of a positive voltage, V_1 , at time, t_1 , to the metal electrode (gate), P1, produces a depletion region under that gate at the *p-n junction*. If the CCD is then illuminated, photoelectrically generated electrons will be trapped or stored within this depletion region or potential well. Now, if a voltage, V_2 , at time, t_2 , is applied to gate, P2, located close enough to P1 such that their depletion region overlap to a small extent, the storage potential well will then extend to gate P2 (Figure III-2b). If V_1 is slowly reverted back to zero at time, t_3 , (Figure III-2c), the potential well will be located at time, t_4 , only under P2, thereby effectively moving the charges from P1 to P2 (Figure III-2d). By repeating the process with next gate, P3, the charge can be moved to P3. Thus, by sequentially varying the voltages of each capacitor (Figure III-2e), a charge packet can be moved vertically in a stepwise fashion to the end of the array into a serial register. This process is called parallel shifting. In a similar fashion, collected charges can be transferred horizontally along the serial register (serial shifting) towards an output amplifier where the electronic charge is converted to a voltage representing the light intensity of the pixels. The voltage is then digitised by an Analog-to-Digital Converter (ADC) to be stored or displayed on a computer (see Figure III-2)

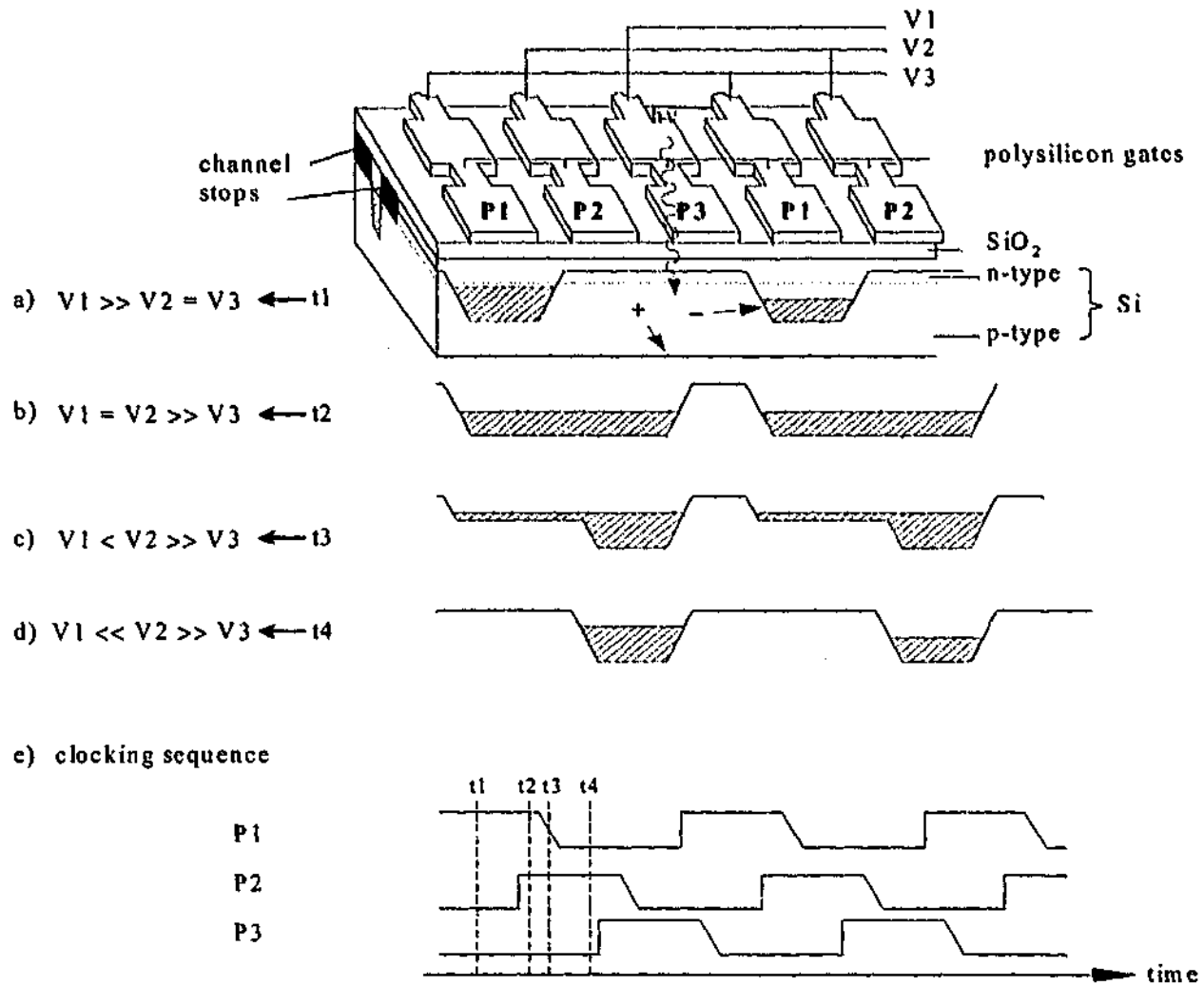


Figure III-2. Schematic diagram depicting a Charge Coupled Device in a three-phase architecture. Also shown in this schematic is the charge transfer process and clocking sequence in a parallel shift (see text for details).

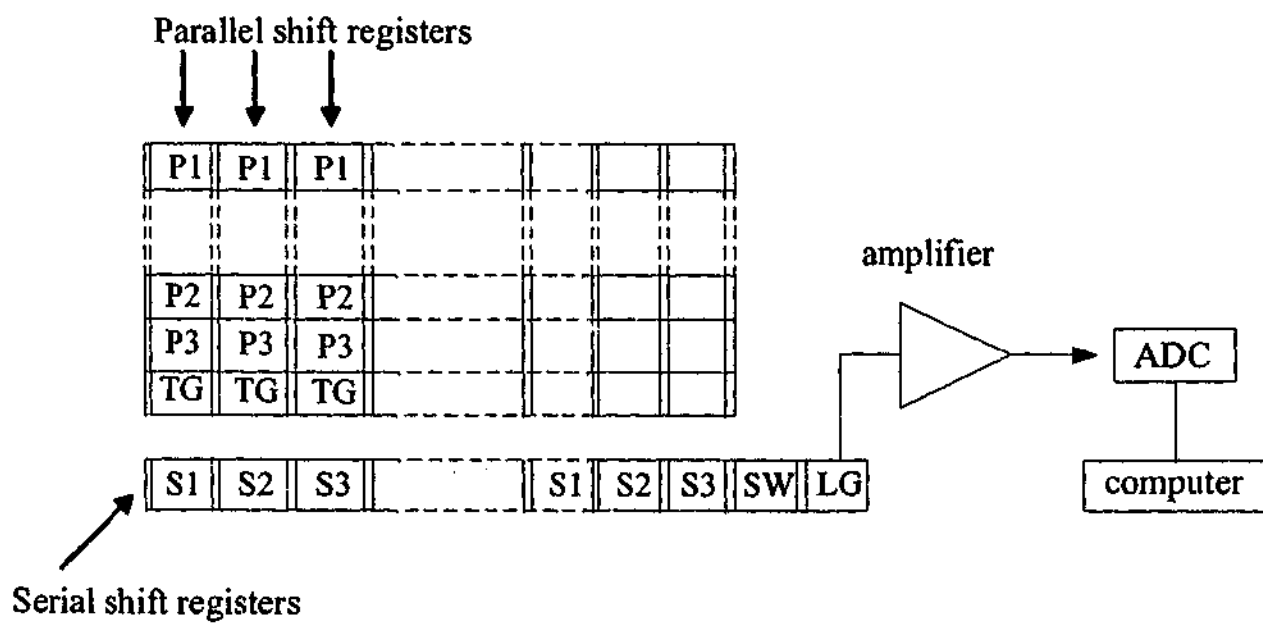


Figure III-3. Schematic diagram showing components required to readout the CCD serial register.

III.2.1 CCD features

Various changes have been implemented to CCD's over the years to enhance their performance. The features listed in Table III-1 are the predominant reasons why CCD's have become ubiquitous in dispersive spectroscopy. Front illuminated CCD's are opaque to photons of wavelength less than 400 nm due to absorption by surface components. Back-illumination of CCD's provides 'access' to blue-photons as the light interacts directly with the substrate. However, short-wavelength radiation cannot penetrate very deeply the CCD substrate and, thus, thinning of the back-illuminated CCD's (to depletion depths) offers enhanced quantum efficiencies at shorter wavelengths. The quantum efficiency in the UV or visible region can be further improved by applying anti-reflective coatings.

Insulators, semiconductors and conductors are characterised by a valence and conducting energy bands ('levels') separated by an energy gap, E_{gap} . The main difference among these materials is the magnitude of the energy gap. Insulators and semiconductors have large and small E_{gap} respectively while conductors have overlapping valence and conduction bands and thus, $E_{gap} = 0$. In the absence of light, the small magnitude of E_{gap} make CCD susceptible to electrons being promoted to the conduction band by thermal agitation leading to an unwanted noise: dark current. The contribution of dark current to a signal can be quite significant but can be drastically reduced by cooling the detector. Most of today's CCD's are equipped with thermoelectric coolers or are manufactured with an option for use with a cryogen.

One of the most important features of a CCD is its charge-transfer efficiency. In the original architecture, the depletion region was located directly under the gate electrode and was susceptible to random defects present at the interface between the electrode and p-type substrate which could trap electrons. The charge-transfer of these surface-channel capacitors was found to be poor. Most of today's CCD's use a buried-channel architecture whereby an n-type layer is deposited on the substrate (see Figure III-2). This architecture was found to have charge-transfer efficiencies exceeding 99.998%.

Table III-1. Features implemented to improve the performance of a CCD array detector. The efficiency of these features will vary depending on the architecture used as well as the manufacturer. DR stands for Dynamic Range and QE for Quantum Efficiency.

Features	Consequence
Back-illumination	Increases QE
Thinning of Si wafer	Increases QE
Buried n-channel	Reduces Dark Current
Thermo-Electric Cooler	Reduces Dark Current
Anti-reflective Coating	Increases DR & QE
Increased Well-Capacity	Increases DR & QE
Pixel Binning	Increases Sensitivity & DR

III.2.2 Noise considerations

III.2.2.1 Readout noise

The three main sources of noises are the reset, flicker and resistor noise which occur at the output stage. The reset noise originates from the Field-Effect transistor (FET) reset switch used to set the initial voltage prior to readout is known to have magnitude kT/C where k is the Boltzmann constant, T the temperature in Kelvin, and C the capacitance. The flicker noise (also called $1/f$ -noise or pink noise) is due to the presence of traps due to imperfections in the semiconductor at the MOSFET. The resistor noise (also called white noise) has magnitude $4kTRB^{1/2}$ where R is the resistance of the switch in Ohms and B the noise bandwidth in Hz.

These sources of noise can be eliminated or reduced by using a circuit called a Correlated Double Sampler (CDS) with Dual Slope Integrator (DSI). At the beginning of a readout sequence an integrating capacitor is initially grounded to remove previously transferred charges. During its reset phase, reset noise is sampled and stored in the integrator. In the next phase, the pixel information is transferred to the integrator where the noise level, common to both signals, is subtracted leading to a noise-free video signal which is then sampled by the ADC yielding a noise-free digitised video signal proportional to the charge or intensity of that particular pixel.

III.2.2.2 *Dark current*

Dark current arises predominantly from thermally excited electrons generated either in the substrate close to potential wells active during exposure to light or at the Si:SiO₂ interface due to surface defects. These electrons may get trapped in these wells leading to spurious noisy information during readout. In the first case, the dark current can be drastically reduced by simply lowering the operating temperature of the CCD. According to the manufacturer of the CCD chip used in this study, SITe, the number of electrons accessing the valence band at room temperature can be reduced roughly by a factor of two for every four to seven degree drop in temperature. A feature called Multi-Phase Pinning (MPP) is used to reduce the number of electrons at the Si:SiO₂ interface. This process involves applying a large negative voltage to electrodes already negatively biased thereby attracting holes and filling the interface states.

III.2.2.3 *Cosmic Ray Events*

A cosmic ray is loosely defined as a particle from outer space, such as a helium nucleus, for example. It can interact with the CCD substrate and also create charge in the pixels as it passes through the detector. The rate of cosmic ray events in a CCD on earth is approximately 1 per minute per square centimeter. SITe's ST-001A CCD is approximately 2 square centimeters in area leading to 2 cosmic ray events being detected every minute. As a result, such events will seriously affect the information read from a CCD if the latter has been exposed for more than a few minutes. Statistical algorithms¹⁶ have been developed to identify the presence of cosmic ray events when CCD are exposed for several minutes (very common in astronomy).

However, at short CCD exposures, cosmic ray events are easily recognisable by their characteristic sharp appearance in a spectrum. It usually only occupies 1 or 2 pixels, and thus can easily be differentiated from the typically broader structure of a transition in a spectrum, which is generally no less than 5-7 pixels.

III.2.3 Design and Construction of CCD imager

III.2.3.1 The CCD chip

A SITE ST-001A CCD chip was used to build the imager. The chip is a two-dimensional array consisting of 330 rows and 1132 columns of pixels each measuring $24 \mu\text{m}$ a side. The ST-001A is a 3-phase, buried-channel, thinned and back-illuminated, and thermo-electrically cooled CCD with MPP option. The characteristics of the ST-001A chip are listed in Table III-1 while a picture of the ST-001A imager is displayed in Figure III-4.

Table III-2. Characteristics of SITE's ST-001A CCD imager.

Pixel size	$24 \mu\text{m} \times 24 \mu\text{m}$
Imaging Area	$26.4 \text{ mm} \times 7.92 \text{ mm}$
Dark Current	$80 \text{ pA/cm}^2, < 3\bar{e} / \text{pixel} / \text{s}$
Well Capacity	$380,000 \bar{e}'\text{s}$
Charge-Transfer Efficiency	$> 99.995\%$
Quantum efficiency	30-60% from blue to red
Thermo-Electric Cooler	228 K

III.2.3.2 CCD Housing Design

The CCD housing, made from a single block of aluminium cube (weighing 5.5 Kg and measuring $160 \text{ mm} \times 160 \text{ mm} \times 80 \text{ mm}$), acts as a heat-sink for the CCD detector. A picture of the housing of the CCD camera can be seen in Figure III-4 and Figure III-5. On the rear side a 127 mm diameter cylinder 60 mm deep was machined out while on the front side a 125 mm diameter cylinder 10 mm deep was machined out. The deeper hole at the rear houses the electronics and wiring of the detector. A nylon reducing flange connected to the front of the housing enables the camera to be coupled to a Jobin-Yvon monochromator through a 50 mm diameter lateral detection port. This extension-tube ensures that the camera can be moved in and out without exposing the CCD-chip to ambient light. A Printed Circuit Board (PCB) 120 mm in diameter holding the circuitry that controls the CCD is mounted on nylon standoffs inside the aluminium housing. Power is supplied to the PCB and thermoelectric cooler through multi-pole connectors

located on the sides of the housing while connection for the video, trigger and computer are located on the back-plate. The CCD housing is mounted on a translation stage with fine adjustments enabling easy focus of the CCD.

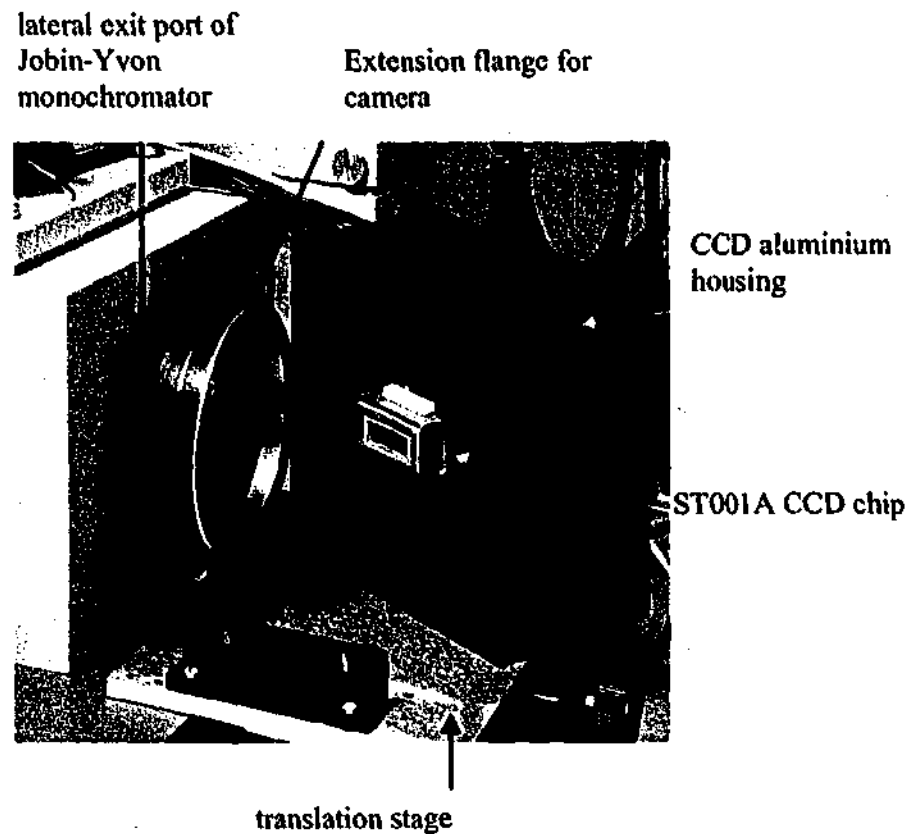


Figure III-4. Front view of CCD camera showing the ST-001A chip, housing and extension tube.

III.2.4 CCD Electronics and Logic Design

The electronics and logic circuitry was designed by Dr. Richard Morrison who also assembled the components on the PCB's designed by the author. A picture of the PCB is displayed in Figure III-5. The PCB contains components for video processing, clock generators and communication between the CCD chip and a Macintosh computer.

A program written in 'C' by Dr. R.J.S. Morrison provides an interface for communication between the computer (Macintosh Power PC) and the CCD controller (an EPROM) located on the PCB in the camera. Figure III-6 shows the input window with the options available to the user when operating the CCD detector. Before all 'experimental' exposures, the CCD-chip is briefly pre-exposed to ambient light for an amount of time controlled by the 'Clear time' parameter. The information stored on the CCD during the pre-exposure period is then dumped into the serial register of the chip and cleared. The number of readouts of the serial register is controlled by the 'Serial reg

clears' parameter. This flushing process can be repeated a number of times by altering the value of the 'Frame clears' parameter. The pre-exposure and flushing sequence is useful in removing any signal previously stored on the chip. The optimal values for these parameters are shown in Figure III-6. The delay parameters ensure efficient reading of the charges stored on the CCD; the values of 60 and 50 shown in Figure III-6 represent 100 and 20 μ s respectively. The 'Repeats' parameter is generally used in combination with an oscilloscope as it enables the user to see a 'live' image of the CCD chip. The magnitude of the previously-mentioned parameters can be varied by the user, however, once optimal values for these variables are determined they remain unchanged during normal operation. Thus, generally only three parameters need to be altered by the user during an experiment: the 'Binning', '# Line reads' and 'Exposure time' parameters. The first two determine the type of image recorded (full-frame or binned pixels) while the last one controls the magnitude of the experimental exposure time. An image can be stored either as a two or one dimensional array of pixels. In the former case, each row of pixels is transferred to the serial register one at a time and each pixel read and stored. This can be achieved by setting the 'Binning' value to one and the '# Line reads' to 330. While in the latter case, every row is transferred and accumulated (binned) in the serial register before being read and stored on the computer; in this case, the values of these parameters are simply reversed.

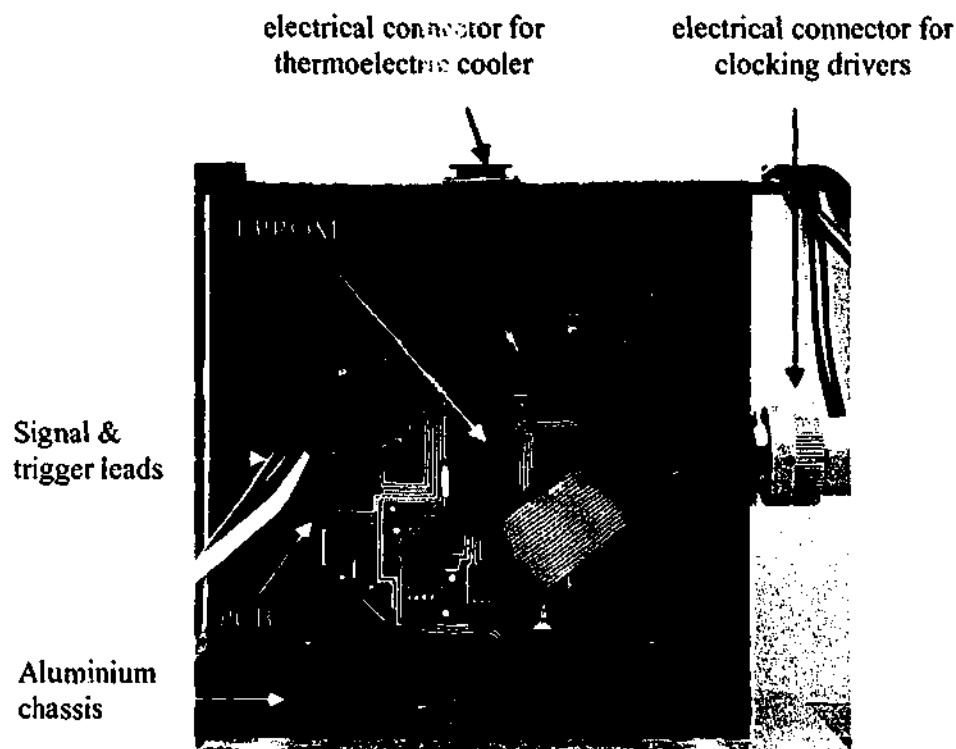


Figure III-5. Rear view of CCD camera showing the printed-circuit board, housing and electrical connections.

Clear time (s)	1.00	
Parallel shift delay	60	
Binning	330	<input type="checkbox"/> Save Ascii
# Line reads	1	<input type="checkbox"/> Save HDF
Frame clears	2	<input checked="" type="checkbox"/> Display full frame
Exposure time (s)	0.10	<input checked="" type="checkbox"/> IEEE interface
Serial reg clears	2	<input type="button" value="Ok"/>
A/D delay	50	<input type="button" value="Quit"/>
Repeats	1	

Figure III-6. Picture showing options available to the user during operation the ST-001A CCD detector.

Once issued, these commands initiate the program stored in the EPROM which uses a 10 MHz oscillator for clocking the gate electrodes of the CCD-chip and synchronising the video readout sequence. The TTL signals of the clocks generated by the EPROM are processed through level-shifter circuits to adjust the high and low voltages to those specified by the manufacturer for each gate and DC bias required to drive the CCD-chip (see Figure III-7 for illustration of signal processing).

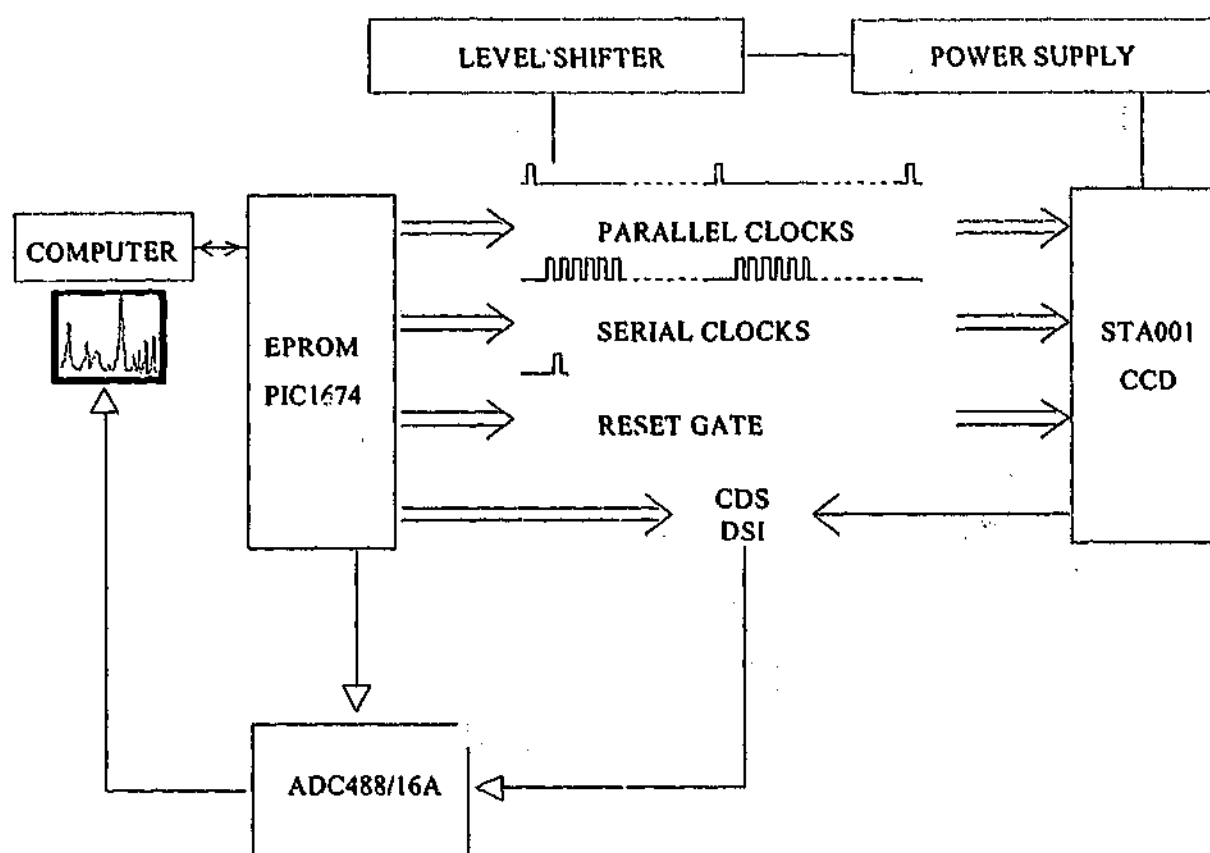


Figure III-7. Block diagram illustrating the signal processing of the CCD system

The CCD can be operated in one of two modes: full-frame or binning modes. In the full-frame mode a two-dimensional image is obtained similar to that of a photographic film as illustrated in Figure III-8. In this mode, the parallel clocks are set such that each row is shifted once before the serial clocks are initiated to read the charges stored in each pixel. The voltages V_1 , V_2 and V_3 , are first applied column-wise, shifting the first row of pixels through a transfer gate into a serial register. Now, the voltages are applied row-wise to shift the pixel's information horizontally through an amplifier and a correlated double sampler with a dual-slope integrator before digitisation in the analogue-to-digital converter (ADC). This process is repeated 1132 times thereby digitising the first row of pixels. The actual image is 1100 pixels long, there are 16 dark pixels on either side serving as reference dark pixels. The whole cycle is repeated a further 329 times thereby providing a two-dimensional digital image of the CCD.

In the binning mode, however, all rows are shifted vertically such that the information stored in a column is now accumulated in a single 'super' pixel in the serial register. The charges are then shifted horizontally to be read one at time. The binning-

mode is essential when optimising or monitoring an experiment as it yields a faster and more sensitive response at the expense, however, of resolution. A typical 'two-dimensional' and corresponding binned spectrum are shown in Figure III-8.

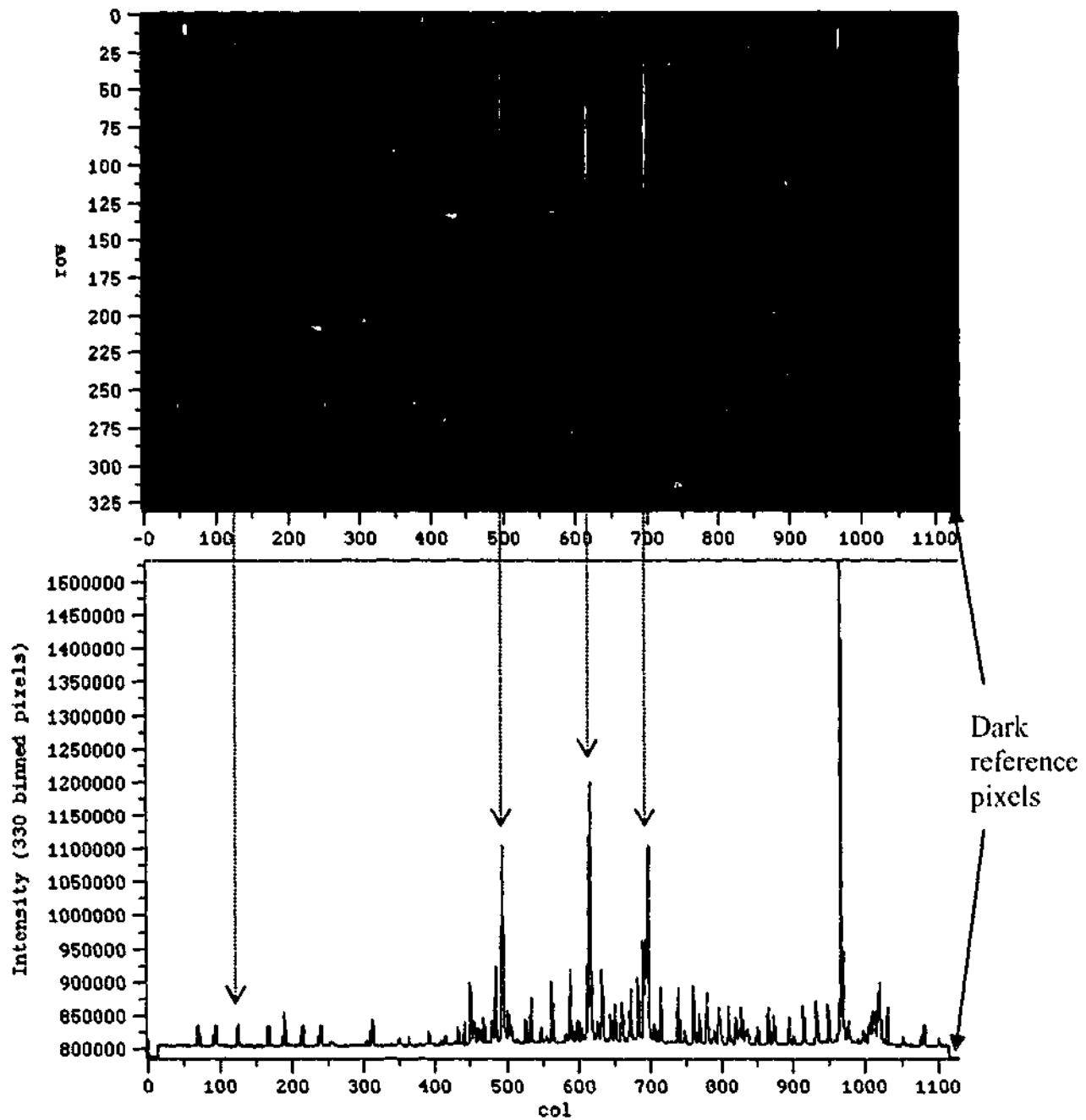


Figure III-8 Picture illustrating a typical full-frame (330×1132 pixels) image (top) and binned ($! \times 1132$ pixels) image. Light intensities in the full-frame picture are colour-coded from blue to red representing intensities in the range from zero and 32767 (saturated) ADC counts. Double-sided arrows show the correspondence between the colours of the full-frame output and intensities of the binned output.

III.2.5 Performance Testing of ST-001A imager

III.2.5.1 Experimental Setup

In this study, the ST-001A CCD imager coupled to a Jobin-Yvon monochromator has been used to provide a quick means of characterising and monitoring emission of species generated in corona excited supersonic expansions and by infrared laser powered pyrolysis. Emission dispersed by the monochromator is collected and recorded by the CCD imager mounted on a translation stage with fine control enabling fine adjustment of the detector position near the focal plane of the monochromator. Figure III-9 shows a typical setup for the CCD detector.

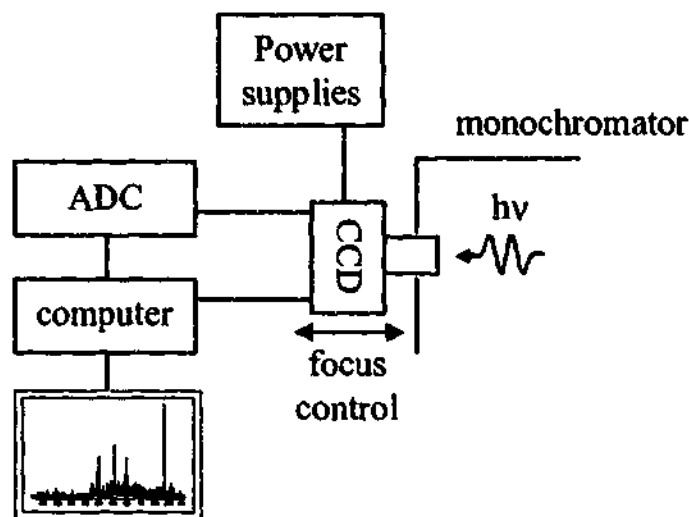


Figure III-9. Schematic illustration of experimental setup of CCD imager. The detector is mounted on a translation stage in order to adjust its 'focus'.

III.2.5.2 Tests

The performance of the imager was assessed by measuring the dark current as a function of temperature and time, and also by testing the linearity of its response to electromagnetic radiation. The first test was performed to monitor the temperature of the CCD as the ThermoElectric Cooler (TEC) is powered by an adjustable power supply (7 V limited to 2.7 A). The TEC equipped with sensors is connected to a 10 V power supply and its current measured. This current, when measured in μA corresponds to the CCD temperature in Kelvin. Figure III-10 shows the relationship existing between the temperature and the current resulting from the voltage applied to the TEC. The

temperature's dependence on the current can be adequately expressed using a quadratic model as supported by the magnitude of R^2 which represents the quality of fit ($R^2 = 1$ indicates a perfect fit). Within the range of zero to 2.5 amps this model has been applied to predict temperatures for the dark current tests.

With the current set at the maximum of 2.7 A, the temperature was monitored as a function of time. As can be observed in Figure III-11 the temperature drops sharply in the first five minutes to a minimum of 233 K before rising and equilibrating to approximately 240 K after 40 minutes. The increase in temperature can be explained by the fact that the heat-sink (the housing) is 'saturated' and is not able to dissipate the heat, as a result the TEC loses its efficiency as a heat-pump leading to an increase in temperature of the detector.

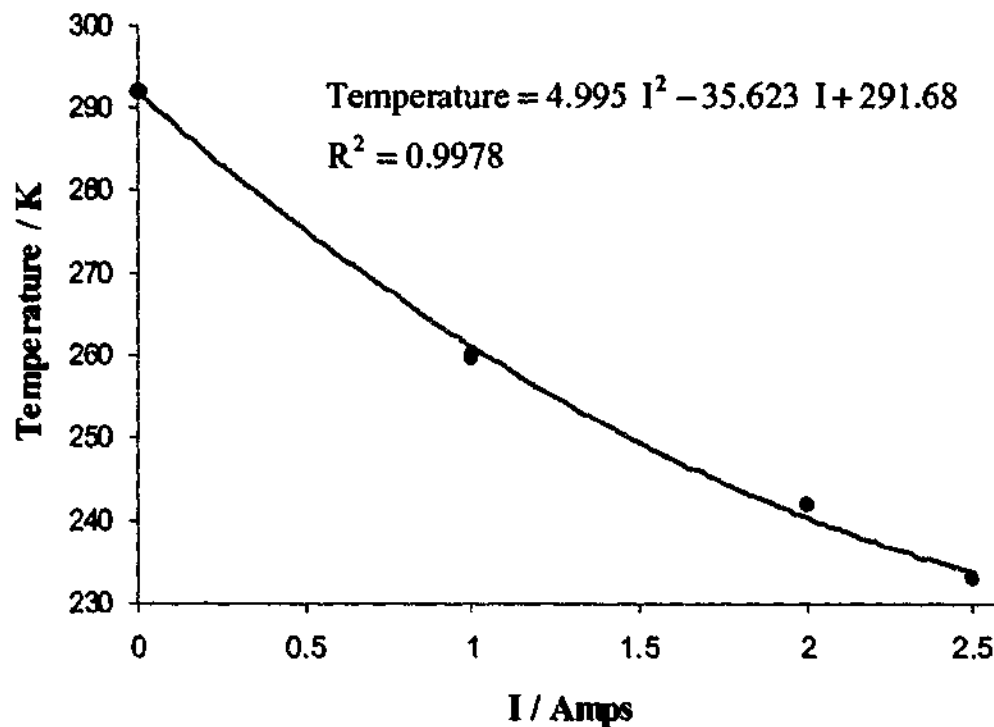


Figure III-10 Variation of temperature with respect to current resulting from the voltage applied to the TEC.

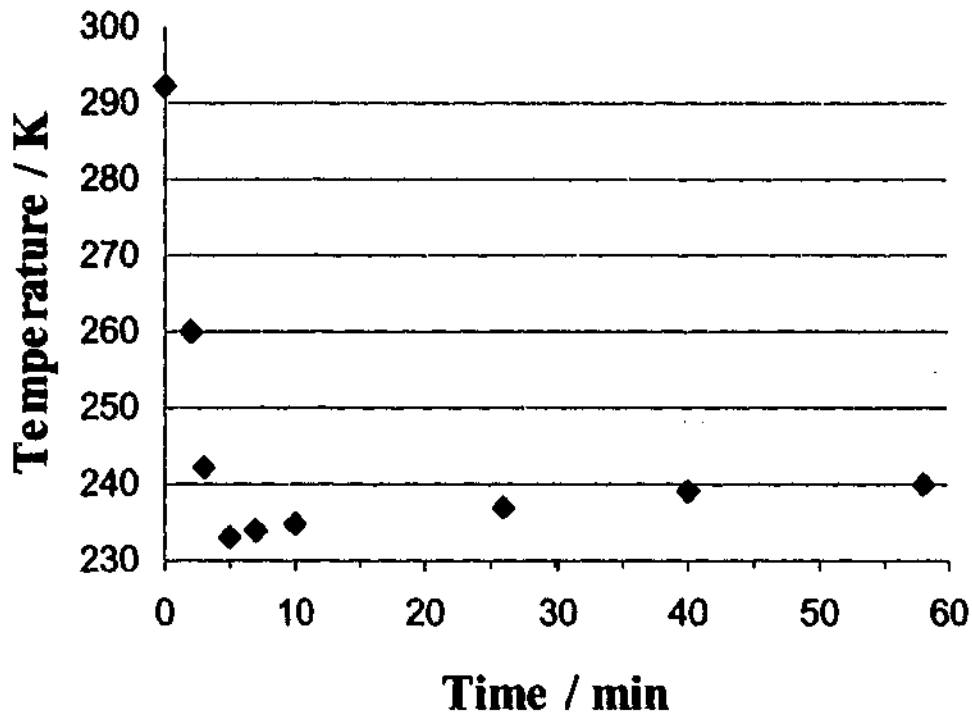


Figure III-11 Plot of the time evolution of the temperature of the ST-001A CCD imager as the thermoelectric cooler is powered to 2.7 A.

When measuring the dark current, the slits of the monochromator were closed and room lights turned off to minimize the amount of ambient light reaching the CCD thereby enabling experiments with extended exposures to be carried out. The magnitude of the dark current was measured as a function of temperature (as predicted by the current) and exposure time. The exposure time was first set to 1.5 seconds and measurements recorded at different current settings. The experiment was then repeated for an intermediate exposure of 10 seconds and a extended exposure of 120 seconds. The magnitude of the dark current is indicated by the magnitude of the root-mean-square noise. As can be observed in Figure III-11 for short exposures, the dark current count is more or less at its minimum at approximately 260 K (1 Amp). However, as the exposure time increases, the current needs to be further increased to reduce the dark current signal. Nevertheless, the dark current signal is indeed reduced by roughly a factor of 2 for every 4-7 degree drop in temperature as indicated by the manufacturer. For experiments conducted with exposures of 10 and 120 seconds, the dark signal could not be measured at temperatures higher than the ones indicated in Figure III-12 because the detector became saturated with background radiation under these conditions.

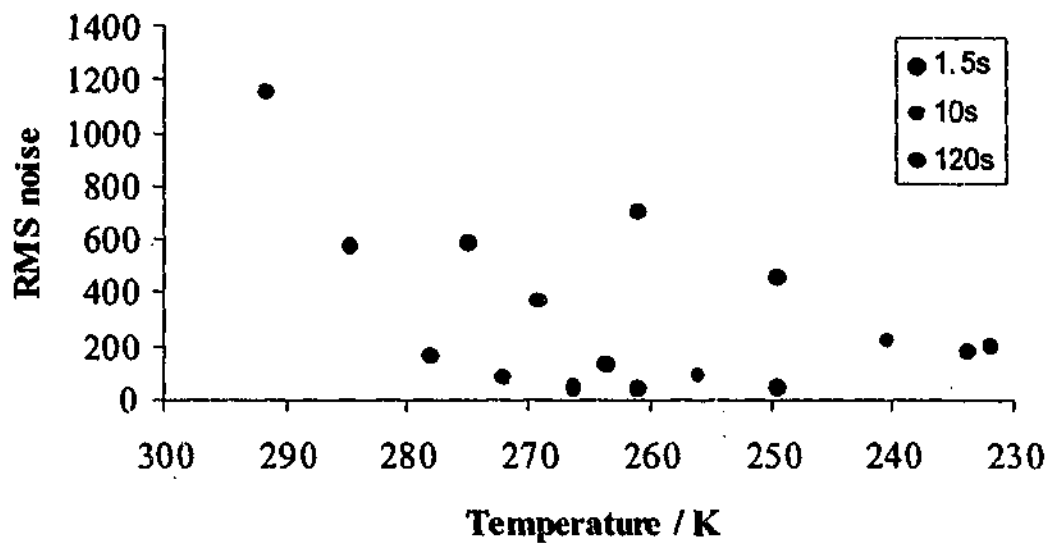


Figure III-12 Dark current measured at different lengths of exposure and temperatures.

The last set of tests carried out was performed to investigate the detector's response to electromagnetic radiation. The image of a Krypton pen-lamp (manufactured by Oriol Optics) was focused onto the entrance slits on the Jobin-Yvon monochromator set at $2 \mu\text{m}$. The intensity of the atomic line of Krypton centered at 557.03 nm was measured at different lengths of exposure and the results are displayed in Figure III-13. For short exposures up to six seconds the CCD's response is adequately linear but slowly departs from linearity at longer exposures. According to the manufacturer, the charge transfer efficiency is 0.99995 at 500 electrons but is 0.99999 at 5000 electrons, thereby indicating that the CTE is improved when more charges are transferred. This expected behaviour may account for the positive departure from linearity of the detector at long exposures as more charges are collected and transferred under these conditions.

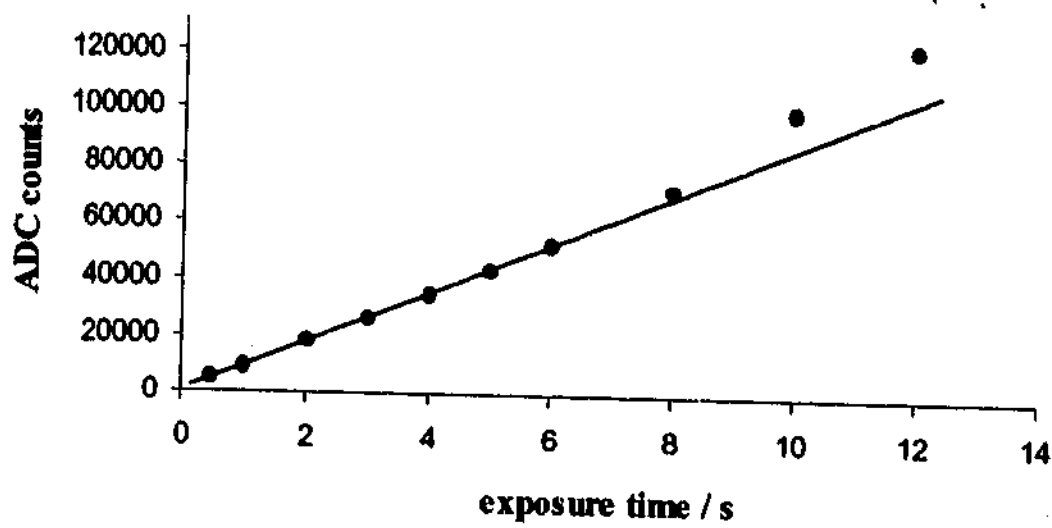


Figure III-13. ST-001A response to electromagnetic radiation. The intensity of a Krypton line at 557.03 nm was measured at different exposures.

IV Towards High Resolution Spectroscopy of Transients with Low Internal Energies

IV.1 Introduction

Chemical reactions proceed by the 'breaking' of chemical bonds followed by the formation of new ones in the process of going from reactants to products. It follows that transient molecular or atomic species acting as intermediates between reactants and products must be generated in order for a chemical reaction to proceed to completion. These reactions may take place in a laboratory environment, in the atmosphere or even in space. Consequently, transients are short-lived molecules that are mechanistically important reaction intermediates dictating the path a reaction will follow and, thus, the products. It is therefore imperative to not only identify transients generated in a reaction but, also, to study them in order to gain insight on chemical reaction processes and possibly control such a chemical reaction to favour one product over another.

Spectroscopy has played an important role in the discovery and study of transients as analyses of their spectra have provided important information on their structure and molecular properties, thereby greatly enhancing our knowledge and understanding of these labile species. In the field of spectroscopy, transients are usually produced from

the breakdown of carefully selected parent compounds or precursors before being probed by a variety of techniques. Transients were first studied in the 1920's in the emission of flames and discharges and, since then, they have been observed in both emission and absorption using a wide variety of laboratory techniques: oven-based and laser-based pyrolysis, UV and laser photolysis, electron impact, atomic abstraction, ... Using the same precursor, each technique may lead to distinct sets of breakdown products as their differing environments may favour unlike reaction pathways. As a result, the choice of precursors and transient-generating techniques is important as they contribute differently to the discovery and study of transient molecules. These short-lived molecules are also of astronomical interest as they have been observed in the spectra of comets and, more generally, in extraterrestrial media. The reader is referred to books written by Herzberg¹ and Setser² and references therein for details on techniques developed to produce transients.

With the advent of supersonic expansions in the 1970's quite a few of the previously mentioned techniques have been adapted to supersonic expansion systems. One of the first methods used to produce transients in jets was oven evaporation carried out by Smalley *et al.*³ and Ahmad-Bitar *et al.*⁴ in 1977. Laser photolysis^{5,6} and ablation⁷, atomic abstraction⁸ and discharge techniques⁹⁻¹¹ have also been combined with supersonic expansions to generate rotationally cold transients.

In this study, transient molecules have been generated by way of infrared laser powered pyrolysis (IRLPP) and corona excited supersonic expansion (CESE). These two methods will be presented in detail in the following sections. The IRLPP technique was used primarily as a simple emission source to test the CCD-based detection system presented in chapter III. The IRLPP study has also been prompted by the observations of McNaughton *et al.*¹² in their infrared absorption study of NCN produced by IRLPP of NCN₃. During their experiments, a purple glow was observed in the laser path and was assigned solely to the CN radical when the emission spectrum was recorded in the visible region with a linear CCD-based detection system. The CESE technique was used as it is one of the simplest techniques used to generate transients with low rotational energies in order to simplify their spectra.

IV.2 InfraRed Laser Powered Pyrolysis

The use of infrared (IR) lasers for inducing chemical reactions is a wide and well developed field. The first high-power IR molecular laser was built by Patel *et al.*^{13,14} in the mid 1960's. It operates around 10.6 μm involving rotational transitions occurring between the $3_0^1 1_1^0$ and $3_0^2 2_2^0$ vibrational levels of the CO_2 molecule. Belief that such lasers could be used to either control reaction pathways or separate isotopic species prompted a variety of studies in the late 1960's and early 1970's. In 1972, Tardieu de Maleissye *et al.*¹⁵, and De Hemptinne and De Hemptinne¹⁶ were among the first to realise the benefits of pyrolysing gas samples with a CO_2 InfraRed Laser. A few years later, this method was coined Laser Powered Homogeneous Pyrolysis by Shaub and Bauer¹⁷. The next major contribution to IRLPP was that of Russell and co-workers who were the first to couple FTIR to IRLPP.¹⁸⁻²² Recently, McNaughton *et al.*¹² performed the first high resolution FTIR study of gases generated by way of IRLPP. Numerous studies involving pulsed laser were soon to follow, as well as the construction of other infrared lasers such as N_2O and CO . The reader is referred to the reviews of Russell²³ and Steinfeld²⁴, as well as References²⁵ and ²⁶ for detailed description of the work that has been carried out in this field.

IRLPP is an alternate transient generating method which overcomes some of the inherent drawbacks of conventional flow pyrolysis. The most important feature of IRLPP methods is the fact that heat energy required to produce transients is dispersed homogeneously and conveyed directly into the precursor gas. As a result, the walls remain relatively cool thereby effectively eliminating secondary processes, which normally occur at the hot walls of conventional pyrolysis methods.

In a typical IRLPP experiment a precursor gas sample and a chemically inert photosensitiser gas, typically SF_6 , are premixed before introduction in an evacuated glass cell. The gas mixture is then irradiated with a high-power CO_2 IR laser, which is absorbed by the photosensitiser molecules and rapidly converted into translational energy (heat) through effective relaxation processes. Subsequently, the translational energy is transmitted to the precursor molecules via efficient collisional energy transfers which may lead to the generation of transient species in an excited state. On one hand, the emission can be collected to characterise or monitor the species generated, and on the other hand, an absorption spectrum can be recorded by probing the transients with a

broadband IR radiation.(McNaughton *et al.*¹²) The main advantage of IRLPP over conventional pyrolysis techniques is direct delivery of heat to the precursor molecules.

IV.2.1 IRLPP cell and optical setup

The IRLPP cell and optical setup are illustrated in Figure IV-1. The cell is a four-way 200 mm long Pyrex tube 40 mm in diameter equipped with a pair of 50 mm diameter and 25 mm diameter glass flanges, and a pair of 5 mm diameter Pyrex tubes. The flanges are 'O'-ring sealed with 50 mm diameter, 3 mm thick CaF₂ windows, and 25 mm diameter, 5mm thick ZnSe windows. The 5 mm tubes are fused to glass ball-joints for easy 'O'-ring connection on the inlet side to a glass vacuum line where the precursor is prepared or introduced, and on the outlet side to a rotary pump. The flow of gas is controlled by a Teflon needle-valve located on the inlet side where a Baratron gauge is placed to measure the cell pressure.

In a typical experiment, a slowly-flowing gas mixture consisting of a precursor and SF₆ is irradiated through the ZnSe windows by a Synrad 48-2, 40 W CO₂ infrared CW laser emitting between 10.5 and 10.7 μm. The CO₂ laser has an adjustable output power and is water-cooled. A fire brick located on the side opposite to the laser acts as a beam stopper and absorber. Emission resulting from the interaction of the IR laser and the gas mixture is collected and recorded on one side by a Bruker FT spectrometer and on the other side by a Jobin-Yvon monochromator equipped with a CCD detector.

On the FT side a CaF₂ lens is placed a focal length away from the centre of the cell to 'collimate' the emission source, the beam is then focused onto the entrance aperture of the FT spectrometer by a 250 mm focal length off-axis parabolic mirror. On the monochromator side two CaF₂ lenses are used, one to 'collimate' the source and the other to focus the beam onto the slits of the monochromator.

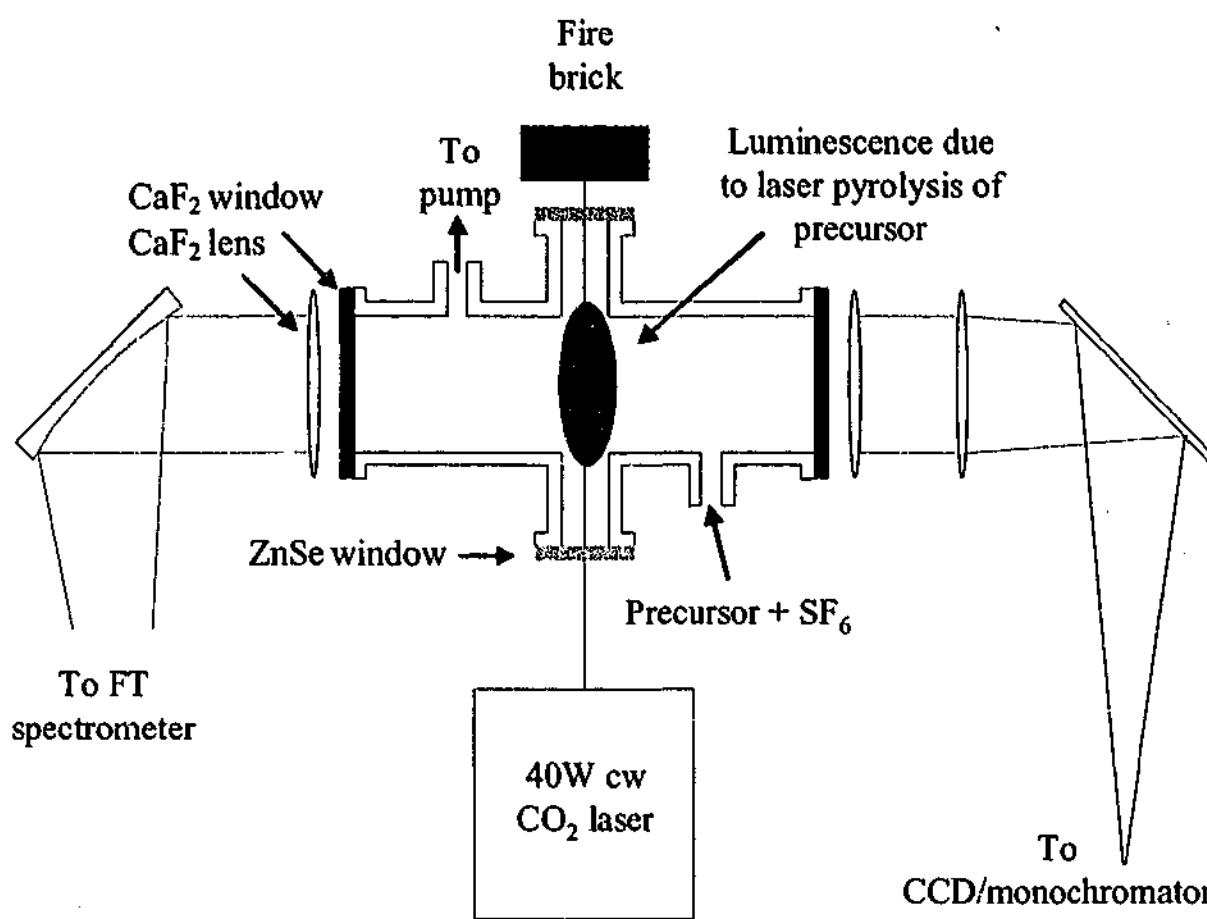


Figure IV-1 Schematic of IRLPP cell and typical optical setup.

Prior experience in the laboratory using the IRLPP technique has enabled quick optimisation of experimental conditions, and, thus only a limited number of tests were required to optimise the system. Tests on the IRLPP system were carried out using NCN₃ as a precursor and will be presented in Chapter V where the emission of breakdown products resulting from the IRLPP and CESE of NCN₃ are presented and discussed.

IV.3 Corona Excited Supersonic Expansion

Corona excited supersonic expansion (CESE) has been shown to be one of the simplest methods of producing rotationally cold free radicals and ions. CESE is a combination of the techniques of supersonic free jet expansion and corona discharge. In the following sections, historical backgrounds and theories of these techniques are presented before the CESE method is described.

IV.3.1 Supersonic Free Jet Expansions

IV.3.1.1 Historical background

Supersonic free jet expansion was developed from the technique of molecular beam. In 1911, Dunoyer²⁷ designed the first apparatus for generating an 'oven' (molecular) beam by heating a sample of sodium and allowing the vapour to effuse through an orifice into an evacuated chamber. Later, Stern^{28,29} initiated the first in depth study of molecular beams by designing a series of experiments beginning in the 1920's to investigate a number of physical phenomena previously inaccessible to experimental analysis. In 1931, Rodebush³⁰ reported the possibility of achieving higher molecular intensities than the effusive source utilised by Dunoyer and Stern. He suggested the coupling of a tube slit, more commonly called a skimmer, to a nozzle source. However, it was not until 1951 that Kantrowitz and Grey³¹ developed the theory of supersonic jet flow, and predicted higher molecular intensities, narrower velocity distribution, higher velocities and cooler internal degrees of freedom than conventional oven beams. They proposed a design coupling a skimmer to a converging-diverging nozzle source. That same year, in an attempt to verify this theory, Kistiakowsky and Slichter³² showed that, higher intensities than conventional effusive sources could indeed be achieved. However, due to lack of pumping capacity the beam intensities from their experiments fell short of Kantrowitz and Grey's predictions.

In 1954, Becker and Bier³³ utilised a system with a higher pumping capacity and obtained beam intensities close to those predicted by the theory predicted by Kantrowitz and Grey. Two years later in their experiments on hydrogen-seeded argon beams, Becker *et al.*³⁴ demonstrated the narrow velocity distribution as predicted by Kantrowitz

and Grey. In 1960, Hagen and Henkes³⁵ were among the first to demonstrate the relaxation of the internal degrees of freedom in a molecular beam as predicted by Kantrowitz and Grey by means of velocity analysis of beams extracted from jet sources. Although the effects of condensation were observed in 1956 by Becker *et.al.*³⁶, it was not until 1961 that Henkes³⁷ and Bentley *et.al.*³⁸ detected clusters of molecules in seeded beams for the first time. A series of theoretical treatments were undertaken in the 1960's which improved the understanding of the theory of supersonic free jet expansions first advanced by Kantrowitz and Grey.

In 1962, Muntz³⁹ performed one of the first spectroscopic studies of molecular beams and recorded the first evidence of *freezing* of the internal states. For the first time spectroscopists were able to isolate a gas sample and produce it with low internal temperatures. In the mid 70's, Smalley *et.al.*^{3,40-44} undertook the first laser spectroscopic studies of supersonic expansions of molecules seeded in monoatomic carrier gases. In some of their studies^{3,44}, they omitted the skimmers to also study radially expanding monomer species, and thus, generated the first *free jet* supersonic expansions. Studies by Ryali and Fenn⁴⁵ revealed that clustering of molecules in an expansion is confined to the central region of the beam. This observation was of great importance since it indicated that the use of a skimmer would impede spectroscopic studies of the seeded molecules as the concentration of the monomer species is greatly reduced along the expansion axis of the beam.

An abundance of studies coupling supersonic free jet expansions to a variety of spectroscopic techniques have been reported since; they cover the spectral range of the electromagnetic spectrum lying between the microwave to the UV.

IV.3.1.2 Theory

One of the most used parameters characterising a flow regime is the Knudsen number

$$K_n = \lambda_0 / d \quad (\text{IV.1})$$

where λ_0 represents the mean-free path of the gas and d the diameter of the orifice through which the high-pressure gas enters an evacuated system; the mean free path being defined by

$$\lambda_0 = \frac{kT}{\sigma P} \quad (\text{IV.2})$$

where k is the Boltzmann constant, T the absolute temperature in Kelvin, σ the molecular cross-section and P the vacuum pressure.

In a typical supersonic free jet expansion experiment an inert monoatomic gas at high pressure is allowed to flow through a small orifice (*i.e.* nozzle) before undergoing an adiabatic expansion into an evacuated chamber. During expansion, atoms communicate with each other mainly through inelastic binary collisions, and efficient collisional energy transfers convert the random thermal motion of the gas before expansion into directed mass flow. This process has the effect of narrowing the velocity distribution, thereby reducing the translational temperature of the gas.

If a small amount of molecular gas is introduced in the system, the cooled translational degrees of freedom of the gas mixture provide a refrigeration medium for the internal degrees of freedom of the seeded molecules. As the latter come into equilibrium with the translational cold bath *via* non-radiative collisional energy transfers, the vibrational and rotational (in some cases electronic as well) degrees of freedom of the seeded species are relaxed. As the expansion proceeds, the cooling process continues until the density of the gas mixture becomes too low to provide the number of collisions necessary to convert any remaining energy in the internal degrees of freedom of the seeded molecules. From this point on, all degrees of freedom are *frozen* as the expanding gas enters a state of free flow. The cold environment existing in the free flow region provides the means for otherwise highly unstable species to survive. Generally, the equilibration rate between translational and rotational degrees of freedom is faster than between translational and vibrational, and thus,

$$T_{trans} < T_{rot} < T_{vib} \quad (IV.3)$$

where T_{trans} , T_{rot} and T_{vib} are the translational, rotational and vibrational temperatures in the free flow region, respectively. The extent of cooling is also limited by complex formation as well as condensation (clusters) since the heat of formation of these species is converted into random motion, which will warm up the gas in the expansion.

In an expansion, the core portion of the expansion located behind the Mach disk can be considered as isentropic as it is shielded from any background perturbation by a jet boundary all around and by a Mach disk at the front.⁴⁶ As a result, isentropic equations of state can be utilised to describe intensive and extensive properties of an expansion:

$$T = T_0 / [1 + \frac{1}{2}(\gamma - 1)M^2] \quad (\text{IV.4})$$

$$P = P_0 / [1 + \frac{1}{2}(\gamma - 1)M^2]^{\gamma(\gamma - 1)} \quad (\text{IV.5})$$

$$\rho = \rho_0 [1 + \frac{1}{2}(\gamma - 1)M^2]^{(1 - \gamma)} \quad (\text{IV.6})$$

where T_0 , P_0 and ρ_0 are the initial temperature, pressure and density, respectively; T , P and ρ are the same quantities at mach number, M ; γ is the ratio of heat-capacities of the carrier gas, C_p/C_v . The mach number, M_x , at a distance x from the nozzle orifice is defined by

$$M_x = A \left(\frac{x}{d} \right)^{\gamma - 1} \quad (\text{IV.7})$$

where A is a constant depending on γ and is equal to 3.26 for monoatomic gases and d is the nozzle diameter. The terminal mach number, M_∞ , is defined by the ratio of the terminal velocity, V_∞ , and the local speed of sound, a :

$$M_\infty = V_\infty / a \quad (\text{IV.8})$$

and V_∞ is defined by

$$V_\infty = \sqrt{2 \frac{\gamma}{\gamma - 1} \frac{R}{W} (T_0 - T)} \quad (\text{IV.9})$$

where R is the molar gas constant and W the molar mass of the gas. In general, only a knowledge of the Mach number is required to evaluate parameters characterising a supersonic regime described in Equations (IV.4), (IV.5) and (IV.6).

IV.3.1.3 Relaxation of internal degrees of freedom

The minimum quanta of energy available in the rotational degrees of freedom are small compared to the thermal energy, kT , transferred during collision; the minimum quanta are much larger for the vibrational degrees of freedom. As a result, collision-induced energy transfers are more likely to depopulate the rotational energy levels of a molecule, and cause rotational rather than vibrational relaxation. Hence, cooling of the rotational degrees of freedom is more drastic than that of the vibrational degrees of freedom, although Powers *et al.*⁴⁷ have shown that vibrational degrees of freedom can be more efficiently cooled by using a pulsed supersonic nozzle.

In general, any relaxation process dissipating energy with magnitude of the order of kT could be induced by collision whether it be rotational, vibrational or, even electronic (*i.e.* spin-orbit). Since the different internal degrees of freedom are cooled to a different degree in an expansion, the principle of equipartition of these energies is not applicable. As a result, the internal degrees of freedom of such a system are in a state of non-equilibrium. Furthermore, the application of the Boltzmann temperature distribution to such a system is not appropriate. This theoretical implication has been the subject of controversy as studies have shown both thermal⁴⁸ and athermal⁴⁹ distributions. The cooling limit defined by the terminal Mach number, M_∞ , was found to be a function of the product of the stagnation pressure in atmospheres, P_0 , and the nozzle diameter, d ⁵⁰:

$$M_\infty = 1.33(P_0 d)^{0.4} \quad (\text{IV.10})$$

IV.3.1.4 Application to spectroscopy

Traditionally, optical spectroscopic investigations of gases were performed in a non-flowing environment, and only spectra of diatomic and small polyatomic molecules could be analysed. Since the spacing between rotational transitions decreases with increasing molecular weight, the rotational structure in the spectra of large systems can become highly congested. Furthermore, if the vibrational spacings are relatively small, vibrational bands will overlap and the spectrum will consist of highly congested overlapping bands. As a result, spectral analysis of large systems was not viable. Initially, two techniques were developed in an attempt to reduce congestion in the spectra of large molecules. The first, consisting of cooling the sample in its cell, is limited by the reduced vapour pressure of the sample at low temperatures. Although the use of multipass cells could overcome the problem of sensitivity due to the low vapour pressure, the low operating temperature was still too high and, as a result, the spectra were still unresolvable. For these molecules, temperatures lower than their freezing points are needed to relieve the spectral congestion. Any attempts to use this technique to cool a sample to these temperatures would only result in freezing that sample and, thus, further reduce the amount of available molecules in the gas phase to the vapour pressure of the solid.

The second technique involves isolating a sample in a matrix. Although very cold temperatures can be achieved and large molecules can be studied in isolation, this technique suffers from two major drawbacks, which could hinder spectroscopic

analysis. First, the rotational energies carrying the geometrical information of a molecule cannot be measured since the molecules do not rotate in the matrix. Second, interactions between the sample and host molecules forming the matrix can lead to serious perturbations, which only complicate the analysis.

The advent of molecular beam techniques renewed interest in the field of molecular spectroscopy, as spectroscopists were able to isolate a gas sample and produce it with low internal temperatures. The principal advantage for spectroscopic analysis of monomer species is the simplification of previously congested spectra due mainly to the drastic reduction in the number of observed rotational transitions. Thus, spectroscopists were able to record and analyse spectra of large molecules as vibrational bands previously masked by the spectral congestion could easily be identified. Studies coupling supersonic expansions to a variety of spectroscopic techniques have been reported.

Recently, the technique of Enclosive Flow Cooling (EFC) has been developed in order to yield supercooled species. Although the internal energies attainable are not as low as the ones obtained in supersonic free jets, the EFC technique has its own advantages over the latter. The EFC technique is presented in detail in Chapter VIII.

IV.3.2 Corona Discharge

IV.3.2.1 Historical background

A corona discharge is a phenomenon, which occurs when an intense electric field is present between electrodes in gaseous media. Coronas were frequently observed and reported by sailors as their sail ships were caught in thunderstorms. When the rounded head of the masts of the ships were struck by lightning during a storm, the wet masts acted like lightning rods, and a light display in form of a crown was observed; sailors called this phenomenon St Elmo's fire.⁵¹

The advent of high-voltage sources many years later enabled scholars to produce electrical discharges within a laboratory setting. The discharges were subsequently referred to as corona (*crown* in Latin) discharges. In some of these controlled experiments, corona discharges were observed when excessive voltages were present in insulated systems. Corona discharges were found to produce electromagnetic radiation, audible noise, ozone, heat, mechanical erosion and electric wind.

In electrical equipment, minimisation of the occurrence of corona discharges was essential as they may have lead to disastrous results. However, in some fields, the properties of corona discharges have been found to be very useful. For example, the effects of corona discharges enable plastic films to be wetted by printing inks, they are used to separate ores and to generate ozone. Corona discharge has also been used as a means to charge particles or surfaces in xerography, electrostatic paint spraying, and in the manufacture of sandpaper.⁵²

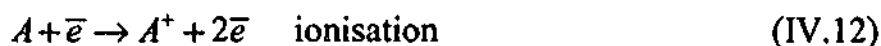
IV.3.2.2 Theory

A thorough and more technical description of the theory behind corona discharges is beyond the scope of this work; numerous textbooks about coronas are available.⁵¹⁻⁵³ In the following a concise qualitative explanation of the principal processes involved in corona discharges is offered.

Electrical or corona discharges are electrostatic events that occur in the presence of gaseous media and strong electric fields. In the initial stages of a corona discharge when the applied voltage, V , is less than the critical voltage, V_s , electrons, (\bar{e}), are only generated by the interaction of cosmic or UV rays, $h\nu$, with the gaseous particles, A :



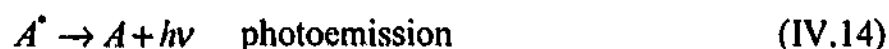
At the onset of the discharge where $V = V_s$, there are enough highly energetic electrons to collide with the gas particles and ionise some of them by dislodging one of their outer-lying electrons, thereby increasing the number of free electrons:



If the gas density is fairly high, further collisions of this nature will generate even more free electrons, resulting in an avalanche of electrons. This will in turn cause multiple secondary avalanches. An unbroken chain of such avalanches constitutes a self-sustaining discharge. Unless a large current-limiting impedance is connected in series with the corona discharge, the current can rise from 10^{-17} to a few thousand amperes as the avalanche proceeds. In such environments, collisions between gas-phase atoms or molecules (A) and electrons (\bar{e}) tend to generate ions. However, if the kinetic energies of the colliding particles are not sufficient for ionisation to occur, excited metastable atoms, molecules and radicals (A^*) may also be formed



This collection of metastable ions, atoms, molecules and radicals is called plasma. As the plasma particles, A^* , revert back to a stable lower-lying energy state via radiative processes, emission ranging from the radio wave to the X-ray region of the electromagnetic radiation will occur:^{53,54}



The process described by Equation (IV.14) is of great importance as spectroscopic study of their emission may not only reveal the nature of species generated during this process but also yield information about their molecular structures and properties.

IV.3.3 Corona Excited Supersonic Expansion

The combination of supersonic expansions and corona discharge has enabled spectroscopists to easily generate free radicals and ions with low internal energies. Searcy was one of the first to use CESE to generate a molecular beam of metastable helium atoms.¹¹ Close to a decade later, CESE was used to generate rotationally-cold free radicals.⁵⁵⁻⁵⁷ In 1986, Engelking⁵⁸ produced an in depth study of parameters critical for the stable operation of CESE technique and later, in 1991. The pioneering work of the previously-mentioned authors has enhanced the understanding of processes involved in the technique of CESE. As a result, numerous studies have been reported using this method to generate transient species with low internal energies.

In a typical CESE experiment, a high-pressure molecular mixture consisting of a precursor gas seeded in a carrier gas, usually a rare gas, is exposed to a coronal electrode located in a glass or quartz nozzle, and expanded in an evacuated chamber. Application of a high voltage through a set of current limiting resistors to the electrode (anode) results in a discharge current generating highly energetic electrons. The current passes through the gas in the throat of the nozzle making connection to ground by ionic and electronic conduction on the low-pressure side of the nozzle. Violent collisions between these highly energetic electrons and the carrier gas atoms lead to the production of metastable rare gas atoms, which upon interaction with precursor molecules *via* complex reaction pathways then produce excited short-lived species or transients. Further collisions between these newly formed transients and rare gas atoms during the supersonic expansion into the vacuum cause a considerable reduction in the rotational temperature of the transients, typically less than 50K, leading to significant simplification of their spectra. Thus, CESE is a simple and highly effective technique

for the production and study of rotationally cold polyatomic transients. Production of free radicals is not only dependent on the choice and concentration of precursors, but also on critical parameters such as the nozzle geometry, the position of the coronal electrode relative to the nozzle throat and the discharge current.

IV.3.4 CESE chamber and performance testing

IV.3.4.1 The CESE chamber

The chamber, as illustrated in Figure IV-2a), is made of a 500 mm long stainless steel tube 170 mm in diameter. At one end, a gate valve leading to the pumping system is connected to the chamber while a nozzle assembly mounted on a flange seals the opposite end. Four 50 mm long, 70 mm diameter stainless tubes terminated by flanges are welded to the chamber in a cross fashion yielding four viewing ports 150 mm from the nozzle end. The top vertical viewing port consists of a simple 50 mm window-mounted flange used to monitor the discharge with the eye while the bottom port is unused and thus, sealed with a flange. A 95 mm long 65 mm diameter stainless steel tube mounted on a flange is inserted in both horizontal ports such that the tubes intrude the chamber by 45 mm on either side leaving an 85 mm gap where the nozzle is centered as shown in Figure IV-2 b). The interior of each tube is finely threaded, and fitted with a 50 mm diameter CaF₂ window and lens (60 mm focal length) using threaded optical mounts. Each window is held in position against an 'O'-ring by a brass disc optical mount threaded on the outside. The location of the lens can be easily adjusted by screwing the optical mount. The CESE chamber is then mounted on a stainless steel frame equipped with vertical adjustments enabling the chamber to be raised to the level of the emission port of the FT spectrometer and the entrance slits of the monochromator.

On the gate-valve side, a 12.5 mm stainless tubing connected to a valve-system provides direct access to a two-stage Varian SD-700 rotary pump (35 m³/h nominal pumping rate). The gate-valve is connected to an Edwards EH500 mechanical booster pump which is also connected to the rotary pump (350 m³/h nominal pumping rate for the combination). A valve system has been designed to enable the rotary pump to only either evacuate the chamber or back the booster pump. The chamber is equipped with a Dynavac CG8 thermistor and an ionization gauge sensitive to pressures between 10 and 10⁻⁷ Torr. During normal operation, the chamber is initially evacuated to a few milli-

mechanical booster pump backed by the rotary pump.

The nozzles are made from 6.25 mm diameter quartz tubing flame-collapsed and ground back to pinholes of 100 to 500 μm in diameter typically. The nozzle assembly, as illustrated in Figure IV-2c), consists of a 170 mm diameter flange with a centered Cajon fitting for the nozzle, and a translation stage equipped with a micrometer holding a nylon Cajon-type fitting (mounted on a post) aligned with the fitting located on the flange. Once in position, the nozzle gripped by the nylon fitting can be moved from 0 to 25 mm at intervals of 0.010 mm by the micrometer. The nylon fitting also provides additional insulation from the high-voltages applied to the electrode located inside the nozzle. A 1.6 mm diameter stainless steel rod connected to a high voltage power supply (0-20 kV) through an adjustable current-limiting ballast resistor (0.5 to 24 M Ω) is inserted in the quartz tubing via a Teflon 'tee' Swagelock connector. The latter is also connected to the gas input.

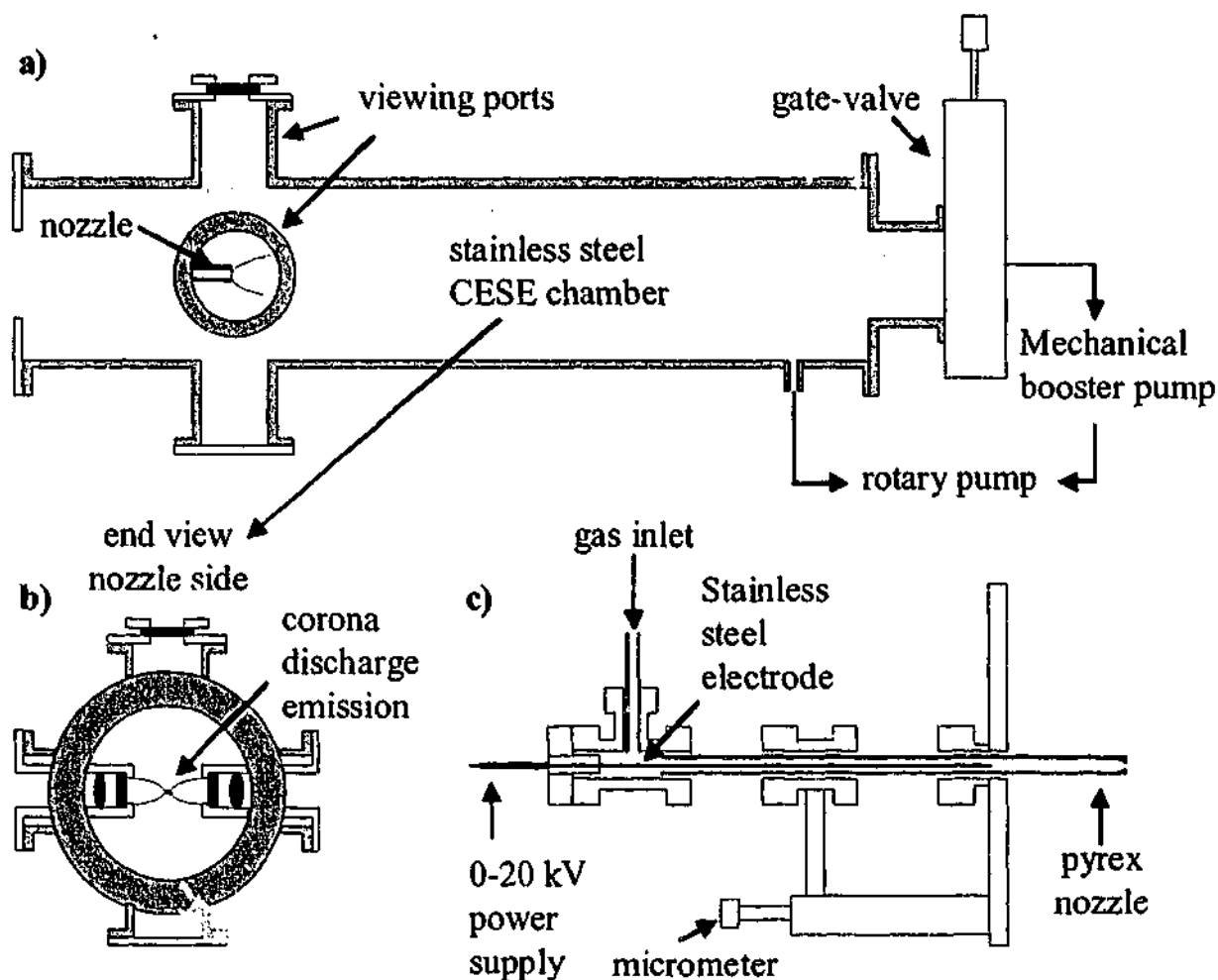


Figure IV-2 Schematic illustration of CESE chamber: a) side view of chamber showing the viewing ports on the nozzle-side and pumping system used in CESE experiments; b) endview of chamber on the nozzle-side showing the corona discharge emission collected by the CaF_2 optics; c) nozzle assembly showing the electrical connection to the electrode and the translation system used to move the nozzle.

IV.3.4.2 Performance testing

In a typical CESE experiment, a gas precursor is seeded in a carrier gas, usually a rare gas, at high pressures (760 – 1100 Torr), and the gas mixture is introduced in the CESE chamber ($\approx 10^{-3}$ Torr) through a pinhole nozzle (100-500 μm). The gas mixture is then energised as it reaches the nozzle throat by a current (10-320 μA) resulting from the application of a voltage of a few kV to the electrode. The optical setup utilised in the CESE experiments is the same as the one used with the IRLPP technique (see illustration in Figure IV-1 in section IV.2.1). With this setup, images of the corona discharge and nozzle are formed on the entrance slits of a Jobin-Yvon HR1000 monochromator and on the aperture wheel of the FT spectrometer.

In order to quickly determine parameters influencing the intensity of light emitted and ascertain the system's ability to cool down the rotational energies of species generated in a CESE, spectra were recorded with a ST-001A CCD detector coupled to the monochromator. Spectra of the A-X system of the OH radical generated in a CESE were recorded and analysed to test the performance of the present system. The OH radicals results from the CESE breakdown of H_2O molecules present as impurities in He gas. The concentration of water is of the order of 25 ppm in the high-purity grade He gas used in this study.

Helium at 100 Torr of positive pressure was introduced in the CESE chamber through a 250 μm pinhole nozzle. A current of 10 μA was generated by the application of 2 kV to the stainless steel electrode. With the monochromator wavelength centered at 313.5 nm, the CCD detector was exposed for 60 seconds and the emission spectrum recorded. Long exposures were required as the QE of the detector around 300 nm is approximately 30 % and the slits were set at 20 μm . The $A^2\Sigma - X^2\Pi$ CCD-spectrum of the OH radical showing a section of the 0-0 and 1-1 bands is shown in Figure IV-3.

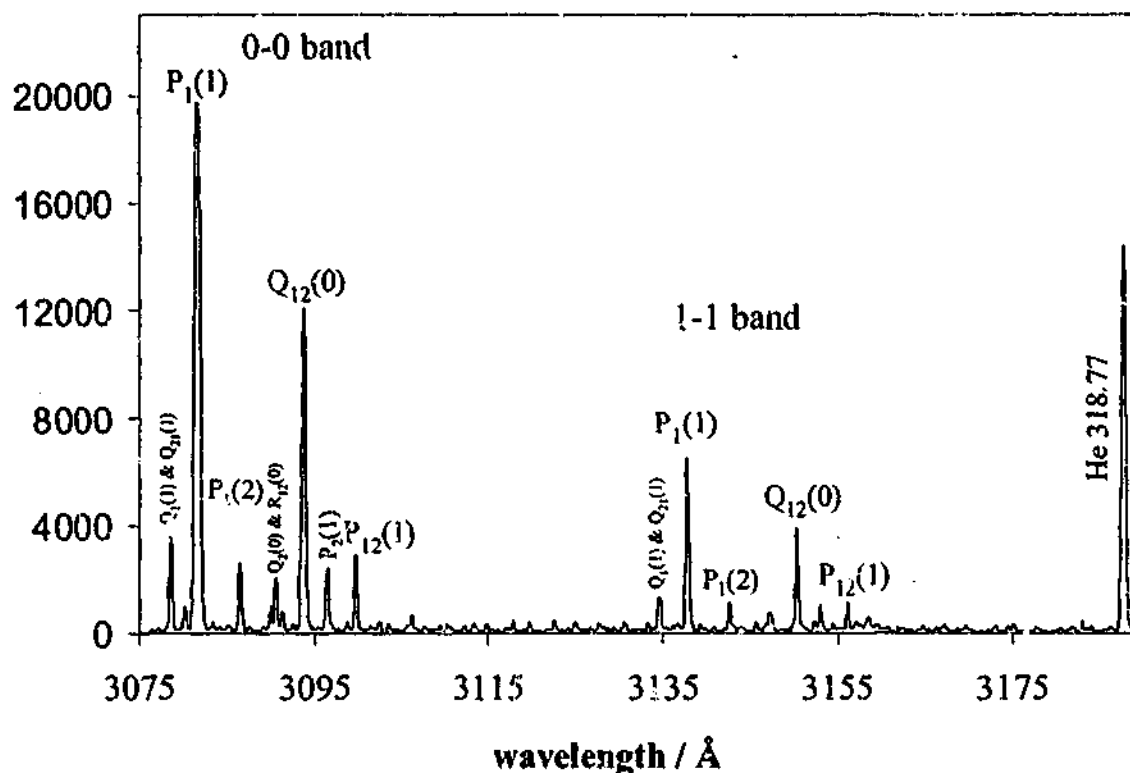


Figure IV-3 Portion of the A-X spectrum of OH generated in a corona excited supersonic expansion H_2O impurities (25 ppm) in He.

First, the intensity of the $P_1(1)$ transition was monitored as a function of distance downstream from the nozzle orifice in order to locate the region with the most intense emission. This experiment was executed at 100, 200 and 300 Torr of positive pressure and the results are summarized in intensity v/s distance plots illustrated in Figure IV-4. At 100 Torr, the intensity of the $P_1(1)$ transition, although a little erratic, has a general downward trend for all magnitudes of current tested but does not show the inverse quadratic behaviour predicted by theory. The irregular behaviour of the intensity may be due to the instability of the discharge typically observed in this study at low pressures. Increasing the magnitude of the current has an unexpected trend which can only be attributed to partial fouling or clogging of the nozzle. At 200 Torr the intensities are also irregular, however, they seem to reach a maximum around 500 μm . At 300 Torr, the exposure time was reduced to 30 seconds as the CCD became saturated. In this case, the change in intensity is regular and clearly reaches a maximum value around 800 μm from the exit plane of the nozzle. In summary, the most intense spectra were recorded at 300 Torr of positive pressure of He at a distance of 800 mm from the nozzle exit plane; the unexpected influence of the current is attributed to partial clogging of the nozzle.

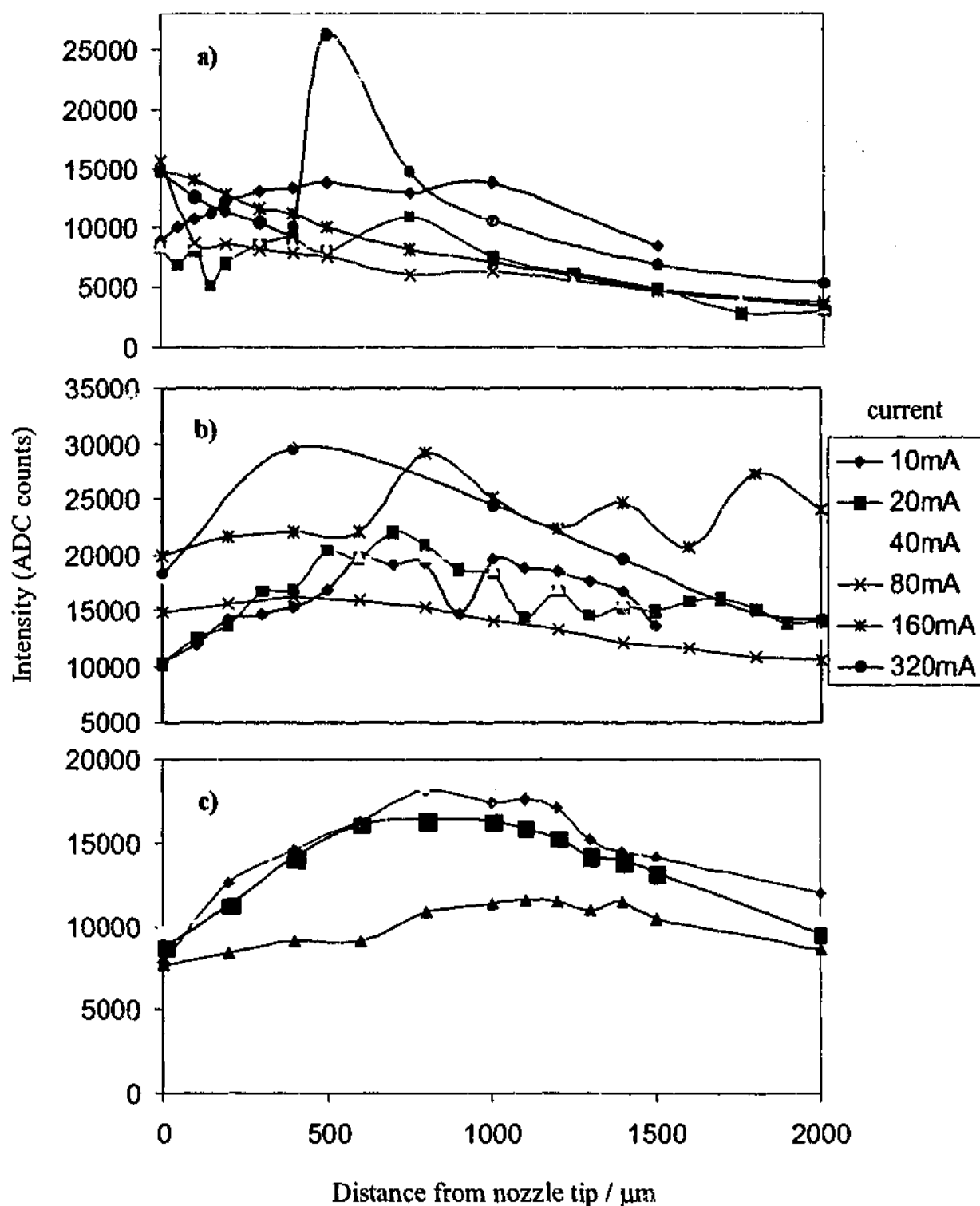


Figure IV-4 Dependence of Intensity of $P_1(1)$ transition of OH A-X system on distance from exit plane of nozzle in CESE setup and magnitude of corona discharge current at a) 100 Torr, b) 200 Torr and c) 300 Torr of backing pressure of He.

Although equilibrium is not achieved in the jet, the rotational temperature can be approximated by the Boltzmann population distribution. The rotational temperature was estimated by considering the relative intensities of observed rovibronic transitions. Theory has shown that the intensity of an emitting transition with wavenumber value of ν can be described by

$$I_{em} \propto \frac{C_{em} \nu^4}{Q_R} S_{J'} (2J'+1) e^{-BJ'(J'+1)hc/kT} \quad (IV.15)$$

where C_{em} is a constant depending on the change of dipole moment and the total number of molecules in the initial vibrational level, $S_{J'}$ the part of the Franck-Condon factor depending on the rotational quantum number, J , $BJ'(J'+1)hc/kT$ the energy of the rotational level J in wavenumbers and Q_R the rotational partition function. The Hönl-London factor, $S_{J'}$, for a P-branch is described by

$$S_{J'}^p = \frac{(J'+1+\Lambda')(J'+2+\Lambda')}{4(J'+1)}$$

where Λ is the electronic orbital angular momentum quantum number. Thus, a plot of $\ln\left(\frac{I_{em}}{2J'+1}\right)$ against $J'(J'+1)$, should result in a straight line with slope $-Bhc/kT$ and intercept $A S_{J'}$, where $A = \ln \frac{C_{em} \nu^4}{Q_R}$. However, in the presence of only a few rotational transitions, the rotational temperature can be estimated by determining the ratio of intensities of transitions of a band by using the following equation.

$$\ln\left(\frac{I_{em_1}}{I_{em_2}}\right) = \ln\left(\frac{S_{J'_1}(2J'_1+1)}{S_{J'_2}(2J'_2+1)}\right) - [J'_1(J'_1+1) - J'_2(J'_2+1)] Bhc/kT$$

where A_1 and A_2 differing only by ν^4 are assumed to be equal at large values of ν , and, thus A_1/A_2 is equal to one. This method was adopted to estimate the rotational temperature of the spectrum since only the first two or three transitions in any branch were observed, as illustrated in Figure IV-3.

Only the intensities of the $P_1(1)$ and $P_1(2)$ transitions belonging to the 0-0 band were selected due to their larger signal-to-noise ratio. In order to determine the part of the expansion with the coldest rotational temperature, the OH spectrum was recorded at different distances from the nozzle orifice and its temperature estimated. This was

achieved by altering the position of the nozzle with respect to the slits of the monochromator (using the micrometer), thereby effectively moving the image of the corona discharge on the slits. These experiments were then repeated at different values of current and pressure. The calculated temperatures are summarized in the plots shown in Figure IV-5.

Under the experimental conditions observed in this study, the coldest region of the expansion is located around 1500 and 2000 μm or six to eight nozzle diameters downstream of the nozzle orifice. It should be noted, however, that for experiments where 300 Torr of positive pressure of Helium were used, the temperature does not seem to have reached its minimum at 2000 μm . As explained by theory, after a certain point in the expansion molecules 'run out' of colliding partners and cannot transfer anymore internal energy, and, thus are 'frozen'.

The rotational temperature, T_{rot} , also decreases with backing pressure as can be observed by the overall trend at 100, 200 and 300 Torr. This observation seem to agree with the theory which predicts that there is a pressure dependence on the location of terminal Mach, M_{∞} , as expressed by Equation (IV.10).

Thus, depending on whether the highest intensity or the coldest rotational temperature is required in a study the region of the expansion investigated will differ. Due to the lack of sensitivity of the near-IR and mid-IR detectors of the FT spectrometer the most intense portion of the expansion was studied. However, the high sensitivity of the CCD detector enabled studies of the expansion to be carried out at large distances downstream from the nozzle orifice.

The 'grassy' structures present in the OH spectrum of Figure IV-3 are not due to noise. The intensities of these features were increased by a factor of 30 and compared to a hot spectrum of OH. The spectra displayed in Figure IV-6 shows one to one correspondence between the rotationally hot OH spectrum and the one recorded in this study. This observation is quite typical of spectra of molecules generated in supersonic expansions as rotationally warm OH radicals are generated probably by colliding with warm background gases present at chamber pressures around 10^{-3} - 10^{-4} Torr.

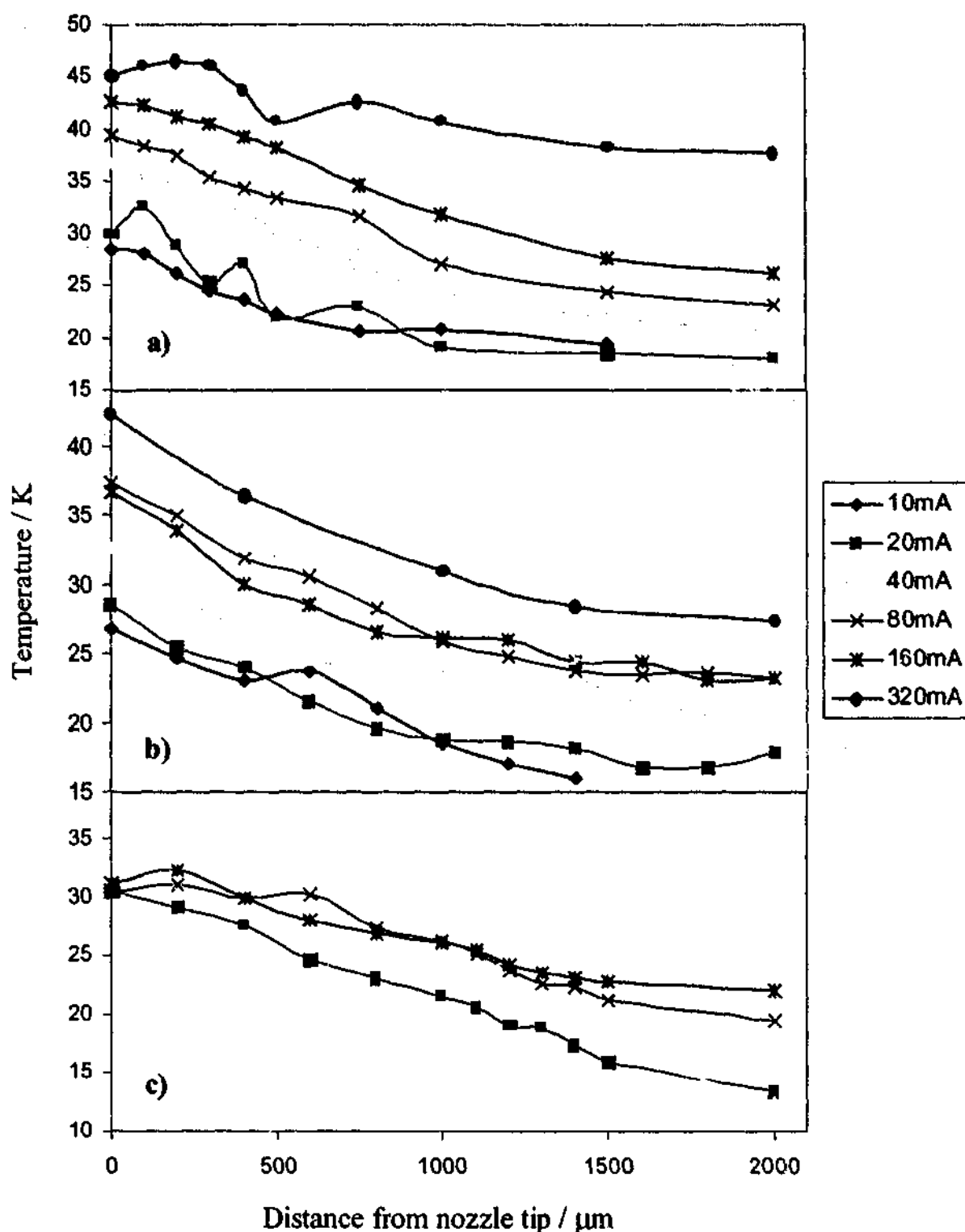


Figure IV-5 Rotational temperatures estimated using the ratio of $P_I(1)$ and $P_I(2)$ transitions of the 0-0 band of the A-X electronic system of the OH radical generated in a CESE. All spectra were recorded with the center wavelength of the monochromator set at 313.5 nm and its slits at 20 μm, and CCD exposure times of 60 seconds. Helium backing pressures of 100, 200 and 300 Torr above atmosphere were used and the resulting temperature profiles are illustrated in figures a), b) and c) respectively. In each case, spectra were recorded at different voltage settings to monitor the effect of current on the temperature profile.

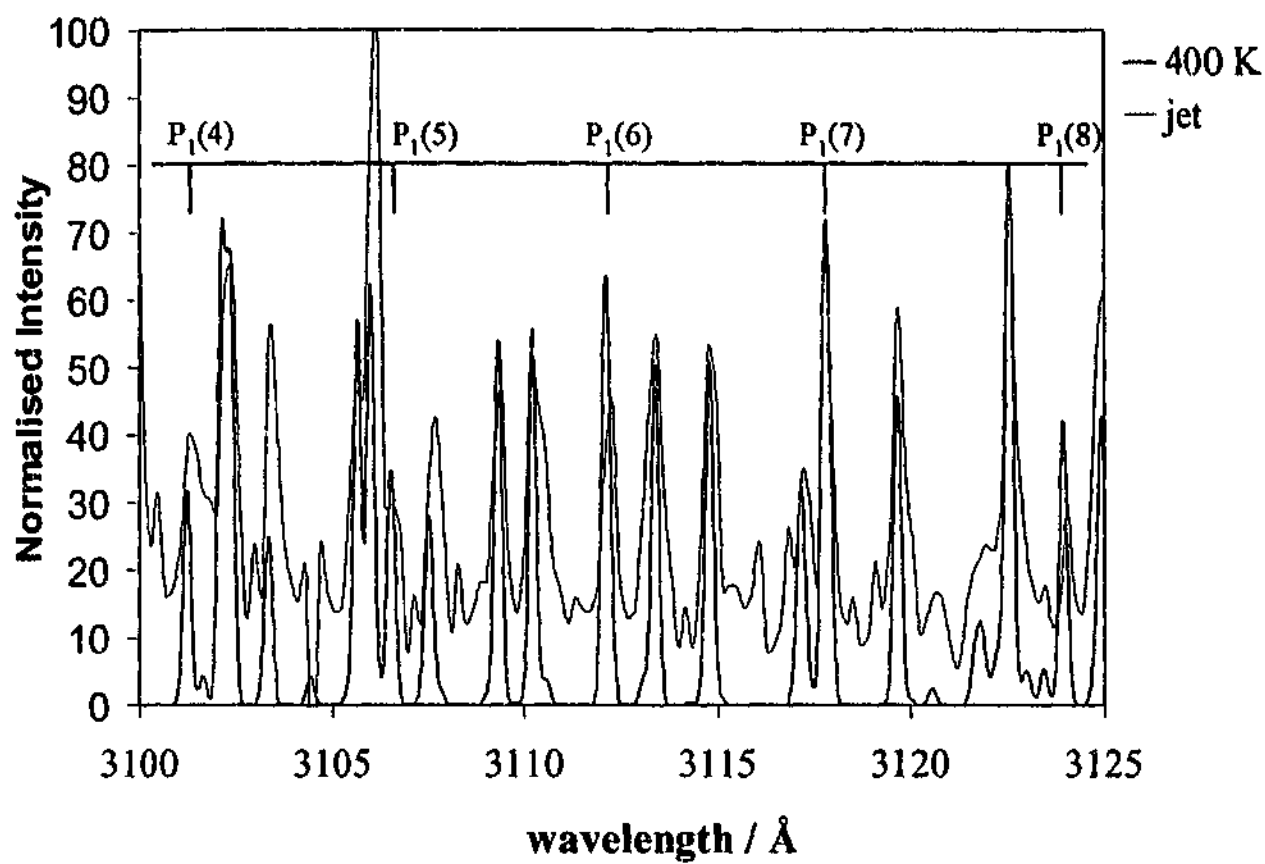


Figure IV-6 Comparison of grassy portion of jet spectrum of OH to that of a spectrum recorded at 400K.

V UV/vis Emission Spectrum of the Cyanonitrene Radical

V.1 Introduction

Cyanonitrene radicals (NCN) are reaction intermediates of considerable importance in pyrolysis and combustion reactions of nitramine propellant molecules where the CN-bond is extensive.¹ NCN is also of astrophysical importance as it has been identified in the UV/vis emission spectra of the Brörsen-Metcalf² and Austin³ comets and is believed to be a precursor to the CN radical commonly observed in the interstellar medium.

The UV/vis emission spectrum of the $A^3\Pi_{u,inv} - X^3\Sigma_g^-$ system of NCN was originally observed by Jennings and Linnett in 1960.⁴ NCN was generated by introducing hydrocarbons in a flow of active nitrogen, N_2 , and was proposed as a potential candidate for a spectral structure observed at 329 nm. However, its molecular origin could only be confirmed four years later when Herzberg and Travis⁵ recorded and studied the high resolution UV/vis absorption spectrum of both NCN and isotopically substituted NCN generated by flash photolysis of diazomethane. Their subsequent analysis yielded estimates of the origin of the 000 000 band, rotational constants of both states, and the spin-orbit coupling constant of the A-state. They also performed the

vibrational analysis of an emission spectrum of NCN recorded by Warsop (unpublished work) and reported a series of band heads belonging to the same electronic system of NCN.

In 1965, Milligan *et al.*⁶ recorded and studied the ultraviolet spectrum and the first low-resolution infrared absorption spectra of NCN generated by photolysis of cyanogen azide, NCN_3 , trapped in argon, nitrogen, carbon monoxide and carbon dioxide matrices. They observed vibrational fundamentals of NCN at 423 and 1475 cm^{-1} respectively but did not assign them. That same year, Wasserman *et al.* observed NCN and CNN by electron spin resonance spectroscopy, and Pontrelli and Anastassiou⁷ observed a new spectral feature at 332.7 nm and tentatively assigned it to vibrationally excited triplet NCN. This band was later observed by Kroto⁸ when NCN was inadvertently produced while attempting to generate CCO by photolysis of NCN_3 in the presence of CO. Upon investigation, Kroto assigned the 332.7 nm absorption feature to the $\tilde{c}^1\Pi_u - \tilde{a}^1\Delta_g$ electronic transition of NCN. The high resolution analysis of this system, presented in a following paper⁹, provided estimates of rotational parameters of the lower and upper states, as well as Renner-Teller parameters of the upper $^1\Pi_u$ state. In 1969, Okabe and Mele¹⁰ found that $\text{CN}(B^2\Sigma)$ and $\text{NCN}(A^3\Pi_u)$ were produced in the vacuum-ultraviolet photodissociation of NCN_3 . However, they did not detect any fluorescence from the $\tilde{c}^1\Pi_u$ state of NCN previously observed by Kroto.^{8,9} In this study, they also reported energetically favourable mechanisms for the production of the CN and NCN radicals in their respective electronic states.

Two theoretical studies on the ground state of NCN were undertaken in the 1970's by Thomson¹¹ and Williams¹². In 1972, Thomson performed the first *ab initio* calculations of equilibrium geometry and energy levels of ground state linear triatomic molecules while Williams, in 1974, performed *ab initio* calculations of the spin-spin interactions, λ_{ss} , of ground triplet states of linear triatomic molecules.

In 1989, Smith *et al.*¹ performed laser-induced fluorescence studies of species generated in a microwave discharge of N_2 and CF_4 , and observed off-diagonal, ($\Delta v_i \neq 0$), transitions belonging to the $A^3\Pi_{u,jmv} - X^3\Sigma_g^-$ system of NCN. In 1994, Martin *et al.*¹³ and Suter *et al.*¹⁴ performed more theoretical calculations and determined infrared frequencies and geometries of the isoelectronic molecules CCO, CNN and NCN.

In 1995, McNaughton *et al.*¹⁵ generated NCN by InfraRed Laser Powered Pyrolysis (IRLPP) of NCN_3 . In this study, they observed and recorded the high resolution infrared absorption spectrum of the ν_3 fundamental and $2_1^1 3_0^1$ hot band with a Fourier transform spectrometer,¹⁵ and the visible emission of the $A^2\Pi_{inv} - X^2\Sigma_g^-$ 'Red' system of CN ($\Delta\nu = 1, 2, 3$ & 4 sequences) with a CCD/diffraction grating spectrometer at low resolution.¹⁶ The analysis of their infrared spectrum yielded the first direct estimates of parameters belonging to the ν_3 fundamental of NCN.

In 1996, Beaton *et al.*¹⁷ re-examined the 000 000 band of the $A^3\Pi_{u,inv} - X^3\Sigma_g^-$ system of NCN using laser excitation spectroscopy. The spectrum was recorded at higher resolution than that of Herzberg and Travis⁵, and thus, provided molecular parameters of higher accuracy than previously reported. In a report appearing later that year, Hensel and Brown¹⁸ recorded the laser magnetic resonance spectrum of the ν_3 fundamental of NCN complementing the previous study of McNaughton *et al.*¹⁵ In another laser excitation study of the A-X system of NCN, Beaton and Brown¹⁹ observed and analysed rovibronic transitions of the ν_2 hot band (the 010 010 transition) which consists of two vibronic sub-bands systems due to the Renner-Teller effect: the $^3\Delta_g - ^3\Pi_u$ and $^3\Sigma_g^- - ^3\Pi_u$ transitions. They reported new estimates of the Renner-Teller parameter and, upper and lower bending vibrational wavenumbers. After noticing some discrepancies in the assignment of the 011 010 hot band of McNaughton's infrared study, Wienkoop *et al.*²⁰ (from the Brown group) re-investigated that band by infrared laser magnetic resonance and obtained indirect estimates of vibrational wavenumbers belonging to the ν_1 and ν_2 modes of the ground state as well as the molecular parameters of the hot band.

The most recent experimental work performed on NCN is that of Bise *et al.*²¹ who studied the spectroscopy and photodissociation dynamics of the singlet and triplet states of NCN using fast beam photofragment translational spectroscopy. In particular, they observed and recorded the spectrum of the $B^3\Sigma_u^- - X^3\Sigma_g^-$, $\tilde{c}^1\Pi_u - \tilde{a}^1\Delta_g$ and $\tilde{d}^1\Delta_u - \tilde{a}^1\Delta_g$ of NCN occurring in the UV region.

In 2000, Perić *et al.*²² performed high-level *ab initio* calculations of the potential energy surfaces belonging to the $X^3\Sigma_g^-$, $1^1\Delta_g$ and $1^1\Sigma_g^+$ electronic states of NCN. In 2001, Rajendra and Chandra²³ performed similar type of extensive *ab initio* calculations

on several valence-type excited states of NCN. In the process, they were able to determine equilibrium geometry, electronic structure and various molecular properties. That same year, Perić *et al.*²⁴ performed large scale configuration interaction (CI) calculations and determined accurate bending potential energy surfaces for the 1^3A_1 and 2^3B_1 components of the $A^3\Pi_u$ excited electronic state of NCN and vibronic transition moment functions for the $A^3\Pi_{u,inv} - X^3\Sigma_g^-$ system of NCN.

The aim of this study is to characterise the emission spectra of breakdown products generated in the IRLPP and CESE of NCN_3 with a particular focus on the UV/vis emission spectrum of the $A^3\Pi_{u,inv} - X^3\Sigma_g^-$ of NCN.

V.2 Experimental

In their IR study of NCN generated by IRLPP of NCN_3 ,[†] McNaughton *et al.*¹⁵ introduced BrCN ,[‡] in a bulb containing sodium azide, NaN_3 . They found that the only gas present in the bulb after approximately an hour was NCN_3 , and, also, that a mixing ratio of SF_6 (carrier gas) to NCN_3 of 10:1 was required to optimise the production of NCN upon irradiation by a CO_2 laser. In the IRLPP experiments conducted in this study however, NCN_3 was synthesised using the method originally described by Milligan *et al.*⁶ whereby gaseous BrCN mixed with a carrier gas is passed through a column of dry and finely powdered sodium azide. The latter was obtained from Aldrich in the form of crystals and was carefully ground to a fine powder (see appendix for required precautions). Approximately 50 g of the finely powdered NaN_3 was placed in a glass vessel (as illustrated in Figure V-1) equipped with a sintered glass filter.

[†] MSDS:ChemInfo Record number 3411

[‡] MSDS:ChemInfo Record number 515

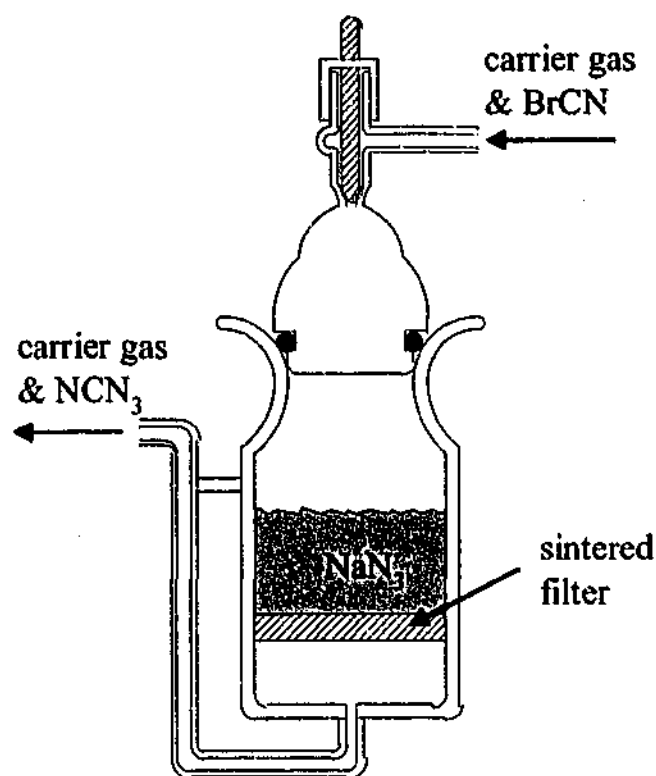


Figure V-1 Schematic of cell designed for the reaction of NaN_3 and BrCN to generate NCN_3

BrCN has an ambient vapour pressure of 92 Torr, thus, in order to achieve the optimum mixing ratio of 10:1 as found by McNaughton *et al.*¹⁶ with close to 100 Torr of carrier gas, the vapour pressure of BrCN had to be reduced to approximately 10 Torr. Crystals of BrCN (< 0.5 g), also obtained from Aldrich, were thus placed in the cold finger of a glass manifold connected to the top of the glass column containing the azide compound. The cold finger was then partially submerged in a slush bath reducing the temperature, T_{BrCN} , of the cold finger to -10°C and consequently limiting the vapour pressure of BrCN , P_{BrCN} , to 6-7 Torr. SF_6 gas at a pressure, P_{SF_6} , of 60-70 Torr was then introduced to the manifold to maintain a mixing ratio of SF_6 to BrCN of roughly 10:1. The combined gases were subsequently slowly flowed through the column of dry finely powdered NaN_3 . The gas mixture consisting of SF_6 and the newly formed NCN_3 (and possibly unreacted BrCN) was then introduced to the four-way IRLPP cell previously described in Section V.2.1. The $\text{SF}_6 / \text{NCN}_3$ mixture was then irradiated by an IR CO_2 laser delivering 30 to 35 W at $10.6\ \mu\text{m}$. Subsequent excitation of the gaseous mixture resulted in a purple-violet glow localised along the laser path. A summary of typical experimental conditions used in the IRLPP experiments is provided in Table V-1.

During normal operating conditions the cell pressure was less than two Torr; after 6-8 hours of continuous operation, the surface of the NaN_3 crystals would be saturated with bromine resulting in no more NCN_3 being produced. The crystalline azide was then reactivated by the method described by Marsh²⁵ whereby hydrazine hydrate (approximately 1 ml of hydrate for every 7 g of azide) is added to the de-activated NaN_3 dissolved in water. The filtered solution is then added drop wise to rapidly stirred dry acetone. The precipitate, active NaN_3 , is then filtered out and recovered with yields varying from 60 to 90 %.

Table V-1 Summary of experimental conditions for the generation of NCN by IRLPP of NCN_3 .

T_{BrCN}	P_{BrCN}	P_{SF_6}	Laser Power	CCD exposure	Slit width
-10 °C	6-7 Torr	60-70 Torr	30-35 W	10-30 s	150 μm

In the CESE experiments, NCN_3 was generated the same way as in the IRLPP experiments but was seeded in neon, Ne, and argon, Ar instead of SF_6 . A different slush bath was used to reduce the temperature of the cold finger to -28°C and consequently limiting the vapour pressure of BrCN to 2-3 Torr. The carrier gases were used at pressures, $P_{\text{Ar/Ne}}$, ranging from 100 to 200 Torr leading to mixing ratios of between 33:1 and 200:1. The resulting mixture was then introduced into the nozzle of the corona discharge chamber described in Section IV.3.4. Two to three kV were subsequently applied to the stainless steel electrode via a current-limiting ballast resistor generating a current of 3-5 mA. Due to the fast flowing conditions required for supersonic expansion experiments, the active sodium azide crystal only lasted two to three hours. Typical conditions of the CESE experiments are summarised in Table V-2.

Table V-2 Summary of experimental conditions for the generation of NCN by CESE of NCN_3 .

T_{BrCN}	P_{BrCN}	$P_{\text{Ar/Ne}}$	Corona Discharge	CCD exposure	Slit width
-28 °C	2-3 Torr	100-200 Torr	2-3 kV 3-4 am	< 1-3 s	100 μm

In both experiments, emission was then collected at right-angles to the 'source'. On one side, the UV/vis emission was recorded by a CCD/diffraction grating spectrometer while on the opposite side, the IR emission by a FT spectrometer. These instruments have been described in detail in Chapter II.

V.3 Results & Discussions

V.3.1 Production of NCN_3

In order to monitor the production of NCN_3 , spectra of the gas mixture prior to and after entering the NaN_3 column were recorded at low resolution in the IR region between 2000 and 2250 cm^{-1} with the FT spectrometer. The IR spectrum of the gas mixture prior to entering the azide column, which consists of SF_6 and BrCN , is depicted in black in Figure V-2. The intense absorption around 2200 cm^{-1} is due to the CN stretching vibrational mode of BrCN . However, the IR spectrum of the gas mixture exiting the azide column depicted in red shows three additional intense absorptions in that region. These features are the ones observed by Shurvell and Hyslop²⁶, and Milligan *et al.*⁷ in their IR study of NCN_3 , thus providing evidence that the target molecule was produced. In addition, the combination bands of BrCN have nearly disappeared in the red spectrum suggesting that most BrCN has reacted to produce NCN_3 .

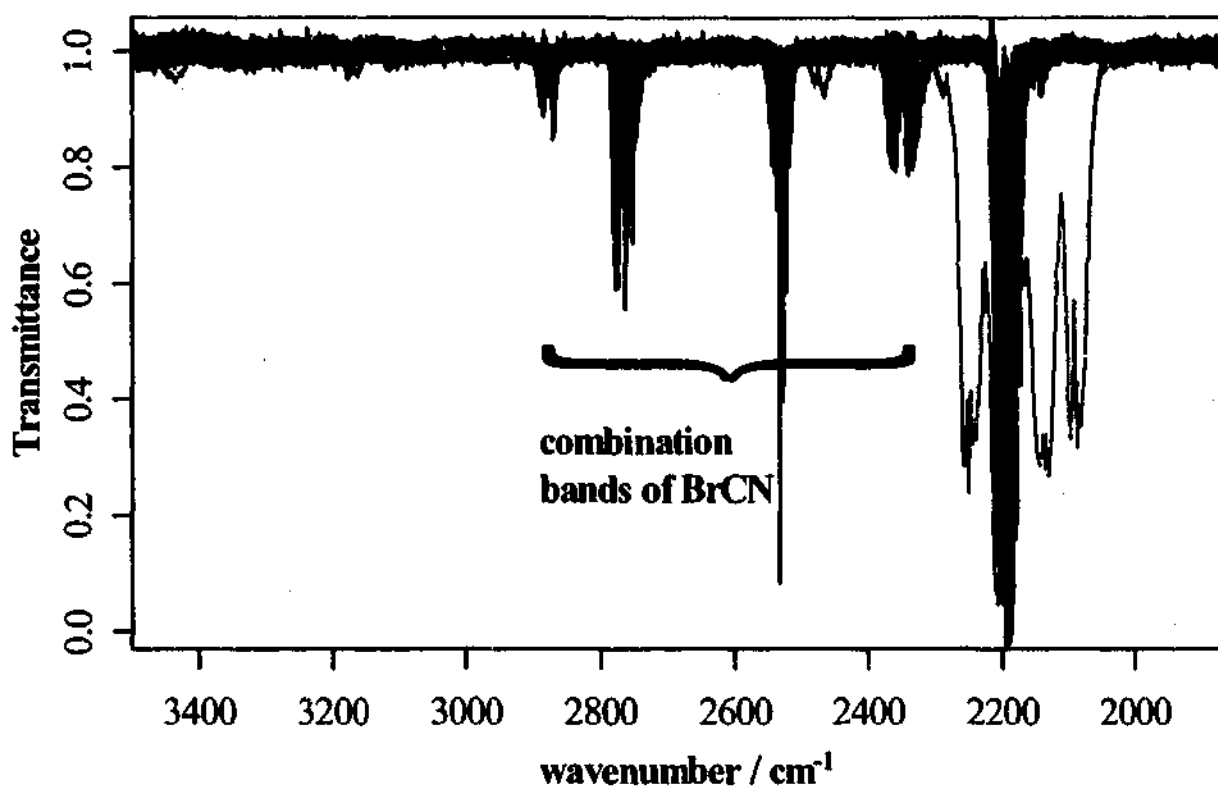


Figure V-2 IR spectrum of BrCN (black) and NCN₃ (red) recorded with a Fourier transform spectrometer. The red trace was recorded after a gaseous mixture consisting of a carrier gas and BrCN were flowed through a column of NaN₃ while the black trace represents the spectrum of a gaseous mixture consisting of a carrier gas and BrCN.

V.3.2 Characterisation of IRLPP & CESE emission spectra.

In this study, characterization of NCN₃ breakdown products generated by way of IRLPP and CESE has been achieved by analysing their UV/vis emission spectra recorded with a CCD/diffraction grating spectrometer. The resolution varied from 10 cm⁻¹ at 35700 cm⁻¹ (280 nm) to 0.5 cm⁻¹ at 9100 cm⁻¹ (1100 nm) as the reciprocal linear dispersion of the monochromator varied from 0.08 nm/mm at 280 nm to 0.05 nm/mm at 1100 nm. Survey spectra of emitting species generated by IRLPP of NCN₃ shown in Figure V-3 were recorded between 270 and 1120 nm at 15 to 20 nm intervals. Exposure times of the CCD detector ranged from 5 to 30 seconds depending of the emission intensity in a particular spectral region and the Quantum Efficiency (QE) of the CCD in that region. The spectral regions lying between 270 and 300, 420 and 610, 840 and 910, and 965 and 1080 nm were void of features and, thus, were omitted from the survey spectrum shown in Figure V-3.

In the region surveyed, only transitions belonging to the NCN and CN radicals were observed. In particular, the $\Delta v = 0$ vibrational sequences belonging to the $A^3\Pi_{u,inv} - X^3\Sigma_g$ system of NCN located at 329 nm, the $\Delta v = -1, 0, +1$ sequences of the $B^2\Sigma_u - X^2\Sigma_g$ system of CN at 358, 388 and 421 nm respectively, and the $\Delta v = 0, +1, +2, +3$ and $+4$ sequences of the $A^2\Pi_{inv} - X^2\Sigma_g$ system of CN located at 1100, 920, 792, 695 and 621 nm respectively were observed and recorded (see Figure V-3).

Spectra of the emission of NCN₃ breakdown products generated by way of IRLPP and CESE were also recorded with a Fourier transform spectrometer at low resolution in the near and mid-infrared regions. While no infrared emission was observed in the IRLPP experiments, intense atomic transitions of argon and neon and weak molecular transitions belonging to the $A^2\Pi_{inv} - X^2\Sigma_g$ of the CN radical were observed. The latter forms the focus of the following study and, thus, will be presented in the next chapter.

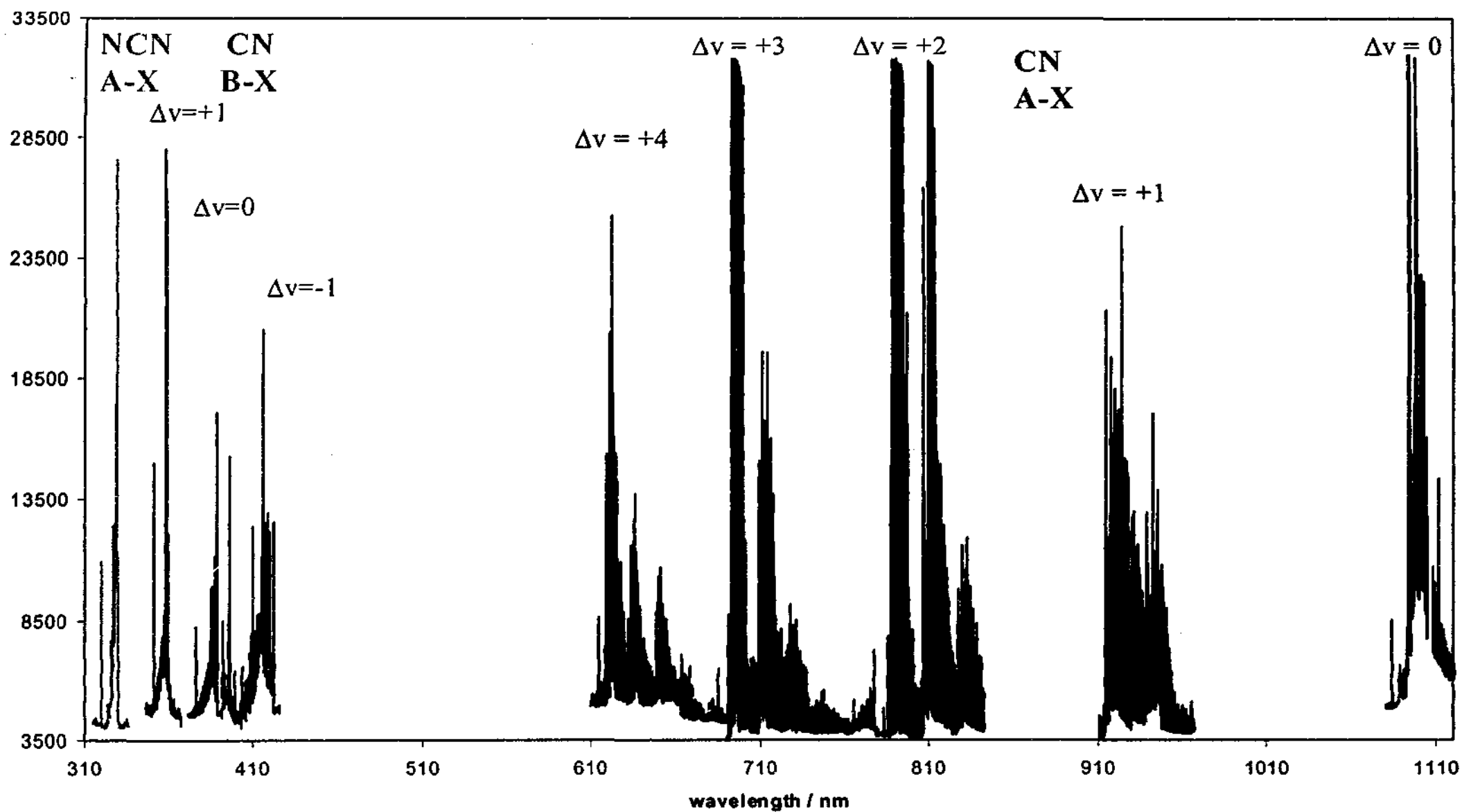


Figure V-3 Survey spectrum of emitting species generated in the IRLPP of NCN_3 showing the A-X electronic system of NCN and both the A-X and B-X systems of CN. The intensities only reflect the CCD exposure times and not the transition moments of the bands. Regions where no spectral features are observed were left out of the survey spectrum.

V.3.2.1 Breakdown mechanism for the production of NCN and CN

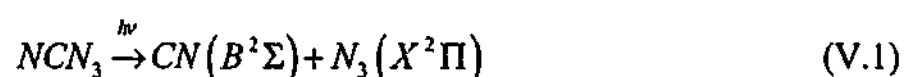
Tay-Lim¹⁶ proposed a mechanism for the breakdown of NCN_3 by IRLPP which involved the production of the azide radical, N_3 , and N_2 as reaction intermediates. Quite surprisingly, neither N_3 ($\tilde{A}^2\Sigma_u - \tilde{X}^2\Pi_g$), which emits around 270 nm,²⁷⁻³⁰ nor N_2 ($A^3\Sigma_u^+ - X^1\Sigma_g^+$, $C^3\Pi_u - B^3\Pi_g$ and $B^3\Pi_g - A^3\Sigma_u^+$) which emits all across the UV and visible regions³¹ were detected. At 270 nm, the CCD was exposed for 30 seconds; with a quantum efficiency exceeding 20% at this wavelength, the lack of N_3 and N_2 spectral features in this region of the spectrum cannot be attributed to the response of the CCD detector. Since transition moments are inversely proportional to lifetimes and the transit time in the IRLPP cell is much less than one second, N_3 ($\tilde{A}^2\Sigma_u$) and N_2 ($C^3\Pi_u$ and $B^3\Pi_g$), with lifetimes of approximately 20 ns,²⁸ 40 ns³² and 5 μs ³² respectively, can be ruled out as possible breakdown products of the IRLPP of NCN_3 . However, $\text{N}_2(A^3\Sigma_u^+)$, with a lifetime ≥ 1 s, seems a good candidate for a breakdown product in the IRLPP of NCN_3 as also proposed by Obake and Mele in their photodissociation studies of NCN_3 .¹⁰

An expanded view of the IRLPP spectrum showing the NCN A-X structure along with the $C^3\Pi_u - B^3\Pi_g$ spectrum of N_2 generated in a CESE of compressed air are illustrated in Figure V-4a). Comparison of the two spectra shows that two of the transitions in the NCN structure located at 30444 and 30601 cm^{-1} coincide with the 3-3 and 4-4 bands of N_2 at respectively. The 0-0 and 1-0 rovibronic bands belonging to the C-B system of N_2 are intense transitions, thus, their absence in the IRLPP spectrum seem to suggest that the coinciding transitions in the NCN spectrum do not belong to nitrogen.

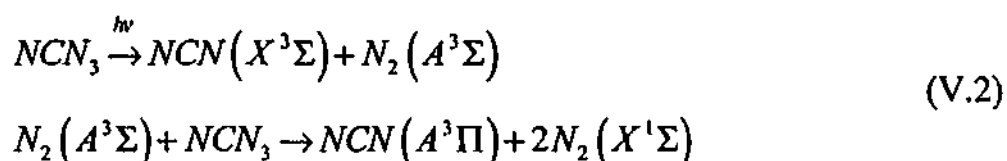
Transitions belonging to the C-B system of N_2 were however observed in the emission spectrum of the CESE of NCN_3 seeded Neon as illustrated in Figure V-4b). Nevertheless, it is unclear whether the source of N_2 is actually NCN_3 or air impurities (or both) due to the observation at 280 nm of the $\Delta\nu=1$ sequence of the A-X system of the OH radical generated by the CESE of H_2O , most probably from air. Further spectra recorded with Ar as carrier gas as illustrated in Figure V-4c) show no N_2 signature bands in the spectral region of interest. Thus, the N_2 bands observed in the emission

spectra of NCN_3 seeded Neon must have originated from a leak in the system and not from the breakdown of the azide parent compound. Furthermore, the absence of N_2 spectral features in the CESE emission spectrum of NCN_3 seeded Argon seems to support the fact that, as in the case for NCN generated by IRLPP, $\text{N}_2 C^3\Pi_u$ and $\text{N}_2 B^3\Pi_g$ are not generated as breakdown products of NCN_3 , and transitions coinciding with the N_2 bands must be due to a molecule other than nitrogen.

Okabe and Mele studied a series of mechanisms for the production of NCN and CN as breakdown products of the photolysis of NCN_3 .¹⁰ Using thermodynamic arguments, they found that the two most energetically favourable mechanism were

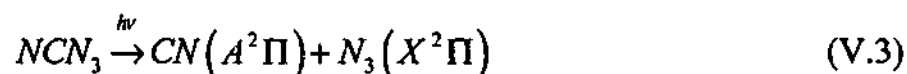


for the production of $\text{CN}(B^2\Sigma)$, and



for the production $\text{NCN}(A^3\Pi)$.

Absence of the $\tilde{A}^2\Sigma_u - \tilde{X}^2\Pi_g$ system of N_3 at 270 nm in both sets of experiments seem to indicate that is generated in a non-emitting state. This observation is in agreement with the mechanism described by Equation (V.1), where N_3 is generated in its ground $\tilde{X}^2\Pi_g$ electronic state. Since the $A^2\Pi_{inv} - X^2\Sigma^+$ system of CN was also observed, the following reaction should also take place



The $\text{N}_2 A^3\Sigma_u^+ - X^1\Sigma_g^+$, $C^3\Pi_u - B^3\Pi_g$ and $B^3\Pi_g - A^3\Sigma_u^+$ systems were also absent from the spectra recorded in this study. Of these electronic systems, only the $A^3\Sigma_u^+ - X^1\Sigma_g^+$ has a lifetime long enough to prevent its detection. As a result, N_2 must be generated in it's A-state upon separation from NCN_3 , which also in agreement with Okabe and Mele's mechanism for the production of NCN shown in Equation (V.2)

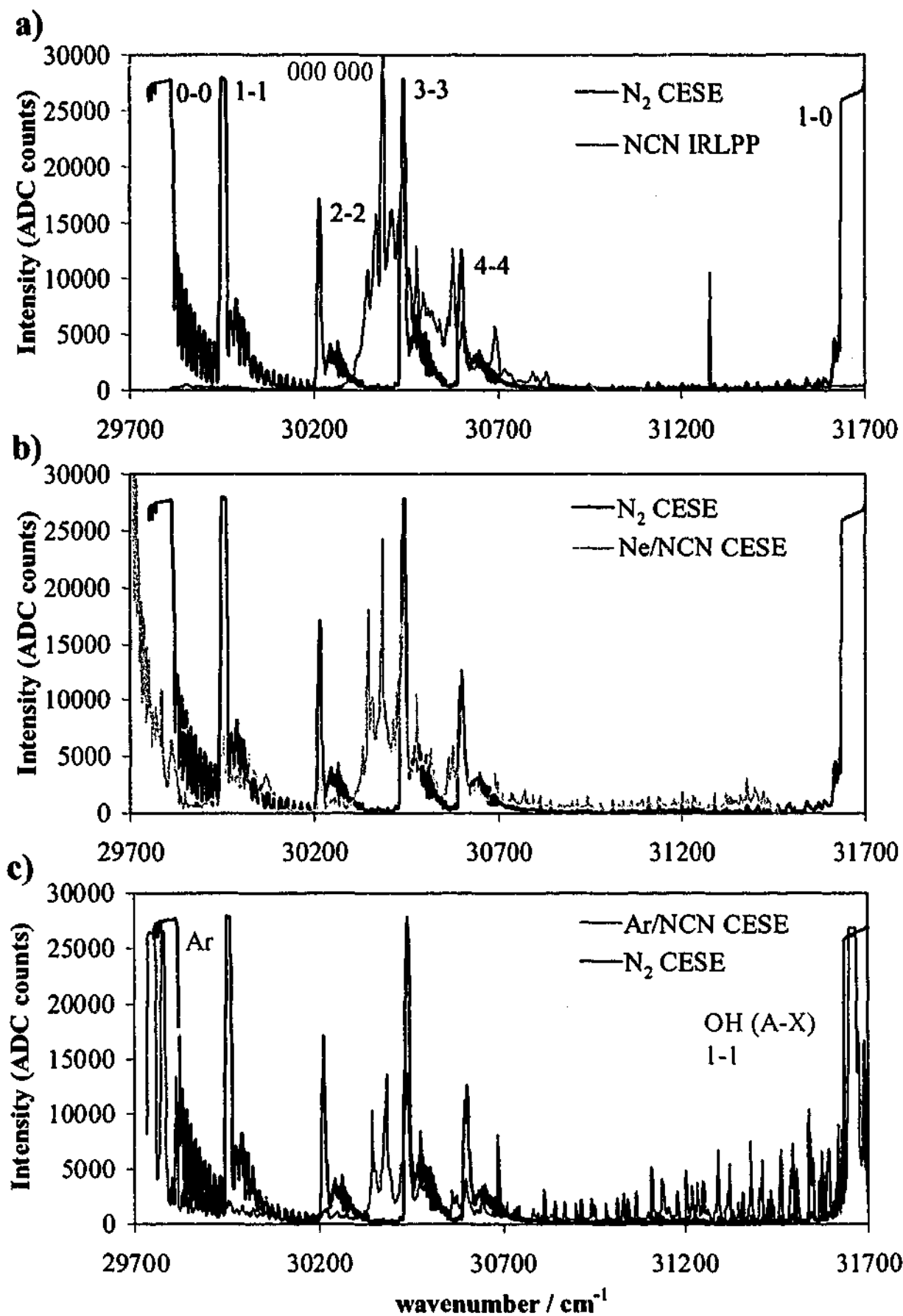


Figure V-4 The spectrum of the C-B electronic system of N₂ generated in a corona discharge of air showing the $\Delta v=0$ sequence (in blue) has been plotted with the spectrum of the A-X electronic system of NCN generated by
 a) IRLPP of NCN₃ (in pink); b) CESE of NCN₃ seeded in Neon (in orange);
 c) CESE of NCN₃ seeded in Argon (in blue-green); structures observed also include Ar atomic transitions at 299745, 29775 cm⁻¹, and rotational transitions belonging to the *P* and *Q* branches of the 1-1 band of the A-X system of the OH radical.

V.3.3 UV/vis emission spectrum of NCN

V.3.3.1 'Qualitative' Analysis

Although the features of the IRLPP spectrum are broad as illustrated in Figure V-5, the most intense peak located at $30388(\pm 1) \text{ cm}^{-1}$ is a likely candidate for the 000 000 vibronic transition of NCN first observed at 30384 cm^{-1} by Herzberg⁵ and recently by Beaton and Brown.¹⁷ Using the relative wavenumber-distance from the 000 000 band, the remaining features could not be assigned with confidence. In an attempt to properly assign the remaining features of the spectrum, NCN was generated in a CESE of NCN_3 seeded in Neon and its emission spectrum recorded (see Figure V-5a). Most of the unresolved features in IRLPP spectrum are partially resolved in the CESE spectrum of NCN: the most intense feature of the IRLPP spectrum with approximate width of 12 cm^{-1} actually consists of two peaks one of which with approximate width of 5 cm^{-1} . Since these vibronic structures consist of unresolved rotational transitions, the observed reduction in bandwidth is attributable to the rotational cooling which occurs in supersonic expansions. The CESE spectrum also shows three additional broad features appearing at 30018 , 30033 and 30066 cm^{-1} .

Comparison of the spectra of NCN generated in CESE of NCN_3 seeded in Ne and Ar illustrated in Figure V-5b) reveal some interesting differences mainly in the region around the 000 000 vibronic transition. Not only are the relative and overall intensities different but also, some transitions present in the CESE spectrum of NCN_3 seeded Ne are not observed when Ar is used as a carrier gas. Three of the features missing from the NCN_3 seeded Ar are of moderate intensities and are located at 30331 , 30372 and 30414 cm^{-1} in the NCN_3 seeded Ne emission spectrum. The differences in the observed spectra could be attributed to different energetically accessible mechanisms leading to the excitation of different modes of vibration.

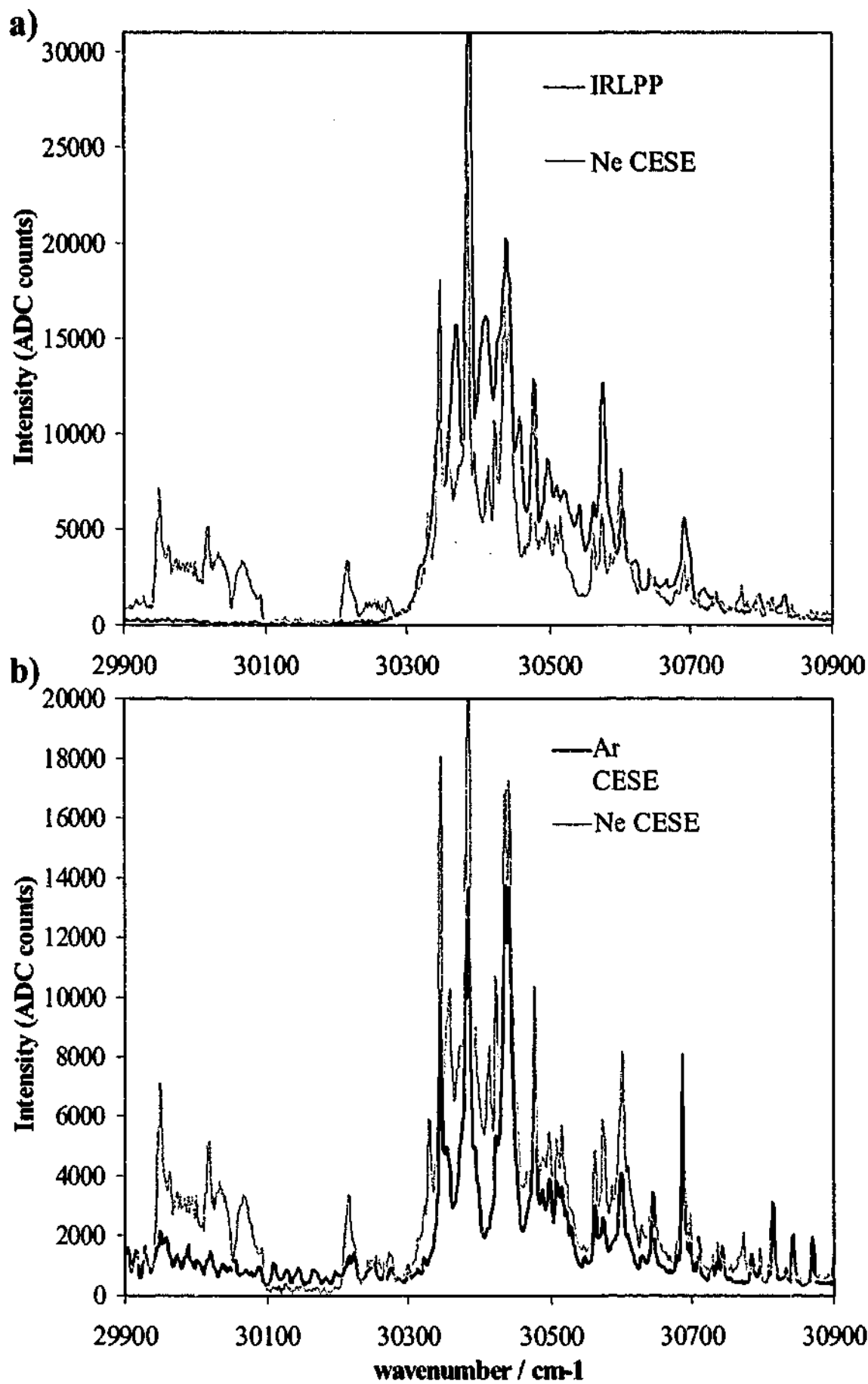


Figure V-5 The spectrum of the A-X electronic system of NCN generated by a) IRLPP and CESE of NCN_3 ; b) CESE of NCN_3 seeded in Ne and Ar.

V.3.3.2 'Quantitative' Analysis

Assuming that anharmonicity constants of NCN contribute negligibly to its vibronic energy, transitions involving non-degenerate vibrational modes, ν_1 and ν_3 , can be estimated by simply adding (subtracting) $\nu_1\omega_1$ and/or $\nu_3\omega_3$ to (from) the energy of the vibrationless electronic transition (000), T_0 , where ν_1 and ν_2 represent the vibrational quanta of modes 1 and 2, and ω_1 and ω_2 their vibrational wavenumbers. For example, the 100 000 and 100 100 transitions can be estimated by

$$\begin{aligned} T_0 + \nu_1'\omega_1' &\approx 100\ 000 \\ T_0 + \nu_1'\omega_1' - \nu_1''\omega_1'' &\approx 100\ 100 \end{aligned} \quad (\text{V.4})$$

where the 'prime' sign denotes the excited electronic state and 'double-prime' the ground state; also, ω_i and ν_i are interchangeable at this level of approximation.

In the case of the A-X system of NCN, the $A^3\Pi$ excited electronic state consists of three non-degenerate spin states separated by the $A\text{ cm}^{-1}$ where A is the spin-orbit constant. Thus, the energy of the spin components of the 100 000 transition can be approximated by

$$\begin{aligned} {}^3\Pi_2 &\approx 100\ 000 + A \\ {}^3\Pi_1 &\approx 100\ 000 \\ {}^3\Pi_0 &\approx 100\ 000 - A \end{aligned} \quad (\text{V.5})$$

Since A is negative, the order of the spin components is inverted leading to the ${}^3\Pi_0$ lying above the ${}^3\Pi_1$, and the ${}^3\Pi_2$ state below it.

For vibronic transitions involving the bending mode, ν_2 , Renner-Teller interactions leading to additional splittings have to be taken into account. Expressions for these multiplet splittings with excitation of one quantum of vibration have been described in detail in Chapter III. When more than one vibrational quantum in the bending mode is excited, the set of general equations given by Hougen³³ should be used. It should be noted that all transitions involving bending mode vibrations in the $A^3\Pi$ excited electronic state possess three central components also separated by A wavenumbers. Using these 'guidelines' and the vibronic energy values reported in the literature, most of the A-X system can be mapped for comparison with spectra observed in this study.

Some 45 peaks were measured between 30000 and 30700 cm^{-1} where most vibronic bands belonging to the $A^3\Pi_{u,mv} - X^3\Sigma_g^-$ electronic transition of NCN are located. Twenty-five of the measured peaks were assignable to the vibronic bands belonging to the A-X system of NCN, twelve of which are the diagonal bands ($\Delta v_i = 0$) observed by Herzberg and Travis⁵, and Beaton and Brown¹⁷; they are listed in Table V-3 while unassignable transitions are listed in Table V-4. The three broad structures located to the blue of the 1-1 band of N_2 around 30050 cm^{-1} may belong to the $\tilde{c}^1\Pi_u - \tilde{a}^1\Delta_g$ system of NCN observed by Kroto.⁹ Three peaks have been assigned to off-diagonal hot bands lying to the red of their corresponding multiplet components of the 000 000 band. However, they are present only in CESE spectra of NCN_3 seeded Ne. Thus, it seems that Ar as a carrier gas provides a better refrigeration medium for the cooling of the vibrational degrees of freedom of NCN than Ne does.

From the transitions listed in Table V-3 two spectroscopic parameters have been extracted: Δv_2 and Δv_3 . Estimates of these parameters were obtained by simple subtraction of the wavenumber value of the 000 000 transition from the wavenumber value of transitions diagonal in v_2 and/or v_3 :

$$v_2 \Delta v_2 \approx E(0v_2 0 0v_2 0) - E(000 000)$$

with a similar expression for Δv_3 . By adding the wavenumber value of Δv_2 and Δv_3 to their corresponding ground state vibrational energies, v_2'' and v_3'' , estimates of v_2' and v_3' can be obtained respectively. Table V-5 shows the A-state and X-state vibrational energies obtained to date. Herzberg's estimate of v_3' , has also been calculated in a similar fashion by the author using his data. These values should however be used only as rough guides in determining new vibronic transitions.

Table V-3 Peaks assigned to vibronic transitions belonging to the $A^3\Pi_{u,inv} - X^3\Sigma_g^-$ of NCN. Peaks with the superscript H and B have also been observed by Herzberg⁵ and Beaton^{17,19} respectively; remaining peaks have been assigned using the 'guidelines' explained in the text. Bands in the last two columns belong to vibronic states equally excited in ν_1 ; since the $\Delta\nu_1 \approx 2 \text{ cm}^{-1}$, these bands are overlapped by vibronic bands listed in the third column, and, thus, are not observed at the resolution at which the spectra were recorded.

Value / cm^{-1}	State	Assignment		
30680	$^3\Gamma_3$	030 030	130 130	230 230
30650	$^3\Sigma^-$	011 011	111 111	211 211
30641	$^3\Gamma_4$	030 030 ^H	130 130	230 230
	$^3\Phi_2$	020 020	120 120	220 220
30601	$^3\Gamma_3$	030 030	130 130	230 230
30586	$^3\Delta_1$	011 011	111 111	211 211
30573	$^3\Sigma^-$	010 010 ^B	110 110	210 210
30562	$^3\Phi_3$	020 020 ^H	120 120 ^H	220 220 ^H
30547	$^3\Delta_2$	011 011	111 111	211 211
30522	$^3\Phi_4$	020 020	120 120	220 220
30515	$^3\Delta_1$	010 010 ^B	110 110	210 210
30508	$^3\Delta_3$	011 011	111 111	211 211
30497	$^3\Pi_1$	002 002 ^H	102 102 ^H	202 202 ^H
30483	$^3\Pi_0$	001 001	101 101	201 201
30478	$^3\Delta_2$	010 010 ^{H,B}	110 110 ^H	210 210 ^H
30465	$^3\Sigma^+$	011 011	111 111	211 211
30460	$^3\Pi_2$	002 002	102 102	202 202
30443	$^3\Pi_1$	001 001 ^H	101 101 ^H	201 201 ^H
30437	$^3\Delta_3$	010 010 ^B	110 110	210 210
30423	$^3\Pi_0$	000 000 ^{H,B}	100 100 ^{H,B}	200 200 ^{H,B}
30414	$^3\Delta_1$	112 013	212 113	312 213
30386	$^3\Pi_1$	000 000 ^{H,B}	100 100 ^{H,B}	200 200 ^{H,B}
30381	$^3\Sigma^+$	010 010 ^B	110 110	210 210
30372	$^3\Delta_2$	112 013	212 113	312 213
30346	$^3\Pi_2$	000 000 ^{H,B}	100 100 ^{H,B}	200 200 ^{H,B}
30331	$^3\Delta_3$	112 013	212 113	312 213

Table V-4 List of unassigned peaks observed in the spectral region of the $A^3\Pi_{u,inv} - X^3\Sigma_g^-$ system of NCN. Highlighted values represent peaks of moderate intensities, the remaining represent either weak features or shoulders.

Value / cm^{-1}	Value / cm^{-1}
30698	30593
30692	30529
30687	30488
30630	30469
30621	30393
30616	30358
30610	30324
30598	30313

Table V-5 Wavenumber values of A-state and X-state vibrational modes of NCN. All values are calculated from spectroscopic data with the exception of McNaughton *et al.*¹⁵ who observed ν_3'' but performed high level *ab initio* calculations to estimate ν_1 and ν_2 of the ground X-state of NCN, and Milligan *et al.*⁶ who observed ν_2'' and ν_3'' of NCN. All parameters were obtained from gas phase studies with the exception of Milligan's which was performed in matrices.

	A-state			X-state		
	ν_1	ν_2	ν_3	ν_1	ν_2	ν_3
This work	—	519	1523.9	—	—	—
Herzberg ⁵	—	460	1524.5	—	370	—
Beaton ^{18,20}	1226	526	—	1224	429	—
McNaughton ¹⁶	—	—	—	1230	395	1466.5
Milligan ⁷					423	1475

V.4 Conclusions

Cyanogen azide, NCN_3 , has been successfully generated by flowing BrCN seeded in sulfur hexafluoride, SF_6 . Irradiation of the gas mixture by a 40W CO_2 laser resulted in a purple/violet glow localised about the laser path, which was recorded with both a Fourier transform spectrometer and CCD/diffraction grating spectrometer. While no molecular emission were observed in the infrared with the FT spectrometer, an extensive emission spectrum was observed and recorded from the ultraviolet to the near-infrared regions by the CCD detector at a resolution of 7 cm^{-1} . Characterisation of the emission enabled the identification of the NCN and CN radicals as the only breakdown species generated in the IRLPP of NCN_3 emitting in the 270 nm – 1110 nm spectral range. In the process, transitions belonging to the $A^3\Pi_{u,inv} - X^3\Sigma_g^-$ system of NCN ($\Delta v_i = 0$ mainly) and, both the $B^2\Sigma_u - X^2\Sigma_g^-$ ($\Delta v = 0, \pm 1$) and $A^2\Pi_{inv} - X^2\Sigma_g^-$ systems ($\Delta v = 0 - 4$) of CN were observed. With the exception of the 000 000 band of the A-X system of NCN , features observed in the emission spectrum of the IRLPP of NCN_3 could not be assigned with confidence as they were too broad. These broad features have been partially resolved in the CESE experiments revealing structures belonging to vibronic bands of the $A^2\Pi_{inv} - X^2\Sigma_g^-$ and possibly the $^1\Delta_g - ^1\Pi_u$ systems of the NCN radical. Of the 45 peaks measured between 30000 and 30700 cm^{-1} , 25 were assigned to spin-orbit and Renner-Teller multiplets of the A-X system. Furthermore, the three peaks missing from the CESE spectra of Ar/NCN_3 have been tentatively assigned to off-diagonal hot bands of the A-X system of NCN , which suggests that cooling of vibrational degrees of freedom may be more favoured in an argon environment than in neon. Despite the limited number of transitions observed and the low resolution of the CESE spectra, estimates of Δv_2 and Δv_3 were obtained. These values provided indirect estimates of ν_2 (519 cm^{-1}) and ν_3 (1523.9 cm^{-1}) of the $A^3\Pi_{u,inv}$ -state of NCN which are in excellent agreement with the value calculated from Herzberg's study⁵ and reported by Beaton^{17,19} respectively.

In the emission spectra of breakdown products generated in the CESE of NCN_3 seeded in neon, the $\Delta v = 0$ sequence of the C-B system of N_2 was observed as well as the A-X system of the NCN radical, and both the B-X and A-X systems of the CN radical. The source of N_2 however, is believed to be an air leak in the vacuum system as

UV/vis CESE spectra void of N_2 signature bands were observed when neon was replaced with argon. Furthermore, evidence gathered in this study seem to indicate that $N_3(X^2\Pi)$ and $N_2(A^3\Sigma)$ are produced in primary processes of the breakdown of NCN_3 in both IRLPP and CESE environments.

In addition, three peaks not assignable to N_2 or neon which are missing from the CESE spectra of Ar/ NCN_3 are believed to belong to a hot vibronic band; three other broad features located at 30018, 30033 and 30066 cm^{-1} are believed to belong to the $\tilde{c}^1\Pi_u - \tilde{a}^1\Delta_g$ electronic transition previously observed by Kroto in absorption.⁹ Prior to this study, the $\tilde{c}^1\Pi_u - \tilde{a}^1\Delta_g$ system had never been observed in emission.

To date, this is the only spectroscopic study performed on NCN in a supersonic expansion. The work undertaken in this study not only showed that NCN could be generated by CESE of NCN_3 but, also, that CESE should be the method of choice for studying the vibronically congested UV/vis emission spectrum of NCN. Usually supersonic expansion experiments are conducted with drastically higher backing pressures than the 100 to 200 Torr used in this study. Thus, CESE used to its full potential should further cool the rotational degrees of freedom NCN leading to further resolution of its vibronic structures. A high resolution study of NCN generated by CESE of NCN_3 is required as it would provide better evidence of the bands observed in this study and, more importantly, high quality rotational, vibrational and electronic parameters of the NCN radical. Unfortunately, these studies could not be undertaken as our FT spectrometer is not equipped for UV/vis spectroscopic studies and no funding was available to upgrade the existing system with appropriate optics and detector.

VI High Resolution FT Jet-Emission Spectrum of the Cyano Radical from the mid to near-IR

VI.1 Introduction

The Cyano (CN) radical plays an important role as an intermediate in chemical reactions involving nitrile compounds, and of flames and electrical discharges when trace amounts of carbon and nitrogen are present. The CN radical is also of astrophysical importance as it has been observed in the spectra of extraterrestrial sources such as the Sun, comets, and, stellar and interstellar atmospheres. In addition, the CN radical has been used as a chemically pumped, electronic transition laser.^{1,2} The extensive body of work reported in the literature probably makes CN one of the most studied radicals, and possibly one of the most studied diatomic systems. For a thorough review of the work performed on the CN radical the reader is referred to the studies of Jenkins *et al.*,³ Douglas and Routly,⁴ Kotlar *et al.*⁵ and Prasad *et al.*^{6,7}, as well as the compilation of Huber and Herzberg⁸. In the following section only previous investigations pertinent to the present study will be reviewed chronologically.

The CN spectrum was reportedly first observed over a century ago,³ and ever since then, a variety of precursors have been utilised to produce this radical, and a wide variety of techniques developed to study it in the laboratory. Initial studies consisted mainly of exhaustive recording and classifying of data. In 1920, Heurlinger⁹ performed the first vibrational analysis as they assigned transitions belonging to the Red ($A^2\Pi_{inv} - X^2\Sigma_g^-$) and Violet ($B^2\Sigma - X^2\Sigma$) system of CN. Their vibrational numbering of the A state however, came into doubt, and was subsequently increased by two quanta as a result of the study of Asundi and Ryde¹⁰ who observed $\Delta v = 1-4$ ($v'=1-5$, $v''=0-4$) transitions belonging to the Red system of CN down to the edge of the near-infrared region around $10\,900\text{ cm}^{-1}$.

The first rotational analysis was reported by Jenkins *et al.*³ in 1931, when they used a 21 foot grating spectrometer to record transitions belonging to the $\Delta v = 3, 4$ and 5 ($v'=4-8$, $v''=1-3$) sequences of the $A^2\Pi_{inv} - X^2\Sigma_g^-$ system of CN generated by mixing CCl_4 to a stream of active nitrogen. They extracted the first set of rotational constants of the A-X system of CN. They also observed some strong perturbations in rotational transitions involving the vibrational level $v=6$ of the A excited electronic state. In a similar experiment, Wager,¹¹ in 1943, observed further perturbations as they collected evidence that the A ($v=9$) and B ($v=0$) excited electronic states of CN were also interacting.

In 1948, Herzberg and Phillips¹² proposed a further increase of one quantum in the vibrational numbering of the A-state of CN as they extended the 'field of view' of the Red system down to 6200 cm^{-1} in their low-resolution emission study of this radical. They observed the $\Delta v = -1, 0, 1$ and 2 ($v'=1-2$, $v''=0-3$) bands of the A-X system of CN. This new vibrational numbering has been adopted in the present study. In 1955, Douglas and Routly⁴ performed the first extensive study of the Red system and extended the range of 'observed' vibrational levels of the A-state of the CN. In 1961, Kiess and Broida¹³ reinvestigated the perturbation previously observed by Wager,¹¹ and provided a detailed analysis of the rotational levels involved in the perturbation, and their intensities. In 1963, Davis and Phillips¹⁴ also performed an extensive study of the Red system of CN at a resolution of 0.2 cm^{-1} . They observed the $\Delta v = 1-7$ ($v'=1-12, 15$, $v''=0-8$) In 1965, Jeunehomme,¹⁵ using an electrodeless discharge in acetonitrile, observed the emission spectrum of the Red system of CN. In this study, he reported first estimates of oscillator strengths and lifetime measurements for vibrational levels one to

nine of the A state ($6-7\mu s$). In 1968, Leblanc¹⁶ reacted methane with active nitrogen, and recorded the emission spectrum of both the A-X and B-X electronic systems of the CN radical at low-resolution. In the process, he observed new vibrational transitions in both systems. In 1970, Fay *et al.*¹⁷ performed a perturbation analysis of the A-X transitions recorded by Davis and Phillips¹⁴. In addition, they derived general expressions enabling the prediction of wavenumbers of vibrational bands belonging to all isotopic forms of CN.

The first *ab initio* calculations were performed in 1970 by Schaefer and Heil¹⁸ leading to the determination of potential energy curves of low-lying electronic states of CN. Treffers¹⁹, in 1975, was the first to observe rotational transitions of the fundamental of CN. In addition, he studied intensity variation of the 0-0 band of the Red system of CN at various temperatures, and subsequently obtained an estimate for the oscillator strength, $f_{0,0}$, of that band ($f_{0,0} = 3.3 \times 10^{-3}$). The first laboratory measurement of the microwave spectrum of CN was recorded by Dixon and Woods²⁰ in 1977 as well. They observed pure rotational transitions from the first two vibrational levels of the ground state of CN.

One of the most significant spectroscopic contributions to the A-X system of CN was the extensive analysis of the high-resolution near-IR spectrum recorded by Cerny *et al.*²¹ in 1978. Fourteen bands belonging to the $\Delta v = +1, 0, -1$ and -2 sequences lying between 11000 and 4000 cm^{-1} were observed and recorded at a resolution of 0.016 cm^{-1} with a Fourier transform spectrometer. The CN radical was generated in a C_2H_2/N_2O flame. The ensuing analysis yielded accurate molecular parameters empirical in nature due to the presence of interactions between the A and X electronic states. The Full-Width at Half-Maximum (FWHM) of the observed transitions of 0.080 cm^{-1} is mainly due to the Doppler effect at the elevated temperatures of their experiment ($T \sim 3000K$). A year later, Katayama²² studied the relaxation of selectively excited vibrational levels of the A state of CN. The A-X lifetime estimates were in agreement with those previously measured. In 1980, Kotlar *et al.*⁵ performed a thorough perturbation analysis of Cerny's data and were successful at extracting a set of deperturbed molecular constants. In both Cerny's and Kotlar's studies Zare's²³ R^2 -Hamiltonian was used to describe the term energies of CN. However, Brown's N^2 -Hamiltonian is used in the present study.

Using a tunable IR diode laser, Davies and Hamilton²⁴ were able to observe and record ten rovibrational transitions of the fundamental of CN in 1981. Estimates of the radiative lifetimes of the B-X, A-X and B-A systems of CN were obtained by Cartwright and Hay²⁵ in 1982 through *ab initio* calculations. In 1983, Skatrud et al.²⁶ extended the microwave observations to the first four vibrational levels of the ground electronic state of CN generated in a low-pressure glow-discharge of a gaseous mixture of methane and nitrogen. In 1984, Taherian and Slanger²⁷ generated CN($A^2\Pi$) radicals by photodissociation of C₂N₂ with an F₂ laser (157.6 nm) and determined the radiative lifetimes of the first six vibrational levels (4.3–8.5 μs).

In 1989, Richard *et al.*²⁸ generated the CN by CESE of acetonitrile, CH₃CN, and recorded the first jet-cooled FT-spectrum of this radical at a resolution of 0.25 cm⁻¹. They observed the 0-0 and 1-1 bands of the B-X system. In 1991, Ito *et al.*²⁹ further extended the microwave observations of CN($X^2\Sigma$) to $\nu=10$. In this study, the CN radical was produced by a dc glow-discharge He containing trace amounts of CO and N₂ at liquid nitrogen temperature. The same year, Davis *et al.*³⁰ recorded the FTIR spectrum of CN generated in a nitrogen filled carbon-tube furnace at 2500 K at a resolution of 0.01 cm⁻¹. They were the first to observe complete vibrational band structures of the $\Delta\nu=1$ and 2 sequences of the X-state of CN, and were able to extract ground-state molecular parameters of high accuracy.

In 1992, the B-X and A-X electronic systems of jet-cooled CN spanning the UV, visible and IR regions (27000-2500 cm⁻¹) were recorded with a Fourier transform spectrometer by Rehfuss *et al.*³¹ The CN radical was generated by CESE of CH₃CN seeded in helium or argon. They observed the $\Delta\nu=0$ sequence up to $\nu=15$ of the B-X system, thus superseding the previous B-X study of Engelman who had observed the $\Delta\nu=0$ sequence up to $\nu=7$;³² they also observed the $\Delta\nu=-1$ sequence up to $\nu=13$. Subsequent analysis of the B-X spectrum recorded at a resolution of 0.02 cm⁻¹ yielded very accurate molecular parameters for the B-state of CN. In the near-IR to mid-IR region they observed the $\Delta\nu=0, \pm 1, \pm 2$ and ± 3 sequences of the A-X system of CN at low-resolution. They were, however, unable to obtain high-resolution spectra with good signal-to-noise ratio for the A-X system, and, thus, did not report any molecular parameters for the A-state of the CN radical.

In a concurrent study, Prasad *et al.*⁶ also observed the B-X system of CN by CESE of methyl azide and diazoacetonitrile seeded in helium at high-resolution with a Fourier transform spectrometer between 25000 and 28000 cm^{-1} . They observed the $\Delta v = 0$ ($v = 0-7$), and the $\Delta v = 1$ ($v = 1-9$) sequences of the violet system of CN and obtained very accurate spectroscopic constants. Later that year, Prasad and Bernath⁷ reported observing the FT jet-emission spectrum of the A-X transition of CN generated by CESE of diazoacetonitrile seeded in helium. They recorded the spectrum from 16000 to 23000 cm^{-1} at a resolution of 0.025 cm^{-1} . The spectrum recorded not only showed rotational cooling but, also, spin-orbit cooling as transitions from only one of the spin-orbit components ($^2\Pi_{3/2}$) of the A-state were observed. Combining all previously recorded microwave, infrared and UV data, to their A-X data, they performed a global fit and obtained very accurate spectroscopic parameters as well as potential energy curves for the three electronic states involved. In 1995, Klisch *et al.*³³ studied the microwave spectrum of CN in the 1THz region. They observed rotational transition from the first two vibrational levels of the X-state and reported rotational parameters of these levels. In 2001, Liu *et al.*³⁴ studied the CN radical by Concentration Modulation Laser Spectroscopy, CMLS, and observed all twelve rotational branches of the 2-0 band of the A-X spectrum of CN generated in an ac glow discharge of helium 'contaminated' with trace amount of acetonitrile. After constraining all ground state parameters and a few A-state parameters, they were able to extract more accurate values than reported by Cerny *et al.*²¹ for $T_{2,0}$, A_2 and B_2' .

The aim of this study is to record the jet-cooled emission Fourier transform spectrum of the CN radical from the edge of the visible to the mid-infrared region of the electromagnetic spectrum at high resolution. Although this section of the Red system has already been studied by Cerny *et al.*²¹ at higher resolution with an FT spectrometer, the linewidths of the observed transitions are rather broad (0.80 cm^{-1}) due mainly to Doppler broadening at the elevated temperature of their experiment ($T \sim 3000K$). In a supersonic expansion, the translational temperature is less than 300 K, thus, the linewidth should be narrower by at least a factor of three. In addition, perturbations observed at high rotational levels in their study will not be observed in this study as high-lying rotational levels do not have appreciable populations in supersonic expansions due to rotational-cooling. As a result, the parameters obtained from this study should be free of the effect of perturbation, and of higher accuracy than that of Cerny *et al.*²¹

VI.2 Experimental

Electronically excited CN radicals were generated by CESE of acetonitrile, CH_3CN , seeded in carrier gases such as helium, neon and argon. In a typical CESE experiment, the carrier gas at high-pressures ($P_{\text{cg}} \sim 380\text{-}570$ Torr) was bubbled through a sample of CH_3CN placed in dry ice ($T_s \sim -50^\circ\text{C}$) to maintain a sample pressure, P_s , of one to two Torr. The gas mixture was then passed through a Pyrex nozzle containing a stainless steel electrode held at high voltage (0-17 kVolts) through a current limiting (1-8 mA) ballast resistor (adjustable from 0.5 to 24 $\text{M}\Omega$) before undergoing a supersonic expansion in a stainless steel evacuated chamber held at pressures, P_e , of 0.1 to 2 Torr. Similarly to the IRLPP experiments, emission from the excited species was collected at right angles to the molecular flow using two detection systems. On one side the corona discharge near-IR to UV/vis ($9000\text{-}37000\text{ cm}^{-1}$) emission was monitored at low resolution with a CCD/diffraction grating spectrometer while on the opposite side, a Fourier transform spectrometer was used to record high-resolution near and mid-IR spectra. For near-IR studies ($8500\text{-}14000\text{ cm}^{-1}$) the FT was equipped with a Si:diode detector, a quartz beamsplitter and a 680nm red-pass optical filter while for mid-IR and near-IR studies ($1850\text{-}9500\text{ cm}^{-1}$) a liquid nitrogen-cooled In:Sb detector and a KBr beamsplitter were used. The typical experimental conditions are summarised in Table VI-1.

Table VI-1 Summary of typical experimental conditions used to record the A-X spectrum the CN generated by CESE of methylcyanide.

$T_s / ^\circ\text{C}$	P_s / Torr	P_{cg} / Torr	P_c / Torr	Corona Discharge		
-50	1-2	380-570	2-5	4-15 kV	3-7 mA	24.5 M Ω
<hr/>						
CCD						
	Exposure	Slit width	Spectral Range	Resolution		
	< 2 s	50 μm	9000-30000 cm^{-1}	0.5-10 cm^{-1}		
<hr/>						
FT						
	Detector	Beamsplitter	Spectral range	Aperture	Resolution	
	In:Sb	KBr	1850-9000 cm^{-1}	1.7 mm	0.035 cm^{-1}	
	Si:diode	Quartz	8500-14000 cm^{-1}			

's' subscripts relate to the sample, 'cg' subscripts to the carrier gas and 'c' subscripts to the chamber.

VI.3 Results & Discussions

During the course of this study, fouling or clogging of the nozzle has occurred repeatedly, seriously impeding the work undertaken in this investigation. This problem, most probably due to gradual buildup of soot or polymers of breakdown products generated in the discharge, has been attributed mainly to the high chamber pressures resulting from the low-pumping capacity of the existing system. Due to the small amount of funding received for this project, a mechanical booster pump was borrowed from Dr. Evan Bieske at Melbourne University, and coupled to a two-stage rotary pump for the CESE experiments. The nominal pumping speed of the combination of pumps was estimated at 5800 L/min . However, most CESE studies reported in the literature successfully use pumping systems with speeds of the order of 15000 to 30000 L/min resulting in chamber pressures of ≤ 100 mTorr. In the present study, the pressure measured inside the corona discharge chamber was seldom below 0.5 Torr, as a result, nozzle-clogging events were quite frequent.

At these low operating pressures, the frequency of nozzle-clogging events was found to be dependent on the discharge current, the size of the nozzle and the type of

carrier gas used. Limiting the current to less than 7 mA with a 570 mm diameter nozzle was found to significantly reduce nozzle-clogging events. In addition, helium seemed to have a greater 'affinity' to clogging than neon or argon when tested under the same experimental conditions. The intensity of the CN emission was weaker when using argon as a carrier gas, as a result, most spectra measured in this study were obtained using neon or helium as a carrier gas. Figure VI-1 illustrates the intensity variation observed when using argon, neon and helium as carrier gases under similar corona discharge settings.

In Fourier transform spectroscopy, optical filters are used mainly to prevent the occurrence of aliasing and to reduce source related noise. Narrow bandpass filters are usually utilised to enhance the signal-to-noise ratio. Unfortunately, the laboratory is not equipped with optical filters appropriate for the regions under investigation. Lacking the appropriate optical filters meant that large spectral bandwidth had to be recorded at a time leading to significantly larger amount of scans required to enhance the S/N ratio.

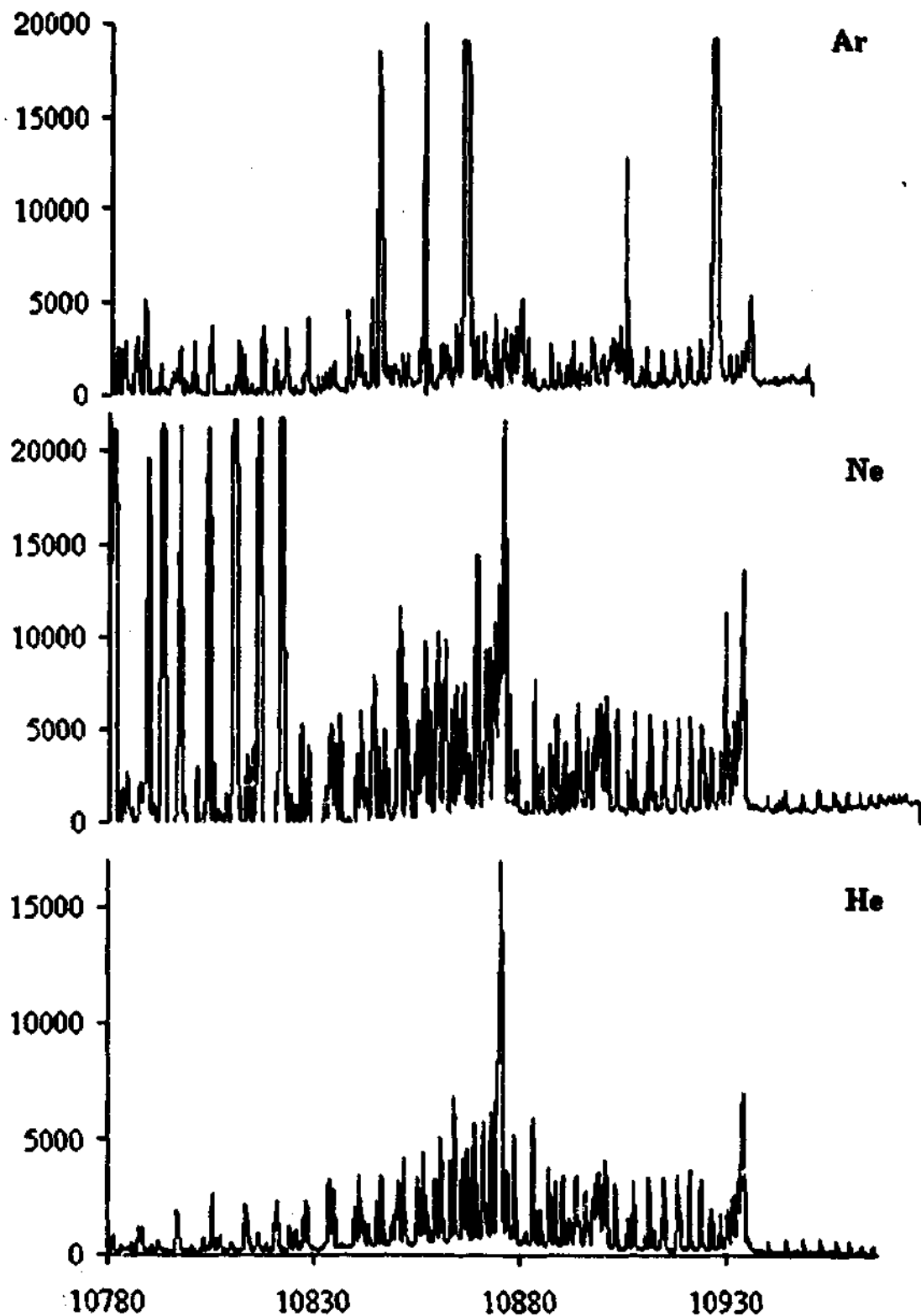


Figure VI-1 CCD spectrum of the 1-0 band of the A-X system of CN generated by CESE of CH_3CN seeded in argon, neon and helium. These spectra, recorded under similar experimental conditions, clearly show that CH_3CN seeded in neon produce the most intense spectra. However, the coldest spectra are obtained when using helium as a carrier gas.

VI.3.1 Characterisation of CESE emission spectra.

In this study, characterisation of CH_3CN breakdown products generated by way of CESE has been achieved by analysing the emission spectra recorded with a CCD/diffraction grating spectrometer. Survey spectra of emitting species generated by CESE of CH_3CN were recorded between 270 and 1120 nm at 15 to 20 nm intervals. Exposure times of the CCD detector ranged from 0.5 to 2 seconds depending of the emission intensity in a particular spectral region and the Quantum Efficiency (QE) of the CCD in that region. In the region surveyed, only transitions belonging to CN and CH radicals were observed. In particular, the $\Delta v = 0$ vibrational sequences belonging to the $A^2\Delta - X^2\Pi$ system of CH located at 431 nm, the $\Delta v = -1, 0, +1$ sequences of the $B^2\Sigma_u - X^2\Sigma_g$ system of CN at 358, 388 and 421 nm respectively, and the $\Delta v = 0, +1, +2, +3$ and $+4$ sequences of the $A^2\Pi_{inv} - X^2\Sigma_g$ system of CN located at 1100, 920, 792, 695 and 621 nm respectively were observed and recorded. Emission spectra of species generated by CESE of CH_3CN and NCN_3 are quite similar. The only difference, as illustrated in Figure VI-2, being the presence of the A-X system of the CH radical (and the absence of NCN, obviously) in the spectrum recorded in this study.

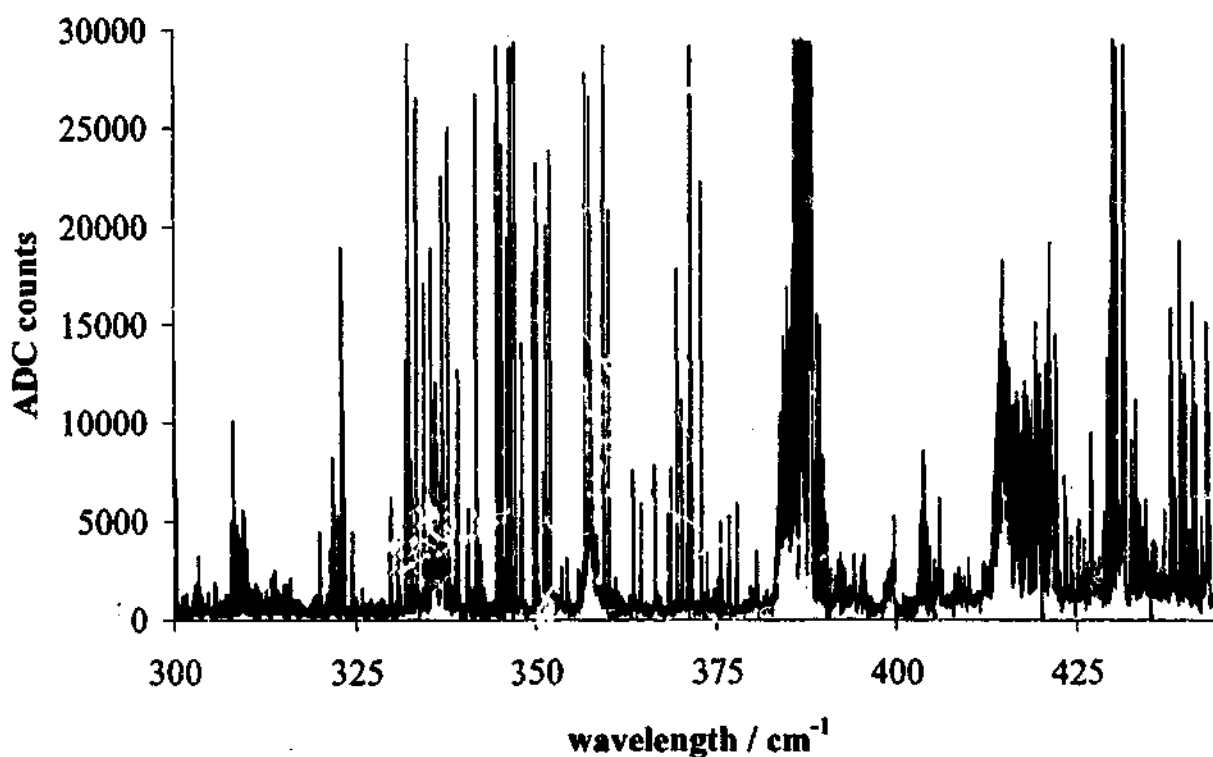


Figure VI-2 Portion of the UV/vis spectrum observed when CH_3CN seeded in Ne is exposed to a corona discharge in a supersonic expansion. The part with $\lambda > 440$ nm is similar to that recorded with NCN_3 as precursor.

VI.3.2 High Resolution FT emission spectrum of the A-X system of jet-cooled CN

In the present study, the Red spectrum of CN has been recorded at a resolution of 0.035 cm^{-1} with a Fourier transform spectrometer. The portion of the A-X spectrum lying between 8500 and 14000 cm^{-1} was recorded by co-adding 40 scans. The signal-to-noise ratio (S/N) of the strongest transition of the 1-0 band of CN lying in that region is larger than 540:1. For the region lying between 1850 and 9000 cm^{-1} , over 500 scans were co-added yielding a S/N of 136:1 for the strongest transition of the 0-1 band, and 13:1 for the 3-6 band. The FT spectrum of the A-X system of jet-cooled CN is shown in Figure VI-3 and Figure VI-4. The portion of the spectrum lying between 2500 and 4200 cm^{-1} has not been displayed as the CN bands are not easily discernible due to the overwhelming presence of neon atomic lines in the region, and the poor S/N of the CN bands in that region of the spectrum. Both sets of spectra were calibrated to neon atomic lines obtained from the NIST Atomic Spectra Database.

VI.3.2.1 Vibrational Assignment

The $A^2\Pi_g - X^2\Sigma^+$ spectrum of the CN radical is centered at 9116 cm^{-1} (0-0 band) with fundamental wavenumbers, ω_e^* , of 2069 cm^{-1} in the ground electronic X-state and, ω_e' , 1813 cm^{-1} in the first excited electronic A-state, and first-order anharmonicities, $\omega_e x_e$, of approximately 13 cm^{-1} in both states.^{5,7} Thus, the $\Delta v = -1, -2, \dots$ vibrational sequences are located roughly at multiples of $\omega_e^* - 2\nu(\omega_e x_e) \text{ cm}^{-1}$ or $2069 - 2\nu(13) \text{ cm}^{-1}$ to the red of the central 0-0 band while the $\Delta v = +1, +2, \dots$ sequences at multiples of $\omega_e' - 2\nu(\omega_e x_e) \text{ cm}^{-1}$ or $1813 - 2\nu(13) \text{ cm}^{-1}$ to the blue, where ν is the vibrational quantum number. Furthermore, the bands within each sequence, $\Delta v = \pm 1, \pm 2, \dots$, are separated by approximately $\Delta\omega_e \pm 2\nu(\omega_e x_e) \text{ cm}^{-1}$ or $255 \pm 2\nu(13) \text{ cm}^{-1}$ as can be seen in Figure VI-3 and Figure VI-4. As a result of the spin-orbit interaction in the excited state, each band is composed of two sub-bands originating from the $^2\Pi_{1/2}$ and $^2\Pi_{3/2}$ spin-orbit components of the A-state.

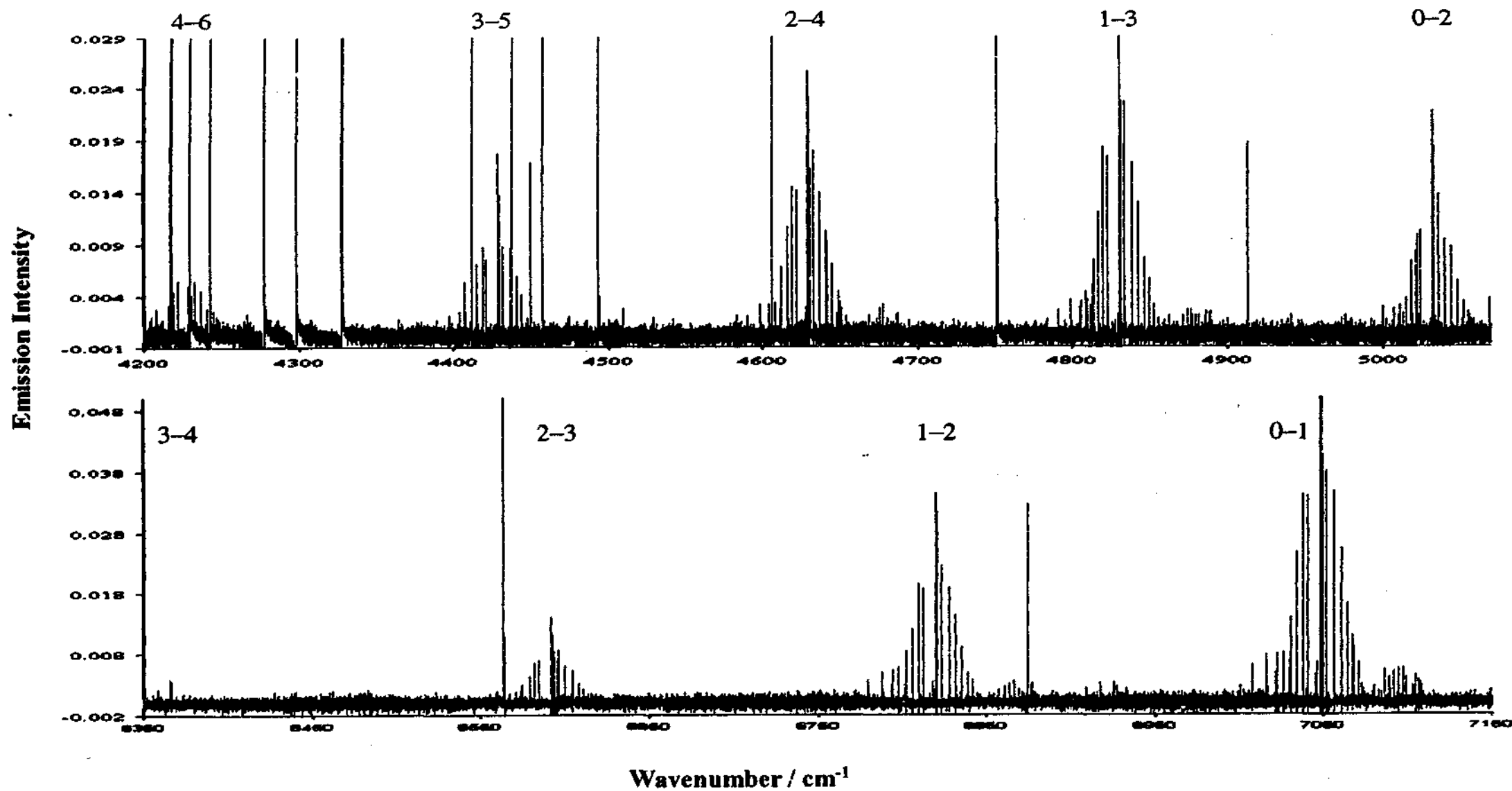


Figure VI-3 FT spectrum of the Red-system of CN generated by CESE of CH₃CN showing the $\Delta v = -2$ and -1 sequences. The spectrum was recorded at a resolution of 0.035 cm^{-1} .

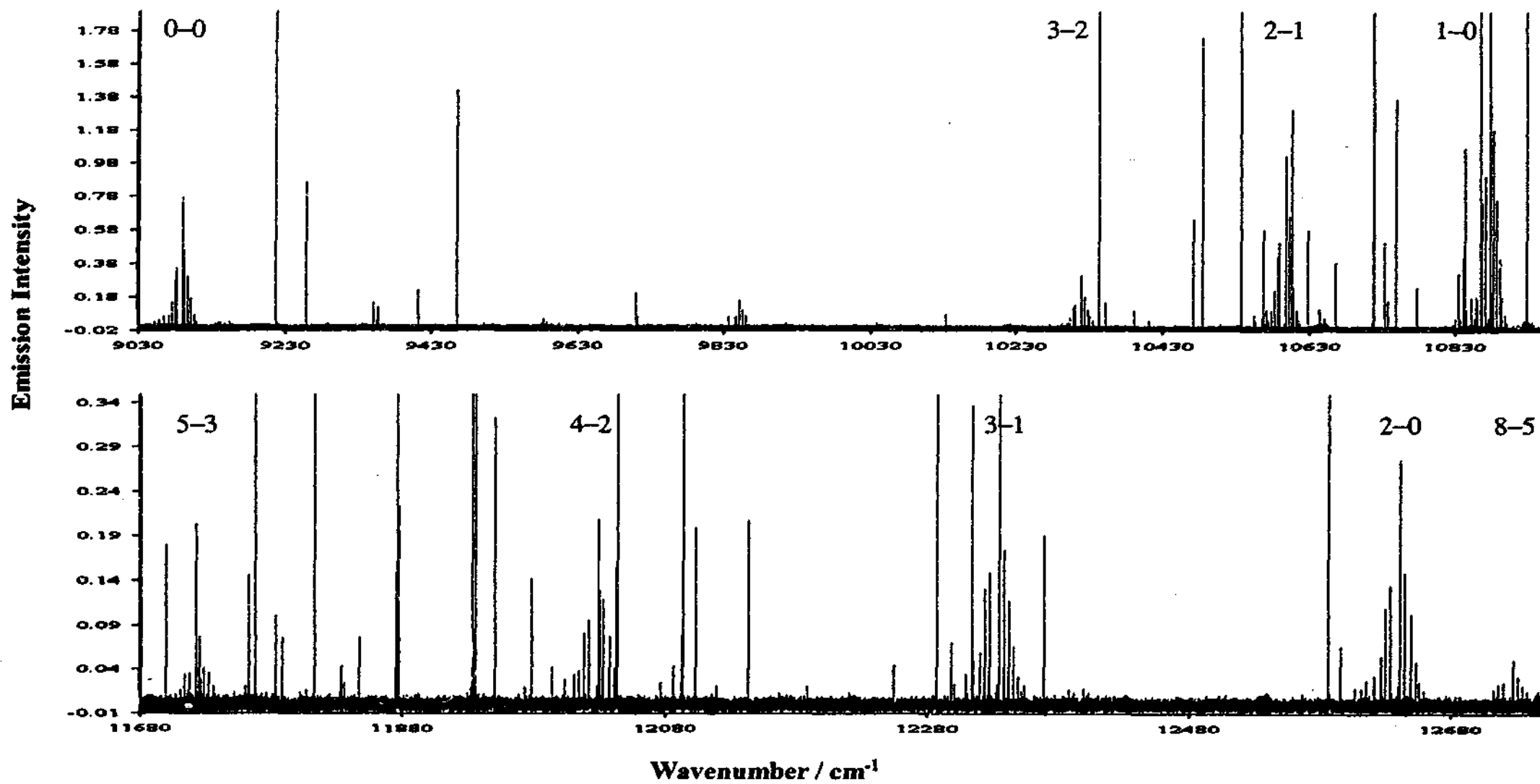


Figure VI-4 FT spectrum of the Red-system of CN recorded at a resolution of 0.035 cm^{-1} showing the $\Delta v=+1$ and $+2$ sequences, as well as the 0-0 and 8-5 bands.

High Resolution FT Jet-Emission Spectrum of the Cyano Radical from the mid to near-IR VI-120

The 670 measured lines were assigned to 22 vibrational transitions between the A-state vibrational levels $v' = 0-5, 8$ and X-state levels $v'' = 0-7$; these bands are listed in Table VI-2 along with Franck-Condon Factors (FCF's) reported by Prasad and Bernath.⁷ However, transitions belonging to the two spin-orbit components were only observed in 9 of the 22 bands: $v' = 0-3$.

Table VI-2 Wavenumber of observed ro-vibrational bands in blue & orange, and FCF's⁷ in black, of the A-X system of CN. Values highlighted in red are the origins of newly observed bands, orange ones indicate that both spin-orbit components were observed for these bands, while values highlighted in green are bands that were not observed despite favourable FCF's.

$v'' \setminus v'$	0	1	2	3	4	5	8
0	9115.6892	10903.4103	12665.5659				
	0.495	0.321	0.127				
1	7073.2652		10623.1419	12359.718			
	0.372		0.239	0.195			
2	5057.1388	6844.8600		10343.592	12054.532		
	0.113	0.348		0.097	0.182		
3		4855.0705	6617.2261			11750.088	
		0.224	0.207			0.122	
4		2891.6460	4653.8016	6390.378	8101.3178		
		0.055	0.288	0.0811	0.151		
5			2716.7930	4453.369		7849.6550	12751.858
			0.106	0.296		0.158	0.083
6				2542.817	4253.757		
				0.161	0.259		
7						4055.066	
						0.198	

VI.3.2.2 Rotational Assignment

The rovibrational structure of the $A^2\Pi_1 - X^2\Sigma^+$ spectrum of the CN radical is rather complex for a diatomic molecule. The lower-lying $^2\Pi_{3/2}$ state is labeled F_1' while the $^2\Pi_{1/2}$ is designated F_2' . Each rotational level in the upper state actually consists of two distinct states labeled e and f (Λ -doublets). The e and f states associated with a particular rotational level, J , have opposite parity which alternate with J . Similarly, each rotational level in the ground $X^2\Sigma^+$ state consists of two distinct states labeled F_1'' and F_2'' , or e and f , and their parities also alter with J . The transition selection rules (see Chapter I) dictate that each spin-orbit sub-band of the A-X system consists of six rotational branches: P, Q and R branches for both $F_1' - F_1''$ and $F_1' - F_2''$; by convention, the branches of these sub-structures are distinguished from one another by attaching the subscripts of the levels involved as indicated in Table VI-3. In order to further indicate the origin and destination levels of a branch, an alternate labeling scheme has been adopted in this study: the subscripts e and f are also used. This scheme in combination with an energy level diagram (see Chapter I) are useful in assigning spectra of $^2\Pi - ^2\Sigma$ systems.

Table VI-3 Branch labelling-scheme for a $^2\Pi_{3/2} - ^2\Sigma$ system. Changing the first subscript, 1, to 2 yields the scheme for $^2\Pi_{1/2} - ^2\Sigma$ transition.

$F_1' - F_1''$			$F_1' - F_2''$		
P_{11}	Q_{11}	R_{11}	P_{12}	Q_{12}	R_{12}
$P_{1,1e}$	$Q_{1,1e}$	$R_{1,1e}$	$P_{1,2f}$	$Q_{1,2f}$	$R_{1,2e}$

The A-X electronic transition of CN can be easily recognised by the presence of strong (the Q_{11} and Q_{21} branches) and weak (the R_{11} and R_{21} branches) red-degraded heads in each sub-band. The structure of the 1-0 band of CN showing the red-degraded heads is illustrated in Fig x (CCD spec centered at 920.18 nm); the weak band-head of the $^2\Pi_{1/2} - ^2\Sigma$ system is too weak to be observed. This CCD spectrum has been

collected close to the nozzle tip, and, thus, is rotationally warm as the molecules have not undergone enough collisions. A rotationally cold spectrum collected approximately $160 \mu\text{m}$ downstream of the previous one clearly showing individual branches is shown in fig . In this region of the supersonic expansion, the CN radical has also undergone spin-orbit relaxation as indicated on one hand by the decrease in intensity of the ${}^2\Pi_{1/2} - {}^2\Sigma$ sub-band and on the other hand by an increase in the intensity of the lower-lying ${}^2\Pi_{3/2} - {}^2\Sigma$ sub-band. These type of rotationally cold spectra enable easy assignment of transitions of individual branches as their origin are clearly observed as illustrated in Figure VI-5.

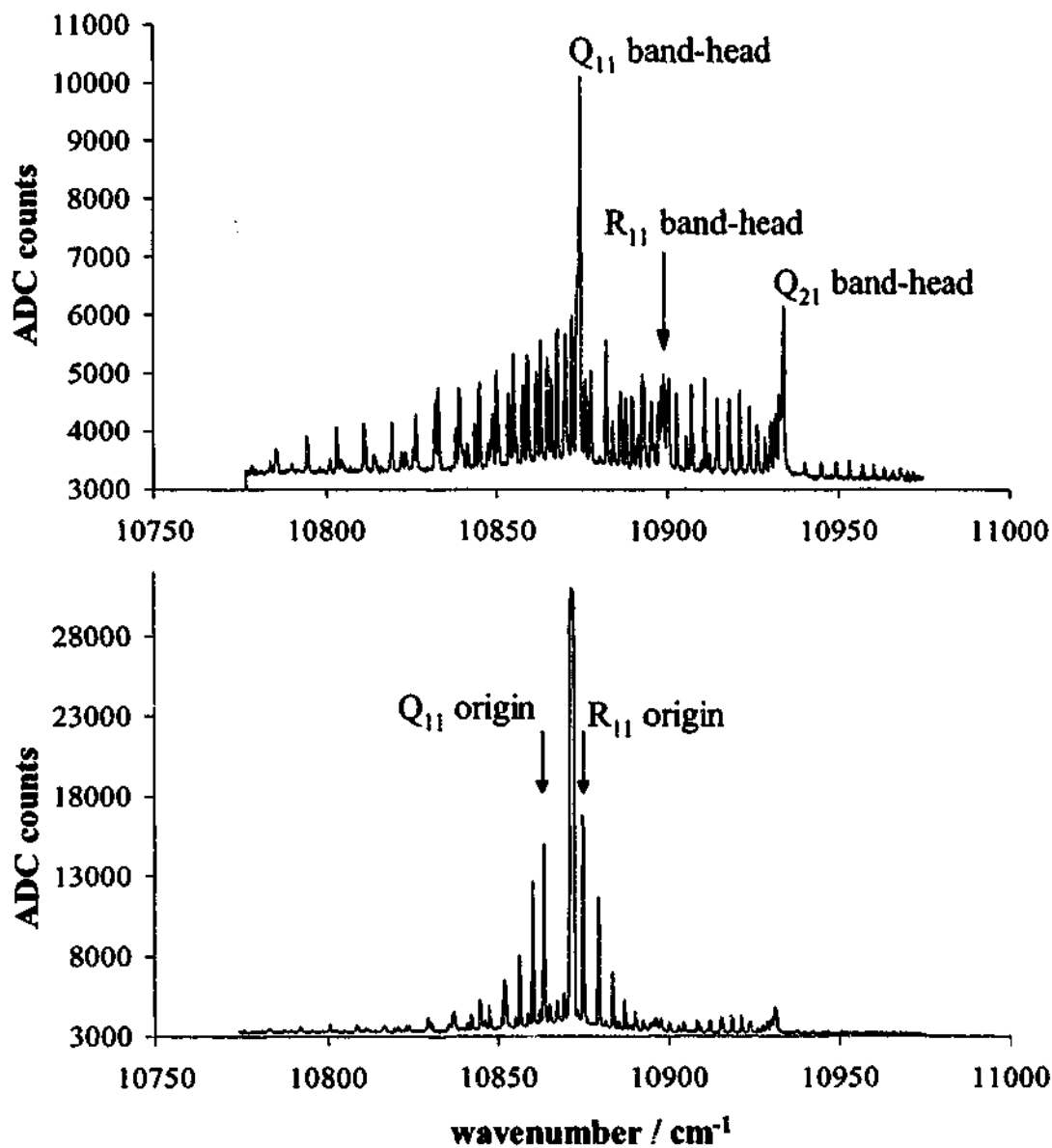


Figure VI-5 CCD spectrum of the 1-0 band of the $A^2\Pi_g - X^2\Sigma^+$ of the CN radical showing the typical profile of a rotationally warm band highlighted by the presence of Q₁₁, R₁₁ and Q₂₁ band-heads at the top, and that of a rotationally cold one highlighted by the appearance of the origin of the Q₁₁ and R₁₁ branches.

With the nozzle fixed at this location, spectra were subsequently recorded with a FT spectrometer at high resolution. A portion of the high resolution spectrum of the A-X system of CN showing a spin-orbit cold and warm 0-0 band is illustrated in Figure VI-6a) and b). As shown in Figure VI-6a), at low J's the Q_{12} and P_{11} branches are not observed as separate structures due to the resolution at which the spectrum was recorded. This observation also applies to the Q_{11} and R_{12} branches. In addition, the R_{11} band-head is only observed in the warmer spectra where higher-lying rotational levels are populated. Rotationally cold spectra were used mainly for initial assignment of the rotational transitions, whenever possible slightly warmer spectra showing the second sub-band were measured as they provided important information about the ${}^2\Pi_{1/2}$ state which has never been observed at high resolution in a jet.

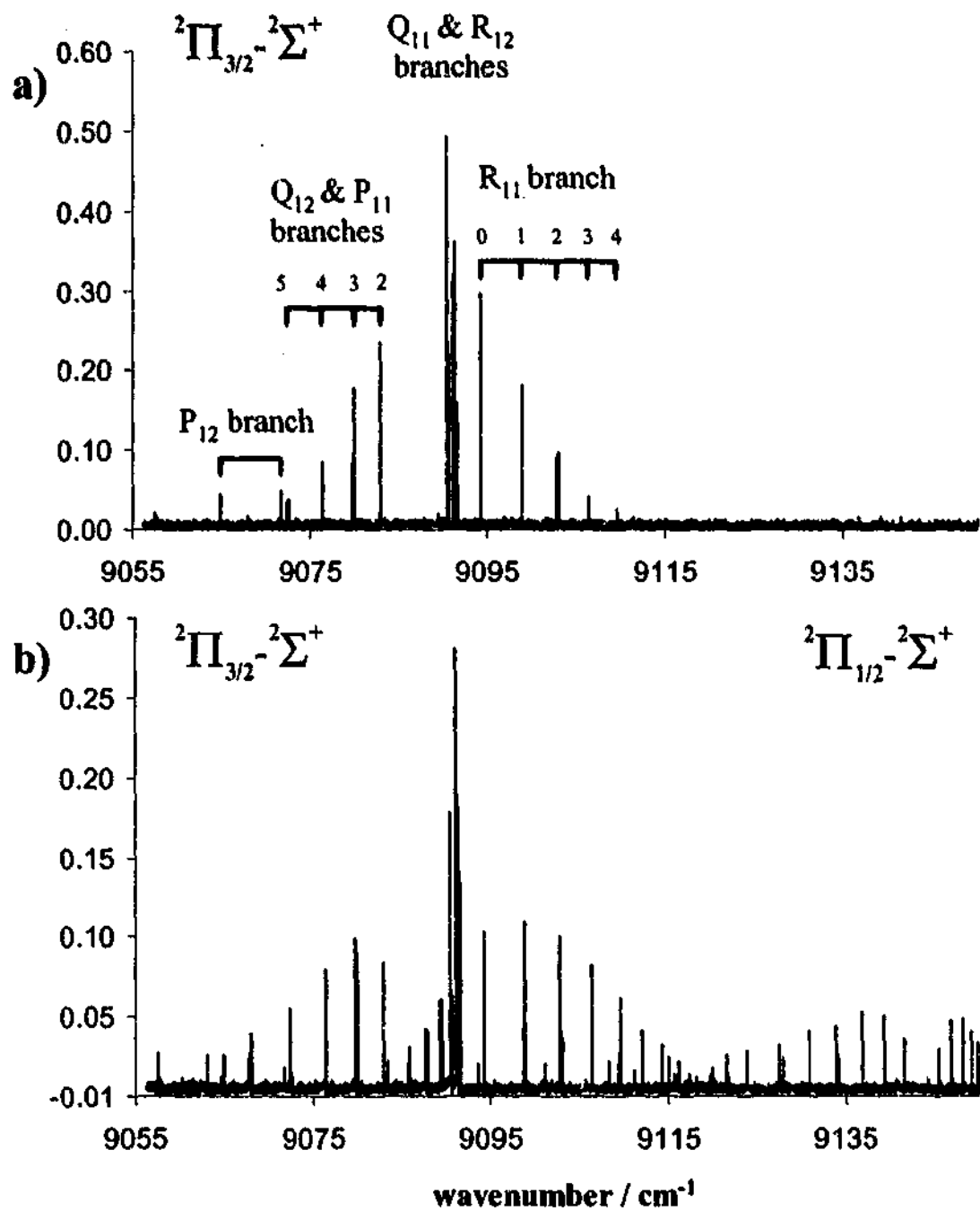


Figure VI-6 High-resolution FT spectrum of the 0-0 band of the red-system of CN showing spin-orbit cold and warm structures in a) and b) respectively. The former was used primarily for assignment of rotational transitions.

VI.3.2.3 Data Reduction

A total of 670 transitions measured at a resolution of 0.035 cm^{-1} were assigned to 22 vibrational bands belonging to the $A^2\Pi_1 - X^2\Sigma^+$ system of the CN radical. A list of the observed transitions is provided a 3.5" Disk labeled 'CN data' at the end of the thesis. The data recorded in this study were fitted to Brown's effective N^2 -Hamiltonian³⁵ previously described in Chapter I using the weighted non-linear least-squares method as first proposed by Zare *et al.*²³ The FORTRAN program used, LSQFIT, was originally written by Dr. Clive Jarman and later modified by Dr. Tsuyoshi Hirao. LSQFIT allows the user to fit rovibrational transitions to a variety of electronic states defined by the N^2 -Hamiltonian of Brown *et al.*³⁵. Parameters used to describe the ground-state rovibrational levels of the $^2\Sigma$ are the vibrational energy (relative to $v=0$ in the ground state), $T_{0,v}$, the inertial rotational constant, B_v , the centrifugal distortion constants (CDC's), D_v and H_v , and the spin-rotation constant, γ_v . The excited $^2\Pi$ levels are described by the vibrational energy, $T_{0,v'}$, the spin-orbit constant, A_v , the inertial rotational constant, B_v , the centrifugal distortion constants, D_v and H_v , and the λ -type doubling constants, p_v and q_v .

In initial band-by-band fits, the ground X-state parameters were held constant to the deperturbed values reported by Kotlar *et al.*⁵ while in the A-state, H_v , p_v and q_v were also fixed to values reported by them. Since transitions from both spin orbit components were available for $v'=0,1,2$ and 3 , the spin-orbit parameter, A_v , was fitted for these levels. For vibrational levels 4, 5 and 8 where transitions from only the $^2\Pi_{3/2} - ^2\Sigma$ sub-system were observed, Kotlar's A_v values were used. However, these values were first transformed from the R^2 -Hamiltonian representation of Zare *et al.*²³ to the N^2 -Hamiltonian representation of Brown *et al.*³⁵ using the approximate formulation of Brown *et al.*³⁵ and Amiot *et al.*³⁶ (see Appendix). A fit using Kotlar's⁵ deperturbed ground-state constants yielded an initial variance of 410 which could not be improved with the use of additional parameters. In their study, Kotlar *et al.*⁵ used the A-X data reported by Cerny *et al.*²¹. In the absence of pure rotational and rovibrational data, their ground state parameters are merely effective constants as they probably have some A-state 'character'. A useful parameter displayed by LSQFIT, labeled DIV, represents the ratio of Residual to Uncertainty of a transition; a DIV value of one or less indicating

that a line has been properly fitted. Using Kotlar's constants to predict pure rotational and rovibrational transitions clearly showed that they do not adequately describe the ground state rovibrational levels of the CN radical as DIV-values ranged from 0.2 to 5 for pure rovibrational transitions and from 7 to over ten thousand for pure rotational transitions.

The same test was performed using the ground state constants reported by Prasad and Bernath's⁷ yielding DIV-values of less than 4 for pure rovibrational transitions and less than 100 for pure rotational transitions. This large disparity in the predictions can only be explained by the fact that, in their study, Prasad and Bernath⁷ performed global fits of their visible A-X data as well as microwave^{20,26,29,37} (freed from hyperfine splitting), infrared³⁰ and UV/vis^{6,31} data from other studies while Kotlar *et al.*⁵ only used the A-X data reported by Cerny *et al.*²¹ However, a fit with the ground state parameters fixed to their reported values yielded a variance of 4.5 without much improvement obtained with the use of additional parameters in the upper-state. Upon close examination of Prasad and Bernath's⁷ constants, it was observed that they had used Kotlar's A_v values without transformation. It was thus decided to include the microwave data used by Prasad and Bernath⁷ and the infrared data reported by Davis *et al.*³⁰ and Davies and Hamilton.²⁴ in the fits performed in this study.

At first, the uncertainties reported by Prasad and Bernath⁷ were used to weight the microwave data. After a series of fits it was observed that the residuals of most microwave transitions were much smaller than their uncertainties. The weights were adjusted accordingly to a minimum value of 1.0×10^{-8} which effectively clamped down the ground-state rotational and spin-rotational constants. The infrared data did not require this treatment as their residuals were never much smaller than their uncertainties. Constants not contributing significantly to the energies of both states were removed. In particular, all ground and upper H_v constants were set to 0, and the λ -type doubling constants for vibrational levels 4, 5 and 8. Subsequent fits showed that the variance only changed in the third decimal place indicating that these higher-order CDC's were not required as to be expected in the absence of highly populated rotational states. A similar reasoning was used to justify the removal of the λ -type doubling constants for vibrational levels 4, 5 and 8 in the upper state. In the final fit, $T_{0,v}$, B_v , D_v and γ_v were set as free parameters with the remaining ground-state parameters set to 0, and $T_{0,v}$ and B_v were set as free parameters for all upper-state vibrational levels.

The A_v and D_v were set as free parameters only for levels $v' = 0-3$ but fixed to Kotlar's transformed values for the remaining levels, and the λ -type doubling constants were also fixed for all upper-state levels.

At the start of the numerical analysis, all 670 observed transitions were assigned uncertainties of 0.003 cm^{-1} (-1σ). In the final fit, transitions with residuals lying between $-2\sigma \text{ cm}^{-1}$ and $-4\sigma \text{ cm}^{-1}$ (131 blended transitions) were assigned uncertainties of $3\sigma \text{ cm}^{-1}$, while those having residuals larger than $-4\sigma \text{ cm}^{-1}$ (101 transitions with small S/N) were assigned uncertainties of 100 cm^{-1} thereby virtually removing them from the fit. The parameters obtained from the final fit are summarised in Table VI-4; the standard deviation of the fit was 1.02 or 0.0049 cm^{-1} for the 569 lines fitted.

Table VI-4 X and A state molecular constants obtained in this study from band-by-band weighted non-linear least-squares fit to Brown's N^2 Hamiltonian.³⁵ The figures in parentheses represent one standard deviation in the last two digits.

CN $X^2\Sigma^+$ Spectroscopic Constants / cm^{-1}				
v	$T_{0,v}$	B_v	$D_v \times 10^6$	$\gamma_v \times 10^3$
0		1.891090511(106)	6.3990(59)	7.2552829(45)
1	2042.42400(50)	1.8736658902(45)	6.40409(29)	7.1741399(66)
2	4058.55044(43)	1.8561875139(41)	6.42778(27)	7.0834667(96)
3	6048.33996(65)	1.8386528195(41)	6.42210(27)	6.9818002(96)
4	8011.76457(70)	1.8210597967(55)	6.45417(80)	6.8650266(97)
5	9948.77311(88)	1.80340422(23)	6.439(23)	6.72039(36)
6	11859.3255(12)	1.785685594(32)	6.5362(47)	6.543702(50)
7	13743.3618(21)	1.76789872(10)	6.513(15)	6.31452(17)

CN $A^2\Pi_1$ Spectroscopic Constants / cm^{-1}				
v	$T_{0,v}$	A_v	B_v	$D_v \times 10^6$
0	9115.68946(68)	-52.66189(87)	1.707006(20)	6.054(93)
1	10903.41083(69)	-52.58209(98)	1.689719(16)	6.020(73)
2	12665.56623(74)	-52.5087(11)	1.672428(12)	6.073(39)
3	14402.1428(12)	-52.4379(21)	1.655003(25)	5.85(14)
4	16113.0819(15)		1.637888(96)	
5	17798.4281(21)		1.62181(17)	
8	22700.6307(26)		1.56722(20)	

The results from this study are compared to those of Kotlar *et al.*⁵, Cerny *et al.*²¹ and Prasad and Bernath⁷ as these are the only other studies performed on the A-X system of CN at 0.035 cm^{-1} resolution or better. The ground electronic X-state spectroscopic parameters are compared in Table VI-5, and the first excited electronic A-state parameters in Table VI-6. Comparison the standard errors of the ground-state spectroscopic constants estimated in this study to those of Cerny *et al.*²¹ and Prasad and Bernath⁷ indicate that all three studies are as accurate as one another. Comparison of the A-state parameters however, reveal that Cerny's B_v and CDC's are slightly more accurate. Considering the relatively small amount of data fitted in this study (570) and the small range of 'observed' rotational levels ($J < 20$), the results obtained may be qualified as more accurate than those of both Cerny *et al.*²¹ (J 's up to 90, fitted 3600 lines) and Prasad and Bernath⁷ (same range of J 's, fitted over 2000 lines including B-state transitions).

Comparison of the magnitude of the ground-state spectroscopic constants in Table VI-6 shows strong agreement between the parameters obtained in this study and those of Prasad and Bernath.⁷ This was expected as the same pure rotational transitions were used in both studies although the extent of rovibrational transitions used was different. For adequate comparison of the A-state spectroscopic constants the values of Cerny *et al.*²¹ and Kotlar *et al.*⁵ were transformed from the \hat{R}^2 -Hamiltonian to the \hat{N}^2 -Hamiltonian representation. The disagreement between their values and the ones estimated in this study are small but significant as they are 5 to 30 times larger than the respective standard errors of parameters obtained in this study. Comparison of the A_v parameters show that their original A_v values seem to show better agreement with the ones estimated in this work than the transformed A_v 's.

Table VI-5 Comparison of X state molecular constants obtained in this study to those of Kotlar *et al.*⁵, Cerny *et al.*²¹ and Prasad and Bernath.⁷ The figures in parentheses represent one standard deviation in the last digits. All values are in wavenumbers.

v	$T_{0,v}$				B_v			
	Kotlar	Cerny	This Study	Prasad	Kotlar	Cerny	This Study	Prasad
0					1.891035	1.8910827(43)	1.891090511(106)	1.89109067(19)
1	2042.424	2042.42261(49)	2042.42400(50)	2042.41851(68)	1.873611	1.8736591(44)	1.8736658902(45)	1.87366616(21)
2	4058.557	4058.55176(67)	4058.55044(43)	4058.54467(67)	1.856142	1.8561802(44)	1.8561875139(41)	1.85618743(21)
3	6048.374	6048.34766(90)	6048.33996(65)	6048.3368(93)	1.838628	1.8386440(47)	1.8386528195(41)	1.83865304(26)
4	8011.849	8011.7734(21)	8011.76457(70)	8011.7554(11)	1.821067	1.8210468(74)	1.8210597967(55)	1.82105956(34)
5	9948.955		9948.77311(88)	9948.7499(23)	1.803461		1.80340422(23)	1.80340517(99)
6	11859.668		11859.3255(12)	11859.2870(31)	1.785808		1.785685594(32)	1.78568568(62)
7	13743.960		13743.3618(21)	13743.3235(30)	1.768110		1.76789872(10)	1.76789664(76)

v	$D_v \times 10^6$				$\gamma_v \times 10^3$			
	Kotlar	Cerny	This Study	Prasad	Kotlar	Cerny	This Study	Prasad
0	6.3899	6.4072(12)	6.3990(59)	6.4094(47)	7.18	7.417(33)	7.2552829(45)	7.25517(63)
1	6.3978	6.4162(13)	6.40409(29)	6.4157(45)	7.05	7.367(33)	7.1741399(66)	7.17398(89)
2	6.4057	6.4263(13)	6.42778(27)	6.4239(44)	6.92	7.272(46)	7.0834667(96)	7.0833(14)
3	6.4135	6.4367(18)	6.42210(27)	6.4355(43)	6.79	7.190(45)	6.9818002(96)	6.9819(16)
4	6.4214	6.4445(51)	6.45417(80)	6.4403(26)	6.66	7.212(144)	6.8650266(97)	6.8645(16)
5	6.4292		6.439(23)	6.58(13)	6.53		6.72039(36)	6.7208(17)
6	6.4371		6.5362(47)	6.545(75)	6.40		6.543702(50)	6.5436(16)
7	6.4450		6.513(15)	6.207(98)	6.28		6.31452(17)	6.3137(16)

Table VI-6 Comparison of A state molecular constants obtained in this study to those of Kotlar *et al.*⁵, Cerny *et al.*²¹ and Prasad and Bernath.⁷ The figures in parentheses represent one standard deviation in the last digits. All values are in wavenumbers.

v	$T_{0,v}$			B_v		
	Kotlar N ²	This study	Cerny N ²	Kotlar N ²	This study	Cerny N ²
0	9115.672	9115.68946(68)	9115.67109(35)	1.7070704	1.707006(20)	1.7071199(43)
1	10903.399	10903.41083(69)	10903.39928(53)	1.6897935	1.689719(16)	1.6898438(44)
2	12665.551	12665.56623(74)	12665.55715(105)	1.6724637	1.672428(12)	1.6725231(49)
3	14402.111	14402.1428(12)	14402.1331(31)	1.6550808	1.6550002(25)	1.655150(100)
4	16113.061	16113.0819(15)	16113.1192(96)	1.637645	1.63789(10)	1.637695(29)
5	17798.383	17798.4281(21)		1.6201561	1.62181(17)	
			Prasad			Prasad
8	22700.408	22700.6307(26)	22700.6453(36)	1.5673716	1.56722(20)	1.567449(27)

v	A_v			D_v			
	Kotlar R ²	Cerny R ²	This study	Kotlar N ²	Kotlar	This study	Cerny
0	-52.6495	-52.65010	-52.66189(87)	-52.6209	6.1323	6.054(93)	6.1497
1	-52.5742	-52.57602	-52.5820(11)	-52.5455	6.1417	6.020(73)	6.1613
2	-52.4922	-52.50026	-52.5087(11)	-52.4634	6.1534	6.073(39)	6.1746
3	-52.4035	-52.4289	-52.4379(21)	-52.3746	6.1675	5.85(14)	6.1877

The vibrationally dependent spectroscopic parameters of the $X^2\Sigma^+$ and $A^2\Pi$, electronic states of CN were fitted independently to $(\nu+1/2)$ expansions leading to a set of effective equilibrium molecular constants listed in Table VI-7.

Table VI-7 Effective Equilibrium Molecular Constants for the $X^2\Sigma^+$ and $A^2\Pi$, electronic states of CN obtained by fitting vibrationally dependent spectroscopic parameters to $(\nu+1/2)$ expansions. The figures in parentheses represent one standard deviation in the last digits. All values are in wavenumbers.

	$X^2\Sigma^+$	$A^2\Pi$
$Y_{1,0}$	2068.6655(86)	1813.297(15)
$Y_{2,0}$	-13.1126(25)	-12.7799(41)
$Y_{3,0}$	-7.09E-03(21)	-2.09E-03(30)
$Y_{0,1}$	1.89978377(47)	1.71509(70)
$Y_{1,1}$	-1.737392E-02(52)	-0.01678(36)
$Y_{2,1}$	-2.471E-05(15)	-6.9E-05(39)
$Y_{3,1}$	-4.52E-07(12)	
$Y_{0,2}$	6.377(18)	
$Y_{1,2}$	0.0181(38)	
k	γ_k	A_k
0	7.264(17)	-52.7029(16)
1	-0.0379(96)	0.0836(19)
2	-0.0115(12)	-2.27E-03(46)

VI.4 Conclusions

The CN radical was generated by CESE of CH₃CN seeded in helium, neon and argon, and its emission spectrum recorded with both a CCD/diffraction grating spectrometer and a Fourier transform spectrometer. Spectral features belonging to the $A^2\Pi_1 - X^2\Sigma^+$ electronic system of the CH radical, and the $A^2\Pi_1 - X^2\Sigma^+$ and $B^2\Sigma^- - X^2\Sigma^+$ of the CN radical were identified between 9000 and 37000 cm^{-1} in the low-resolution CCD emission spectrum.

Transition belonging to the Red $A^2\Pi_1 - X^2\Sigma^+$ system of CN generated by CESE of CH₃CN seeded in helium and neon were observed and recorded between 8500 and 14000 cm^{-1} , and 1850 and 9000 cm^{-1} with a Bruker IFS120HR spectrometer at a resolution of 0.035 cm^{-1} with S/N ratio exceeding 500 for the strongest bands. These spectra were calibrated with/to neon atomic transitions observed between 2500 and 13500 cm^{-1} . A total of 22 vibrational bands were observed, and assigned to the A-X system of CN with $\nu' = 0-5, 8$ and $\nu'' = 0-7$. These bands were rotationally cold and most of them, also showed spin-orbit cooling. Rotational temperatures as low as 35K, and vibrational temperatures exceeding 4500K were estimated using a one-temperature model. Of the 22 bands observed in this study, only nine consisted of transitions from both spin-components, $A^2\Pi_{3/2}$ and $A^2\Pi_{1/2}$. These nine bands involved the A-state vibrational levels $\nu' = 0-3$. Rotational assignment of the 22 observed bands was readily achieved despite the complexity of the band-structures as branch-origins were easily singled-out in the rotationally-cold spectra provided by the supersonic expansion. A total of 670 transitions were measured and assigned to these 22 vibrational structures.

Pure rotational transitions reported by Prasad and Bernath,⁷ and pure rovibrational transitions observed and reported by Davis *et al.*³⁰ and Davies and Hamilton²⁴ were coupled to the assigned transitions of the present study, and fitted to Brown's \hat{N}^2 -Hamiltonian.³⁵ This global fit to 50 spectroscopic constants yielded an overall standard deviation was 1.02. As a result, observed transitions could be predicted to within 0.0049 cm^{-1} . The band-by-band fits performed in this study yielded accurate spectroscopic constants for vibrational levels $\nu' = 0-5, 8$ and $\nu'' = 0-7$ in the A-state and X-state of the CN radical respectively. They are of comparable quality to those reported by Cerny *et al.*²¹ and Prasad and Bernath.⁷

The magnitude of the spectroscopic constants obtained in this study are in excellent agreement with those reported by Prasad and Bernath,⁷ but are significantly different from the constants reported by Cerny *et al.*²¹ and Kotlar *et al.*⁵ It is believed that Cerny's constants, though very accurate, do not adequately describe the individual electronic states as microwave transitions reported by Prasad and Bernath.⁷ are inaccurately predicted using their ground-state parameters. Thus, their constants are merely empirical parameters describing the A-X system. On the other hand the close agreement between the constants of this study and those of Prasad and Bernath⁷ seem to suggest that a global fit of the combined data set is required as it would probably supersede all previous studies performed on the A-X system. This combination would provide the most complete and accurate description of the A-state to date ($v' = 0-5, 8-21$).

Finally, of the 50 spectroscopic constants obtained in the band-by-band study 46 were fitted to polynomials in $(v+1/2)$ leading to a set of 21 effective equilibrium molecular constants describing the vibrational and rotational energies of both states, the X-state distortion and spin-rotation constants, and the A-state spin-orbit constants. This latter calculation seems to indicate that a fit of the raw data to a Dunham-type expansion may yield results that are more accurate. Unfortunately, at the present time the available fitting program is not equipped to deal with Dunham-type expansions for doublet-states.

VII An Enclosive Flow Cooling cell for Simplification of Gas-Phase Spectra

VII.1 Introduction

VII.1.1 *Spectral simplification by cooling*

High-resolution spectroscopic studies of gases are routinely conducted at room temperature. Investigation of diatomic or small polyatomic molecules generally yields simple and well-resolved spectra that can easily be assigned and analysed. However, room-temperature spectra of larger polyatomics can often be extremely congested and quite complex due to the combination of closely spaced transitions with broad features, overlapping band structures, and the presence of hot bands. Even with today's advances in technology (in terms of spectroscopic instruments and computers) the task of assigning and analysing room-temperature spectra of larger polyatomic molecules is still arduous and sometimes impossible.

According to theory, both the linewidth and the spectral bandwidth are proportional to temperature and thus, spectroscopists have been resorting to cooling techniques to achieve spectral simplification^{*}. However, a reduction in temperature is

^{*} see Chapter I for theoretical explanation

also accompanied by a reduction in the partial pressure of the gas of interest thereby reducing the sensitivity of traditional cooling techniques. Several attempts have been made at developing techniques that would be highly sensitive and yield simplified spectra, the first of which being the use of cold long absorption path cells.¹ Although this technique did increase the sensitivity, it was limited to investigating gases with appreciable vapour pressures at these operating cryogenic temperatures.²

VII.1.2 Available non-equilibrium cooling techniques

Supersonic expansion was the first method developed allowing gases to be successfully studied at temperatures well below their freezing point. Only a brief description will be offered as this technique has already been described and reviewed in Chapter IV. The technique of supersonic expansion consists of forcing a high pressure gas mixture through a pinhole nozzle (typically $\approx 200 \mu\text{m}$) into an evacuated chamber. The mixture consists of a small amount of spectroscopic gas usually diluted in a rare carrier gas (typically $< 1:100$). As the high-pressure gas-mixture proceeds through the nozzle, numerous inelastic collisions take place between the carrier and sample gases enabling the latter to disperse a substantial amount of its internal energies. Although the extent of cooling can be quite dramatic as rotational temperatures of a few Kelvin are readily achievable, supersonic expansions have several drawbacks. These disadvantages along with some of their consequences are listed in Table VII-1.

Table VII-1 Disadvantages of supersonic expansion techniques and their main consequences.

Drawback	Consequence
Short optical path length	Low sensitivity
Non-equilibrium condition	Presence of hot-bands;
Lack of temperature control	Limits type of investigation
Large pumping capacity	Expensive
Large gas-flows	Large amount of sample required

The most important drawback is probably the short optical path defined by the overlap between the probing radiation and the volume of collisionally-cooled gases. The resulting lack of sensitivity not only dictates the signal-to-noise ratio (S/N) but also affects the precision of the spectral measurements, and, thus, becomes an important factor in the spectroscopic study of poor absorbers or transitions of weak intensities. In order to increase the sensitivity of this technique several modifications were made. First, the pinhole-nozzles were replaced by slit-nozzles, then the flow of gas was changed from being continuous to pulsed, and finally, multi-reflection systems were adapted to supersonic jets. Although these modifications go some way to improve the sensitivity of supersonic expansions, optical paths are still of the order of 20 *cm*, and, in addition, the remaining drawbacks cannot be improved as they are intrinsic to the technique.

Collisional-cooling is an additional technique that was initially developed to perform low-temperature spectroscopic studies in the microwave region. This technique is quite similar to the traditional cooling methods whereby a small amount of condensable spectroscopic gas is introduced in a cold cell (10-30 *cm* in length) containing a non-condensable buffer gas under 'static'[†] conditions. As the absorber gas diffuses through the cell it rapidly cools down via inelastic collisions with the cold background gas before eventually condensing on the cell walls. Collisional-cooling differs however from traditional methods in that the partial pressure of the spectroscopic gas can be maintained at an appreciable level by constantly injecting the cell with a fresh amount of sample. The sensitivity of this method is enhanced not only by the substantial vapour present at these cryogenic temperatures but also by the increased optical path length. This increase in sensitivity result in the need for less sample while the long residence time of the sample in the optical volume result in a state of quasi-equilibrium. In addition, the temperature can be readily controlled by altering the type and amount of cryogen used. All of these factors make this method an interesting alternative to supersonic expansions. The method of collisional-cooling was pioneered by Messer and De Lucia in 1984 to measure pressure broadening parameters of the CO-He system at 4 *K*.³ Similar low-temperature helium pressure-broadening studies on other molecules followed.⁴⁻⁸ Originally called collisional cooling it was later coined more appropriately diffusive trapping by Barnes *et al.*⁹ who performed the first IR study using this technique as they recorded the CO₂ spectrum at low-resolution at 95 *K* to test the efficiency of their cell. Using the same apparatus, they later went on to record the first IR spectrum of clusters formed in such collision-cooling cells.¹⁰ Wiley *et al.* have

[†] referring to flow conditions, 'static' means a condition of no flow

adapted their low-temperature cell and demonstrated the application of diffusive-trapping in the IR region when they studied linewidth and lineshape of N_2O and CH_3F around 10 K using a tunable diode laser.^{11,12} At around the same time Newnham *et al.* designed a collisional-cooling cell similar to that of Messer's pioneering cell but with an optical path length of 25 cm.¹³ In their study, they not only showed that they could supercool molecules and form clusters but, they also demonstrated that the method of diffusive trapping was efficient at cooling both vibrational and rotational degrees of freedom. Although diffusive trapping can overcome most of the disadvantages intrinsic to supersonic expansions, it has a couple of drawbacks. The first one is the fact that the sample gas has to be diluted by a factor of approximately 10,000 in order to minimise the heat load on the buffer gas thus limiting the sensitivity of this technique. The second drawback is the fact that at high cell pressures, the sample mean free path is so small that it tends to reach the cell walls before reaching the volume occupied by the probing radiation.

The shortcomings of diffusive trapping methods can be overcome by using the technique of Enclosive Flow-Cooling. The latter is a relatively new method enabling the study of gases in a temperature regime where the gas of interest has a vanishingly small vapour pressure. Only a brief description will be offered at this stage as it will be discussed in detail in the Experimental section of this chapter. In a typical EFC experiment, a pre-cooled buffer gas is introduced through radial holes located along the length of the cell while the gaseous sample is injected axially. Under flow conditions, the buffer gas tends to constrict the sample to the center of the chamber where it can interact with a probing infrared radiation. This technique is an adaptation of the diffusive trapping method and thus, shares many of its attributes. The major difference being the fact that both the pre-cooled buffer gas and the room-temperature sample continuously flow through the cell which is constantly evacuated. This flow regime ensures that the room-temperature sample always encounters freshly pre-cooled buffer molecules thereby reducing the possibility of any heat build-up and propagation through the cell. The flow of buffer gas down the cell-wall has a dual purpose. At first, it cools down the sample gas upon inelastic collisions then, it acts as a barrier shielding the gas of interest to a certain extent from the wall where it would certainly condense. The spectroscopic gas is thus constrained to the center of the cell, thereby maximising the overlap between the sample and the axial infrared radiation probe. Contrary to diffusive trapping where operation at high pressures tend to cause the sample to diffuse more

rapidly to the cell wall, the limit imposed by pressure is only due to pressure-broadening contribution to linewidths.

Enclosive-flow cooling was pioneered in 1995 by Bauerecker *et.al.*¹⁴ They built a dual-pass Enclosive-Flow Cooling cell with a total optical path of 80 *cm* and designed it for use with liquid nitrogen. In this pioneering study, they demonstrated the attributes of this new technique by recording FTIR low-resolution spectra of gases collisionally-cooled to 135 *K*. A second study by Taucher *et.al.*¹⁵ was used to demonstrate the sensitivity of this new cooling method when coupled to a tunable diode laser. The following year, the cell was improved with the implementation of multi-reflection optics yielding a maximum optical path of 40 *m*.^{16,17} They demonstrated the potential that the EFC technique had in cluster studies. Further improvements enabled the use of liquid helium as a cryogenic coolant and in 2001, Bauerecker *et.al.* reported the first infrared spectral investigation of molecular clusters generated by collisional-cooling methods between 5 and 20 *K*. An excellent review of the history of collisional-cooling techniques is also offered in that particular paper. At the same time, Kunzmann *et.al.*¹⁸ reported a detailed study of nanoparticles generated using Bauerecker's new EFC cell.

Some of the most important features of the previously mentioned cooling techniques are summarised in Table VII-2. It is quite clear that a liquid helium-cooled EFC cell has superior attributes than both supersonic expansion and diffusive trapping. The method of enclosive flow cooling provides substantially longer optical path lengths, a quasi-equilibrium environment and a well-defined controllable temperature, as well as being more economical (smaller pumping requirement and amount of sample). In addition, molecules can also be generated with rotational temperatures of the order of a few Kelvin, a temperature regime previously accessible only by supersonic expansion and diffusive trapping. To date, no high-resolution spectroscopic study of significance has been performed using enclosive-flow cooling. The only high-resolution studies performed have been to assist in the evaluation of this technique.

Table VII-2 Relevant features of most common collisional-cooling techniques. The optical paths quoted for the Enclosive-Flow Cooling and Supersonic Expansion techniques are that of systems equipped with multi-pass optics coupled to a broadband infrared source. When laser diodes are used with the EFC system, a 40 *m* optical path has been achieved.

	Optical path / <i>cm</i>	T _{cell} range / <i>K</i>	Thermodynamic Equilibrium	Pumping requirements	Amount of sample
Supersonic Expansion	≈10	Not controllable	No	High	Large
Diffusive Trapping	5 →25	1.7 →300	quasi	Low	Small
Enclosive- Flow Cooling	100 →2000	4.2 →300	quasi	Low	Small

VII.2 Methodology

VII.2.1 Design of Enclosive Flow-Cooling cell

An enclosive-flow cooling chamber similar to Bauerecker's dual-pass design¹⁴ has been designed and built in order to generate gases at cryogenic temperatures. A schematic of the chamber used in this study can be seen in Figure VII-1 while detailed technical drawings are displayed in Appendix B. The enclosive-flow cooling system is composed of four main parts: a dewar, an EFC cell, a connecting flange assembly and a transfer-optics chamber. The dewar is a double-walled stainless steel chamber 300 *mm* in diameter and 750 *mm* in length. The inner-wall of the dewar is wrapped with a few closely wound layers of Mylar foil 50 μm thick to prevent radiant heat from the hot wall reaching the cold wall. Subsequently, the volume between the walls is evacuated to approximately 10^{-4} Torr in order to minimise heat conduction from the outer-wall. The cryogen is delivered to the dewar through a stainless-steel tube 12.5 *mm* in diameter located approximately 50 *mm* from the bottom surface. This feature helps to minimise the cryogen boil-off and thus, ensures a rapid filling. The nitrogen boil-off exits through a short tube placed on the opposite side of the 'hot' flange.

The 90 *mm* diameter EFC cell located inside the dewar is composed of a stainless-steel chamber containing a removable colander, a mirror, an input port for the coolant/buffer gas and an exit port to evacuate the system. The stainless steel chamber is connected to the 'cold' flange where it is sealed with indium wire, since a vacuum tight connection at cryogenic temperatures is required. The 'cold' flange is in turn connected to the 'hot' flange by a narrow tube 150 *mm* in length. It was calculated that, at this distance, the heat load from the 'hot' flange would cause nitrogen to boil-off at an acceptable rate of roughly 1.2 *L/hr*. Further insulation from the 'hot' flange is achieved with Styrofoam fitted around the narrow extension of the EFC cell.

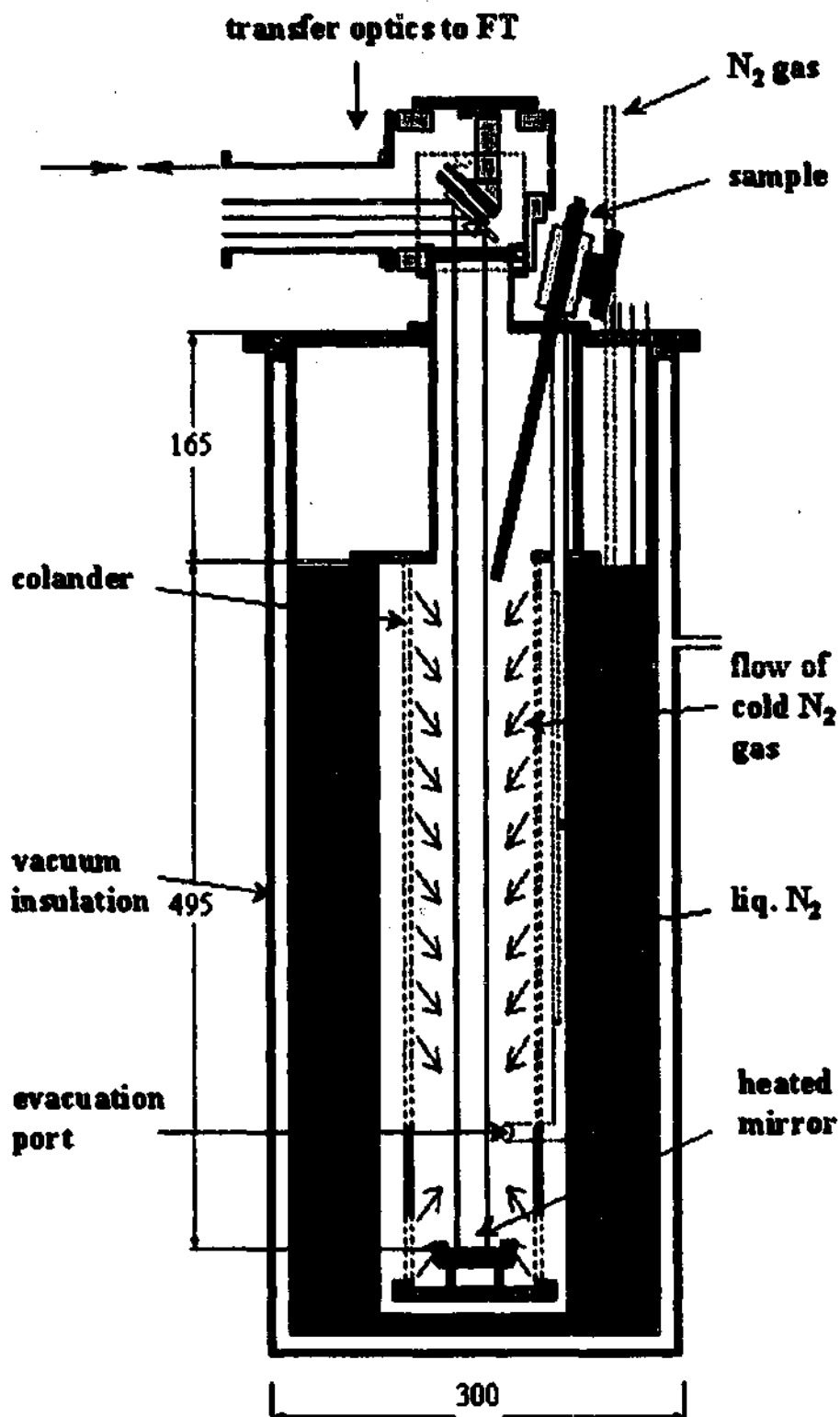


Figure VII-1 Schematic of prototype Enclosive Flow Cooling system that was designed and built to generate collisionally-cooled molecules. This collisional-cooling system is vertically coupled to an IFS120HR spectrometer. Dimensions are in *mm*.

The cell is also equipped with five sets of thermocouples wires: three are equally spaced vertically, inside the colander to measure the temperature gradient of the cell while the remaining two are used to monitor the mirror and nozzle temperature. These wires are inserted in vacuum feedthrough connectors and sealed with Epoxy resin while electrical wires are soldered to electrical vacuum connectors (both are manufactured as KF25 fittings).

The colander is made of 0.5 *mm* thick stainless steel 90 *mm* in diameter and 550 *mm* long. It has 14 staggered rows of 8 radially located holes of 0.25 *mm* in diameter separated by approximately 30 *mm*. A flat mirror 50 *mm* in diameter is located on a copper support at the bottom of the EFC cell; heat is administered to the mirror via the copper support in order to prevent or reduce condensate matter from forming on its surface. The support is mounted on three fibre-glass stilts to reduce heat-conduction from the mirror to the flange and the rest of the system. A region 60 *mm* in length located just above the mirror is void of holes. This feature enhances the flow of nitrogen from the bottom of the cell thereby further reducing the amount of sample reaching the mirror surface. An evacuation port located some 80 *mm* above the mirror is made of a stainless steel tubing 12.5 *mm* in diameter; it is connected to the 'hot' flange via an ultra-torr fitting. From there, a KF-25 fitting is used to make connection to a diaphragm-valve and eventually to a Varian SD-700 two-stage mechanical pump. The buffer gas is administered to the outer region of the colander through a stainless steel tubing 6.25 *mm* in diameter. The tubing is ultra-torr fitted to the 'hot' flange then wound five times around the EFC chamber before penetrating the wall of the chamber approximately 250 *mm* below the expected maximum level of liquid nitrogen. This feature enables precooling of the buffer gas.

A 500 *mm* long retractable steel tube 6 *mm* in diameter is inserted through a ball-valve located at the top of the EFC cell, allowing the spectroscopic gas to be injected toward the center of the colander. A 10 *W* resistive heater is attached to the end of that tube (on the low-pressure side) to prevent the spectroscopic gas from freezing before entering the colander. The ball-valve is Cajon-fitted to the 'hot' flange at an angle of 5.7° to the normal. All metal-to-metal connections in the 'hot' regions are sealed with 'O'-rings.

Mirrors placed in the transfer optics box enable the source radiation from the FT spectrometer to enter the EFC chamber via a CaF_2 window, which also isolates the EFC vacuum from the FT vacuum via an 'O'-ring seal. Thus, the transfer-optics assembly is connected to the FT spectrometer, forming one vacuum system.

VII.2.2 Design of Transfer Optics

A transfer-optic system was designed to guide a broadband infrared source from the FT spectrometer through the EFC cell onto a Mercury-Cadmium-Telluride detector. The layout of this transfer-optic system is illustrated in Figure VII-2. Two types of gold-coated mirrors are used in the present setup. Mirrors A, B and D to H are all flat and square with 50 mm sides except A, which has 25 mm sides and F, which is circular with a radius of 25 mm. Mirrors C and I are 50 mm diameter off-axis parabolic mirrors with focal lengths of 250 mm and 25 mm, respectively. Mirror C is used to collimate the source radiation before entering the EFC cell while I brings the parallel beam to a focus on the MCT detector. Both mirrors C and I are mounted on translation stages to facilitate focal distance adjustments. The rays traced in dashed lines represent the portion of the parallel beam entering the EFC cell, which is actually located beneath mirrors E and G pointing in a direction perpendicular to the plane of the page. The beam reaching mirror D is oval-shaped with dimensions 25 mm \times 27 mm (height \times width) but is close to being circular with diameter 22 mm when reaching mirror H. Mirrors D, E, G and H can all be adjusted externally enabling the optical system to be optimised while under a vacuum.

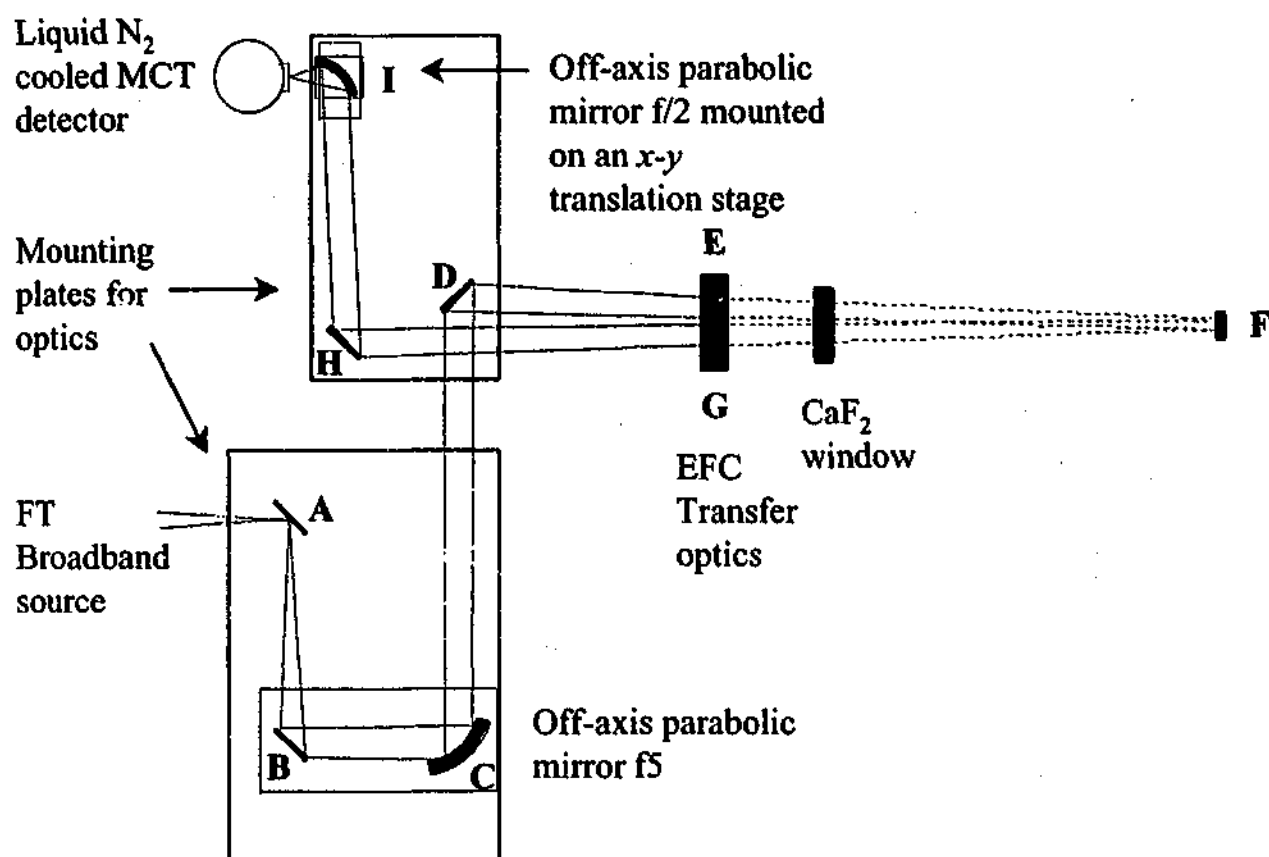


Figure VII-2 Schematic of the optical design used to couple the FT spectrometer to Enclosive-Flow Cooling cell.

VII.2.3 Mode of operation

The EFC cell is first evacuated at room temperature. It is then isolated from the pump before the dewar was filled with liquid nitrogen up to the level of the 'cold' flange. Evacuation before cooling is necessary to remove as much water vapour as possible since the latter may obstruct the holes of the colander upon freezing. Isolation of the cell from the pump is also required as backstreaming gases and oils may also block the holes or deposit on the mirror. At this point, the cell is filled with nitrogen gas at a pressure equal to that expected during operation (< 4 Torr). Once equilibrium is set (when all thermocouples indicate approximately the same temperatures), the pump valve is opened and the nitrogen flow adjusted accordingly to maintain the original pressure. The system is again allowed to come to equilibrium at which stage the flow of nitrogen (represented by the internal arrows in Figure VII-1) tends to create a 'layer' of gas near the wall. As the spectroscopic gas is introduced to the cell it collides with the

in the background but is constrained to the center portion of the cell on its way to the exit port. This feature represents the strength of the EFC technique as it increases the overlap between the probing infrared radiation and the spectroscopic gas thereby increasing the sensitivity of the experiment. The flow rate of both the buffer and the absorber gases are controlled and measured with flowmeters. The quality (S/N) and intensity of spectra collected was found to depend of the flow rates of both gases as well as on the pumping speed and on the operating temperature. Typical flow rates for nitrogen ranged from 30 to 800 *ml/min* while that of the spectroscopic gas ranged from 10 to 30 *ml/min*. During operation, the nozzle temperature is always set at 10 to 20 degrees above the freezing point of spectroscopic gas, while that of the mirror is set 20 to 30 degrees above the temperature observed at the bottom of the cell.

VII.2.4 *Experimental Setup and Conditions*

A top view of the experimental setup is illustrated in Figure VII-3. Three sets of transfer optics are used to couple the FT spectrometer to the EFC cell. The first set located in the back channel of the sample chamber of the spectrometer was used to 'collimate' the source radiation but yielded a slowly converging beam instead.

All spectra were recorded with an IFS120HR Brüker™ Fourier transform IR spectrometer equipped with a globar (broad band IR source), a KBr beamsplitter and a liquid-nitrogen cooled Mercury-Cadmium-Telluride (MCT) photodetector. The 1.3 *mm* aperture was selected to record spectra at both high (0.0019 cm^{-1}) and low (0.1 cm^{-1}) resolutions. Initially, spectra of N₂O were recorded in order to ascertain the efficiency of the existing EFC cell. For these experiments, a 2000 cm^{-1} - 2400 cm^{-1} bandpass filter was used cut down the wavenumber range. Once the experimental conditions were considered satisfactory, the mid-IR spectrum of R152a was recorded. In this case, a longwave-pass optical filter ($< 1650\text{ cm}^{-1}$) was used to cut off wavenumbers larger than 1500 cm^{-1} while the CaF₂ window imposed the red limit at around 900 cm^{-1} . These small wavenumber ranges ensured a reduction in the noise level.

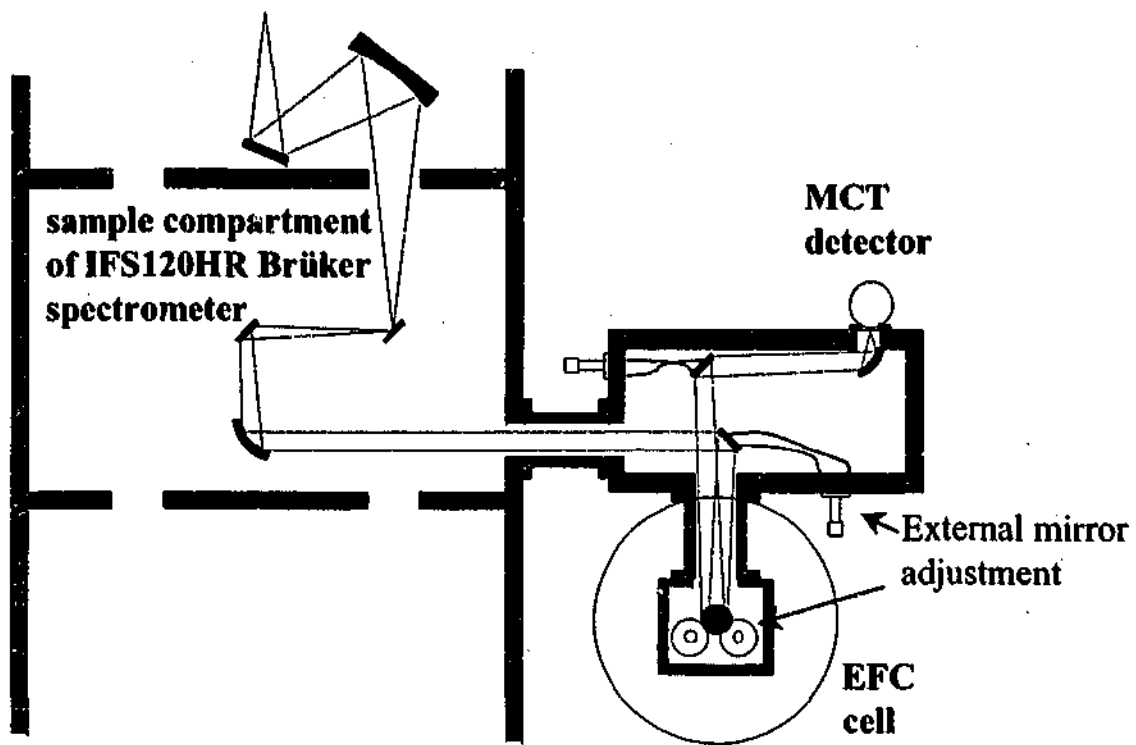


Figure VII-3 Schematic of experimental setup showing how the EFC cell is optically coupled to the FT spectrometer.

VII.3 Results & Discussions

VII.3.1 Test for efficiency of EFC cell: N_2O spectra

The N_2O spectrum has long been used as an infrared standard for calibration and, its wavenumber values and intensities are well-documented. The fact that N_2O is a strong infrared absorber makes it a useful molecule to test the efficiency of newly-designed instruments in the infrared region. Consequently, it was decided to record the Fourier transform infrared spectrum of N_2O in order to test the cell's ability to enclose and cool a gas.

The first test was performed to ascertain how well the buffer gas enclosed the sample in this particular cell. Under enclosive-flow conditions, it can be safely assumed that the sample gas occupies only the inner-volume of the colander and that of the narrow extension leading to the window located at the top, leading to a total volume of approximately 4.7 L. However, under 'static' conditions it will occupy the entire volume of the EFC cell including the narrow extension, yielding a total volume of 9.7 L. Thus, if an amount of gas under enclosive flow conditions is allowed to equilibrate under 'static' conditions, the concentration of the spectroscopic gas in the latter case should be halved since the volume has increased by a factor of approximately two. This fact should also be reflected by a similar change in absorbance assuming that the same amount of sample would be present in the cell under both conditions.

Two sets of low-resolution spectra were recorded. The first one consisted of recording a spectrum of N_2O in an "enclosive flow" and measuring the absorbance value of a line position. Immediately after, all valves connected to the EFC cell were closed simultaneously to completely isolate the cell. The system was then allowed to come to equilibrium before a second spectrum was recorded and the absorbance of the same line measured. According to the Beer-Lambert law, absorbance is inversely proportional to volume. Assuming that the optical path length is the same in both experiments as well as the amount of sample, the ratio of absorbance of a line in one spectrum to that of the same line in the other spectrum should be inversely proportional to the ratio of their respective volumes. An absorbance ratio of 1.67 was measured while that of the volumes inversed is 2.06. Thus, it seems that the present system is not fully

enclosing the spectroscopic gas. This experiment was conducted at room temperature to ensure that any discrepancies could not be attributed to sample condensation.

In a second set of tests, the cooling ability of the system was investigated. The high-resolution Fourier transform spectrum of the ν_3 band of N_2O , centered at 2200 cm^{-1} , was initially recorded at room temperature then at 110 K . The spectra shown in were recorded at a resolution of 0.0019 cm^{-1} . The room temperature spectrum displayed in Figure VII-4a) was acquired with the EFC system isolated from the pump. The N_2O partial pressure was less than 0.10 Torr while that of nitrogen was 10 Torr , yielding a mixing ratio of 100:1. A total of five scans were co-added yielding a S/N of 105:1. Using Boltzmann's equilibrium equation for thermally populated rotational energy levels (see Appendix II), the rotational temperature, T_{rot} , was estimated at $286 \pm 6\text{ K}$ while the cell temperature, T_{cell} , was 292 K .

The collisionally-cooled spectrum displayed in Figure VII-4b) was recorded as the EFC cell was evacuated at a slow flowing rate. In this case, gas flow rates were used to determine mixing ratios. Optimum conditions were reached when the sample flow rate was approximately 0.2 Torr/min while nitrogen was being flowed at a rate of 6.4 Torr/min resulting in a mixing ratio of 32:1. Under these flow conditions the pressure inside the EFC chamber was less than 4 Torr , and the cell temperature ranged from 133 K at the top to 106 K at the bottom. Five scans were averaged yielding a signal-to-noise ratio of 48:1. The rotational temperature was estimated at approximately $104 \pm 2\text{ K}$. In an attempt to improve the signal intensity, the amount of sample was increased. Clusters of N_2O were formed instead, as observed by the inflated baseline in Figure VII-4c).

Under standard conditions at 110 K , N_2O is a solid with very little vapour pressure as its melting point is 183 K . Thus, its high-resolution spectrum would be void of rotational structures. However, using the EFC technique, rotational structures were observed at 110 K indicating that the sample had been supercooled. In addition, this technique offers an environment of *quasi-equilibrium* as demonstrated by the agreement between the rotational and cell (translational) temperature.

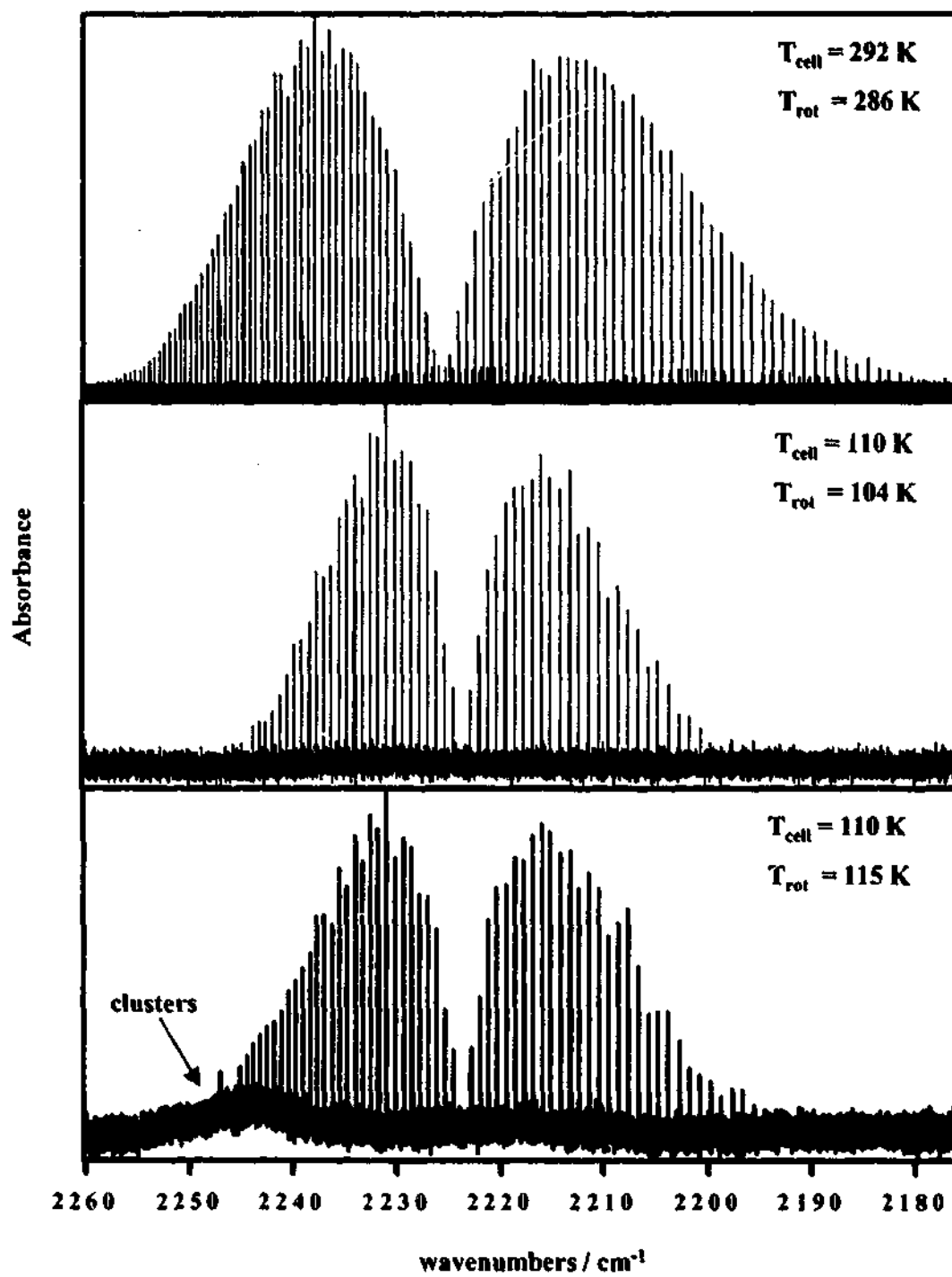


Figure VII-4 High-resolution Fourier transform infrared spectra of N_2O :

- a) at room temperature.
- b) collisionally-cooled with sample rate 0.2 Torr/min.
- c) collisionally-cooled with sample rate > 0.2 Torr/min.

VII.4 Conclusions

The Enclosive-Flow Cooling cell designed and built in this study has been quite successful in generating collisionally-cooled molecules. Initial tests conducted on N_2O as a spectroscopic gas have demonstrated that not only has supercooling been achieved under *quasi*-thermodynamic equilibrium with the present system but it was also found that molecular cluster could be easily produced. However, other tests have shown that the colander of the present EFC cell does not adequately enclose the sample gas. The latter point seems to indicate that more holes may be required in the colander in order to properly enclose a gas. Nevertheless, this study has conclusively shown that the EFC technique coupled to FT spectroscopy is a highly sensitive technique well-suited for the high-resolution spectroscopic study of molecular gases which are intrinsically weak infrared absorbers or of weak modes of vibration belonging to strong infrared absorbers.

Finally, this study has shown the versatility of the EFC technique as demonstrated by the ability to control the operating temperatures; a useful feature, as sometimes it may not be required to cool the sample as much or at all. In addition to providing an environment emulating stratospheric conditions, an EFC cell may also be quite useful in the spectroscopic study of low-temperature gas-phase reactions.

VIII High Resolution FTIR spectrum of the ν_4 mode of HFC 152a.

VIII.1 Introduction

Ozone (O_3) is a molecule of crucial importance to life as it has been found to be the only molecule in the atmosphere capable of absorbing the biologically damaging ultraviolet (UV) radiation ranging between 280 and 320 *nm*. A decrease in the concentration of ozone in the atmosphere may have serious biological ramifications such as increases in skin cancer and cataracts in human populations, low yields of cash crops and inhibited phytoplankton activities that affect the entire marine ecosystem. Studies on ozone started as early as 1930,¹ and it was soon realised that ozone levels were abnormally low but no plausible explanation was put forward. Further studies between 1950 and 1970 demonstrated that oxides of nitrogen, hydrogen, sodium, chlorine and bromine were primarily responsible for the observed low levels of ozone. Of these, the oxides of Cl and Br were considered most detrimental to the molecules of ozone.²

In 1974, Molina and Rowland proposed that UV photolysis of chlorofluorocarbons (CFC's) in the stratosphere release Cl atoms which attack and

destroy ozone molecules (see Table VIII-1).³⁻⁵ These findings, along with the fact that by then man-made CFC's had already been in commercial, household and industrial use for 40 years, prompted the medical, scientific and political communities into action leading to the Vienna convention in 1985.

Table VIII-1 Mechanism of the catalytic reaction that contribute to the destruction of ozone in the stratosphere as proposed by Molina and Rowland³ A similar mechanism is observed for halons with Br atoms being released after the photolysis step.

Reaction				Products		
CFC	+	$h\nu$ UV	→	Cl	+	by products
Cl	+	O ₃	→	ClO	+	O ₂
ClO	+	O	→	Cl	+	O ₂
O ₃	+	O	→	2 O ₂		

Two years later, world consumers and manufacturers agreed to reduce CFC and halon emission to the atmosphere by signing the Montreal Protocol. In the years to follow, changes were made to the Protocol emphasising the urgency for phasing out CFC's and halons, and the need for replacement gases.

The global phase out of ozone unfriendly CFC's and halons led to an abundance of research in finding appropriate substitute gases. Hydrochlorofluorocarbons (HCFC's) and hydrofluorocarbons (HFC's) were proposed as the main alternative to CFC's and halons. The presence of the hydrogen atoms in HCFC's renders the latter susceptible to attacks by OH radicals in the troposphere thereby considerably reducing the amount of Cl atoms reaching the stratosphere where 90% of the ozone is located. Thus, HCFC's have a lower ozone depleting potential (ODP)[†] than CFC's. The same process also applies to HFC's with the added benefit that they do not contain any Cl or Br atoms and, as a result, HFC's are considered to have an ODP of zero. The main HFC's selected as replacement gas for CFC's are CF₃CFH₂ (134a), CF₃CF₂H (125), CHF₃ (23),

[†] ODP is an index used to determine the ozone depletion ability of a compound relative to CFC-11

CF_3CH_3 (143a) and CF_2HCH_3 (152a). An explanation of the numbering system used to label these compounds can be found in the Bibliography as Reference 6.

HFC-152a, which forms the basis of this study, has been proposed as a suitable replacement for Freon 12 as a refrigerant. It can also be used as a temperature sensing agent and an aerosol propellant. As these compounds become available for commercial, household and industrial purposes, it is imperative that both their chemical and physical properties are well known and understood.

VIII.1.1 *Previous Spectroscopic and Theoretical studies of R152a*

There have been numerous studies performed on 1,1 difluoroethane ranging from infrared absorption cross-section measurements⁷, calculation of barriers of internal rotation⁸ and photochemical reaction studies⁹. Of particular interest to this work are spectroscopic studies in the microwave and infrared regions and *ab initio* calculations.

In 1952, Smith *et al.*¹⁰ recorded the first low resolution infrared and Raman spectra of R152a. In their analysis, they assigned the band-types, calculated thermodynamic functions but reported no assignment of the modes of vibration. Two years later, initial estimates of the ground state rotational constants were determined when Solimene *et al.*¹¹ recorded the microwave spectrum of R152a. It wasn't until 1968 that Pylaeva *et al.*¹² after performing a similar study to that of Smith *et al.* calculated the first molecular force field constants.

In 1984, Guirgis *et al.*¹³ decided to reinvestigate the infrared and Raman spectra of 1,1 difluoroethane at low resolution. They performed a normal coordinate analysis and reported a comprehensive assignment of the modes of vibration of R152a as well as force field constants and calculation of thermodynamic properties. They did however express some reservation about their own assignments.

In an attempt to elucidate the assignment of the modes of vibration of R152a, Lucas *et al.*¹⁴ in 1993 performed *ab initio* molecular orbital calculations at the MP2/6-31...level. Two years later, Villamañan *et al.*¹⁵ performed a more extensive microwave study of R152a than that of Smith *et al.* in 1954. They obtained highly accurate estimates of the ground state spectroscopic constants and of four undetermined excited states, as well as structural parameters obtained from *ab initio* calculations. A year later, McNaughton and Evans¹⁶ recorded the first jet-cooled Fourier transform infrared

spectrum of 1,1 difluoroethane at high resolution. In their study, they also recorded gas-phase Raman spectra and performed high level *ab initio* calculations in order to help resolve some ambiguities in the vibrational assignment. The assignment and analysis of the fine structure in the high resolution jet-cooled spectrum yielded accurate spectroscopic constants for the ν_5 and ν_{16} modes. To date, these are the only bands that have been studied at high resolution.

In 1999, Tai *et al.*¹⁷ combined experimental absolute infrared and Raman intensity measurements with those of *ab initio* calculations in order to provide a new or revised assignment of the vibrational modes of some common HFC's. Their results on R152a were in total agreement with that of McNaughton and Evans¹⁶ with the exception of some calculated frequencies and intensities. Finally, in 2000, McKean¹⁸ performed high level *ab initio* calculations on a series of fluorinated ethanes and reported harmonic force field constants. They proposed that the neighbouring ν_8 and ν_{15} bands of R152a had been misassigned by McNaughton and Evans.¹⁶

In this study, 1,1 difluoroethane has been collisionally-cooled in an Enclosive Flow Cooling chamber and its mid-infrared spectrum recorded at high resolution between 900 and 1500 cm^{-1} with a Fourier transform spectrometer. Spectral lines belonging to the fine structure of the weak ν_4 band of R152a were measured, assigned and analysed. The data were fitted to Watson's A-reduced Hamiltonian for asymmetric molecules using a non-linear least-squares program for asymmetric tops written by Pickett.¹⁹

VIII.2 Experiment

Commercial-grade R152a was collisionally-cooled in an enclosive-flow cooling cell and its mid-infrared spectrum was recorded using a Fourier transform spectrometer between 900 cm^{-1} and 1500 cm^{-1} . 20 scans were co-added to generate a survey spectrum of R152a at a resolution of 0.1 cm^{-1} while 200 were co-added for the high-resolution spectrum at a resolution of 0.0019 cm^{-1} yielding a signal-to-noise of 35:1. The best results were obtained with a buffer-to-sample gas mixing ratio of 20:1, a cell temperature ranging from 190 K to 210 K, and a cell pressure of less than two Torr at slow pumping rates.

VIII.3 Results, Analysis & Discussions

CHF_2CH_3 is a near-oblate asymmetric top molecule belonging to the C_s symmetry point-group (see Appendix B for C_s character table) with the asymmetry parameter, κ , equal to 0.75. Being a non-linear molecule it possesses $(3N-6)$ 18 modes of vibration, and the fundamental transitions of these modes belong to two symmetry species labeled a' , *A/C-type* bands, or a'' , *B-type* bands (see Table VIII.2). These band-types result from a change in the dipole moment about the *A* and *C*, and *B* axes respectively, and have distinguishing spectral features: the *A/C-type* bands being characterised by the presence of sharp central *Q-branches* while *B-type* bands are characterised by 'equally' intense *P*, *Q* and *R* branches. The *A* and *C* type band can be further differentiated by the relative intensity of the *Q-branch* with respect to neighbouring *P* and *R* branches with the *C-type* bands having a more intense *Q-branch*. As can be observed from the low-resolution spectrum in Figure VIII-1, this region is quite congested since 8 of the 18 modes absorb in the spectral window investigated: $\nu_4 - \nu_8$ and $\nu_{14} - \nu_{16}$ assigned as per McNaughton and Evans.¹⁶ Most of the band-types were easily assigned: ν_4 and ν_7 are *C-type*, ν_5 is *A-type*, ν_6 is unclear while the remaining bands are *B-type*. This band-type assignment further confirms the assignments of McNaughton and Evans¹⁶ but not the alternate assignment proposed by McKean.¹⁸ An additional band (indicated in red) believed to be the $\nu_9 + \nu_{17}$ combination band was also observed.

The jet spectrum of McNaughton is compared to the EFC spectrum recorded in this study in Figure VIII-1 depicting, on one hand, the superior cooling ability of the jet technique but, on the other hand, revealing the superior sensitivity of the EFC technique in the study of weak transitions. The superior rotational cooling of the jet technique is emphasised by the presence of the ν_8 band, which become completely masked by *R-branch* of the ν_{15} band in a warmer environment such as the one present in the EFC cell. However, bands such as the ν_4 , ν_6 and ν_7 which are slightly discernible in the jet spectrum, form well-developed structures in the collisionally-cooled EFC spectrum.

So far, the ν_5 , ν_{15} and ν_{16} have been studied but only the ν_5 and ν_{16} have been analysed as the ν_{15} has been reported to be highly perturbed.¹⁶ Since these bands had already been examined, the focus of the study was to enhance the *S/N* ratio of the weaker transitions in this region of the spectrum in order to study them. In an attempt to improve the *S/N* ratio the sample partial pressure was increased so as to saturate the

signal of the stronger absorbers in this region; bearing in mind the pressure 'limit' imposed by pressure-broadening effect, operating cell pressures did not exceed 4 Torr. However, at low operating temperatures ($\sim 110-130$ K) and high mixing ratios ($> 30:1$), clustering was observed, and found to increase with sample pressure. It was thus decided to raise the cell temperature, and reduce the sample pressure and mixing ratio accordingly. Enhancement of the S/N ratio of the weaker fundamental bands (as clearly observed in Figure VIII-1) was achieved at cell temperatures around 200 K, sample pressures below 2 Torr and mixing ratios $< 20:1$. Due to its stronger S/N ratio, the ν_4 band of R152a located at 1456.9 cm^{-1} was selected for this study.

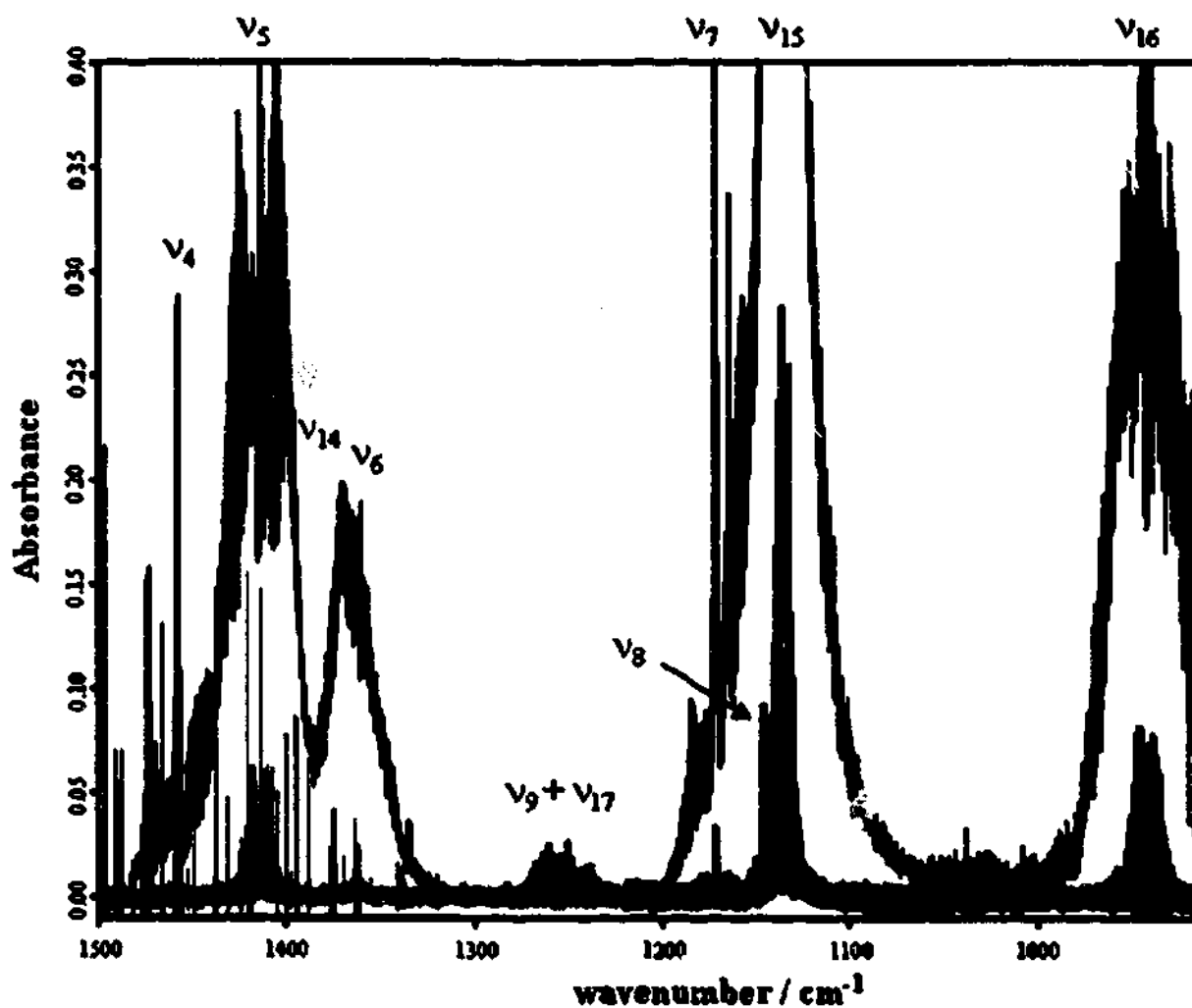


Figure VIII-1 Absorbance spectra of R152a in both a supersonic expansion (green) and an enclosive flow regime (multicoloured). Transitions depicted in cyan are those analysed in McNaughton's jet-study while the remaining bands have been observed at high resolution in this study.

Table VIII-2 Wavenumber value of vibrational modes of R152a observed by Evans.²⁰

mode	cm ⁻¹	mode description	mode	cm ⁻¹	mode description
<i>a'</i>			<i>a''</i>		
v ₁	3016	CH ₃ asym. stretch	v ₁₂	3001	CH ₃ asym. stretch
v ₂	2975.2	CH stretch	v ₁₃		CH ₃ asym. deformation
v ₃	2958.5	CH ₃ sym. stretch	v ₁₄	1364.1	CCH bend
v ₄	1456.9	CH ₃ sym. deformation	v ₁₅	1134.9	CF ₂ stretch
v ₅	1413.2	CC stretch	v ₁₆	941.7	CH ₃ rock
v ₆	1359.7	CCH bend	v ₁₇	390.5	CF ₂ twist
v ₇	1171.1	CF ₂ stretch	v ₁₈	221	CH ₃ torsion
v ₈	1145.1	CF ₂ stretch			
v ₉	868.7	CH ₃ rock			
v ₁₀	569.9	CF ₂ bend			
v ₁₁	470.1	CF ₂ wag			

A section of the high-resolution spectrum showing the ν_4 band is displayed in Figure VIII-2a) along with a simulated spectrum using a rigid-rotor model in Figure VIII-2b). The band-origin of the simulated spectrum was altered until the first sets of *J*-stacks in both the *P* and *R* branches could be superimposed with those of the observed spectrum. Good agreement between the simulated and observed spectra was obtained for the first few *J*'s as could be expected from a rigid-rotor mode, thus enabling easy assignment of the rotational quantum number, *J*. This agreement can be clearly observed in Figure VIII-2a) and b). A simulated spectrum with a rotational temperature of 200 K was found to best fit the *P* and *R* intensity profile of the ν_4 band of R152a.

Loomis-Wood plots using MacLoomis, program written by McNaughton *et al.*²¹, were used to determine the K_c assignment. Although designed for linear Hamiltonians MacLoomis is quite useful and even indispensable in the assignment of the *K* quantum numbers of asymmetric-tops. A Loomis-Wood plot of the ν_4 band of R152a is displayed in Figure VIII-3 showing the $K_c=0,1,3$ and 4 series (see Section **Error! Reference source not found.** a more detailed description of Loomis-Wood plots).

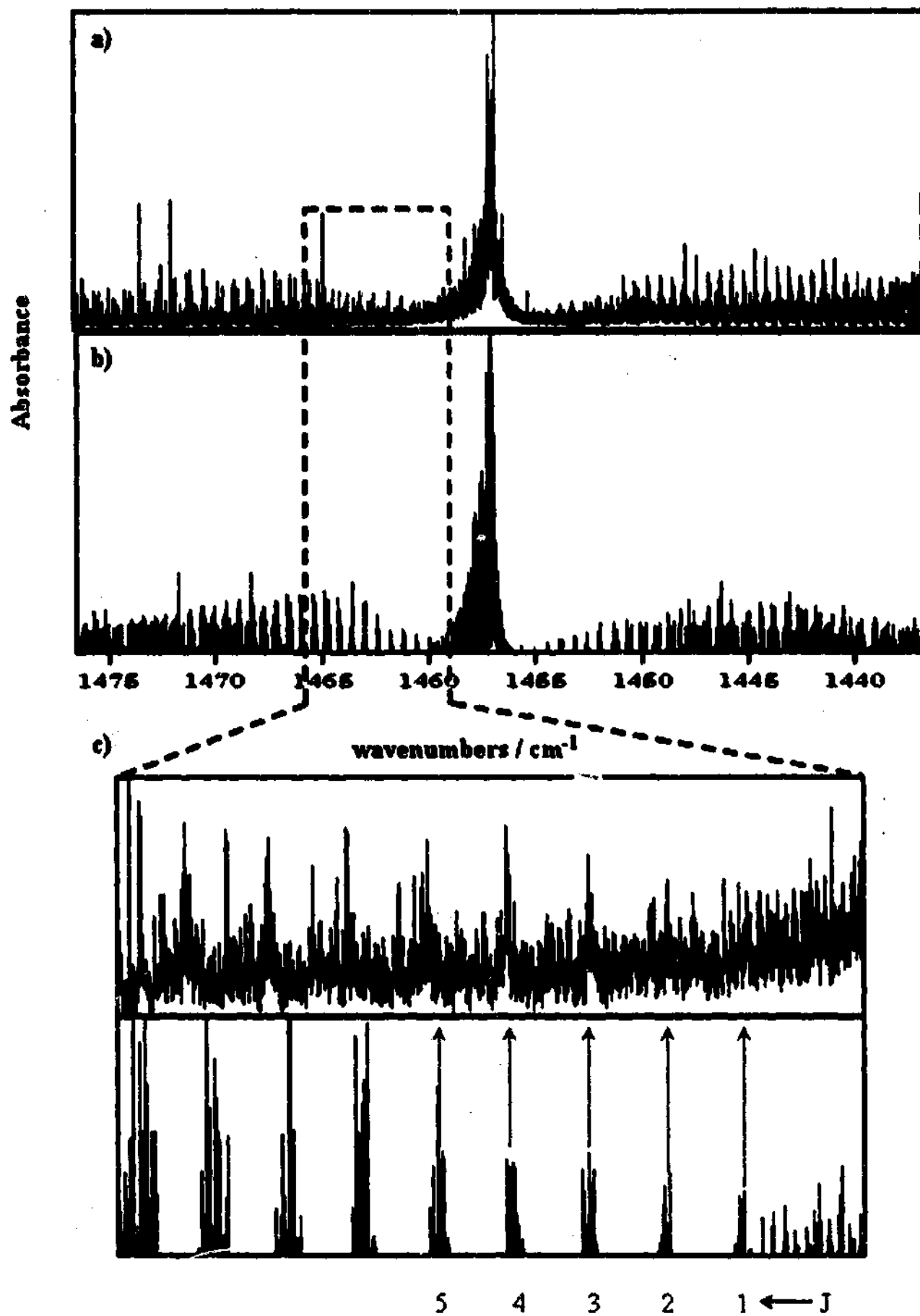


Figure VIII-2 a) High-resolution spectrum of the ν_4 (*C-type*) band of R152a.
 b) Simulation of a *C-type* band of an asymmetric-top molecule using a rigid rotor model centered at the band-origin of the ν_4 band of R152a.
 c) A small section of the band has been expanded to show the agreement between the simulated and observed spectra at low J-values despite the use of a rigid-rotor model for the predictions.

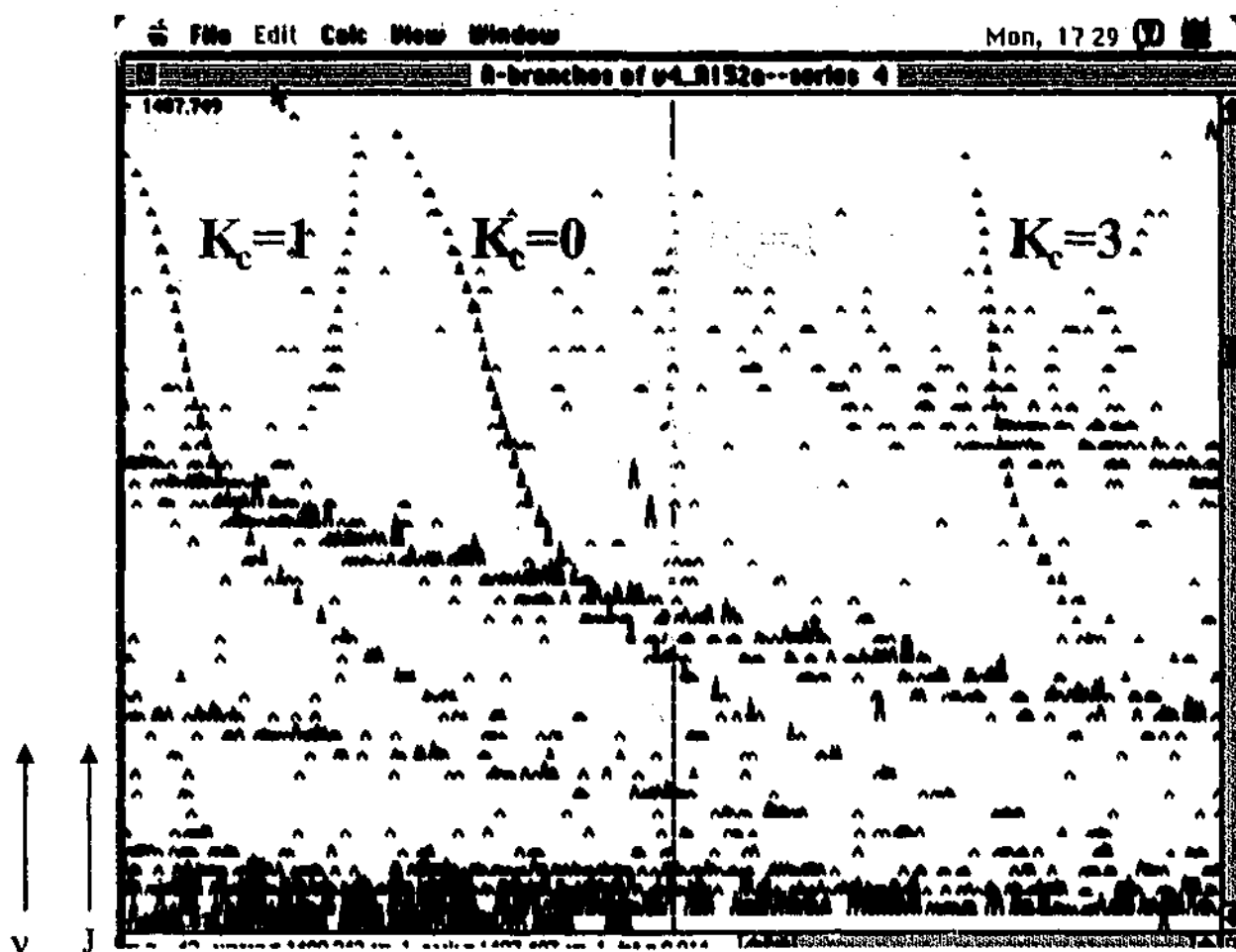


Figure VIII-3 Loomis-Wood diagram generated by MacLoomis showing K_c -patterns of the ν_4 band of R152a.

VIII.3.1 Data Analysis & Discussions

Transitions belonging to the ν_4 band were measured using the Peak-pick function of OPUS 3.1, a software package that controls the FT spectrometer. Some 900 transitions belonging to the ν_4 band were assigned with $J = 2$ to 46 and $K_c = 0$ to 16. Estimates of the molecular parameters of the ν_4 vibrational mode of R152a were obtained by fitting the observed transitions to the A-reduced Hamiltonian of Watson for asymmetric rotors in a weighted least-squares fashion using a program written by Herbert Pickett,¹⁹ SPFIT (see Chapter II for a brief description and reference). In order to assess the J quantum number assignment of the ν_4 band, Ground State Combination Differences (GSCD's) were calculated using the ground state constants of Villamañan *et al.*¹⁵ and compared to those 'observed' in this study (see Appendix C for sample GSCD calculations).

Prior to fitting the data, all resolved transitions were assigned an initial uncertainty, *unc*, of 0.0005 cm^{-1} (roughly 2 standard deviations or 20% of the observed linewidth) which is then weighted according to $weight = 1/unc^2$; blended or 'shoulder' transitions were assigned an uncertainty of 0.005 cm^{-1} . The weighted transitions were subsequently fitted to one isolated excited vibrational state, ν_4 , while the ground vibrational state constants were constrained to Villamañan's¹⁵ values obtained from their extensive microwave study. In the initial stage of the data reduction procedure, only the inertial rotational constants were fitted yielding a standard deviation, σ , of 200. Quartic, followed by higher order Centrifugal Distortion Constants (CDC's) were progressively added to reduce the standard deviation of the fit as is customary in fitting procedures. Any attempts at obtaining well-determined (*i.e.* small uncertainties) mechanically consistent first order CDC's (*i.e.* quartic terms > 0) during these initial fits proved impossible as they yielded standard deviations of the order of 30. At this stage, the only way to reduce σ to a more 'reasonable' value of 8.6 was to fit the data to sextic and octic CDC's. The effective ν_4 spectroscopic constants obtained in this fit are listed in Table VIII-3. The use of these constants to predict the line positions will result in transitions being predicted with uncertainties of 0.0044 cm^{-1} (or roughly 18σ 's).

The need to include sextic and octic centrifugal distortion terms to fit transitions with $J < 47$ combined with the unrealistically large magnitude of the CDC's and the minimum attainable standard deviation of 8.6 is highly indicative of the presence of a perturbation from a neighbouring fundamental, overtone or combination state. Such a state is referred to as a 'perturbing' state, and sometimes a dark state if no transitions to that state are observed (in reality, transitions to the dark state are present but are just far too weak to be detected). In either case, the states involved can interact via Fermi or Coriolis interactions leading to either local or global perturbations of levels of the states involved. In general, Fermi interactions can result in both vibrational and rotational perturbations while Coriolis interactions only affect the rotational levels. The conditions for these types of interactions are dictated by the symmetry of the states involved, and Jahn's rule for Coriolis interactions (see Section I.3).

Generally, global rotational perturbations due to Fermi or Coriolis resonances lead to changes in the inertial rotational constants of the states involved. Thus, even in the absence of transitions to a perturbing dark state, its inertial rotational constants can be determined from the transitions of the perturbed bright state. Loo *et al.*²² and Evans²⁰ have successfully performed fits of this type.

Initial attempts to fit the observed transitions to the ν_4 state and a dark state coupled via Fermi resonance interactions proved to be quite unsuccessful as the magnitude of the fitted first order Fermi constant, F' , changed dramatically from one iteration to another in a single fit. In addition, only a subset, $J < 20$ of the data could be fitted reasonably with a standard deviation of 4.8. Inclusion of transitions with J up to 30 resulted in a standard deviation of 32 accompanied by large changes in the magnitude of the Fermi constant and the inertial rotational constants of the dark state.

Fits to an a -Coriolis coupled dark state were not only stable but, also, generated CDC's of similar magnitude to those of the ground state and yielded a σ value of 2.19. In addition, only three CDC's were fitted with all remaining constants of the bright state fixed to the ground-state values, and only the band origin and the three inertial rotational constants of the dark state were fitted. Inclusion of additional CDC's in the model did not improve the fit, however, these newly fitted parameters were determined with less than 10% uncertainty but at the cost of raising the uncertainty of other CDC's by a factor of roughly 10. They were thus kept constrained to the ground state values in the final fit.

The spectroscopic constants of the ν_4 state along with those of the ground and dark states are displayed in Table VIII-3. The relative magnitudes of the ν_4 and ν_{13} inertial rotational constants obtained from the dark state fit are consistent with the observations of the 3-D simulation of the unperturbed modes where the hydrogen atoms move further from the A-axis in the ν_{13} than they do in the ν_4 mode. As a result, the expected A -value for the ν_{13} is expected to be smaller than its symmetric counterpart. This finding seems to support the claim that the dark state may be the ν_{13} state.

Attempts to further reduce the standard deviation using higher order Coriolis interaction terms were unsuccessful. This may indicate the presence of another 'lurking' dark state interacting with the ν_4 symmetric deformation. Figure VIII-4 shows the residual plot for transitions with $K_c=0-5$ (which become degenerate at high J 's). These plots clearly show that the present model does not adequately represent the observed data beyond $J=37$ for $K_c=0-5$ which further indicate that some type of interaction has not been accounted for. This behaviour is not observed for transitions with higher K_c -values although no transitions with $J>37$ are observed for $K_c>5$. There is however, good agreement between the fitted CDC's of the ν_4 state and their constrained counterparts of the ground state.

Although the overall quality of the fit is reasonable, the parameters obtained in this study cannot be assigned with absolute certainty to the global minimum of the potential energy surface of that mode and, therefore, represent at the very least a local minimum in the potential. In addition, the use of these parameters for prediction of transitions with rotational quantum numbers beyond the range of observed ones is not advised since in some instances as depicted in Figure VIII-4 where the magnitude of the residuals increases with J . The use of parameters listed in Table VIII-3 will enable reproduction of the observed data to within 0.0011 cm^{-1} (or 4.5σ 's) for $J \leq 46$ and $K_c \leq 16$.

Table VIII-3 Molecular constants of the ν_4 state obtained from fitting 922 transitions to Watson's A-reduced Hamiltonian for asymmetric rotors. The ground-state constants were constrained to values obtained by Villamañan.¹⁵ Parameters with the label 'C' have been constrained to the ground-state values during the fits. Values obtained from the isolated fit are displayed again for easy comparison with the dark state fit.

		Ground State		ν_4 state		ν_{13} state	
		Isolated Fit		Dark state Fit		Dark state Fit	
Diagonal Matrix Parameters		Value / cm^{-1}					
T			1456.85482	1456.850631 (49)		1451.0441 (32)	
A		0.316618425	0.3196942	0.3180442 (60)		0.313890 (15)	
B		0.298964584	0.2999833	0.29997034 (48)		0.2987124 (61)	
C		0.172467785	0.1724494	0.1726488 (11)		0.174264 (18)	
Δ_J	$\times 10^{-08}$	15.8505	-122.54	16.909 (63)		C	
Δ_{JK}	$\times 10^{-08}$	6.03364	181.10	C		C	
Δ_K	$\times 10^{-08}$	9.71422	93.70	19.18 (13)		C	
Φ_{JJJ}	$\times 10^{-13}$	2.537	-6508.7	C		C	
Φ_{JJK}	$\times 10^{-13}$	-3.231	5088	C		C	
Φ_{JKK}	$\times 10^{-13}$	5.200	6168	C		C	
$\Lambda_{\delta KKK}$	$\times 10^{-14}$		-1.072				
Λ_{KKKK}	$\times 10^{-14}$		2.57				
		Ground State		ν_4 state		ν_{13} state	
		Isolated Fit		Dark state Fit		Dark state Fit	
Off-Diagonal Matrix Parameters		Value / cm^{-1}					
δ_J	$\times 10^{-08}$	5.764505	87.9742	C		C	
δ_K	$\times 10^{-08}$	15.50316	10.674	12.5 (11)		C	
ϕ_J	$\times 10^{-13}$	1.204	4202.6	C		C	
ϕ_K	$\times 10^{-13}$	18.5065	-393	C		C	
Coriolis Interaction Parameters							
$\xi_{4,13}^a$				0.10136 (19)			
$\eta_{4,13}^{bc}$	$\times 10^{-3}$			0.6710 (60)			
Std Dev			8.6			2.2	
RMS error / cm^{-1}			0.017			0.0011	

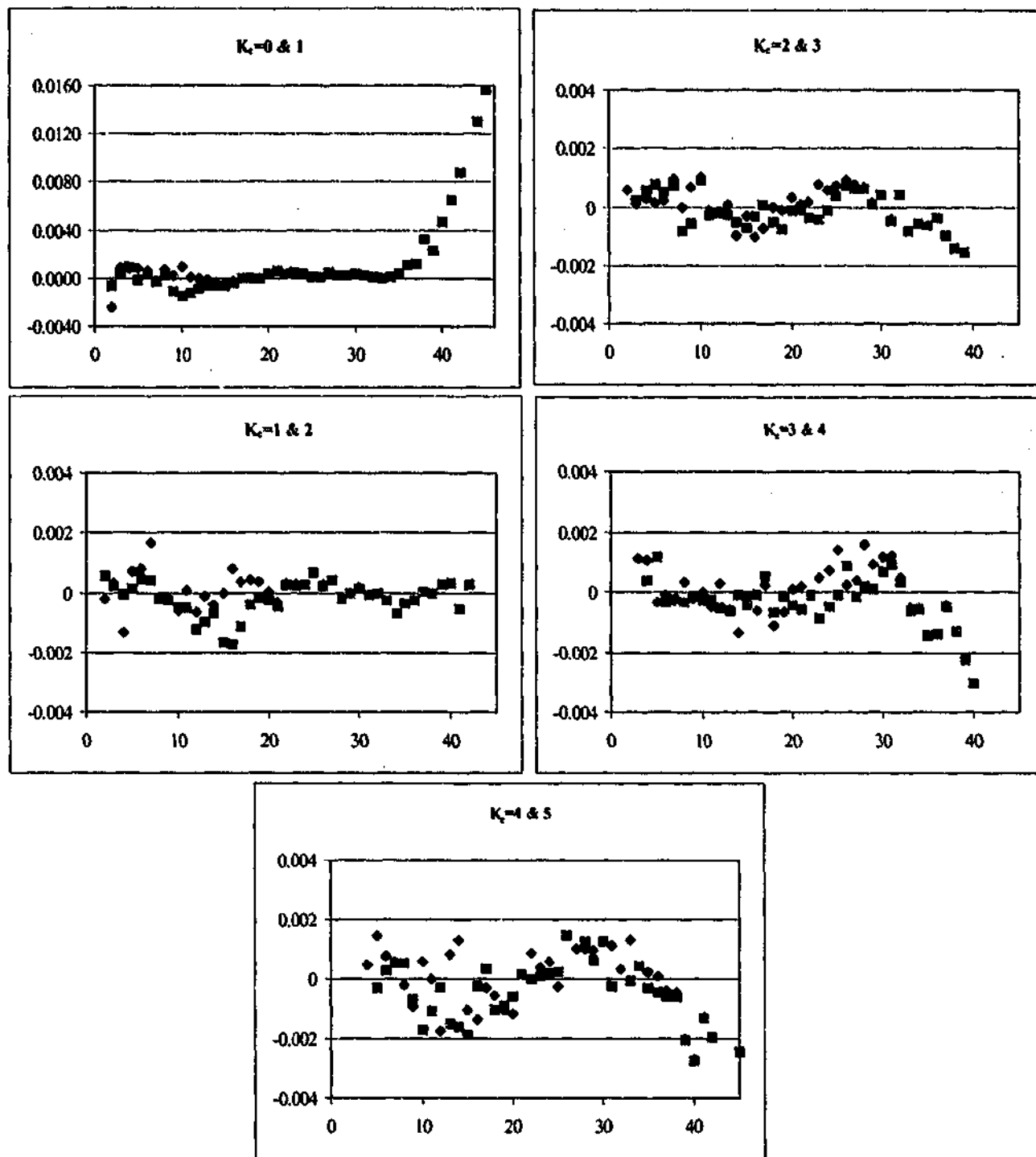


Figure VIII-4 Residual plots for transitions up to $J=45$ and $K_c < 6$. Some definite trends can be observed for all cases shown except for the pair where $K_c=1$ and 2. These residual plot trends are most certainly due to some unaccounted interaction.

Characterisation of the dark state

The band origin of the dark state was estimated at $1451.0441 \text{ cm}^{-1}$. Using the values of the fundamentals determined by Evans²⁰ and listed in Table VIII-2, the best candidates for the dark state are the ν_{13} (a'') state estimated $\sim 1460 \text{ cm}^{-1}$ and the $\nu_{10}+4\nu_{16}$ (a') combination state estimated at 1453 cm^{-1} respectively (although the combination band is expected to be a few wavenumbers to the red due to anharmonic contributions). The fitting procedure described in the previous Section revealed that the two states are coupled via an a -Coriolis interaction. Since a state belonging to the a' species can only couple to another state belonging to the same species via a b -Coriolis interaction, the combination mode can be ruled out as a candidate for the dark state. Both a -Coriolis and c -Coriolis interactions can only occur between modes of different species of C_s symmetry, thus, the ν_{13} (a'') state seems an appropriate choice for the dark state. However, the fact that it is located at lower wavenumber value than its symmetric counterpart raises concern about its assignment as previous molecular orbital calculations place the ν_{13} state above the ν_4 state.

Newly run *ab initio* calculations using Gaussian 98²³ by Dr. Evan Robertson at a higher level of theory than Evans²⁰ (MP2/6-311+ G(d,p)) show that the asymmetric mode is located to the red of its symmetric counterpart. A density functional theory calculation with the same basis set, however, indicates that the ν_{13} mode is located at higher energy than the ν_4 mode. The values of the band origins are reported in Table VIII-4. No scaling of the newly calculated values was performed as the focus of these calculations was on the relative location of the modes rather than their absolute values. The only agreement between the calculations is the fact that these two mode lies very close to each other and, on a theoretical basis, the asymmetric deformation can lie to the red of the symmetric deformation. Thus, the ν_{13} state cannot be discounted as a candidate for the dark state which lies less than 6 cm^{-1} to the red of the ν_4 state.

Table VIII-4 Experimental and unscaled *ab initio* values for the band origins of the symmetric, ν_4 , and asymmetric, ν_{13} , deformation modes of R152a. The numbers in brackets are the IR intensities, ^a values obtained by Evans²⁰

	jet study ^a	this study	MP2/6-311 G(d,p) ^a	MP2/6-311+ G(d,p)	B3LYP/6-311+G(d,p)
ν_4	1456.9	1456.850631	1461(6.4 km/mol)	1506.7(5.2 km/mol)	1483.7(5.1 km/mol)
ν_{13}		1451.0441	1464(0.001km/mol)	1505.6(0.5 km/mol)	1484.1(1.5 km/mol)

VIII.4 Conclusions

This study has conclusively shown that the EFC technique coupled to FT spectroscopy is a highly sensitive technique well-suited for the high-resolution spectroscopic study of gases which are weak infrared absorbers or of weak modes of strong infrared absorbers. The EFC technique has proven superior to supersonic expansions in the spectroscopic study of weak IR transitions. The low resolution spectra recorded using the EFC technique have confirmed Evans' assignment of the ν_8 and ν_{15} bands, and subsequently, raised doubt over McKean's assignment. Similarly to N_2O , thermodynamic equilibrium seems to have been reached as the cell-temperature (180-200 K) is roughly equal to the rotational temperature.

Rotational cooling provided by the EFC technique though not as effective as supersonic expansions has still enabled easy assignment of the rotational transitions of the ν_4 band of R152a. Initial analysis of the ν_4 transitions has revealed the presence of a global perturbation as shown by the inability to fit the data in the isolated fit and, also, the absence of local rotational perturbation in the Loomis-Wood plots. Further analysis has shown that this perturbation can be partially accounted for by an a-type Coriolis interaction with a dark state. The $\nu_{10} + 4\nu_{16}$ and ν_{13} states were the two most likely candidates due to their close proximity to the ν_4 state. Using symmetry arguments, it is believed that the IR dark ν_{13} state is the most likely candidate for the source of this perturbation. This study has as a result produced the first estimates of the location of this IR dark mode, as well as first estimates of its inertial rotation constants. However, despite the 'deperturbation' treatment, the ν_4 state is believed to be still under the influence of some further but much weaker perturbation as observed by the trends in the residual plots and the magnitude of the inertial constants relative to those of the ground state. Thus, the reported constants are still effective constants.

IX Appendix

IX.A Safety Issues

During the course of the studies undertaken for the thesis, numerous hazards associated with equipment and chemicals used have been identified, and appropriate measures taken to minimise the health risks resulting from these hazards. Among the various equipment used in the studies undertaken, the ones which pose the highest health risk are the high voltage power supply (0-18kV/0-8mA) used in the corona excited supersonic expansion experiments, and the Class 4 infrared laser used in the infrared laser powered pyrolysis experiments. While most chemicals used are potential health hazards, special attention has been given to the handling of chemicals such as cyanogen bromide, sodium azide, cyanogen azide and liquid nitrogen.

IX.A.1 Equipment

IX.A.1.1 Corona Discharge power supply

The main health risk in this case is electrocution. The following steps were taken to minimise the health risk and, thus, ensure safe operation of the high voltage power supply:

- ✓ a heavily insulated lead was used to connect the corona discharge electrode to the high-voltage source
- ✓ a grounded pointer attached to an insulated handle provided a means to 'discharge' the electrode before any alteration to the experimental conditions was performed
- ✓ a visible 'High Voltage' sign was erected near the power supply
- ✓ the power supply was placed as far as possible from throughfare passages, as well as other instruments
- ✓ use of the 'Buddy-system' whereby a peer, friend or supervisor maintained regular contact during operation of the power supply

IX.A.1.2 CO₂ laser

The principal concern when using lasers is the damage caused to biological tissues. Although damage to skin tissue has a higher probability of occurrence, protection of the eye is of greater importance as some lasers may cause instant blindness upon exposure, even more so in this case as the CO₂ laser is invisible! High powered lasers are also potential fire hazards. In accordance with the requirements specified by the Australian/New Zealand Standard (AUS/NZS 2.211) lasers are categorised in four classes, I to IV, according to the degree of potential health hazard. Thus, a Class IV laser presents the hazard. The infrared (10.6 μm) CO₂ laser used in the infrared laser powered pyrolysis experiments is a Class IV laser mainly due to its high output power (40W). As $l > 1.4\text{mm}$ are absorbed by the corneal tissue, the retina is not at risk as these l never reached it. However, damaged to the cornea will occur if enough radiation is absorbed by tissue water and tear to cause the temperature rise and subsequent denaturation of proteins in the corneal tissue. Similar processes will also cause the skin to burn. At high power, potentially flammable materials are at risk if exposed for more than a few seconds.

The following steps have been taken to minimise health risks

- ✓ Laser protective eyewear absorbing at 10.6mm
- ✓ Long sleeve garment
- ✓ Optics with infrared antireflection coating
- ✓ Firebrick as a beam stopper
- ✓ Wooden cover enclosing the laser path
- ✓ Warning lights indicating operation of a class IV laser

IX.A.1.3 Glassware

Explosions can result from unintentional chemical reactions or occurrences of high pressure.

Precautions

- ✓ Use of gas at low pressures (*i.e.* < 1 - 1.5 atm)
- ✓ All glassware used as container vessels have been wrapped with a plastic mesh and electrical tape to contain glass debris.

IX.A.2 Chemicals

Liquid N₂

The major concern when using liquid N₂ is large quantity spillage in a closed environment which would have the consequence of reducing the amount of O₂ in the air as well as increasing the amount of nitrogen, both potentially causing asphyxiation. A properly ventilated area in the lab was used.

BrCN¹

Cyanogen bromide, BrCN, is a white crystalline solid, which has a vapour pressure of 92 Torr at 20° C; its melting and boiling point temperatures are 50° and 61° C respectively. When absorbed by the body it is broken down to form the highly toxic cyanide. When exposed to heat, extremely toxic and corrosive chemicals are given off. It also reacts with water and water vapour to generate the flammable and toxic HCN; other decomposition products are HBr, carbon and nitrogen oxides. Inhalation or

ingestion of BrCN (<1.4ppm) can cause severe irritation and injury to the nose, throat and lung tissues. A prolonged exposure is life threatening.

In this work, roughly 0.2 g of BrCN was placed in a cell through which a carrier gas was flowed. After dilution by the carrier gas, the mixture was flowed through a cell containing a column of densely packed pulverised crystals of NaN_3 to generate N_3CN . The new gas mixture was then be probed by the IR source of a FT spectrometer and its IR spectrum recorded. Any leftover BrCN was destroyed using Lunn and Sansone's method² whereby a solution made from water and NaOH was prepared. Addition of 60g of $\text{Ca}(\text{OCl})_2$ per liter of solution of $(\text{BrCN}+\text{H}_2\text{O}+\text{NaOH})$ will then eliminate BrCN.

Precautions

- ✓ have the antidote, amyl nitrite, ready for use; to be administered as prescribed in MSDS by trained personnel.
- ✓ wear chemical protective gloves, coveralls and boots.
- ✓ take off any jewelry and watches and have a change of clothes and shoes ready.
- ✓ use "buddy" system.
- ✓ prepare solution for elimination of BrCN
- ✓ only operate at pressures under 1 ATM.

First-Aid

- ✓ Skin or eye contact: rinse thoroughly with lukewarm water for 15 to 20 minutes; remove contaminated clothing; get medical attention.
- ✓ Ingestion: rinse mouth thoroughly with lukewarm water for 15 to 20 minutes; drink 260 to 300 ml of water.

NaN_3

Sodium azide, NaN_3 , is a white crystalline solid with a vapour pressure of 7.5 mTorr at 20°C. Inhalation, ingestion or skin contact may be fatal thus, extreme care needs to be taken when handling this compound. Sodium azide may explode when subjected to mechanical and thermal shocks. It will react with most metals to form the highly explosive metal-azides, which are more sensitive than nitroglycerine. It will also react with acids, acid chlorides and metal halides to generate explosives compounds.

Surface particles of NaN_3 (<150g) will be activated with hydrazine hydrate (10 mls) in order to enhance its reaction with BrCN to generate N_3CN . In the process NaBr will be formed on the surface of the NaN_3 crystals. The azide can be recovered and reactivated by crystallisation from a saturated boiling aqueous solution with a few milliliters of hydrazine hydrate. Pouring the hot solution into excess acetone will cause NaN_3 to precipitate out.

Precautions

- ✓ Due to the high sensitivity and reactivity of sodium azide, no metal parts was exposed to the sample, and all material and equipment used to handle it will be brand new and unused.
- ✓ No metals or acids will be used.
- ✓ The original sample was pulverised to a fine powder by my supervisor, Dr. Don McNaughton, who was wearing a body and face shield as well as chemical resistant gloves and boots.

First-Aid

- ✓ In case of any contact wash affected area with copious amounts of water for 15 to 20 minutes while removing any contaminated items of clothing.
- ✓ If inhaled remove to fresh air.
- ✓ If ingested, wash out mouth with copious amounts of water.
- ✓ Get medical attention.

N_3CN^4

In its condensed phase, cyanogen azide, N_3CN , is a colourless oil, which detonates when subjected to mechanical and thermal shocks. As a result, this chemical should be used preferably in small amounts so as to reduce the risks associated with it.

In our experiments, it is expected that low amounts of cyanogen azide will be formed, as a flow through method will be used. This method involves flowing $BrCN$ diluted by a carrier gas through a column of finely powdered particles of NaN_3 , thus, ensuring that the newly formed azide will only be present in dilute amounts. Gaseous mixtures containing cyanogen azide will not be trapped to ensure that no condensation of this compound occurs. After its formation, N_3CN will be probed by an IR source of an FT spectrometer in a multipass cell and then pumped out. In some experiments, N_3CN will be used as a precursor to generate transient species in a corona discharge.

Precautions

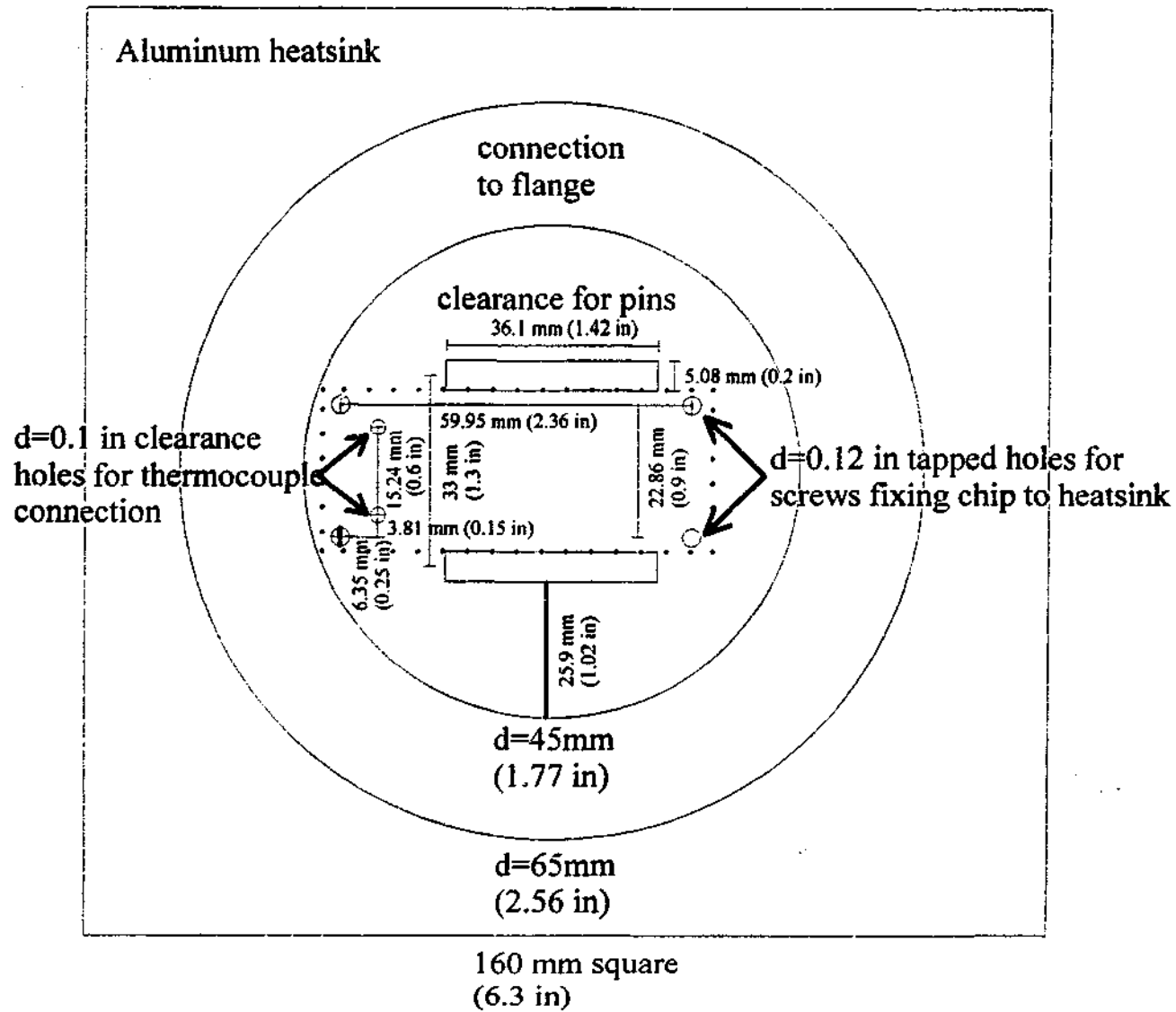
There will be no trapping of this compound.

IX.B Technical Drawings

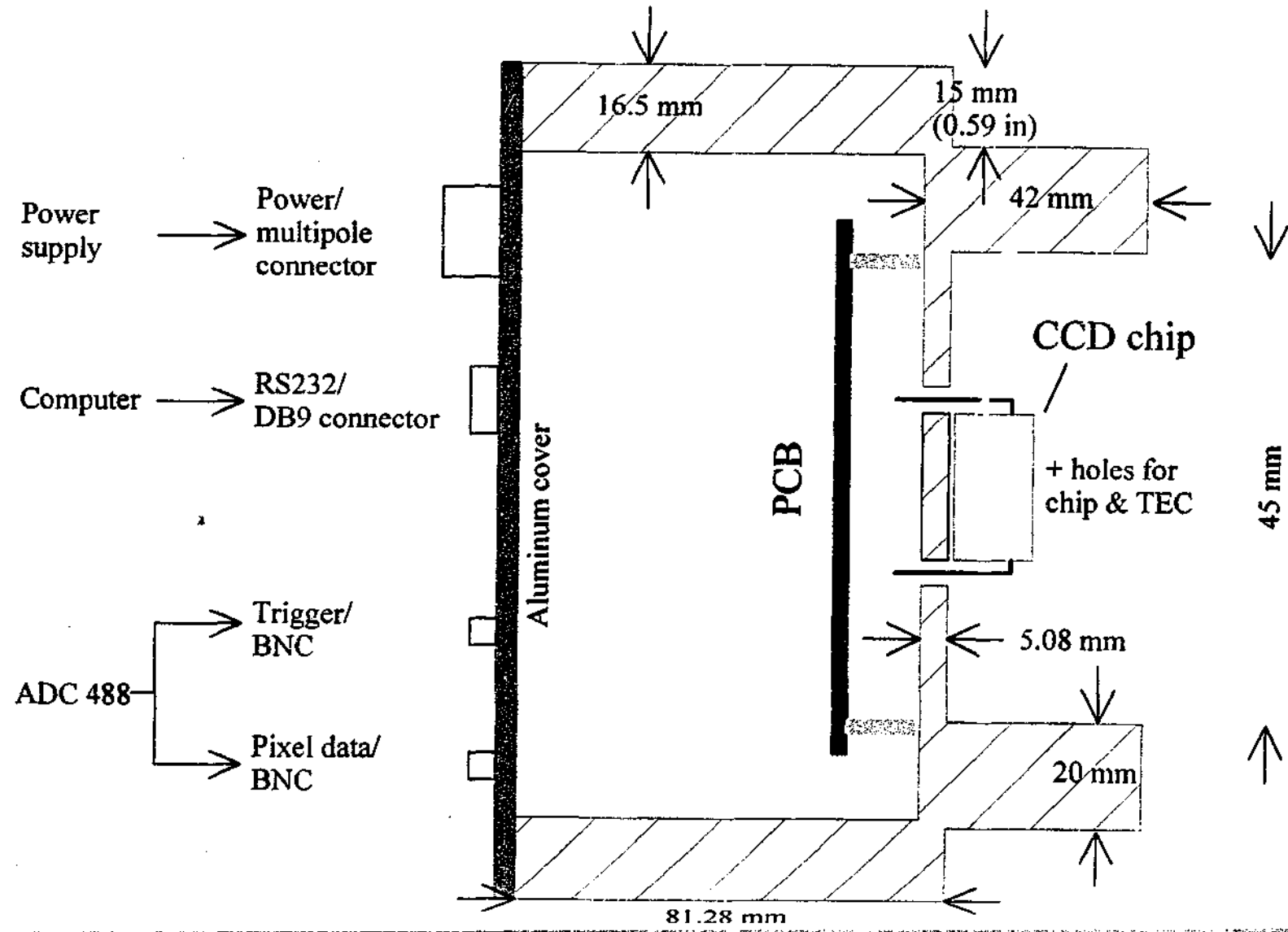
IX.B.1 *CCD detector*

SEE FOLLOWING PAGES FOR SCHEMATIC DIAGRAMS

Schematic drawing of CCD housing showing view where CCD chip is mounted

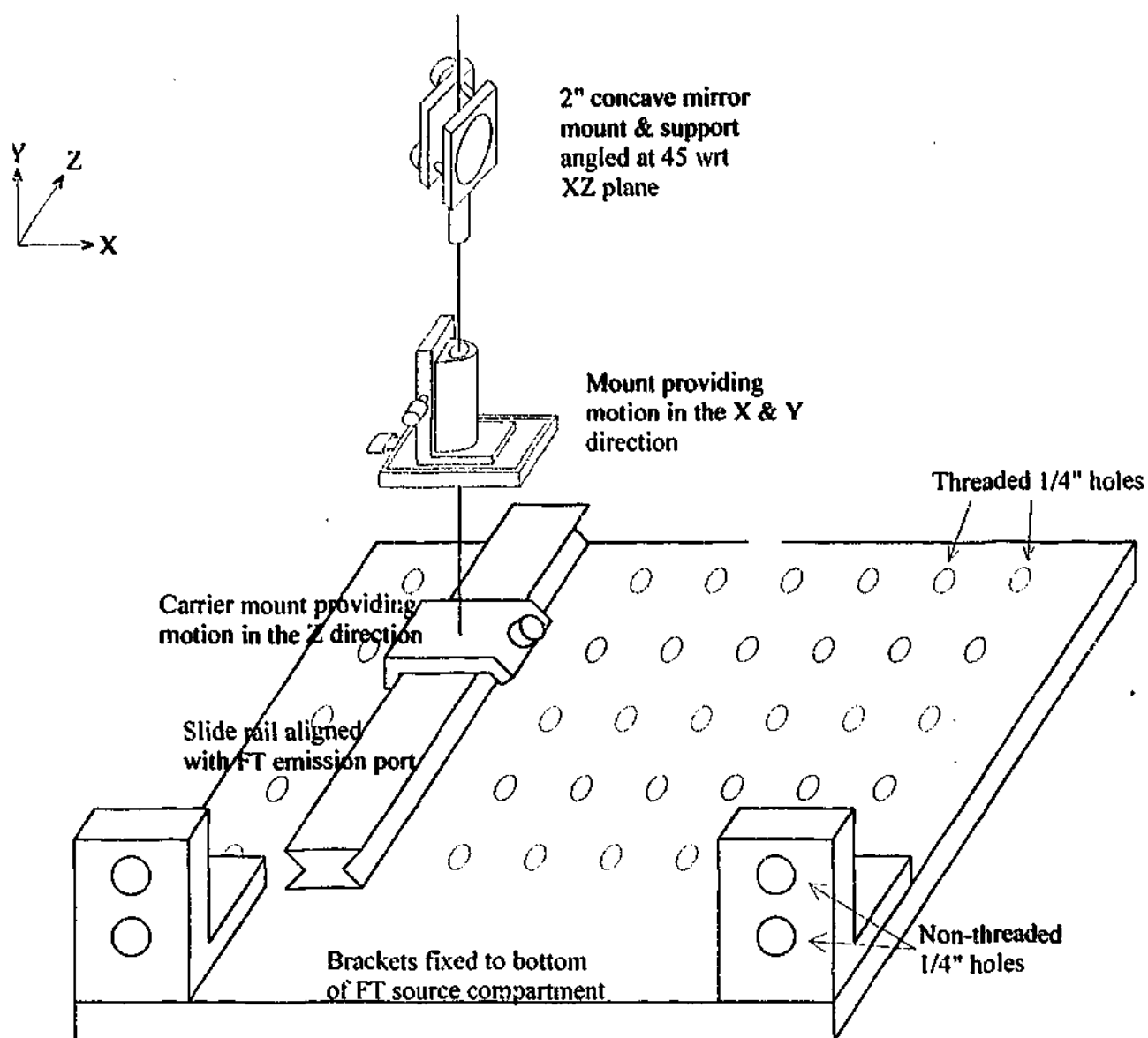


Schematic drawing CCD housing showing a side-view of the detector

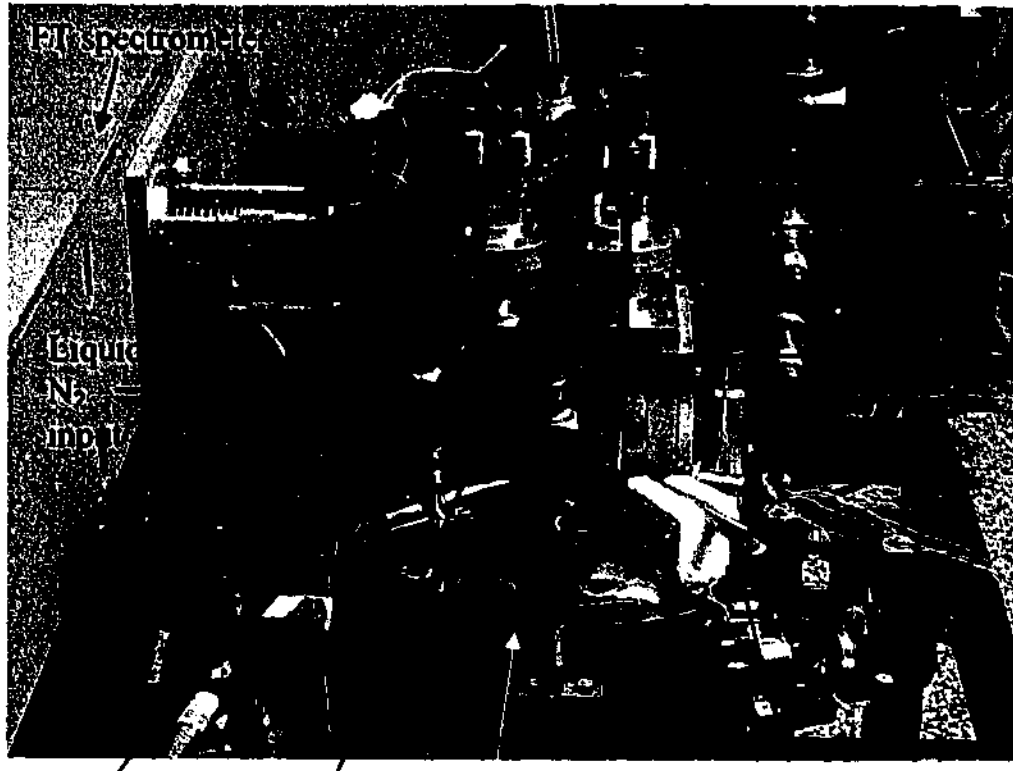


Not Suitable For Microfilming

Schematic drawing of FT emission port design



IX.B.2EFC system



Flange B

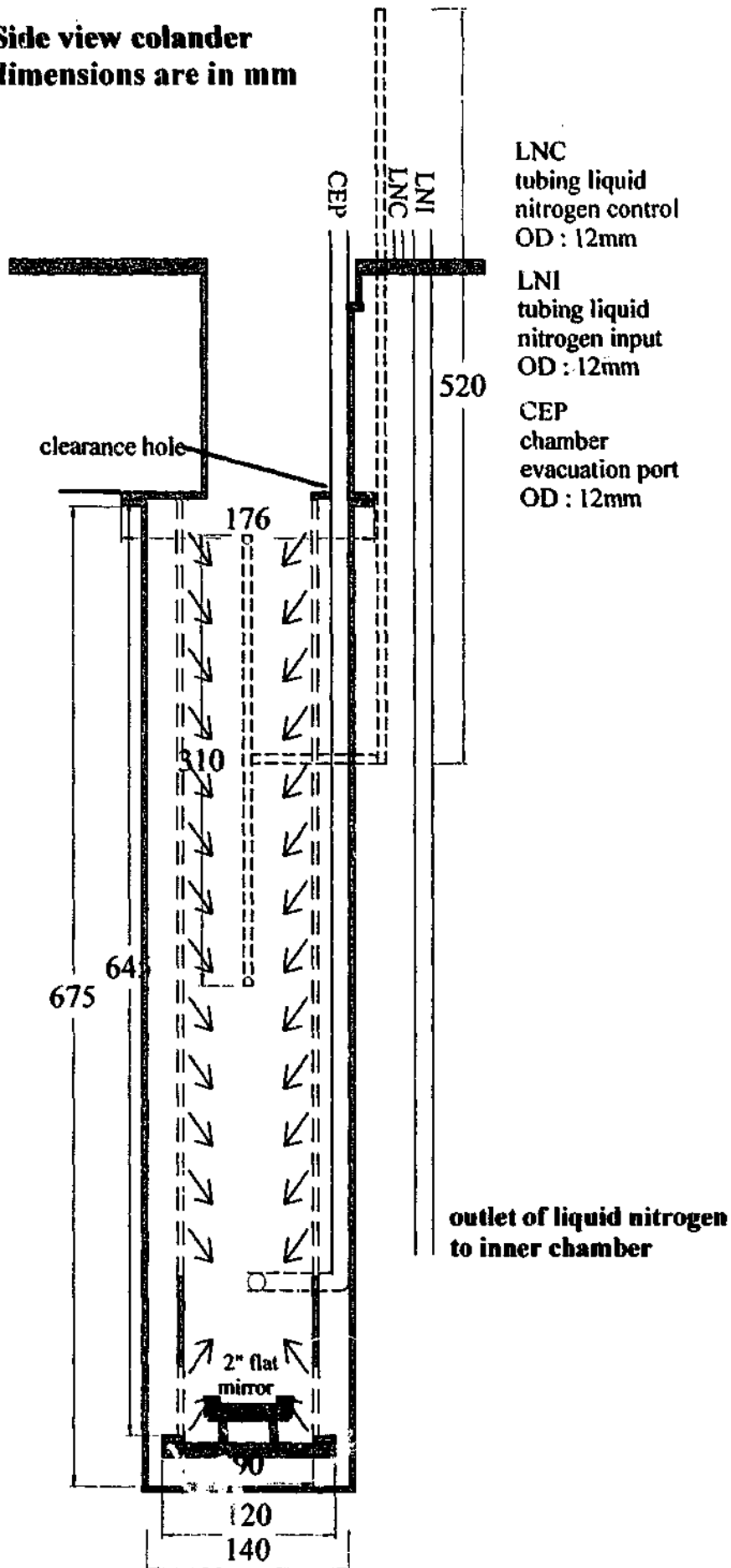
Transfer
Optics Box

Vacuum
chamber

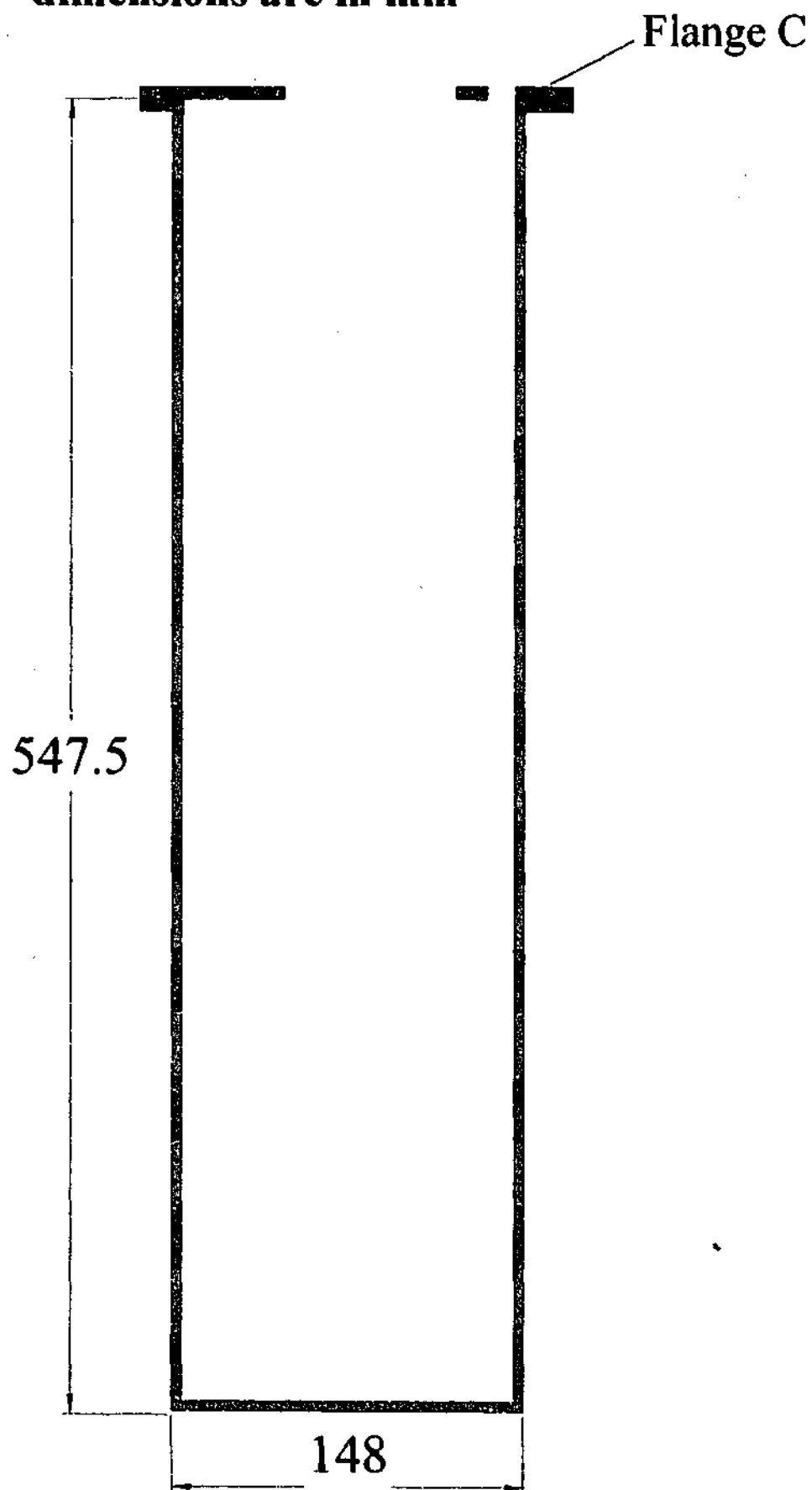
Exhaust to
pump

SEE FOLLOWING PAGES FOR SCHEMATIC DIAGRAMS

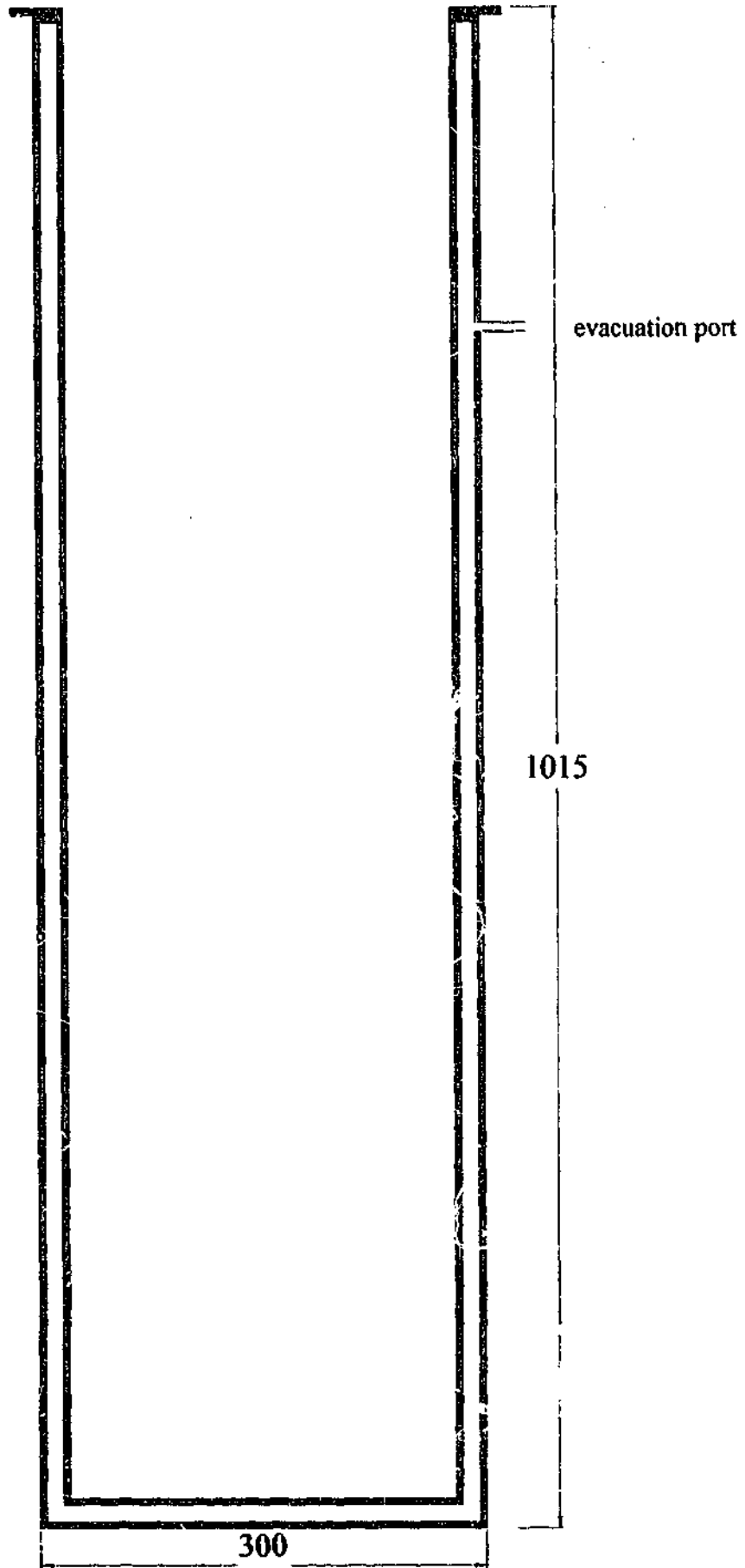
Side view colander
dimensions are in mm



**Side view of inner chamber
dimensions are in mm**

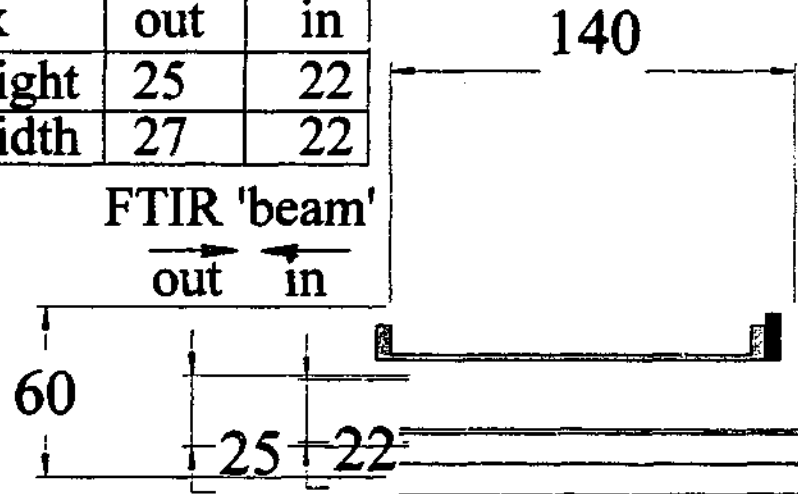


Side view Vacuum Chamber
Dimensions are in mm



dim. beam @ box	out	in
height	25	22
width	27	22

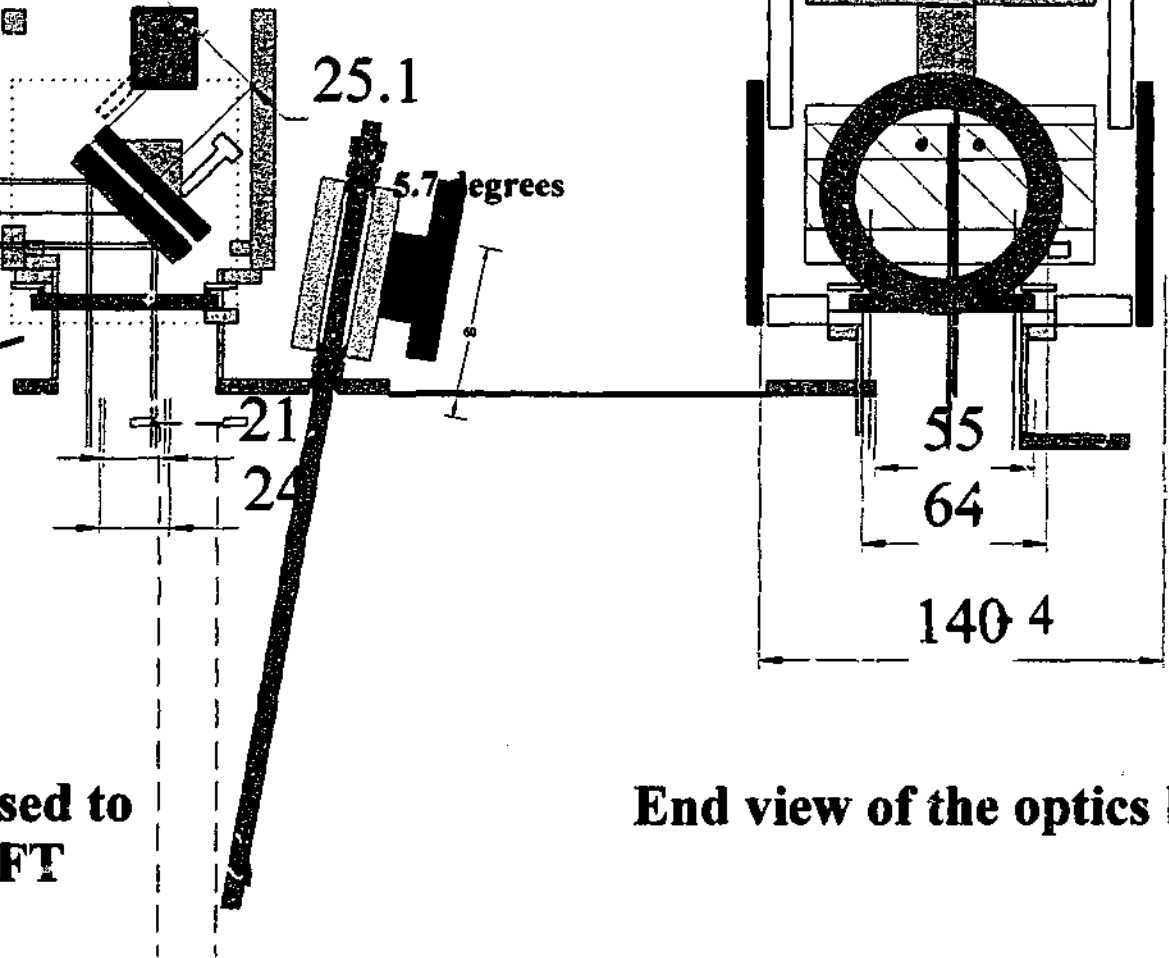
FTIR 'beam'
 out ← in →



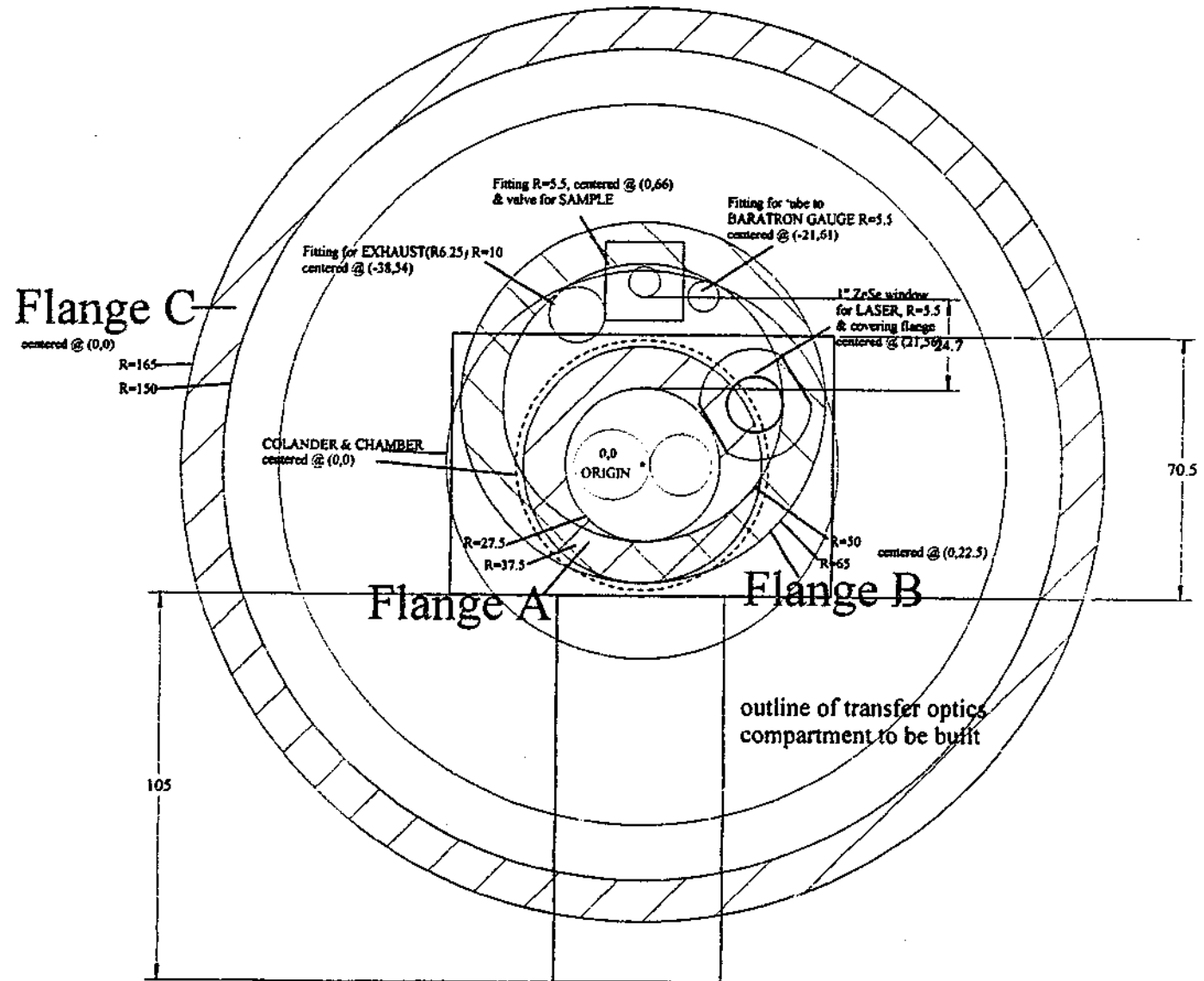
- Flange A R=37.5
- O ring + screws 10mm wide
- Flange B R=65
- O ring + screws 15mm wide

Side view of the transfer optics box used to direct the IR 'beam' to and from the FT spectrometer

Note: mirrors & mounts are offset from center line by 2.5 m



End view of the optics box



Top view of flanges of EFC cell

IX.C R^2 to N^2 transformation

Parameters of Brown's N^2 -Hamiltonian can be calculated from Zare's R^2 -Hamiltonian by using the following equations (see Brown *et al.*⁵ and Amiot *et al.*⁶)

$$\tilde{T}_e + \tilde{G}_v = T_v - B_v + \frac{a_v}{2} + \frac{(A_v - a_v)p_v}{4(A_v - a_v - 2B_v - q_v)}$$

$$\tilde{B}_v = B_v + \frac{q_v}{2}$$

$$\tilde{D}_v = D_v$$

$$\tilde{A}_v = (A_v - a_v) \left\{ 1 - \frac{p_v}{2(A_v - a_v - 2B_v - q_v)} \right\}$$

$$\tilde{p}_v = p_v$$

$$\tilde{q}_v = q_v$$

where parameters of Brown's N^2 -Hamiltonian are tilded, and $a_v = \frac{p_v A_v}{8B_v}$ as calculated by Veseth.⁷

IX.D C_s Character Table & Ground State Combination Differences for R152a

Table IX-1 C_s character table

C _s	E	σ	
a'	1	1	x,y,Rz
a''	1	-1	z, Rx,Ry

Table IX-2 Comparison of $R(J)-E''(J+2)$ and corresponding $P(J)$ wavenumber values

J'	Ka'	Kc'	J''	Ka''	Kc''	P-branch		obs-pred
						obs	pred	GSCD
12	12	0	13	13	0	1449.0947	1449.0950	-0.0003
13	13	0	14	14	0	1448.5303	1448.5306	-0.0004
14	14	0	15	15	0	1447.9705	1447.9704	0.0001
15	15	0	16	16	0	1447.4147	1447.4141	0.0007
16	16	0	17	17	0	1446.8617	1446.8613	0.0004
17	17	0	18	18	0	1446.3120	1446.3123	-0.0004
18	18	0	19	19	0	1445.7657	1445.7666	-0.0008
19	19	0	20	20	0	1445.2237	1445.2236	0.0000
20	20	0	21	21	0	1444.6835	1444.6835	0.0000
21	21	0	22	22	0	1444.1463	1444.1464	-0.0001
22	22	0	23	23	0	1443.6113	1443.6115	-0.0002
23	23	0	24	24	0	1443.0798	1443.0788	0.0010
24	24	0	25	25	0	1442.5483	1442.5486	-0.0003
25	25	0	26	26	0	1442.0207	1442.0203	0.0004
26	26	0	27	27	0	1441.4962	1441.4939	0.0022
27	27	0	28	28	0	1440.9678	1440.9697	-0.0018
28	28	0	29	29	0	1440.4453	1440.4474	-0.0021
29	29	0	30	30	0	1439.9264	1439.9263	0.0001
30	30	0	31	31	0	1439.4074	1439.4071	0.0003
31	31	0	32	32	0	1438.8904	1438.8895	0.0009
32	32	0	33	33	0	1438.3761	1438.3731	0.0030

References to Appendices

1. 515, M. S. D. S. M. C. R. N.
2. Lunn, G., and Sansone, E. B. *Analytical Biochemistry*, 147, 245 (1985).
3. 3411, M. S. D. S. M. C. R. N.
4. Shurvell, H. F., and Hyslop, D. W. *J. Chem. Phys.*, 52, 881 (1969).
5. Brown, J. M., Colbourn, E.A., Watson, J.K.G. and Wayne, F.D. *J. Mol. Spec.*, 74, 294 (1979).
6. Amiot, C., Maillard, J-P. and Chauville, J. *J. Mol. Spec.*, 87, 196 (1981).
7. Veseth, L. *J. Mol. Spec.*, 38, 228 (1971).

I.4 Bibliography

1. Dunham, J. L. *Phys. Rev.*, 41, 721 (1932).
2. Zare, R. N., Schmeltekopf, A.L., Harrop, W.J. and Albritton, D.L. *J. Mol. Spec.*, 46, 37 (1973).
3. Brown, J. M., Colbourn, E.A., Watson, J.K.G. and Wayne, F.D. *J. Mol. Spec.*, 74, 294 (1979).
4. Amiot, C., Maillard, J-P. and Chauville, J. *J. Mol. Spec.*, 87, 196 (1981).
5. Douay, M., Rogers, S.A., and Bernath, P.F. *Mol. Phys.*, 64, 425 (1988).
6. Kopp, I., and Hougen, J.T. *Can. J. Phys.*, 45, 2581 (1967).
7. Herzberg, G., and Teller, E. *Zeitsch. f. Physik*, B21, 410 (1933).
8. Renner, R. *Zeitsch. f. Physik*, 92, 172 (1934).
9. Hougen, J. T. *J. Chem. Phys.*, 36, 1874 (1962).
10. Herzberg, G. *Molecular Spectra & Molecular Structure. II Infrared and Raman Spectra of Polyatomic Molecules*, 9th ed. Princeton, New-Jersey, 1960.
11. Bunker, P. R., and Jensen, P. *Molecular Symmetry & Spectroscopy*, 2nd ed. Ottawa, Canada, 1998.
12. Bernath, P. F. *Spectra of Atoms and Molecules*; Oxford University Press, Inc.: New York, 1995.
13. Duxbury, G. *Infrared Vibration-Rotation Spectroscopy. From Free Radicals to the Infrared Sky* Chichester, 2000.
14. Ray, B. S. *Zeitsch. f. Physik*, 78, 74 (1932).
15. Dennison, D. M. *Rev. Mod. Phys.*, 3, 280 (1931).
16. King, G. W., Hainer, R. M., and Cross, P. C. *J. Chem. Phys.*, 11, 27 (1943).
17. Wang, S. C. *Phys. Rev.*, 34, 243 (1929).
18. Watson, J. K. G. *Vibrational Spectra & Structure* Amsterdam, 1977; Vol. 6.
19. Jahn, H. A. *Phys. Rev.*, 56, 680 (1939).

II.3 Bibliography

1. Johnston, S. F. *Fourier Transform Interferometry: A constantly evolving technology*; Ellis Horwood, 1991.
2. Griffiths, P. R., and de Haseth, J.A. *FT IR Spectrometry* New-York, 1986.
3. Gronholz, J. a. H., W. *Instruments and Computers*, 3, 10 (1985).
4. Glasser, L. *Journal of Chemical Education*, 64, A228 (1987).
5. Glasser, L. *Journal of Chemical Education*, 64, A260 (1987).
6. Glasser, L. *Journal of Chemical Education*, 64, A306 (1987).
7. Perkins, W. D. *J. Chem. Edu.*, 64, A269 (1987).
8. Bell, R. J. *Introductory Fourier Transform Spectroscopy*; Academic Press: New York, 1972.
9. Chesick, J. P. *Journal of Chemical Education*, 66, 128 (1989).
10. Cooley, J. W., and Tukey, J.W. *Math Comput.*, 19, 297 (1965).
11. McNaughton, D., McGilvery, D., and Shanks, F. *J. Mol. Spec.*, 149, 458 (1991).
12. McNaughton, D., McGilvery, D., and Robertson, E.G. *J. Mol. Struct.*, 348, 1 (1995).
13. Bernath, P. F., and McLeod, S. *J. Mol. Spec.*, 207, 287 (2001).
14. Pickett, H. M. *J. Mol. Spec.*, 148, 371 (1991).

III.3 Bibliography

1. Sterken, C., and Manfroid, J. *Astronomical Photometry: A guide*; Kluwer Academic, 1992.
2. McLean, I. S. *Electronic and Computer-aided astronomy: from eyes to electronic sensors*; Ellis Horwood Ltd, 1989.
3. Torr, M., and Torr, D. G. *Appl. Opt.*, 27, 619 (1988).
4. Clevenger, J. O., and Tellinghuisen, J. *Chem. Phys. Lett.*, 231, 515 (1994).
5. Boudreau, D., Laverdure, C., and Hubert, J. *Appl. Spectros.*, 43, 456 (1989).
6. Mutsukura, N., Kabayashi, K., and Machi, Y. *J. Appl. Phys.*, 66, 4688 (1989).
7. Iida, Y., Morikawa, H., Tsuge A., Uwanimo, Y., and Ishizuka, T. *Anal. Sci.*, 7, 61 (1991).
8. Khater, M. A., van Kampen, P., Costello, J. T., Mosnier, J. P., and Kennedy, E. T. *Appl. spec.*, 55, 1430 (2001).
9. Kruse, T., and Roth, P. *Int. J. Chem. Kinet.*, 31, 11 (1999).
10. Pavski, V., Chakrabarti, C. L. and Sturgeon, R. E. *J. Anal. At. Spectrom.*, 9, 1399 (1994).
11. Spiley, C. A. J., P., and Herick, K. *Electrophoresis*, 22, 829 (2001).
12. Soetebeer, U. B., Schierenberg M. O., Schulz, H., Grunefeld, G., Andresen, P., and Blaschke, G. *J. Chromat. B, Biomed Sci. and Applic.*, 745, 271 (2000).
13. Lakowicz, J. R., Szmecinski, H., Nowaczyk, K., and Johnson, M. L. *Proc. Natl. Acad. Sci. USA.*, 89, 1271 (1992).
14. Boyle, W. S., and Smith, G. E. *The Bell system Technical Journal*, 587 (1970).
15. Amelio, G. F., Thompsett, M. F. and Smith, G. E. *The Bell system Technical Journal*, 593 (1970).
16. Hill, R. S., Landsman, W. B., Lindler, D. and Shaw, R. "Cosmic Ray and Hot Pixel removal"; 1997 HST Calibration Workshop, 1997, Space Telescope Science Institute.

IV.4 Bibliography

1. Herzberg, G. *The Spectra and Structures of Simple Free Radicals*; Ithaca: Cornell University Press, 1972.
2. Setser, D. W. *Reaction Intermediates in the gas-phase*; Academic Press, New-York, 1979.
3. Smalley, R. E., Auerbach, D.A., Fitch, P.S. Levy, D.H. and Wharton, L. *J. Chem. Phys.*, 66, 3778 (1977).
4. Ahmad-Bitar, R., Lapatovich, W.P., Pritchard, D.E. and Renhorn, I. *Phys. Rev. Lett.*, 39, 1657 (1977).
5. Monts, D. L., Dietz, T.G., Duncan, M.A. and Smalley, R.E. *Chem. Phys.*, 45, 133 (1980).
6. Heaven, M., Miller, T.A. and Bondybey V.E. *Chem. Phys. Lett.*, 84, 1 (1981).
7. Rohlfing, E. A. *J. Chem. Phys.*, 89, 6103 (1988).
8. Farthing, J. W., Fletcher, I.W. and Whitehead J.C. *J. Phys. Chem.*, 87, 1663 (1983).
9. Brutschy, B., and Haberland H. *J. Phys.*, E10, 90 (1977).
10. Leasure, E. L., Mueller, C.R. and Ridley, T.Y. *Rev. Sci. Instrum.*, 46 (1975).
11. Searcy, J. Q. *Rev. Sci. Instrum.*, 45, 589 (1974).
12. McNaughton, D., Metha, G. F. and Tay, R. *Chem. Phys.*, 198, 107 (1995).
13. Patel, C. K. N., Faust, W. L. and McFarlane, R. A. *Bull. Am. Phys. Soc.*, 9, 500 (1964).
14. Patel, C. K. N., Tien, P. K. and McFee, J. H. *Appl. Phys. Lett.*, 7, 290 (1965).
15. Tardieu de Maleissye, J., Lempereur, F. and Marsal, C. *Compt. Rend. Acad. Sci. Paris, Ser. C*, 275, 1153 (1972).
16. De Hemptinne, M., and De Hemptinne, X. *Mem. Soc. Roy. Sci. Liege, Collect.* 80, 1, 21 (1971).
17. Shaub, W. M., and Bauer, S. H. *Int. J. Chem. Kinet.*, 7, 509 (1975).
18. Grady, A., Markwell, R. D., Russell, D. K., and Jones, A. C. *J. Cryst. Growth*, 106, 239 (1990).

19. Atiya, G. A., Grady, A. S., Jackson, S. A., Parker, N. and Russell, D. K. *J. Organomet. Chem.*, 378, 307 (1989).
20. Atiya, G. A., Grady, A. S., Russell, D. K. and Claxton, T. A. *Spectrochim. Acta Part A*, 47A, 467 (1991).
21. Grady, A., Markwell, Ross, D., and R. D., Russell, D. K. *J. Chem. Soc., Chem. Commun.*, 1, 14 (1991).
22. Grady, A., Markwell, R. D., Russell, D. K., and Jones, A. C. *J. Cryst. Growth*, 110, 739 (1991).
23. Russell, D. K. *Chem. Soc. Rev.*, 19, 407 (1990).
24. Steinfeld, J. I. *Laser Induced Chemical Processes*; Plenum: New-York, 1981.
25. *Spectrochim. Acta Part A*, 43, 129 (1987).
26. *Spectrochim. Acta Part A*, 46, 441 (1990).
27. Dunoyer, L. *Le Radium*, 8, 142 (1911).
28. Stern, O. *Z. Phys*, 7, 249 (1921).
29. Stern, O. *Z. Phys*, 39, 751 (1926).
30. Rodebush, W. H. *Rev. Mod. Phys*, 3, 392 (1931).
31. Kantrowitz, A., and Grey, J. *Rev. Sci. Instr.*, 22, 328 (1951).
32. Kistiakowsky, G. B., and Slichter, W. P. *Rev. Sci. Instr.*, 22, 333 (1951).
33. Becker, E. W., and Bier, K. *Z. Naturforsch.*, 9A (1954).
34. Becker, E. W., and Henkes, W. *Z. Phys.*, 146, 320 (1956).
35. Hagen, O., and Henkes, W. *Z. Naturforsch.*, 15A, 851 (1960).
36. Becker, E. W., Bier, K. and Henkes, W. *Z. Phys.*, 146, 333 (1956).
37. Henkes, W. *Z. Naturforsch.*, 16A, 842 (1961).
38. Bentley, P. G., Bishop, J. and Leece, J. *Instruments and Measurements*; Academic Press: New York, 1961.
39. Muntz, E. P. *Phys. Fluid*, 5, 80 (1962).
40. Smalley, R. E., Ramakrishna, B. L., Levy, D. H. and Wharton, L. *J. Chem. Phys.*, 61, 4363 (1974).
41. Smalley, R. E., Wharton, L. and Levy, D. H. *J. Chem. Phys.*, 63, 4977 (1975).
42. Smalley, R. E., Levy, D. H. and Wharton, L. *J. Chem. Phys.*, 64, 3266 (1976).
43. Smalley, R. E., Wharton, L., Levy, D. H. *J. Chem. Phys.*, 66, 2750 (1977).

44. Smalley, R. E., Wharton, L., Levy, D. H. and Chandler, D. W. *J. Mol. Spec.*, 66, 375 (1977).
45. Ryali, S. B., and Fenn, J. B. *Ber. Bunsen-Ges. Phys. Chem*, 88, 245 (1984).
46. Sherman, F. S. *Rarefied Gas Dynamics*; Academic Press Inc.: New York, 1963; Vol. 2.
47. Powers, D. E., Hopkins, J. B. and Smalley, R. E. *J. Phys. Chem.*, 85, 2711 (1981).
48. Amrein, A., Quack, M. and Schmitt, U. *J. Phys. Chem.*, 92, 5455 (1988).
49. Venkateshan, S. P., Ryali, S. B. and Fenn, J. B. *J. Chem. Phys.*, 77, 2599 (1982).
50. Anderson, J. B., and Fenn, J. B. *Phys. Fluid*, 8, 780 (1965).
51. von Engel, A. *Ionized Gases*; Clarendon Press: Oxford, 1965.
52. Perkins, J. R. Corona Measurements and Interpretation. In *Engineering Dielectrics*; Bartnikas, R., Ed.; American Society for Testing and Materials: Baltimore, 1979; Vol. 1; pp 3.
53. Blair, D. T. A. Breakdown in Gases. In *Electrical Insulation*; Bradwell, A., Ed.; Peter Peregrinus Ltd.: London, 1983; pp 1.
54. Grycz, B. *Fourth State of Matter*; Illife Books Ltd: Prague, 1966.
55. Engelking, P. C. *Chem. Phys. Lett.*, 96, 316 (1983).
56. Droege, A. T., and Engelking, P.C. *Chem. Phys. Letters*, 96, 316 (1983).
57. Carrick, P. G., and Engelking, P.C. *J. Chem. Phys.*, 81, 1661 (1984).
58. Engelking, P. C. *Rev. Sci. Instrum.*, 57, 2274 (1986).

V.5 Bibliography

1. Smith, G. P., Copeland, R.A. and Crosley, D.R. *J. Chem. Phys.*, *91*, 1987 (1989).
2. O'Dell, C. R., Miller, C.O., Cochran, A.L., Cochran, W.D., Opal, C.B. and Barker, E.S. *The Astrophys. J.*, *368*, 616 (1991).
3. Valk, J. H., O'Dell, C.R., Miller, C.O., Cochran, A.L., Cochran, W.D., Opal, C.B. and Barker, E.S. *The Astrophys. J.*, *388* (1992).
4. Jennings, K. R., and Linnett, J.R. *Trans. Faraday. Soc.*, *46*, 1737 (1960).
5. Herzberg, G., and Travis, D.N. *Can. J. Phys.*, *42*, 1658 (1964).
6. Milligan, D. E., Jacox, M.E., Comeford, J.J. and Mann, D.E. *J. Chem. Phys.*, *43*, 756 (1965).
7. Pontrelli, G. J., and Anastassiou, A.G. *J. Chem. Phys.*, *42*, 3735 (1965).
8. Kroto, H. W. *J. Chem. Phys.*, *44*, 831 (1966).
9. Kroto, H. W. *Can. J. Phys.*, *45*, 1439 (1967).
10. Okabe, H., and Mele, A. *J. Chem. Phys.*, *51*, 2100 (1969).
11. Thomson, C. *J. Chem. Phys.*, *58*, 841 (1972).
12. Williams, G. R. *Chem. Phys. Lett.*, *25*, 602 (1974).
13. Martin, J. M. L., Taylor, P.R., Francois, J.P. and Gijbels, R. *Chem. Phys. Lett.*, *226*, 475 (1994).
14. Suter, H. U., Huang, M.-B. and Engels, B. *J. Chem. Phys.*, *101*, 7686 (1994).
15. McNaughton, D., Metha, G.F. and Tay, R. *Chem. Phys.*, *198*, 107 (1995).
16. Tay-Lim, R. High Resolution Infrared Spectroscopy of Molecules Generated by Photolysis and Pyrolysis. Ph.D Thesis, Monash University, 1998.
17. Beaton, S. A., Ito, Y. and Brown, J.M. *J. Mol. Spec.*, *178*, 99 (1996).
18. Hensel, K. D., and Brown, J.M. *J. Mol. Spec.*, *180*, 170 (1996).
19. Beaton, S. A., and Brown, J.M. *J. Mol. Spec.*, *183*, 347 (1997).
20. Wienkoop, M., Urban W. and Brown, J.M. *J. Mol. Spec.*, *185*, 185 (1997).
21. Bise, R. T., Choi, H and Neumark, D.M. *J. Chem. Phys.*, *111*, 4923 (1999).

22. Peric, M., Krmar, M., Radic-Peric, J. and Hanrath, M. *J. Mol. Spec.*, 204, 226 (2000).
23. Rajendra, P., and Chandra, P. *J. Chem. Phys.*, 114, 1589 (2001).
24. Peric, M., Krmar, M., Radic-Peric, J. and Stevanovic, L. *J. Mol. Spec.*, 208, 271 (2001).
25. Marsh, F. D. *J. Org. Chem.*, 37, 2966 (1972).
26. Shurvell, H. F., and Hyslop, D.W. *J. Chem. Phys.*, 52, 881 (1970).
27. Thrush, B. A. *Proc. R. Soc. London Ser.*, A235, 143 (1956).
28. Haas, T., and Gericke, K-H. *Ber. Bunsenges. Phys. Chem.*, 95, 1289 (1991).
29. Douglas, A. E., and Jones, W.J. *Can. J. Phys.*, 43, 2216 (1965).
30. Brazier, C. R., Bernath, P.F, Burkholder and Howard, C.J. *J. Chem. Phys.*, 89, 1762 (1988).
31. Pearse, R. W. B., and Gaydon, A.G. *The Identification of Molecular Spectra*, Third ed.; The Whitefriars Press, Ltd.: London, 1963.
32. Huber, K. P., and Herzberg, G. *Molecular Spectra and Molecular Structure IV. Constants of Diatomic Molecules*; van Nostrand Reinhold Company: New York, 1979.
33. Hougen, J. T. *J. Chem. Phys.*, 36, 1874 (1962).

VI.5 Bibliography

1. Quick Jr., C. R., and Wittig, C. In *Electronic Transition Lasers, I*; Steinfeld, J. I., Ed.; M.I.T Press: Cambridge, Mass., 1976; pp 225.
2. West, G. A., and Berry, M.J. *J. Chem. Phys.*, *61*, 4700 (1974).
3. Jenkins, F. A., Roots, Y.K. and Mulliken, R.S. *Phys. Rev.*, *39*, 16 (1932).
4. Douglas, A. E., and Routly, P.M. *Astrophys. J. Supp.*, *1*, 295 (1955).
5. Kotlar, A. J., Field, R.W. and Steinfeld, J.I. *J. Mol. Spec.*, *80*, 86 (1980).
6. Prasad, C. V. V., Bernath, P.F., Frum, C. and Engelman, R. *J. Mol. Spec.*, *151*, 459 (1992).
7. Prasad, C. V. V., and Bernath, P.F. *J. Mol. Spec.*, *156*, 327 (1992).
8. Huber, K. P., and Herzberg, G. *Molecular Spectra and Molecular Structure IV. Constants of Diatomic Molecules*; van Nostrand Reinhold Company: New York, 1979.
9. Heurlinger, T. *Zeits. Physik*, *1*, 82 (1920).
10. Asundi, R. K., and Ryde, J.W. *Nature*, *124*, 57 (1929).
11. Wager, A. T. *Phys. Rev.*, *64*, 18 (1943).
12. Herzberg, G., and Phillips J.G. *Astrophys. J.*, *108*, 163 (1948).
13. Kiess, N. H., and Broida, H.P. *J. Mol. Spec.*, *7*, 194 (1961).
14. Davis, S. P., and Phillips J.G. *The Red System ($A^2\Pi-X^2\Sigma$) of the CN molecule* Berkeley, California, 1963.
15. Jeunehomme, M. *J. Chem. Phys.*, *42*, 4086 (1965).
16. LeBlanc, F. J. *J. Chem. Phys.*, *48*, 1980 (1968).
17. Fay, T., Marenin, I. and van Citters, W. *J. Quant. Spectrosc. Radiat. Transfer*, *11*, 1203 (1971).
18. Schaefer, H. F., and Heil, T.G. *J. Chem. Phys.*, *54*, 2573 (1971).
19. Treffers, R. R. *The Astrophys. J.*, *196*, 883 (1975).
20. Dixon, T. A., and Woods, R.C. *J. Chem. Phys.*, *67*, 3956 (1977).
21. Cerny, D., Bacis, R., Guelachvili, G. and Roux, F. *J. Mol. Spec.*, *73*, 154 (1978).
22. Katamaya, D. H., Miller, T.A. and Bondybey, V.E. *J. Chem. Phys.*, *71*, 1662 (1979).

23. Zare, R. N., Schmeltekopf, A.L., Harrop, W.J. and Albritton, D.L. *J. Mol. Spec.*, 46, 37 (1973).
24. Davies, P. B., and Hamilton, P.A. *J. Chem. Phys.*, 76, 2127 (1982).
25. Cartwright, D. C. a. H., P.J. *The Astrophys. J.*, 257, 383 (1982).
26. Skatrud, D. D., De Lucia, F.C., Blake, G.A. and Sastry, K.V.L.N. *J. Mol. Spec.*, 99, 35 (1983).
27. Taherian, M. R. a. S., T.G. *J. Chem. Phys.*, 81, 3814 (1984).
28. Richard, E. C., Donaldson, D.J. and Vaida, V. *Chem. Phys. Lett.*, 157, 295 (1989).
29. Ito, H., Kuchitsu, K., Yamamoto, S. and Saito, S. *Chem. Phys. Lett.*, 186, 539 (1991).
30. Davis, S. P., Abrams, M.C., Rao, M.L. and Brault, J.W. *J. Opt. Soc. Am. B*, 8, 198 (1991).
31. Rehfuss, B. D., Suh, M-H., Miller, T.A. and Bondybey, V.E. *J. Mol. Spec.*, 151, 437 (1992).
32. Engelman, R. *J. Mol. Spec.*, 49, 106 (1974).
33. Klisch, E., Klaus, Th., Belov, S.P., Winnewisser, G. and Herbst, E. *Astron. Astrophys.*, 304, L5 (1995).
34. Liu, Y., Duan, C., Liu, H., Gao, H., Guo, Y., Liu, X. and Lin, J. *J. Mol. Spec.*, 205, 16 (2001).
35. Brown, J. M., Colbourn, E.A., Watson, J.K.G. and Wayne, F.D. *J. Mol. Spec.*, 74, 294 (1979).
36. Amiot, C., Maillard, J-P. and Chauville, J. *J. Mol. Spec.*, 87, 196 (1981).
37. Johnson, M. A., Alexander, M.L., Hertel, I. and Lineberger, W.C. *Chem. Phys. Lett.*, 105, 374 (1984).

VII.5 Bibliography

1. Watanabe, A., and Welsh, H.L. *Can. J. Phys.*, **43**, 818 (1965).
2. Herzberg, G. *Astrophys. J.*, **115**, 337 (1952).
3. Messer, J. K. a. D. L., F.C. *Phys. Rev. Lett.*, **53**, 2555 (1984).
4. Wiley, D. R., Crownover, R.L., Bittner, D.N. and De Lucia, F.C. *J. Chem. Phys.*, **89**, 1923 (1988).
5. Wiley, D. R., Bittner, D.N. and De Lucia, F.C. *J. Mol. Spec.*, **133**, 182 (1989).
6. Goyette, T. M., Ebenstein, W.L. and De Lucia F.C. *J. Mol. Spec.*, **140**, 311 (1990).
7. Wiley, D. R., Choong, V. and De Lucia, F.C. *J. Chem. Phys.*, **96**, 898 (1991).
8. Flatin, D. C., Goyette T.M., Beaky, M.M., Ball, C.D. and De Lucia, F.C. *J. Chem. Phys.*, **110**, 2087 (1999).
9. Barnes, J. A., Gough, T.E. and Stoer, M. *Rev. Sci. Instrum.*, **60**, 406 (1988).
10. Barnes, J. A., Gough, T.E. and Stoer, M. *J. Phys. Chem.*, **97**, 5495 (1993).
11. Wiley, D. R., Ross, K.A., Dunjko, V. and Mantz, W. *J. Mol. Spec.*, **168**, 301 (1994).
12. Wiley, D. R., Ross, K.A., Mullin, A.S., Schowen, S., Zheng, L. and Flynn, G. *J. Mol. Spec.*, **169**, 66 (1995).
13. Newnham, D., Ballard, J. and Page, M. *Rev. Sci. Instrum.*, **66**, 4475 (1995).
14. Bauerecker, S., Taucher, F., Weitkamp, C., Michaelis, W. and Cammenga, H.K. *J. Mol. Struct.*, **348**, 237 (1995).
15. Taucher, F., Weitkamp, C., Michaelis, W., Cammenga, H.K., and Bauerecker, S. *J. Mol. Struct.*, **348**, 243 (1995).
16. Bauerecker, S., Taucher, F., Weitkamp, C. and Cammenga, H.K. *SPIE Proceedings*, **2834**, 257 (1996).
17. Taucher, F., Weitkamp, C., Cammenga, H.K. and Bauerecker, S. *Spectrochimica Acta A*, **52**, 1023 (1996).
18. Kunzmann, M. K., Signorell, S., Taraschewski, M. and Bauerecker, S. *Phys. Chem. Chem. Phys.*, **3**, 3742 (2001).

VIII.5 Bibliography

1. Dotto, L., and Schiff, H. *The Ozone War*, 1978.
2. Stolarski, R. S., and Cicerone, R.J. *Can. J. Chem.*, 52, 1610 (1974).
3. Molina, M. J., and Rowland, F.S. *Int. Conf. Environ. Impact Aerosp. Oper. High Atmos.*, 99 (1974).
4. Rowland, F. S., and Molina, M.J. *Rev. Geophys. Space Phys.*, 13, 1 (1975).
5. Rowland, F. S., and Molina, M.J. *Science*, 190, 1038 (1975).
6. - "Invented by Du Pont scientists in the 1930's, the numbering system describing CFC's, HCFC's and HFC's is called the "rule of 90". The digits of the number resulting from the addition of 90 to the compound number reveals the number of carbon, hydrogen and fluorine atoms respectively. In the case of CFC's and HCFC's, any remaining atoms are chlorine atoms.,".
7. Auwera, J. V. *J. Quant. Spectrosc. Radiat. Transfer*, 66, 143 (2000).
8. Crowder, G. A. *Tex. J. Sci.*, 26, 571 (1975).
9. Chen, Z., Tang, X., Wang, M. and Shao, K. *Huanjing Kexue Xuebao*, 16, 258 (1996).
10. Smith, D. C., Saunders, R.A., Nielsen, J.R. and Ferguson, E.E. *J. Chem. Phys.*, 20, 847 (1952).
11. Solimene, N., and Dailey, B.P. *J. chem. Phys.*, 22, 2042 (1954).
12. Pylaeva, L. E., Klochkovskii, Y.V., Sverdlov, L.M. *Izv. Vyssh. Ucheb. Zaved.*, 11, 111 (1968).
13. Guirgis, G. A., and Crowder, G.A. *J. Fluorine Chem.*, 25, 405 (1984).
14. Lucas, K., Delifs, V.B. and Speis, M. *Int. J. Thermophys.*, 14, 993 (1993).
15. Villamañan, R. M., Chen, W.D., Wlodarczak, G., Demaison, J., Lessari, A.G., López, J.C. and Alonso, J.L. *J. Mol. Spec.*, 171, 223 (1995).
16. McNaughton, D., and Evans, C. *J. Phys. Chem.*, 100, 8660 (1996).
17. Tai, S. P., S., Kenny, J.E., Gilbert, B.D. Janni, J.A., Steinfeld, J.I., Taylor, J.D. and Wienstein, R.D. *Spectrochimica Acta A*, 55, 9 (1999).
18. McKean, D. *J. Phys. Chem. A*, 104, 8995 (2000).
19. Pickett, H. M. *J. Mol. Spec.*, 148, 371 (1991).
20. Evans, C. J. *Jet Spectroscopy and the Analysis of complicated Vibration-Rotation Spectra.*, Monash University, 1998.

21. McNaughton, D., McGilvery, D. and Shanks, F. *J. Mol. Spec.*, 149, 458 (1991).
22. Loo, D.-L., Clouthier, D. J., Chan, C. P., Lai, V. W.-M., Ma, E. S. F., and Merer, A. J. *J. Mol. Spec.*, 171, 113 (1995).
23. M. J. Frisch, G. W. T., H. B. Schlegel, G. E. Scuseria, M. A. Robb, J. R. Cheeseman, V. G. Zakrzewski, J. A. Montgomery, Jr., R. E. Stratmann, J. C. Burant, S. Dapprich, J. M. Millam, A. D. Daniels, K. N. Kudin, M. C. Strain, O. Farkas, J. Tomasi, V. Barone, M. Cossi, R. Cammi, B. Mennucci, C. Pomelli, C. Adamo, S. Clifford, J. Ochterski, G. A. Petersson, P. Y. Ayala, Q. Cui, K. Morokuma, N. Rega, P. Salvador, J. J. Dannenberg, D. K. Malick, A. D. Rabuck, K. Raghavachari, J. B. Foresman, J. Cioslowski, J. V. Ortiz, A. G. Baboul, B. B. Stefanov, G. Liu, A. Liashenko, P. Piskorz, I. Komaromi, R. Gomperts, R. L. Martin, D. J. Fox, T. Keith, M. A. Al-Laham, C. Y. Peng, A. Nanayakkara, M. Challacombe, P. M. W. Gill, B. Johnson, W. Chen, M. W. Wong, J. L. Andres, C. Gonzalez, M. Head-Gordon, E. S. Replogle, and J. A. Pople. Gaussian 98; Revision A.11.3 ed.; Gaussian, Inc.: Pittsburg PA., 2002.